AN EMPIRICAL APPROACH TO SIMULATE THE CONCRETE SOFTENING MECHANISM

A MASTER THESIS
SUBMITTED TO THE SCHOOL OF CIVIL, ENVIRONMENTAL
AND MINING ENGINEERING
UNIVERSITY OF ADELAIDE
FOR THE DEGREE OF
MASTER OF ENGINEERING SCIENCE

By
RATNI NURWIDAYATI
October 2011

ABSTRACT

Material properties of concrete play an important role in the analysis of reinforced concrete RC members. One of the most commonly used material properties is the compressive stress strain σ-ε relationship. Uniaxial compression tests on concrete cylinders are used to obtain these material properties of concrete in compression. These tests are effective up to peak stress, but have limited applicability post-peak stress, primarily due to the influence of size. These cause the absence of an accurate material softening stress-strain relationship. Hence, the post-peak softening behavior of a reinforced concrete member is not been able to be simulated accurately since there is not an accurate softening σ-ε relationship for concrete. An alternative approach is required.

Recently, shear friction theory has been used to simulate the softening behavior of concrete. Shear friction theory quantifies the relationship between the shear stress, normal stress, displacement and separation of the softening concrete in relation to the adjacent (non softening) concrete. In this thesis, an approach is presented to extract the shear-friction softening properties of concrete from experimental tests on long concrete prisms. Empirical mathematical expressions are developed which quantify the relationship between the softening stress and the displacement of the softening wedge. These empirical stress-displacement expressions are then applied to the analysis of eccentrically loaded concrete prisms. The theoretical analyses of these eccentrically loaded prisms agree well with the experimental results, indicating the applicability of using this approach to extract the softening shear-friction properties of concrete, from prism tests, and subsequently using these empirical expressions to simulate the post peak response of concrete.

STATEMENT ORIGINALITY

I, Ratni Nurwidayati certify that this work contains no material which has been accepted for the award of any other degree or diploma in any university or other tertiary institution and, to the best of my knowledge and belief, contains no material previously published or written by another person, except where due reference has been made in the text.

I give consent to this copy of my thesis, when deposited in the University Library, being available for loan and photocopying, subject to the provisions of the Copyright Act 1968.

I also give permission for the digital version of my thesis to be made available on the web, via the University's digital research repository, the Library catalogue and also through web search engines, unless permission has been granted by the University to restrict access for a period of time.

Ratni Nurwidayati Date

LIST OF PUBLICATION

The following journal paper was written based on the work presented in this thesis.

Nurwidayati, R., Haskett, M., Oehlers, D. J., and Wu, C. (2011). “Wedge based concrete compression failure in RC members.” Submitted to Materials and Structures.

PUBLICATION

Wedge based concrete compression failure in RC members

[1]Ratni Nurwidayati, [2]Matthew Haskett, [3]Deric J. Oehlers and [4]Chengqing Wu

Mrs. Ratni Nurwidayati
[1]Masters student
School of Civil, Environmental and Mining Engineering
University of Adelaide
South Australia 5005
AUSTRALIA

Corresponding author:
[2]Dr. Matthew Haskett
Research Associate
School of Civil, Environmental and Mining Engineering
University of Adelaide
South Australia 5005
AUSTRALIA
email: mhaskett@civeng.adelaide.edu.au
Tel. +61 8 8303 3710
Fax. +61 8 8303 4359

[3]Professor Deric J. Oehlers
School of Civil, Environmental and Mining Engineering
University of Adelaide
South Australia 5005
AUSTRALIA

[4]Dr. Chengqing Wu

Senior Lecturer,

School of Civil, Environmental and Mining Engineering

University of Adelaide

South Australia 5005

AUSTRALIA

1/7/11
Submitted to Materials and Structures

Wedge based concrete compression failure in RC members

R. Nurwidayati · M. Haskett · D. J. Oehlers · C. Wu

Abstract It is generally accepted that the ductility of a reinforced concrete member is a very important parameter as it governs such things as moment redistribution, moment magnification and the ability to absorb energy. Quantifying the ductility of RC members has been an almost intractable problem for a number of reasons, one of which is that it is difficult to replicate the behaviour of the compression wedge that is formed when concrete softens. A common approach used to quantify the ductility is to use concrete softening stress-strain relationships in conjunction with hinge lengths both of which have to be derived empirically. However these softening stress-strain relationships, that are derived from cylinder tests, have been found to be both size and shape dependent and it has been even more difficult to find empirically derived hinge lengths that are generic. An alternative approach is described in this paper in which the behaviour of the compression wedges are measured directly from simple tests on uniaxially loaded prisms of varying dimensions. It is shown how these prism tests in which there is a uniform strain can be used in the analysis of the compression zone of flexural members in which there is a strain gradient and without the need for hinge lengths. It is suggested that this may be a useful approach in developing new concrete products such as very high strength concrete or fibre concrete, as the effect of the new concrete product on the ductility of flexural members of any cross-sectional properties can be ascertained through a relatively few simple experimental prism tests.

Keywords *Reinforced concrete · Reinforced concrete ductility · Concrete · Concrete softening*

1. Introduction

Tests of reinforced concrete members clearly shows that failure of the concrete in compression, that is the softening of concrete, is associated with the formation of compression wedges [1-3] as in Fig. 1 and researchers have studied this directly through tests on eccentrically loaded prisms [4,5]. However, it is common in research practice not to quantify concrete compressive failure directly through measuring the behaviour of the wedge, but indirectly through the stress-strain relationships from compressive cylinder tests whilst softening [6,7,8]. Unfortunately this indirect approach of using softening stress-strain relationships has been found to be both size and shape dependent [9-13] which limits its application. Furthermore, the use of these empirically derived softening stress-strain

relationships in the analysis of RC members necessitates the use of empirically derived hinge lengths [14-18] which are themselves difficult to quantify [18].

To overcome the problems mentioned above that are associated with concrete softening, an alternative approach is proposed in this paper for quantifying the softening of concrete. It is shown how the behaviour of compression wedges can be measured directly from compression tests on axially loaded rectangular prisms of varying dimensions in which the deformation or effective strain profile is uniform. Furthermore, it is shown how these results can be used to quantify the behaviour of compression wedges in flexural members where the deformation or effective strain profile is no longer uniform but varies linearly. Hence the effect of the concrete on the ductility, that is the rotation at a hinge, can be quantified from a relatively few number of simple prism tests and used to simulate the formation of hinges in RC members of any cross-section. It is suggested that this may be a useful approach in the development of new concrete products, such as high strength concrete, concrete made from pulverised fly ash or concrete with steel or polymer fibres, if the effect of the concrete on the member ductility is important.

The fundamental principles that govern this wedge based approach are first described for uniformly loaded rectangular sections and it is then shown how it can be applied to flexurally loaded members such as in beams. In order to illustrate this approach, a series of tests for quantifying the wedge behaviour are then described and the results used to analysis the compression region in beams as occurs in eccentrically loaded prisms [4,5]. The aim of this paper is not to specifically quantify the behaviour of concrete softening wedges but to illustrate how the wedge behaviour can be quantified and the results used in flexural members to quantify their rotational capacity.

2. Wedge based model

The wedge based model assumes that the concrete material remains linear elastic, that is it has a constant modulus of E_c, and that any non-linearity that might occur is due to micro-cracking along planes that allows shear deformations associated with shear-friction theory [19-22]. The wedge base model is first explained in the context of a prism as in Fig. 2(a) where the displacements δ_a are applied uniformly along the width of the prism $2d_w$ such

that the effective strain δ_a/L_{def} is uniform across the prism width. The wedge based model is then applied to an eccentrically loaded prism where the displacement δ and effective strain δ/L_{def} vary linearly as occurs in flexural members.

2.1 Rectangular axially loaded prisms

Consider the prism in Fig. 2(a) of height $2L_{def}$ and width $2d_w$. Let us assume that the depth of the prism into the page is very large so that the behaviour of cross-sections within the page are identical which simplifies this to a two-dimensional behaviour. A uniform pressure σ is applied to the horizontal surface which induces a contraction $2\delta_a$ over the depth $2L_{def}$. Each half of the prism behaves identically being subjected to a contraction δ_a over a length L_{def}.

The prism in Fig. 2(a) can be tested to failure and the results plotted as in Fig. 3 where the abscissa will be referred to as the effective strain ε_{eff} which is the measured overall contraction over the prism length that is δ_a/L_{def} in Fig. 2(a). On loading in Fig. 3, the stress/effective-strain relationship may be considered to follow a linear path O-A, with a modulus E_c up to a stress αf_p, after which non-linearity occurs in the ascending portion A-C, where the strength peaks at f_p, followed by a descending portion C-D which is often referred to as softening. In the wedge based model, this non-linearity is associated with the formation of micro-cracks in the region of inclined wedge shaped planes as in Fig. 2(b) which allow shearing across the inclined planes to accommodated the non-linearity shown in Fig. 3. For example, the plane A-F in Fig. 2(b) which contains both B-C and D-E on opposing sides of potential sliding planes, will deform through micro-cracking to allow the deformation shown in Fig. 2(c) where sliding of the wedge from B to C shortens the prism by S_w such that the effective strain due to sliding S_w/L_{def} is the non-linear strain in Fig. 3 which in the ascending branch is shown as $\varepsilon_{n\text{-}mic\text{-}asc}$ and that in the descending branch as $\varepsilon_{n\text{-}mic\text{-}des}$. It can be seen in Fig. 2(c) that this sliding action must be accommodated by localised crushing as shown to allow the wedges to move sideways which is the dilation of the member which can be measured [23] but is not the subject of this paper.

In summary, the effective strain ε_{eff} in Fig. 3 consists of the material strain ε_{mat} and that due to micro-cracking ε_{mic}. Another way of visualizing this behaviour is that the

components of the prism A-B, C-D and E-F in Fig. 2(c) when subjected to a stress σ_n can only contract through material contraction δ_{mat} by $\varepsilon_{n\text{-}mat}L_{def}$ where $\varepsilon_{n\text{-}mat}$ is σ_n/E_c and the remaining deformation δ_S can only be accommodated by wedge sliding S_w such that $\varepsilon_{n\text{-}mic}$ is equal to S_w/L_{def}. Hence the total deformation δ in Fig. 2(c) is the sum of δ_{mat} and δ_S.

The prism in Fig. 2(c) consists of four wedges. Let us consider the single wedge in the upper right quadrant which is shown in Fig. 4. The distance L_{def} is any convenient distance that encapsulates the length of the wedge L_w and d_w is now the depth of the wedge. It can be seen that the uniform displacement δ_n which imposes a stress σ_n causes a uniform slip along the sliding plane that causes a contraction S_n. It can also be seen that the effects of micro-cracking which occurs over a finite region are represented by a sliding action along a plane which is referred to as shear-friction theory. The effective strain $\varepsilon_{n\text{-}eff}$ in the quadrant in Fig. 4 is δ_n/L_{def} which comprises that due to the elastic deformation ε_{mat} that is σ_n/E_c and that due to the contraction due to micro-cracking S_n/L_{def}. Hence the contraction due to micro-cracking is given by

$$S = \left(\varepsilon_{eff} - \epsilon_{mat}\right)L_{def} \qquad (1)$$

Equation 1 can be used to convert the effective strains which can be measured experimentally, to contractions S due to micro-cracking as in Fig. 5 where S_p is the contraction at the peak stress f_p. Hence the variation in Fig. 5 can be obtained directly from prism tests as in Fig. 2 and used to determine the behaviour of wedges in prisms as in Fig. 4 where the deformation is uniform. However, in beams the deformation is not uniform which is the subject of the following section.

2.2 Flexurally loaded beams

The prism in Fig. 2(a) which is subjected to a concentric load is now subjected to an eccentric load as in Fig. 6. Because of the eccentricity of load, the deformation δ is now no longer uniform but varies from δ_L on the left to δ_R on the right so that there is a linear variation in the effective strains δ/L_{def} and a rotation θ. Because of the eccentricity of load, a

wedge first forms on the loaded side of the prism as shown in which the depth of the wedge d_w is no longer equal to half the width of the prism d.

The bottom half of the prism in Fig. 6 is shown rotated by 90^o in the clockwise direction in Fig. 7(e). The surface of the prism, A-A in Fig. 7(d), is now subjected to a compressive deformation at the top δ_T and a tensile deformation at the bottom δ_B such that there is a linear variation of the effective strain ε_{eff} in Fig. 7(c) from δ_T/L_{def} at the top to δ_B/L_{def} at the bottom. Micro-cracking starts at a stress αf_p in Fig. 3; this stress αf_p is shown in Fig. 7(b), the accompanying strain $\alpha f_p/E_c$ in Fig. 7(c), and the accompanying deformation $(\alpha f_p/E_c)L_{def}$ in Fig. 7(d) which is shown as line B-B. Hence any deformation within the prism that is greater than the deformation of line B-B requires micro-cracking. Hence any deformation above point C in Fig. 7(d) requires micro-cracking which, therefore, fixes the depth of the wedge d_w as shown.

Let us first consider the behaviour below point C in Fig. 7(d). The linear deformation C-E produces the effective linear strain distribution F-G-H in Fig. 7(c). If the concrete cracks in tension at ε_{ct} at level G, then the strain distribution F-G is a real strain distribution, that is it is a material strain distribution. Hence, the stresses in this region F-G in Fig. 7(b) can be determined from the concrete modulus. Subsequently, the forces in this region can be determined as in Fig. 7(a) where $F_{el.c}$ is the force in the elastic concrete compression region and $F_{el.t}$ is the force in the elastic tension region. If the concrete cracks in tension at level G in Fig. 7(c), then G-H is an effective strain. If reinforcing bars intercepted this crack, then the force in the reinforcing bar F_r would depend on both the crack width Δ_r in Fig. 7(d) and the bond-slip properties, which is dealt with elsewhere using partial-interaction theory [24-29] as this paper is only dealing with concrete under compression.

Let us now consider the behaviour in the micro-cracking region in Fig. 3 that is above point C in Fig. 7(d). Consider level n where the prism must accommodate the deformation H-I. Part of this deformation H-J is accommodated by concrete material straining ε_{mat} as shown in Fig. 7(c) such that the deformation due to material straining H-J is given by $(\sigma_n/E_c)L_{def}$ and the remaining deformation J-I is due to micro-cracking contraction S_n at the wedge interface as shown in Fig. 7(e). It is simple a question of finding the stress σ_n such that the material contraction $\sigma_n L_{def}/E_c$ plus the micro-cracking contraction

from Fig. 5, $S_{n\text{-}asc}$ or $S_{n\text{-}des,}$ depending on whether it is in the ascending or descending branch, equals the required deformation H-I in Fig. 7(d). From this analysis of the wedge, where the depth of which d_w is usually divided into segments in which each segmental is assumed to have a uniform stress, the resulting force in the wedge and its position F_w in Fig. 7(a) can be determined.

The resultant of the forces in Fig. 7(a) and its position can now be determined. If the eccentrically loaded prism in Fig. 6 is being analysed, then the resultant of the forces in Fig. 7(a) needs to be in line with P and this can be obtained by pivoting the displacement D-E in Fig. 7(d) about D until the resultant force is in line. If a beam were being analysed, then it is simply a question of pivoting about D until the resultant force was zero.

3. Rectangular prism tests

These tests [23] were performed simply to illustrate how the wedge properties required for the flexural analysis depicted in Fig. 7 could be obtained from prism tests as depicted in Fig. 2; as such they are not meant to be a comprehensive quantification of the wedge properties.

Four different sizes of prisms were chosen [23] with a width ($2d_w$ in Fig. 2(a)) to height ($2L_{def}$) to depth ratio of 1:2:4 as shown in Table 1 and in Fig. 8. Theoretical shear-friction research on the formation of wedges [19] would suggest that the wedge can be contained within prisms of width to height ratio of 1:2 as in Fig. 8(a). If the height were any less with respect to the width then the platen restraints at the ends would affect the angle of wedge that is α in Fig. 7(e). Wedges form as shown in Fig. 8(a) where the wedge forms into the width ($2d_w$) and over the depth of the specimen. However, they also form at the ends and into the depth and over the width ($2d_w$) of the specimen. Deep specimens, that is specimens as in Fig. 8(b) where the depth was much greater than the width, were chosen so that the wedge formation as in Fig. 8(a) would dominate the behaviour so that the behaviour could be assumed to be two-dimensional.

The elastic modulus of the concrete material was derived from standard cylinder tests [23]. The contraction of the specimens were measured with transducers [23] so from Eq. 1 can be derived the contraction due to wedge slip S. Three or four specimens of each

size were tested and the average of the results for each size is plotted in Fig. 9. The average peak stress f_p and contraction at peak stress S_p are recorded in Table 1 and these were used to non-dimensionalise Fig. 9 as shown in Fig. 10. Curve fitting of Fig. 10 gave the following expression for micro-cracking displacement S for a given stress σ

$$\frac{\sigma}{f_p} = \left[-0.65\left(\frac{S}{S_p}\right)^2 + 5.71\left(\frac{S}{S_p}\right) + 5.04\right] EXP\left[0.03\left(\frac{S}{S_p}\right)^2 - 0.50\left(\frac{S}{S_p}\right) - 1.87\right] \quad (2)$$

where f_p had an average value of 43 MPa and s_p was found to be a function of depth of wedge d_w as follows

$$S_p = 0.0025\, dw \quad (3)$$

Equation 2 provided an accurate fit to the experimental results, as shown in Fig. 11.

4. Analysis of eccentrically loaded prism tests

The analysis depicted in Fig. 7 and using the wedge properties in Eqs. 2 and 3 was applied to Daniel et al's test specimens [5]. The specimens as represented in Fig. 6 had a width *d* of 300mm, height $2L_{def}$ of 360 mm, depth into the page of 180 mm, an average concrete strength of 33 MPa and were tested at eccentricities *e* of 60, 70 and 85 mm. It may be worth noting that the average concrete strength of the prism used to derive Eqs. 2 and 3 was 43 MPa, hence, the shape of the variations in material properties given by Eqs. 2 and 3 and illustrated in Fig. 11 are really only applicable to this strength of concrete. However, to illustrate this analysis technique it has been applied to Daniel et al's specimens which were a bit weaker at 33 MPa.

A typical comparison of the moment-rotations is shown in Fig. 12. Two experimental tests were performed at this eccentricity and these are shown as unbroken lines; the difference between these tests is a gauge of the scatter that can be expected even from supposedly identical specimens and tests. The test results have been compared with the results of theoretical analyses with variations in concrete strength from 43 MPa to

28MPa and which are shown as broken lines. Bearing in mind the scatter between the test results, it is suggested that the shape of the theoretical results compare well with those of the tests. It can be seen that this new approach can simulate the moment-rotation softening without the need for empirical hinge lengths nor softening stress-strain relationships.

The main interest of this research is the non-linearity due to micro-cracking as already illustrated in Fig. 5 for prism tests. Dividing the abscissa θ of Fig. 12 by L_{def} gives the curvature χ. In which case, the initial stiffness or tangent stiffness of the rising branch in Fig. 12 would be the elastic flexural rigidity EI and divergence from this would be due to flexural cracking and micro-cracking. This divergence due to cracking which is the main interest of this research has been plotted in Figs. 13 to 15 for each test specimen in which the eccentricities were 60, 70 and 85mm. It is suggested that the results show that the model can closely represent softening.

The above wedge based analyses have been applied to eccentrically loaded flexural members without any reinforcement as illustrated in Fig. 6. As already explained in the wedge based analyses depicted in Fig. 7, these analyses could also have been applied to reinforced flexural members where the force in the longitudinal reinforcement is a function of Δ_r in Fig. 7(d) [26, 27 and 29]. It can, therefore, be seen that once the wedge properties, such as those in Eqs. 2 and 3, have been derived from prism tests, as in Fig. 8, they can be used to derive the ductility of any reinforced concrete beam such as that in Fig. 1.

5. Conclusions

Quantifying concrete softening and the region over which softening occurs using softening stress-strain relationships and empirical hinge lengths has proved to be a very difficult problem. An alternative approach is described in which the concrete softening behaviour is measured directly through prism tests; it is shown how the results of these prism tests can be used in the analysis of flexural members without the need for softening stress-strain relationships and without the need for empirical hinge lengths. This approach is unique as it does not require stress-strain softening relationships but stress-sliding relationships that can be obtained directly from prism tests. This new wedge based approach has been compared with tests on eccentrically loaded prisms giving good simulation of the softening behaviour

due to micro-cracking. It is suggested that this direct approach may be useful in the development of new concrete materials such as fibre concrete and maybe also be useful in the refinement of existing ductility models for ordinary reinforced concrete.

Acknowledgements

This research was supported by the Australian Research Council Discovery grant DP0985828 “A unified reinforced concrete model for flexure and shear”. The first author has been financially supported by the Directorate General of Higher Education, Department of National Education of Indonesia through a Master degree.

References

1. Van Vliet MRA, Van Mier JGM (1996) Experimental investigation of concrete fracture under uniaxial compression. Mechanics of Cohesive-Frictional Materials 1:115-127
2. Wu C, Oehlers DJ, Rebentrost M, Leach J, Whittaker AS (2009) Blast testing of ultra-high performance fibre concrete slabs and FRP retrofitted RC slabs. Engineering Structures 31: 2060-2069
3. Nemecek J, Bittnar Z (2004) Experimental investigation and numerical simulation of post-peak behavior and size effect of reinforced concrete columns. Materials and Structures 37: 161-169
4. Debernardi PG, Taliano M (2001) Softening behavior of concrete prisms under eccentric compressive forces. Magazine of Concrete Research 53 (4): 239-249
5. Daniell JE, Oehlers DJ, Griffith MC, Mohamed Ali MS, Ozbakkaloglu T (2008) The softening rotation of reinforced concrete members. Engineering Structures 30(11): 3159-3166
6. Carreira DJ, Chu KH (1985) Stress-strain relationship for plain concrete in compression. ACI Journal 82(6): 797-804
7. Popovics S (1973) Numerical approach to the complete stress-strain relation for concrete. Cement and Concrete Research 3(5): 583-599
8. Teng JG, Huang YL, Lam L, Ye LP (2007) Theoretical model for fiber-reinforced polymer confined concrete. Journal of Composites for Construction 11(2): 201-210
9. Markeset G, Hillerborg A (1995) Softening of concrete in compression localization and size effects. Cement and Concrete Research 25(4): 702-708
10. Jansen DC, Shah SP (1997) Effect of length on compressive strain softening of concrete. Journal of Engineering Mechanics 123 (1): 25-35
11. Van Mier JGM (1986) Multiaxial strain-softening of concrete. Matériaux et Constructions 19: 179-190
12. Weiss WJ, Guler K, Shah SP (2001) Localization and size-dependent response on reinforced concrete beams. ACI Structural Journal 98 (5): 686-695

13. Borges JUA, Subramaniam KV, Weiss WJ, Shah SP, Bittencourt TN (2004) Length effect on ductility of concrete in uniaxial and flexural compression. ACI Structural Journal 101 (6): 765-772
14. Baker ALL (1956) Ultimate load theory applied to the design of reinforced and prestressed concrete frames. Concrete Publication Ltd London, pp. 91
15. Sawyer HA (1964) Design of concrete frames for two failure states. Proceedings of the international symposium on the flexural mechanics of reinforced concrete ASCE-ACI: 405-31
16. Corley GW (1966) Rotational capacity of reinforced concrete beams. Journal Structural Engineering ASCE 92(ST 10): 121-46
17. Priestly MJN, Park P (1987) Strength and ductility of concrete bridge columns under seismic loading. ACI Structural Journal (Jan-Feb) Title no. 86-58: 61-76
18. Panagiotakos TB, Fardis MN (2001) Deformation of reinforced concrete members at yielding and ultimate. ACI Structural Journal 98(2): 135-48
19. Mohamed Ali MS, Oehlers DJ, Griffith MC (2010) The residual strength of confined concrete. Advances in Structural Engineering 13(4): 603-618
20. Haskett M, Oehlers DJ, Mohamed Ali MS, Sharma SK (2011) The shear-friction aggregate-interlock resistance across sliding planes in concrete. Magazine of Concrete Research 62(12): 907-924
21. Haskett M, Oehlers DJ, Mohamed Ali MS, Sharma SK (2011) Evaluation the shear-friction resistance across sliding planes in concrete. Engineering Structures 33: 1357-1364
22. Lucas W, Oehlers DJ, Mohamed Ali MS, Griffith MC (2011) The FRP reinforeced concrete shear-friction mechanism. Accepted Advances in Structural Engineering
23. Nurwidayati R (2011) An Empirical Approach to Simulate the Concrete Softening Mechanism in RC members. Master thesis, The University of Adelaide (to be submitted in August 2011)
24. Haskett M, Oehlers Dj, Mohamed Ali MS, Wu C (2009a) Rigid body moment-rotation mechanism for reinforced concrete beam hinges. Engineering Structures 31(5): 1032-1041

25. Haskett M, Oehlers DJ, Mohamed Ali, Wu C (2009) Yield penetration hinge rotation in reinforced concrete beams. ASCE Structural Journal 135(2): 130-138
26. Haskett M, Mohamed Ali MS, Oehlers DJ, Wu C (2009) Influence of bond on the hinge rotation of FRP plated beams. Special edition of Advances in Structural Engineering 12(6): 833-843
27. Muhamad R, Mohamed Ali MS, Oehlers DJ, Sheikh AH (2011) Load-slip relationship of tension reinforcement in reinforced concrete members. Engineering Structures 33: 1098-1106
28. Visintin P, Oehlers DJ, Wu C, Haskett M. A mechanics solution for hinges in RC beams with multiple cracks. Submitted Engineering Structures 17/6/11
29. Muhamad R, Mohamed Ali MS, Oehlers DJ, Griffith MC. The tension stiffening mechanism in reinforced concrete prisms. Submitted International Journal of Advances in Structural Engineering

Table 1 *Detail of concrete prisms*

Prism	Width [$2d_w$] (mm)	Height [$2L_{def}$] (mm)	Depth (mm)	S_p (mm)	f_p (mm)
Test-50	50	100	200	0.04	45
Test-75	75	150	300	0.11	48
Test-100	100	200	400	0.12	42
Test-125	125	250	500	0.15	39

Fig. 1 *Compression wedge in a beam [2]*

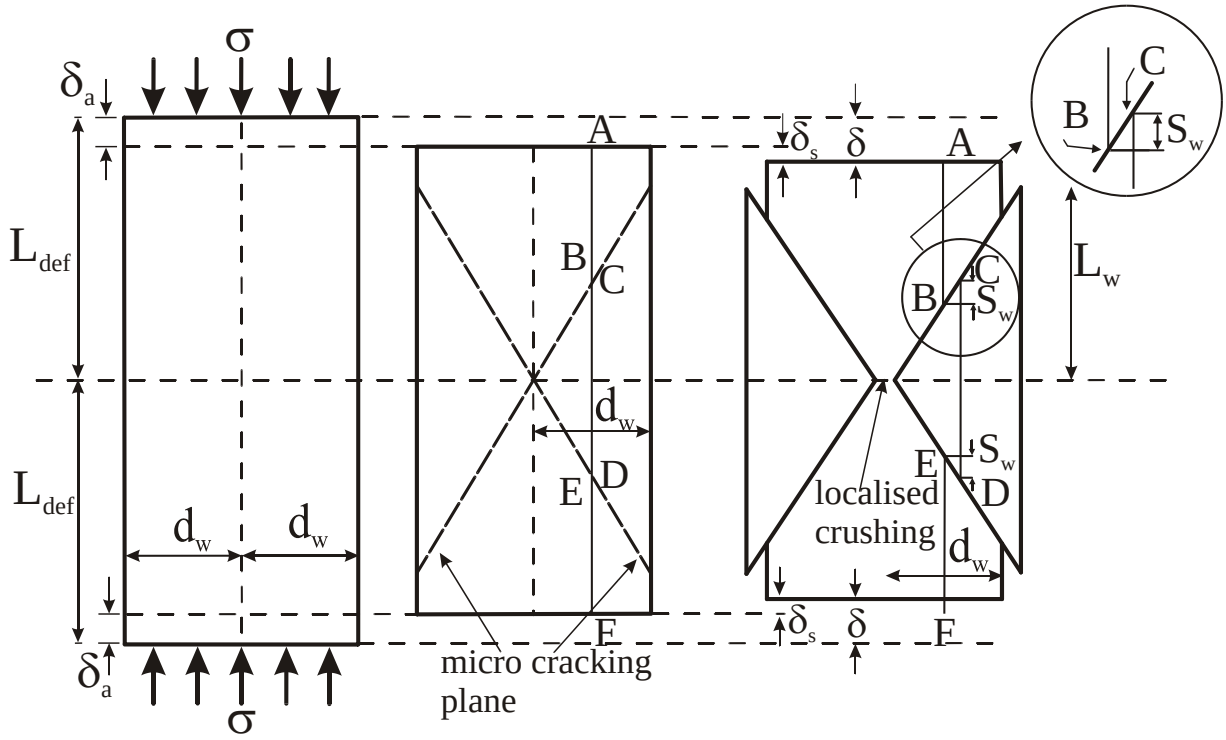

a. prism b. micro-cracking commences c. wedge sliding

Fig. 2 *Concentrically loaded prism*

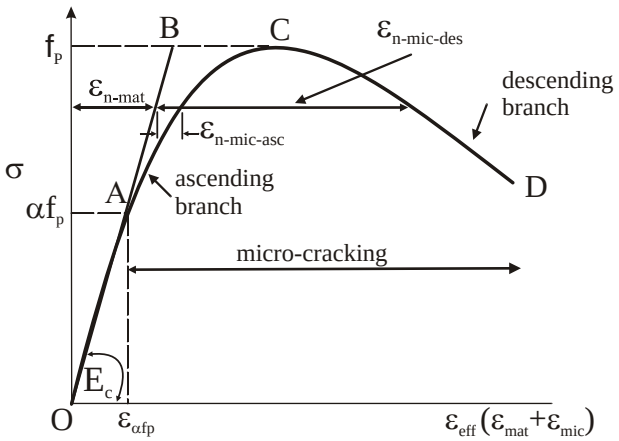

Fig. 3 *Measured concrete material properties*

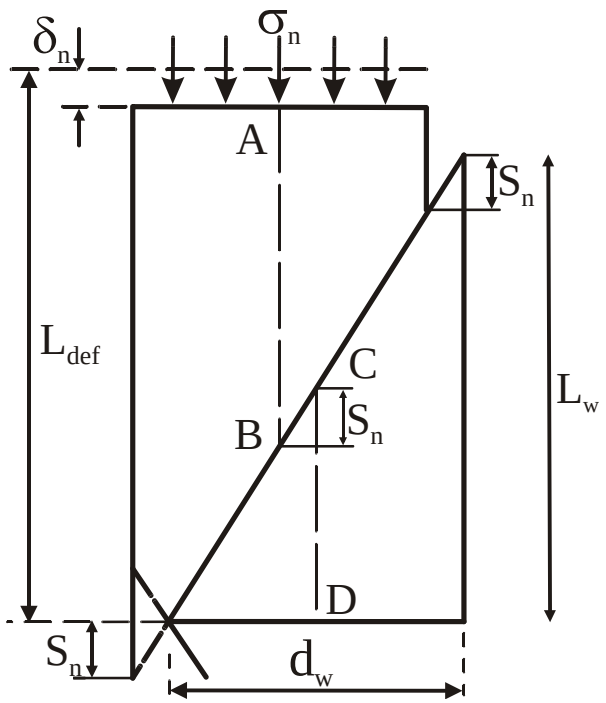

Fig. 4 *Deformation of a single wedge*

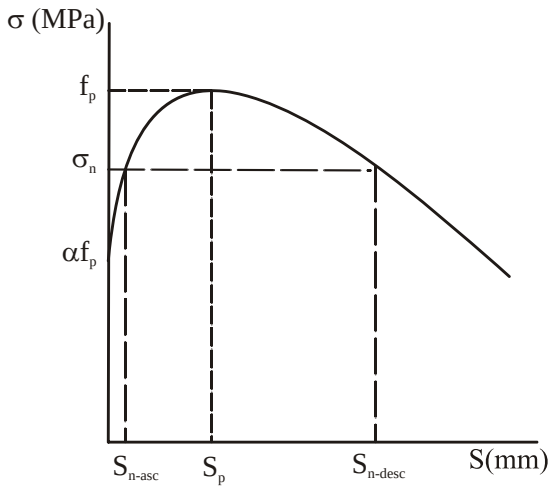

Fig. 5 *Wedge contractions*

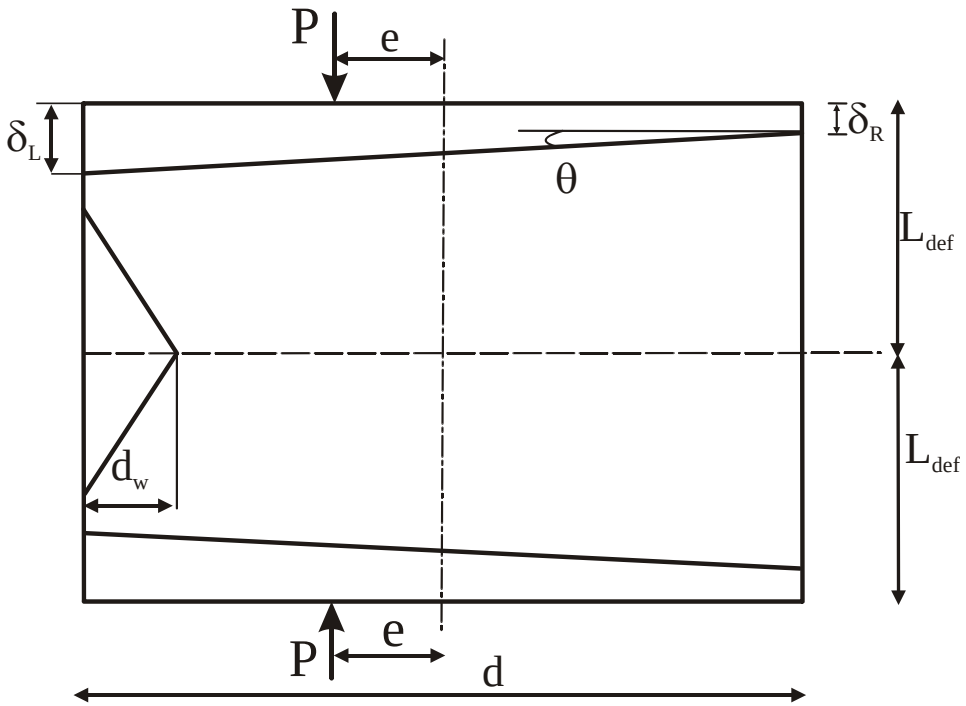

Fig. 6 *Eccentrically loaded prism*

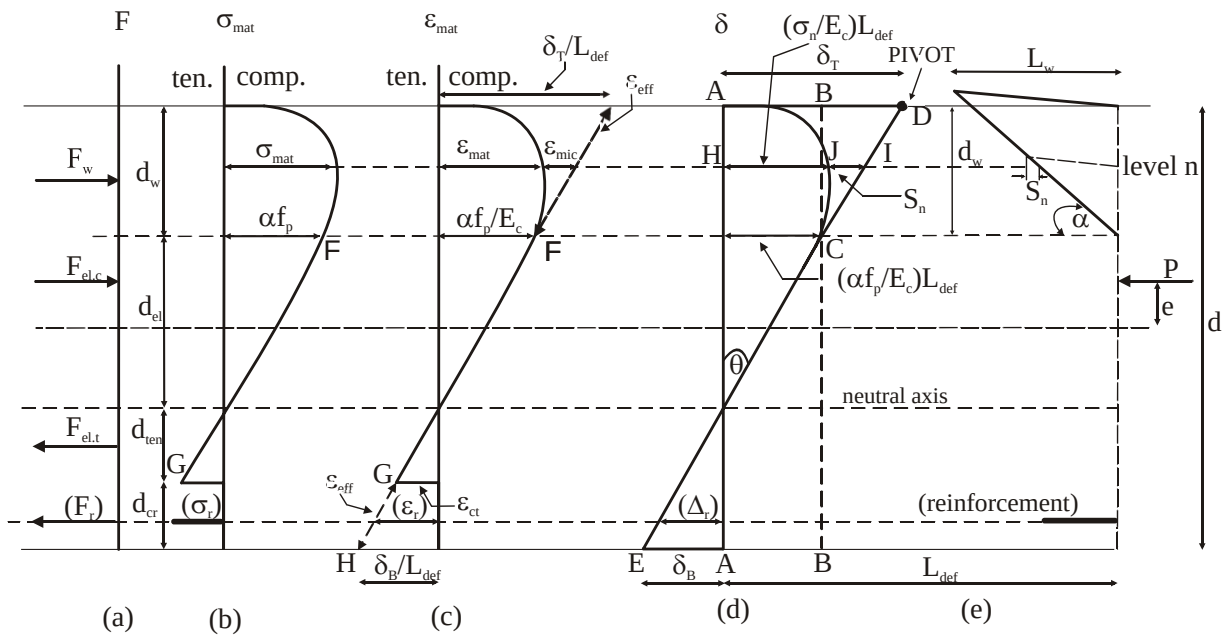

Fig. 7 *Wedge based flexural analysis*

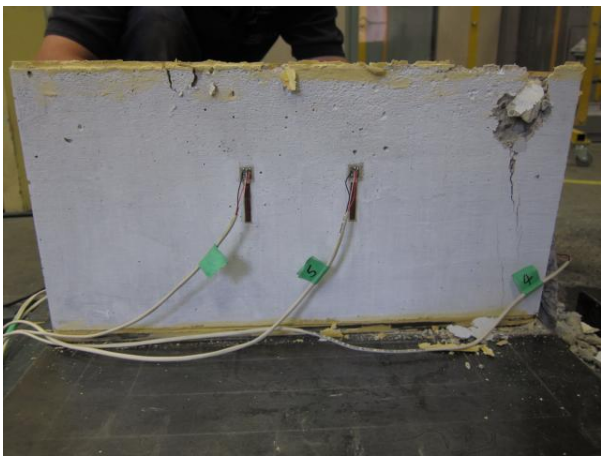

(a). Width ($2d_w$) to height ($2L_{def}$) (b). depth to height

Fig. 8 *Typical formation of wedges*

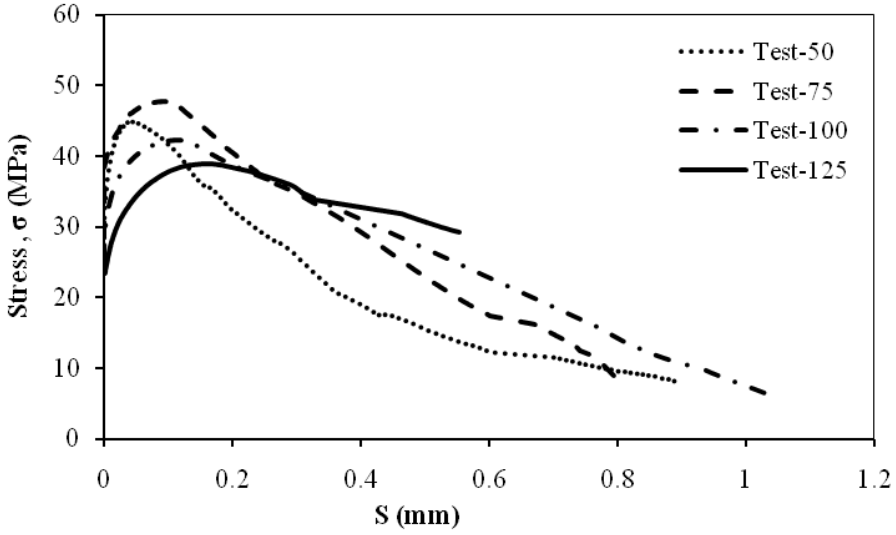

Fig. 9 *Test results*

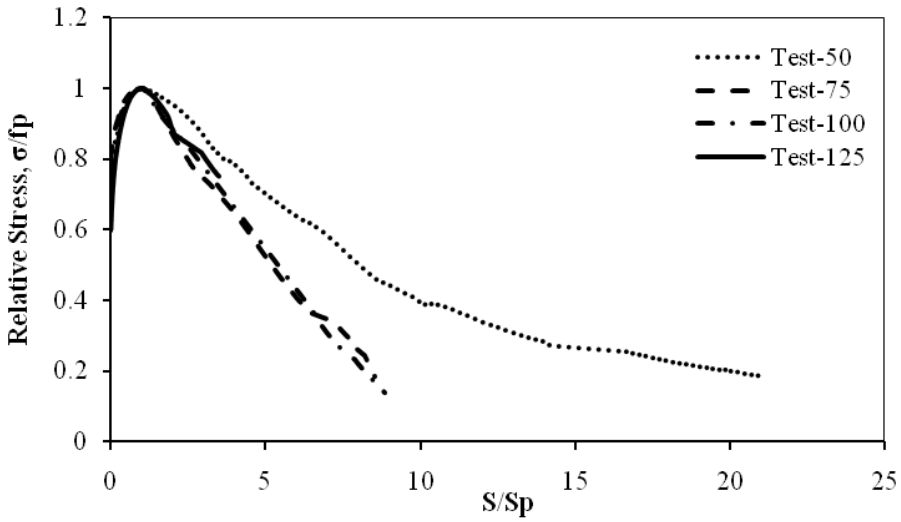

Fig. 10 *Non-dimensionalised test results*

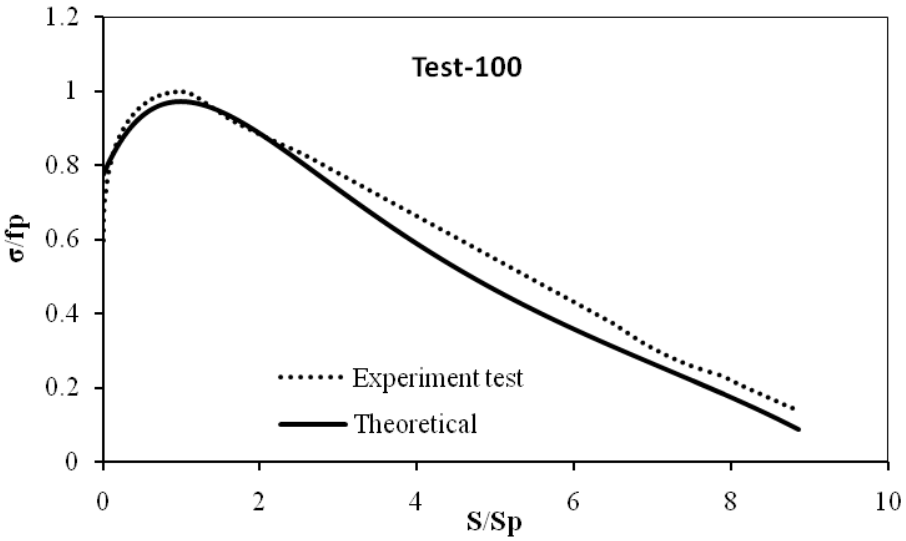

Fig. 11 *Stress-slip comparison*

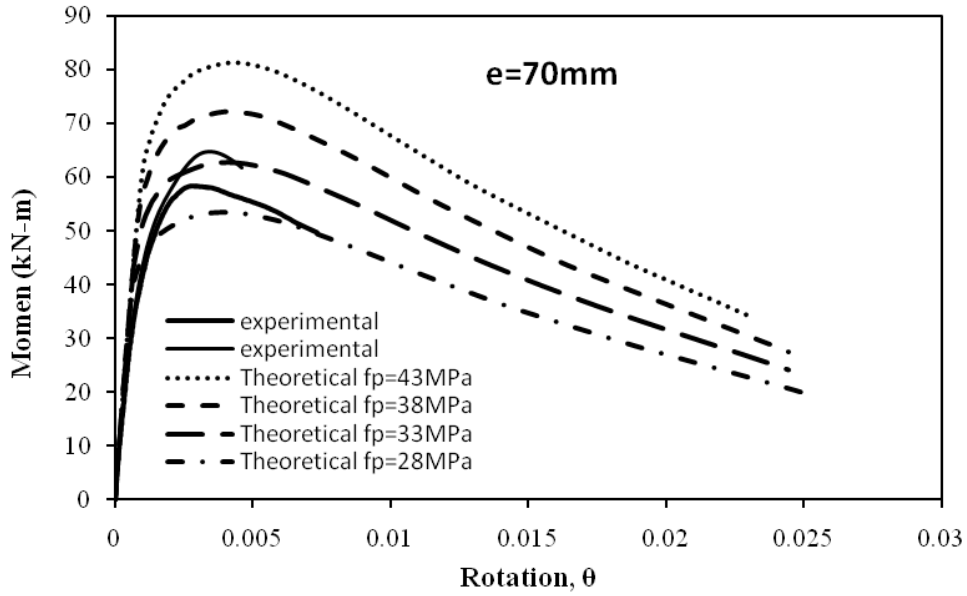

Fig. 12 *Typical moment-rotation comparison*

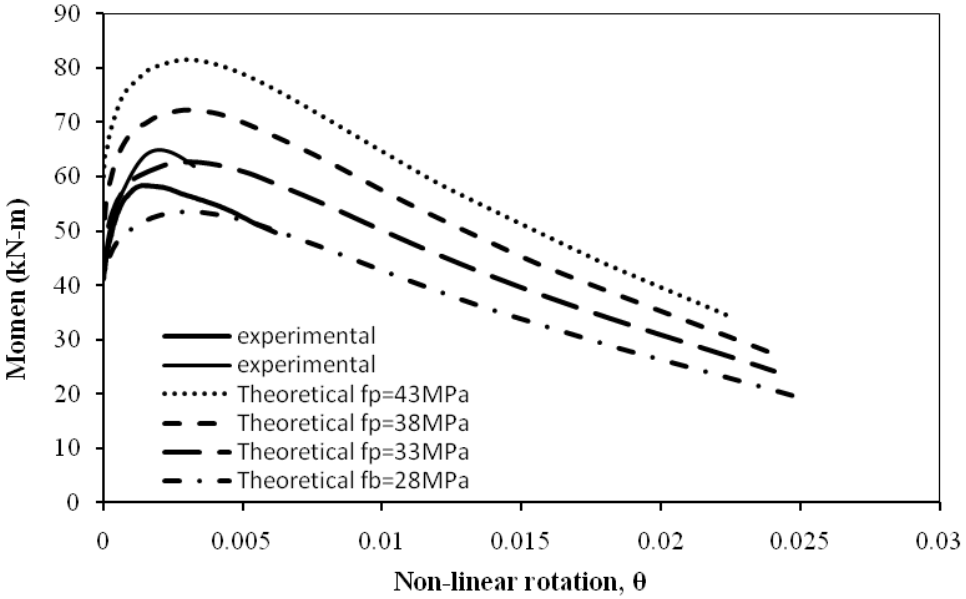

Fig. 13 *Non-linear rotation at e = 70 mm*

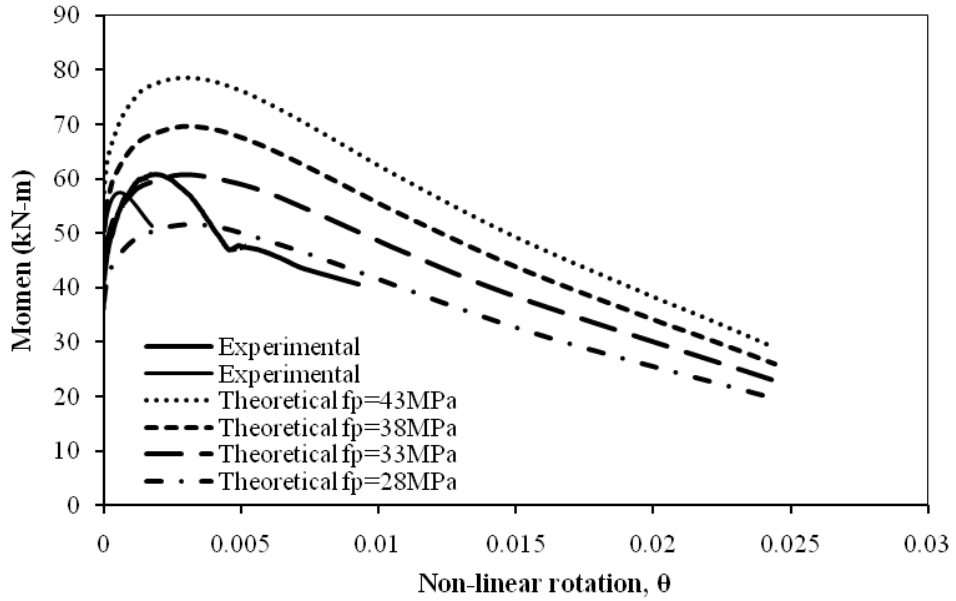

Fig. 14 *Non-linear rotation at e = 60 mm*

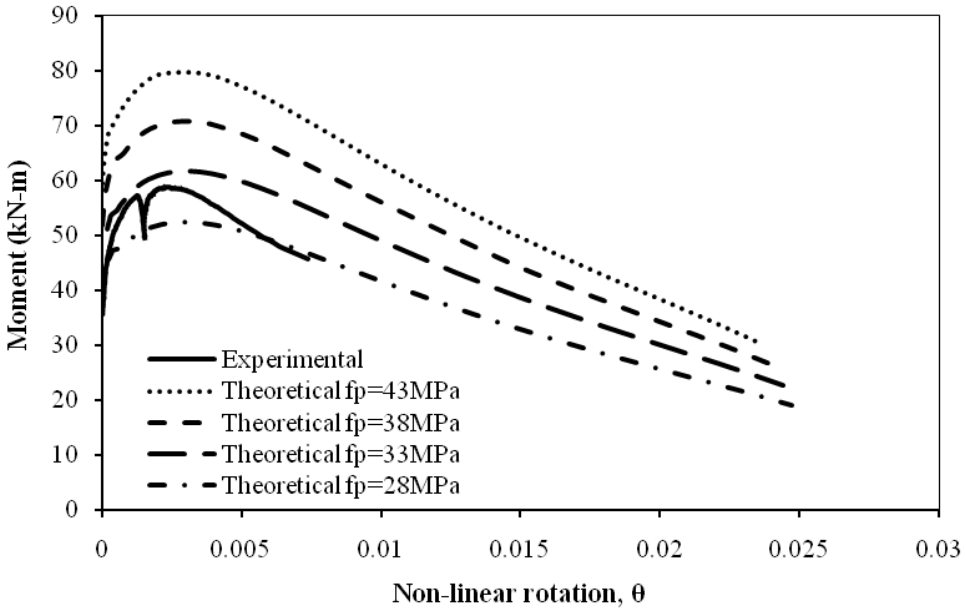

Fig. 15 *Non-linear rotation at e = 85 mm*

ACKNOWLEDGEMENT

The work written in this thesis was carried out at the University of Adelaide in the Departement of Civil, Environmental and Mining Engineering under the supervision of Dr. Chengqing Wu, Professor Deric Oehlers, Dr. Matthew Haskett.

It is a pleasure to thank those who made this thesis possible Dr. Chengqing Wu, Professor Deric Oehlers, Dr. Matthew Haskett for their encouraging, continuing supervision, extraordinary guidance and patience throughout this research from the initial to the final level. Their contribution and supervision enabled me to develop an understanding and complete this research. I also would like to thank them for their commitment to organize weekly meeting to give me invaluable discussion and ideas.

I am gratefull for assistance and support from all of the laboratory staff in the Civil, Environmental and Mining Engineering Deparment, especially to David Hale, Ian Cates, Steven Huskinson and Jon Ayoub for their professional advises and patience throughout the experimental program. I am also thankful to Stephen Carr for providing computing assistance, Barbara Brougham for editing some chapters of this thesis.

I would like to thank to Indonesian Government through Directorate General of Higher Education, Departement of National Education of Indonesia for their financially supported.

Special thanks are extended to my graduate friends, especially Rahimah Muhamad, Phillip Visintin, Bambang Setiawan, Nora Abdullah and Yunita Idris for their assistance, friendship, encouragement and support during the entire period of research.

Deepest thanks and appreciation to my family, my beloved husband Khairil Fiannor Ansyari and son Yuqo Azhari Alifanur for their endless love, encouragement, understanding and continous support through the duration of my study.

Last but not least I dedicates this thesis to my beloved parents Abdul Djebar Hapip dan Kesuma Sekarsih.

Table of Contents

TABLE OF FIGURES

TABLE OF TABLES

Chapter 1: INTRODUCTION

Structure members such as reinforced concrete (RC) slabs and beams bend under external loads. The flexural cracks occur when tensile stresses due to bending exceed the flexural strength of concrete. After formatting the crack, the reinforced bar carries the tensile force to support the applied load. When the load is increased further, the crack become wider and the reinforced bar slip relative to the surrounding concrete.

A moment curvature, M-χ approach currently is used to simulate the reinforced concrete members in flexure. To simulate M-χ approach analysis, material properties of concrete and reinforced bar such as stress strain σ-ε relationship of concrete in compression and σ-ε relationship of reinforcement are required. Full interaction between reinforcement and the concrete is assumed in this approach.

To simulate failure in this analysis, it is assumed that concrete crushing occurs at maximum strain concrete equal to the peak strain at stress strain relationship. This provides an approximation of the flexural capacity at failure, but does not allow for the gradual progression of failure or softening behaviour to be simulated.

To simulate the gradual progression of failure the softening stress strain relationship is used but these are highly size and shape dependant which limits its application. Recently, shear friction theory has been applied to the simulation of the softening behavior of concrete. Shear friction theory quantifies the relationship between shear stress, normal stress, displacement, and separation of the softening wedge across the crack plane.

In this thesis an alternative mechanism is proposed to simulate the gradual softening of concrete directly from compression tests on axially loaded rectangular prisms of varying dimension and slenderness. The behaviour of concrete crushing in compression prior to peak stress can be measured directly from compression tests, and the deformation or effective strain profile is uniform across the concrete cylinder.

At maximum compressive stress, localised deformation of concrete occurs and this localised deformation is responsible for the softening stress-strain relationship concrete post peak strain.

The goal of this thesis is to study experimentally this localised damage region and develop an empirical stress-deformation expressions to simulate the concrete softening mechanism and the subsequently use these empirical expressions in a beam analysis.

The thesis talks the following form:

In **Chapter 1**, the background and the objectives of this research are introduced.

Chapter 2 presents relevant literature related to softening mechanisms in unreinforced concrete. The stress-strain properties of concrete in compression is described initially and followed by shear friction theory.

Chapter 3 presents the first set of experimental tests on rectangular concrete prisms of varying dimensions under uniaxial compression, where the compression strength is 38MPa. Empirical expressions are developed in terms of stress and deformation of the wedges in axial and lateral direction (slip wedge and wedge expansion) which are used subsequently in Chapter 5.

Chapter 4 presents the second set of experimental tests. The steps and the analysis of these experimental tests are the same as the first set of experimental tests. This test is different from first set test in Chapter 3 where the compressive strength of concrete is 23 MPa and the effect of slenderness ratio is analyzed.

Chapter 5 presents the moment rotation analysis of an eccentrically loaded prism. The theoretical moment rotation response is then compared to the experimental test.

Chapter 6 presents the conclusion of this research.

Chapter 2: LITERATURE REVIEW

2.1 Stress-Strain Properties of Concrete in Compression

The stress-strain curve of concrete under uniaxial compression is an essential requirement for ultimate strength design and in the analysis of reinforced concrete members. A compression test on concrete cylinders or cubes is commonly used to quantify a complete the stress-strain σ-ε relationship. A typical stress-strain relationship under uniaxial compression is presented in Figure 2.1. The stress strain relationship can be characterized by two regions: pre-peak and post-peak. The pre-peak region is initially elastic and reflected in a linear stress-strain response under low loads. This pre-peak behaviour is considered to be a material property and can be determined directly from experimental test on concrete cylinders.

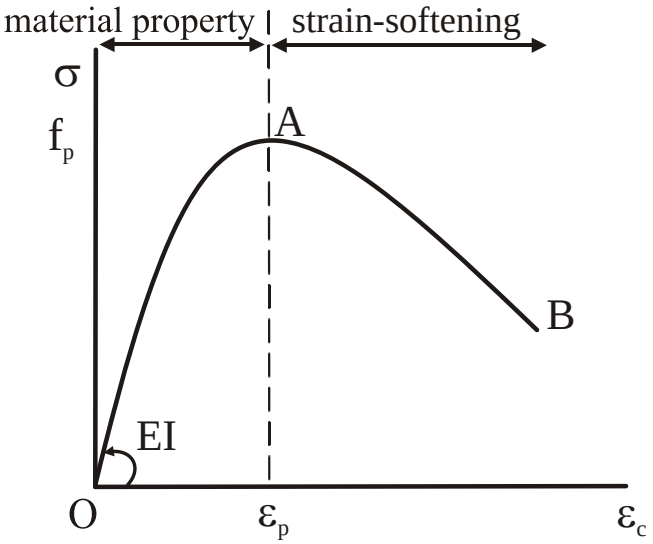

Figure 2.1: A typical compression stress-strain relationship of concrete

The stress-strain behaviour of the concrete becomes nonlinear and inelastic as micro-cracking develops at the interface zone between the aggregate and mortar (Van Vliet and Van Mier, 1996). This occurs when the stress reaches approximately (0.45-0.7) f_p where f_p is peak stress of concrete (Park and Paulay 1975, Palmquist and Jansen 2001). The process of continuing micro-cracking continues up to peak stress. These micro-cracks propagate and coalesce to eventually form a macro-crack in the mortar. A large crack is

formed when peak stress is reached, therefore, the deformations seems to localise in a narrow zone (Van Vliet and Van Mier, 1996). Then the stress gradually decreases with an increase in axial deformation which is commonly referred to as strain-softening (Van Mier and Man 2009).

2.1.1 Material Deformation

Various models have been proposed by many researchers to accurately represent the form of the ascending and descending branches of the stress-strain curve through uniaxial compression tests on unconfined concrete specimens (Hognestad 1951, Saenz 1964, Barnard, 1964, Sargin 1971, Popovics 1973, Carreira and Chu 1985, Yip 1998, Kumar 2004).

Hognestad (1951) modelled the ascending branch up to the peak stress of the stress-strain relationship that is along O-A in Figure 2.1as a parabola

$$\sigma = f_p\left[\frac{2\varepsilon_c}{\varepsilon_p} - \left(\frac{\varepsilon_c}{\varepsilon_p}\right)^2\right] \qquad \textit{Eq.2.1}$$

where ε_p the strain at the peak *stress* of unconfined concrete given by

$$\varepsilon_p = \frac{2f_p}{E_c} \qquad \textit{Eq. 2.2}$$

where σ is stress at a strain of ε_c; f_p and ε_p are the peak stress and the strain at the peak stress of unconfined concrete respectively, E_c is Young's modulus of concrete (MPa) that can be determined as a function of compressive strength of concrete f_c (ACI Committee 363 1992)

$$E_c = 3320\sqrt{f_c} + 6900 \qquad \textit{Eq. 2.3}$$

Sargin (1971) proposed the stress-strain relationship of compression concrete as

$$\sigma = f_p\left[\frac{a\left(\frac{\varepsilon_c}{\varepsilon_p}\right) + b\left(\frac{\varepsilon_c}{\varepsilon_p}\right)^2}{1 + c\left(\frac{\varepsilon_c}{\varepsilon_p}\right) + d\left(\frac{\varepsilon_c}{\varepsilon_p}\right)^2}\right] \qquad \textit{Eq. 2.4}$$

Where the empirical constants *a*, *b*, and *c* were determined from the boundary conditions of the pre-peak portion of the stress-strain curve while the constant *d* was determined from post-peak portion of the curve. Sargin (1971) used the same constants for both the ascending and descending branch.

It should be mentioned that Eq.2.1 and Eq.2.2 are only valid for standard specimens with a height-to-width ratio equal to or greater than 2 when the load is a short-term load applied at a rate that produces a constant strain in the specimen that is loaded for displacement or deformation control (Popovics 1973, Palmquist and Jansen 2001).

2.1.2 Strain Softening

The strain softening occurs before peak stress when micro-cracking begin to form during the pre-peak portion of stress strain curve (Jansen and Shah, 1997) or after peak stress where the stress decrease gradually as increasing axial deformation (Van Mier and Man, 2009). The post-peak region of stress-strain curve in Figure 2.1 or strain softening is not a material property and its behaviour is affected by many factors. Some significant factors which influence the post-peak behaviour are slenderness ratio which is height to width ratio of prism or height to diameter of cylinder specimens, specimen geometry or shape and size of specimens, frictional restraint between loading platens and specimen surface, loading rate, rigidity of the platens (Sangha and Dhir 1972, Kotsovos 1983, Shah and Sangkar 1987, Palmquist and Jansen 2001, Jansen and Shah 1997, Van Mier 1984, 1986, Van Mier *et al.* 1997, Van Vliet and Van Mier 1996, Choi *et al.* 1996, Van Geel 1998, Kim *et al.* 1999, Vonk 1992).

Wang *et al.* (1978) observed one constant only (constant *d* in Eq. 2.4) is not sufficient to determine the descending portion of stress-strain curve accurately. Hence Wang *et al.* (1978) modified Eq.2.4 and quantified two sets of the empirical constants *a*, *b*,*c*, and *d*, for pre-peak and post-peak portions of stress strain relationship.

A post-peak stress-strain relationship that is along A-B in Figure 2.1, has been developed by Popovics (1973) as

$$\sigma = \frac{f_p}{\varepsilon_p} \frac{\varepsilon_c \, n}{(n-1) + \left(\frac{\varepsilon_c}{\varepsilon_p}\right)^n} \qquad \textit{Eq. 2.5}$$

Where σ is axial stress for a given strain ε_c, f_p and ε_p represent peak axial stress and the corresponding axial strain of confined concrete respectively. Carreira and Chu (1985) defined the material parameter n in Eq.2.5 as

$$n = \frac{\mathrm{E_c}}{\mathrm{E_c} - \frac{f_p}{\varepsilon_p}} \qquad \textit{Eq. 2.6}$$

The shape of post-peak portion of the stress-strain relationship is affected by the material parameter n (Figure 2.2). The higher value of n causes the steeper slope of descending branch of curve.

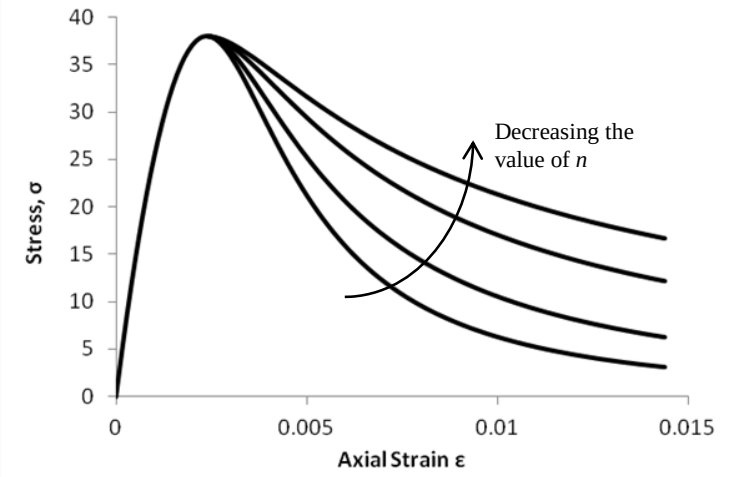

Figure 2.2: Effect of parameter n to stress strain relationship

The form of the stress-strain relationship that is suggested by Popovics (Eq. 2.5) only requires three parameters f_p, ε_p and E_c that can be determined from compression tests.

2.1.2.1 Localisation in Compression

Over many years compressive post-peak behaviour has been recognised as localised phenomenon. Localization means that the descending branch of stress strain curve becomes specimen size dependant and not be regarded as a pure material property

(Markeset and Hillerborg 1995). The localisation of deformation occurs in the post peak region in uniaxial compression test (Van Mier 1984, Jansen and Shah 1997, Van Vliet and Van Mier, 1996) and also occurs in practice (Weiss *et al.* 2001, Kim *et al.* 2001, Borges *et al.* 2004, Lertsrisakulrat *et al*. 2002). The localisation commence in compression just prior to peak stress (Shah and Sangkar 1987, Palmquist and Jansen 2001) or at peak stress (Torrenti *et al.*1993, Van Mier 1984). Because of strain localisation, the post-peak region of stress-strain curve is dependent on specimen size and slenderness and is not a material property. The post-peak response of longer specimens is more brittle.

Consider Figure 2.3, the prism of width W and height H subjected to uniaxial compression load. The increasing load causes the cracks occur in portion of prism height refers as a localised zone or damage zone of length H_d as shown shaded, while the remainder of the specimen (bulk zone) can be considered undamaged.

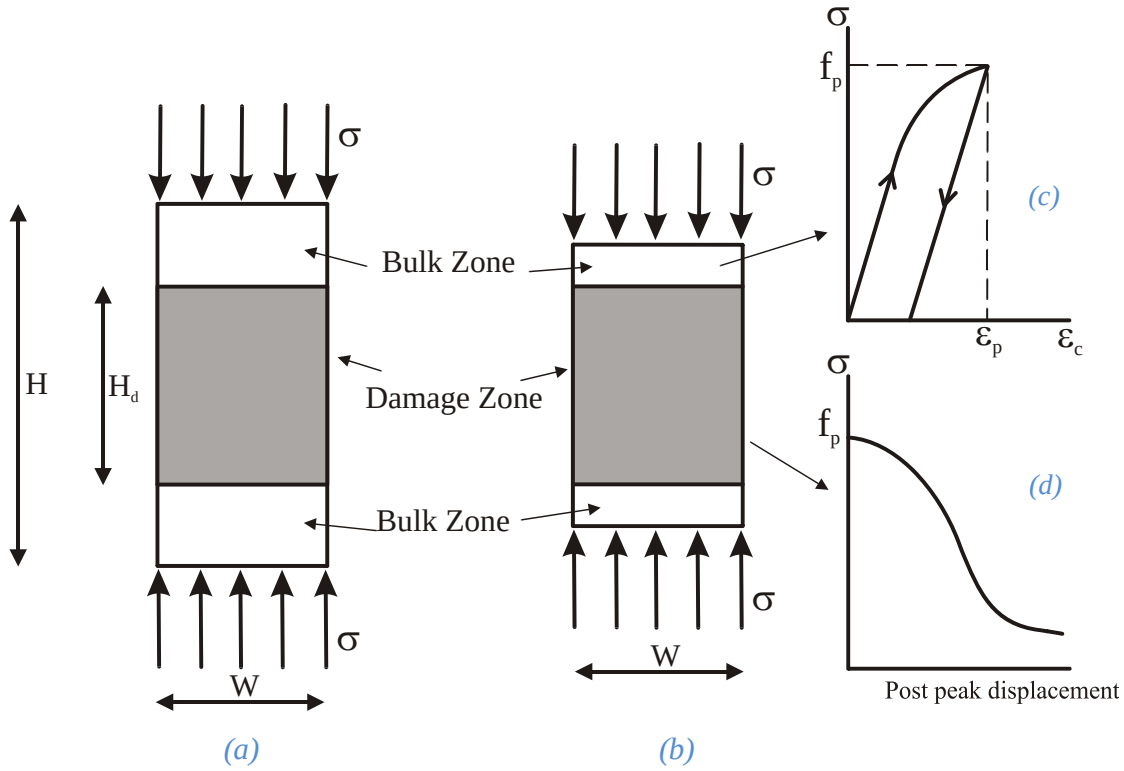

Figure 2.3: Localisation behaviour of concrete in compression

The damage zone length H_d of the centrically loaded specimen is equal to the width W of the specimen at peak load (Palmquisr and Jansen 2001), equal to 2 times

(Palmquisr and Jansen 2001) or 2.5 times (Markeset 1993, Markeset and Hillerborg 1995) of the smallest lateral dimension of the specimen cross section when the specimens failed. Hence for shorter specimens, the damage zone as shown shaded is almost the whole specimen height as shown in Figure 2.3 (b).

The stress strain relationship for undamaged zone (bulk zone) can be defined by Hognestad (1951) in Eq.2.1. Meanwhile, Palmquist and Jansen (2001) proposed the post-peak stress strain relationship for unreinforced concrete specimens with slenderness ratio equal or greater than 2 which take into consideration the length of the damage zone H_d as

$$\varepsilon_c = \left(\varepsilon_p + \frac{\sigma - f_p}{E_c} \right) \frac{H_b}{H} + \frac{1}{a} \left(\frac{f_p}{\sigma} - b \right)^c \frac{H_d}{H} \qquad \textit{Eq.2.7}$$

Where

$$H_d = W \left(2 - \frac{\sigma}{f_p} \right) \qquad \textit{Eq.2.8}$$

And

$$H_b = H - H_d \qquad \textit{Eq.2.9}$$

Where ε_c is strain for a given stress σ, f_p and ε_p represent peak axial stress and the corresponding axial strain respectively, E_c is Young' s modulus, W and H are the width and the height of the prism respectively, H_b is the bulk zone length, H_d the damage zone length, a, b and c are empirical constants.

Lertsrisakulrat *et al.* (2001) evaluate effect of specimen geometries, such as the slenderness ratio, size and shape to the damage zone length H_d based on experimental test for compressive strength 45MPa. The results reveal that at the same cross section, the damage zone length H_d is not significantly affected by the slenderness ratio and the shape of specimen. On the other hand, increasing the cross sections area leads to decrease the damage zone H_d. More detail about slenderness ratio is in Section 2.1.2.2.

Consider Figure 2.3(c) and (d), after the peak load reached, the deformation in the damage zone still increases while the deformation in undamaged zone decreases due to reduction in stress. The concrete cannot be regarded as a continuum anymore due to

the localisation of damage (Van Vliet and Van Mier 1996). Hence the post peak stress-deformation relationship is more suitable used to analyse the softening behaviour instead of stress-strain relationship because softening portion of the curve is not material property but structural response as RILEM recommendation (RILEM TC 148-SSC 2000).

The post peak deformation is calculated by subtracting pre-peak deformation from total deformation of the specimens. Figure 2.4 illustrates the relative or normalised stress in terms of post peak displacement response, where *d* is referred to the lateral dimension *W*. Normalised or relative stress is used to obtain a good comparison between the curves. Normalised or relative stress is stress divided by the peak stress.

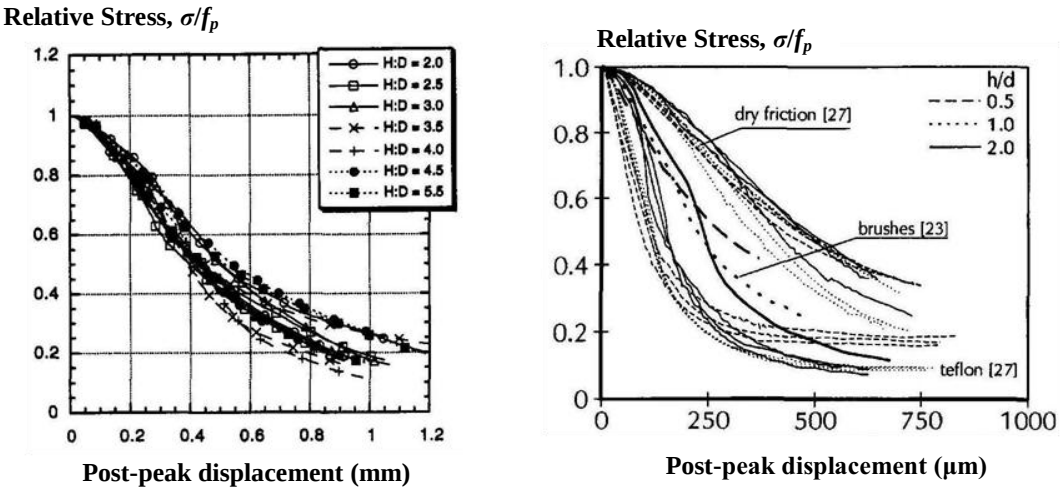

Figure 2.4: Relationship between relative/normalised stress and post peak deformation (Jansen and Shah, 1995 and Van Vliet and Van Mier 1996)

The graphs indicate that slenderness ratio affected to strain softening of concrete. The stress-post peak deformation curve indicates that a localisation of deformation occurs in softening region. The post-peak response or strain softening in compression has to be defined by means of a stress-post peak deformation (Van Mier 1984, Jansen and Shah 1995, Van Mier *et al*. 1997, Fantilli *et al*.2007).

2.1.2.2 Slenderness Ratio

The effect of slenderness of prisms and cylinders to the compressive strength in Round Robin test is depicted on Figure 2.5. In high friction between loading plate and specimen, the compressive strength of all specimens in both normal and high strengths concrete indicate increasing significantly as the slenderness ratio of specimen decreases. The compression strength of DUT prism increases significantly when the slenderness ratio decrease from 0.5 to 0.25. However, Schickert (1980) carried out numerous load controlled compression tests on prism with slenderness ranging between 0.25 and 4 and found that decreasing the concrete strength stops when the slenderness ratio is larger than 2 (Schickert 1980, Kotsovos 1983) or larger than 2.5 (Sangha and Dhir 1972, Newman and Lachance 1964). The same behaviour is shown on ACBM cylinders in Figure 2.5. The compressive strength of cylinder increases slightly with a decreasing of the slenderness ratio from 3 to 2. The specimen strength increases very slightly when increasing slenderness ratios larger than 2 because other mechanisms such as buckling will become more prominent (Schickert 1980). Watanabe *et al.* (2004) evaluated the effect of slenderness ratio on compressive strength of concrete and found that compressive strength of concrete cylinder is not affected by slenderness ratio between 2 and 8 when friction reducing pad is used.

NOTE:
This figure is included on page 11 of the print copy of the thesis held in the University of Adelaide Library.

Figure 2.5: The compressive strength for different slenderness ratio (Van Mier et al. 1997)

The frictional restraint occurs between loading platen and specimen causes a horizontal confinement of the specimens which decreases with increasing distance from the specimens ends as explained many researchers, *e.g*. Schickert (1980), Kotsovos (1983), König *et al*. (1994), Van Vliet and Van Mier (1996). This phenomenon is shown schematically in Figure 2.6. In short specimens the confined zone as shown shaded occurs over almost the whole specimens' volume whereas relatively large unconfined area develops in higher specimens. The initial crack occurs and propagates in the unconfined area at lower load. The higher concrete strength occurs on the lower slenderness of specimen as shown on THD cylinders in Figure 2.7. Hence the concrete strength is affected by the slenderness ratio.

In contrast, the concrete strength is not affected by increasing the specimen slenderness ratio in low friction (Van Mier 1984, König *et al*. 1994, Van Vliet and Van Mier 1996, Van Mier *et al*. 1997). Effect of frictional restraint between loading platen and specimens to concrete strength not discuss here because it is not within the scope of this thesis.

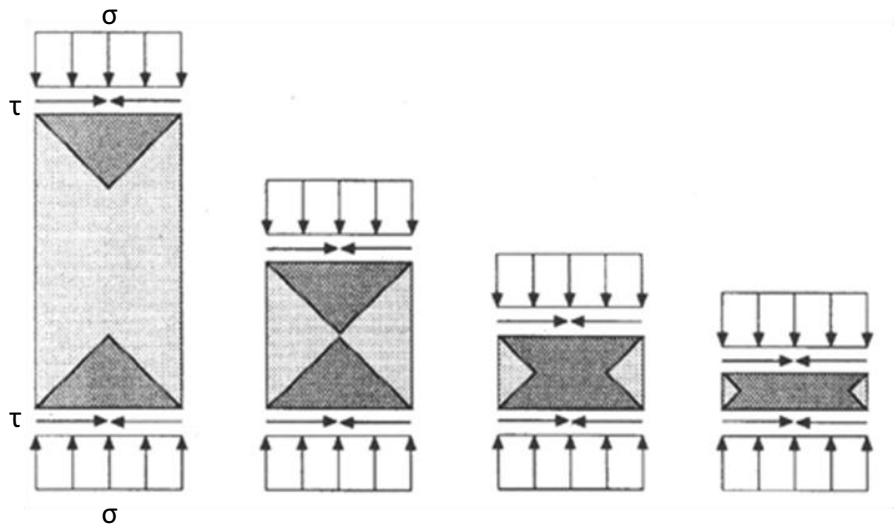

Figure 2.6: Confined zones due to frictional restraint for specimens of different slenderness (Van Vliet and Van Mier 1996)

NOTE:
This figure is included on page 12 of the print copy of the thesis held in the University of Adelaide Library.

Figure 2.7: Effect of slenderness ratio and frictional restraint (König et al 1994)

In terms of stress and strain relationship, the strain at the peak load increase as decreasing the slenderness ratio at high friction is observed as depicted in Figure 2.7. In the post-peak region, the ductility increases with decreasing the slenderness ratio. Hence in strain softening behaviour, decreasing the specimen slenderness causes an increase of the ductility.

2.1.2.3 Size and Shape Effects

The uniaxial compression tests on cube or cylinder concrete are commonly used to estimate the concrete strength of structure members such as beam, slab or column. Different countries use different standard specimens for concrete compression test. 150mm diameter and 300mm height concrete cylinders are used in Australia, Canada, France, New Zealand and the United States while 150mm or 100mm concrete cubes are used throughout the Europe, including Great Britain and Germany (Neville 1988).

To compare the strength between different shape and size of specimens test Neville (1966) developed the general relationship of concrete strength of between specimens for different shape.

Neville (1966) postulated that the compressive strength of concrete is a function of the specimen volume V, maximum lateral dimension W and slenderness ratio. A 6-inch (150mm) cube was chosen as a specimen standard to make comparison to other size or shape specimens. The mathematical expression is developed in British unit as

$$\frac{\sigma}{\sigma_6} = 0.56 + \frac{0.697}{\frac{V}{6HW} + \frac{H}{W}} \qquad \textit{Eq.2.10}$$

Where σ is compressive strength of concrete, σ_6 is compressive strength of 6-inch cube, V and H are volume and height of specimens respectively, W is maximum lateral dimension or diameter (cylinder) or width (prism or cube).

Eq.2.10 is used to obtain the comparison between 6 inch (150mm) cube to 6x12 inch (150×300mm) cylinder. The ratio between the strength of 150×300mm concrete cylinder and 150mm cube is 0.81 (Neville 1966), 0.91 (ASTM Standard C42) and 0.75 (British Standard B.S. 1881:1952).

The compressive strength is influenced by the volume of specimen. The greater volume causes the greater weak region that can reduce the strength. The stress relatively more uniform throughout the specimen on the greater volume and leads increasing the changes of premature failure. A 150×300mm cylinder has a volume approximately 1.65 times than 150mm cube volume. Hence, the compressive strength of cylinders exhibits lower than cubes.

Furthermore, the friction between loading platen and specimens provide some kind of confinement on the specimen. For cubes, almost throughout the specimens were confined while for cylinders, the confinement area reduces some part in central region. The cubes demonstrate the higher strength compare to cylinders (Sigvaldason 1966).

Del Viso *et al.* (2007) observed effect of shape to compressive strength. The results reveal that the peak stress of 100mm cube is higher approximately 7% than 100×200mm cylinder while the strain at peak stress of higher significantly. A comparative study between cylinder and prism with the same slenderness ratio indicates that the peak stress and the strain at the peak stress of prisms are slightly larger than cylinders (Chin *et al*. 2007). The same phenomenon also occurs in Round Robin test. The cylinder has a lower strength than prism (Van Mier *et al*. 1997).

On the other hand, the compressive strength tends to decrease with increasing the size of specimens which is well known as size effect. This phenomenon commonly occurs on quasi brittle materials such as concrete, rock, ice, ceramic, and composite materials (Markeset 2008, Read and Hegemier 1984).

Many investigations have been done by researchers to evaluate the influence of size of the specimen on uniaxial compressive concrete strength (Neville 1956, 1988, Malhotra 1976, Kim *et al*. 1999, Chin *et al.* 1997, Yi *et al.* 2006, Del Viso *et al.* 2007) and on flexural compressive strength (Kim *et al.* 2000 and Yi *et al.* 2002). The compressive concrete strengths of 70mm cubes are considerably higher than 125mm and 150mm cubes for compressive strength between 13MPa to 48MPa (Neville 1988). Malhotra (1976) obtained the similar results on cylinder tests for compressive strength between 7 to 48MPa. The results show the compressive strength of 100 × 200mm cylinders are higher than 150 × 300mm cylinders.

An increase in the size of specimen, on both cylinder and prism with the same height to width, leads to a reduction in compressive strength. Del Viso *et al.* (2007) studied the size and the shape effect by using four different lengths of cubes, 33, 50, 67, and 100mm and two different sizes of cylinder 75×150mm and 100×200mm for high strength concrete. The results revealed that concrete strength of cubes increase with decreasing the size while there is no significant effect of the size on cylinder tests. From the results of the tests over 280 cylinders, cubes and prisms for compressive strength

between 50 to 120MPa where used the same ratio of height to width of 2, Chin *et al.* (1997) found that the compressive strength of prisms 75×75×150 mm and 100×100×200mm are the same while the larger prism 125×125×250mm has lower compressive strength.

A part of the Round Robin test (Van Mier *et al.* 1997), the variation of the size of prism is evaluated by Gobbi and Ferrara (1995) as shown in Figure 2.8. The prisms with cross section 50×50mm, 100×100mm and 150×150mm and three different slenderness ratios (0.5, 1.0, and 2.0) are used. The graph indicates that there is the behaviour of all prisms slightly difference at the same slenderness ratio.

NOTE:
This figure is included on page 15 of the print copy of the thesis held in the University of Adelaide Library.

Figure 2.8: Comparison of stress-strain relationship of prisms of different size and slenderness ratio and loaded between rigid steel platens (Gobbi and Ferrara (1995)

2.2 Shear Friction Theory

The concrete crushed on the compression region is recognised as the concrete softening wedge is shown shaded in Figure 2.9 (b). The concrete softening wedge can be simulated using shear friction theory (Mattock and Hawkins 1972, Walraven and Reinhardt 1981, Walraven *et al.* 1987, Oehlers *et al.* 2007, Mohamed Ali *et al.* 2010, Haskett et al. 2011a, 2011b). Shear friction theory is used to calculate the shear capacity of interfaces between precast member and cast-in-place concrete in the design of precast concrete structural connectors (Walvaren *et al.* 1987), to determine the residual strength and the residual strain capacity of confined concrete cylinders (Mohamed Ali *et al.*

2010), to quantify the behaviour of the softening stress-strain relationship on an eccentrically loaded concrete prism (Debernardi and Taliano 2001, Fantilli *et al*. 2002, Daniell *et al*. 2008), to quantify the rotational capacity of reinforced concrete beams (Oehlers *et al.* 2008, Haskett *et al*. 2009), to derive the shape of the softening wedge and effect of confinement (Oehlers *et al.* 2008), to simulate the formation of the wedges in reinforced concrete beam with multiple crack (Visintin *et al.* 2011), to investigate the shear transfer behaviour in reinforced concrete (Mansur *et al*. 2008 and Rahal 2010).

The shear causes cracks along the sliding plane. The two rough and irregular surfaces of sliding plane are forced to slide relative to the other and cause separation along the crack surfaces or sliding plane. The separation or the widening the crack causes the reinforcement to be stressed. The force will be resisted by friction of confinement and the shear force is transferred across the sliding plane (Haskett *et al.* 2011a, 2011b and Mansur *et al.* 2008). The applied shear force is transferred by dowel action of the reinforcement crossing the crack and by friction between the two sliding surfaces or shear friction.

Now consider a prism in Figure 2.9 of height *H*, width *W* and of the depth into the page is very large so than the behaviour can be considered as two dimensional. A uniform pressure σ is applied to the prism which induces a deformation δ_a over the prism height *H*. The stress strain relationship for this condition is on ascending region O-A as shown in Figure 2.1. The material property can accommodate the deformation.

After peak stress is reached at point A in Figure 2.1, localised damage develops, strain softening commences, and softening wedge start to form as shown in Figure 2.9 (b). It is assumed the wedges develop like shown in Figure 2.9 (b). The material cannot accommodate the deformation and now depend on the shear friction properties. The shear stress τ_N and normal stress σ_N are transferred across the sliding plane.

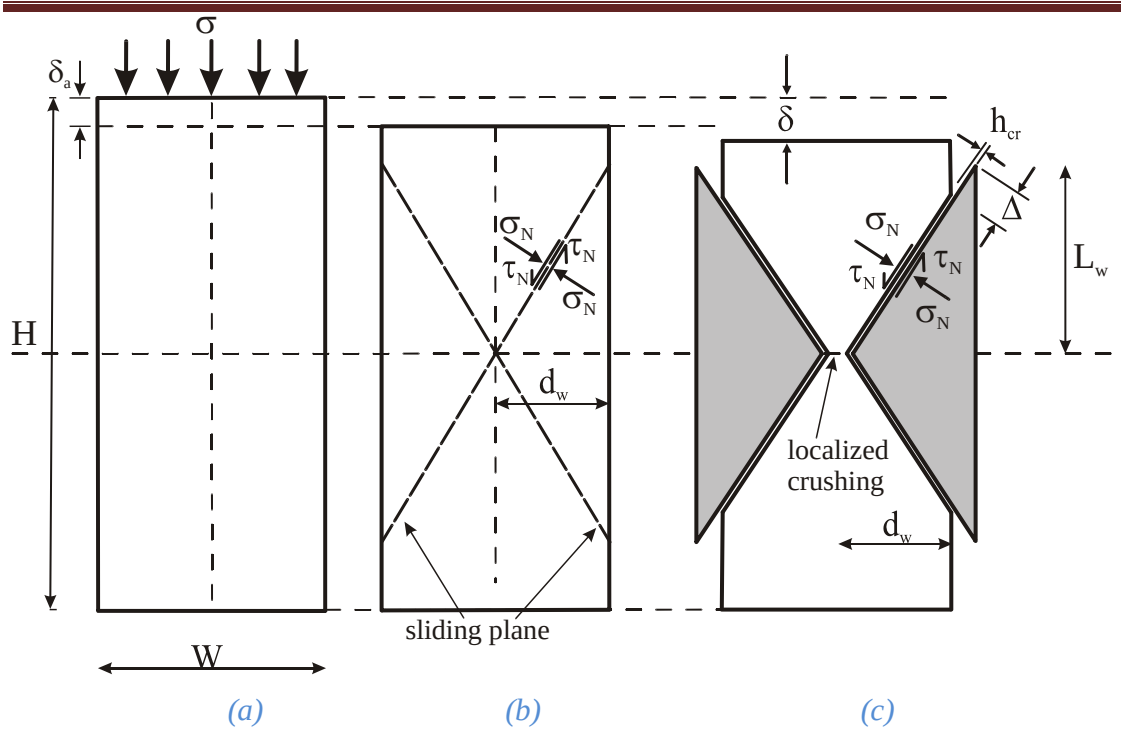

Figure 2.9: Concrete softening wedge

As the load increase, the axial deformation δ increase. The wedge as shown shaded in Figure 2.9 (c) develop at an angle α, the depth d_w that is assumed half on prism width W and separation of the softening wedge across the crack plane h_{cr} (Haskett *et al.* 2011a and 2001b). The angle of the sliding plane α depends on the cohesive and frictional properties of the concrete. The additional deformation δ must be accommodated by sliding of the crack Δ. The shear τ_N and normal stress σ_N that can be transferred across the sliding plane as a function of the sliding the crack Δ and separation of the crack h_{cr} (Walraven and Reinhardt 1981) are given in Eq. 2.11 and 2.12 respectively.

$$\tau_N = -\frac{f_{co}}{30} + (1.8h_{cr}^{-0.8} + (0.234h_{cr}^{-0.707} - 0.20)f_{cc})\Delta \qquad \textit{Eq.2.11}$$

$$\sigma_N = \frac{f_{co}}{20} - (1.35h_{cr}^{-0.63} + (0.191h_{cr}^{-0.552} - 0.15)f_{cc})\Delta \qquad \textit{Eq.2.12}$$

Where τ_N and σ_N are the shear and normal stress respectively, f_{co} is the unconfined compressive strength of cube (MPa), f_{cc} is the confined concrete strength (MPa), h_{cr} is crack separation (mm) and Δ is sliding of the crack. Based on Eq.2.11 and Eq. 2.12, Haskett *et al.* (2011a) develops a family curves of the shear stress τ_N and crack separation h_{cr} response for a given normal stress σ_N and displacement Δ as for concrete strength f_{co} = 50MPa as shown in Figure 2.9.

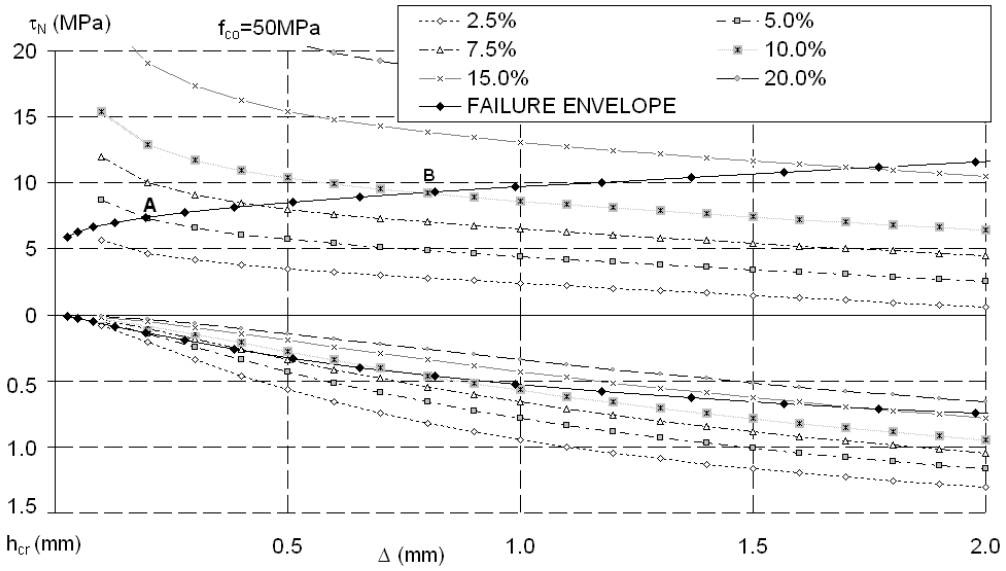

Figure 2.9: The shear stress and crack separation for a given normal stress and sliding the crack

The graph indicates that for a given normal stress σ_N, the shear stress τ_N decreases and the crack separation h_{cr} increases gradually with an increasing the displacement Δ. For an example, the shear stress is approximately 15MPa and there is no crack separation (h_{cr}=0) for a normal stress across the sliding plane 10% when the displacement 0.1mm. The displacement increases to 2.0mm, the shear stress is 7MPa and crack separation increase to 0.9mm.

Chapter 3: PRISM SOFTENING EXPERIMENTS-f_c=38MPa

3.1 Introduction

This chapter explains the uniaxial compression tests on concrete prisms. These tests were carried out in order to determine the axial and lateral deformation, to simulate softening behaviour and to quantify the wedge behaviour of the prisms. These experimental tests were conducted on four different sizes of concrete prisms with the same width: height: length ratio of 1:2:4. Details of specimen geometry, number and size, material properties, and the test rig and instrumentation are described in the following sections in this chapter. Then the observations of each test prism are represented in the test result and finally the analyses of these results are described.

3.2 Design of Specimens

In this section concrete, mortar and aggregate cylinders compression tests to quantify the material properties are described initially. In order to know the material properties of the relative constituents of the concrete, mortar and aggregate core specimens were obtained. After that the details of concrete prism specimens, the size and number are explained and followed by information about the test rig and instrumentation.

It should be mentioned that only material properties of concrete cylinders were required and used in this research. The mortar and aggregate properties were used in a meso-scale simulation research which is a parallel research project at the University of Adelaide. These results are presented here just for complete the report of material properties.

3.2.1 Material Properties

100×200 concrete and mortar cylinders and 58×150mm core aggregate cylinders were tested under uniaxial compression test to determine their material properties such as Young's modulus and compressive strength. Details of compression tests are provided in the next section followed by the results of these material tests.

3.2.1.1 Concrete

Six concrete cylinders of 100×200 mm that had the same curing condition as the concrete prisms (discussed later) were subjected to axial compressive loads in order to quantify material properties such as the compressive strength and Young's modulus of concrete. These experimental tests used a Seidner compression machine with maximum load of 1500kN as depicted in Figure 3.1(a). To quantify Young's modulus, the load applied was approximately 40% of the maximum load and unloads to the zero three times, and then loaded again until the cylinder failed. Three cylinders were tested one day before prism testing started, and three cylinders were tested one day after all prism testing had been completed.

(a) *(b)*

Figure 3.1: (a) Seidner Compression Testing Machine; (b) concrete cylinder

To measure the axial deformation 30 mm strain gauges 1 (SG-1) and 2 (SG-2) were located axially on both side of the cylinder to provide the information related to Young's modulus. Two others strain gauges, strain gauges 3 (SG-3) and 4 (SG-4) were placed opposite each other to monitor the lateral deformation as depicted in Figure 3.1(b) and Figure 3.2. The position of all these strain gauges was half the cylinder height.

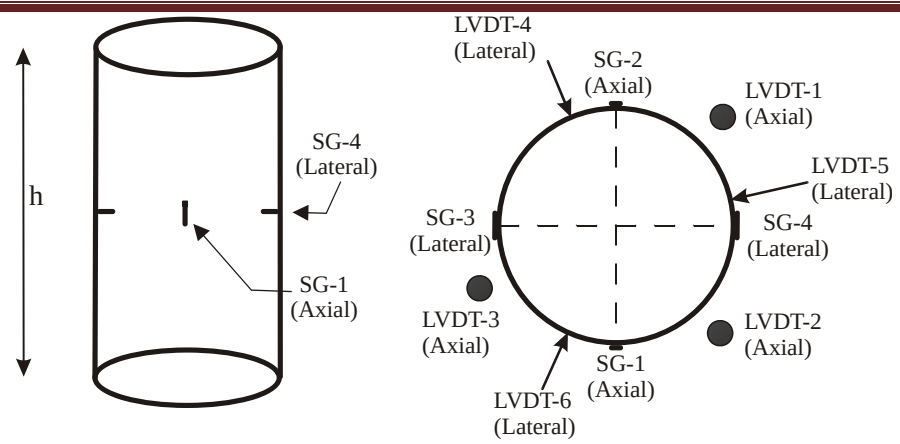

Figure 3.2: The diagram of transducers and strain gauges layout: (a) side view; (b) top view

Beside these strain gauges, in these tests the transducers were also placed on the cylinder specimens to measure axial deformation and lateral deformation. There were three LVDTs for axial deformation (LVDT-1, LVDT-2 and LVDT-3) and three LVDTs for lateral deformation (LVDT-4, LVDT-5 and LVDT-6). The axial and lateral LVDTs were located at 120° spacing. The lateral LVDTs were placed adjacent to strain gauges as shown in Figure 3.2 (b).

3.2.1.2 Mortar

The mortar was produced by separating the aggregate from the concrete. In this research a sieve with an aperture of 4.75mm was used to sieve out the aggregate from the concrete at the time of the pour as shown in Figure 3.3(a). The fresh concrete poured off into the 4.75mm sieve and stirred using hand. The mortar passed through the sieve and the aggregate detained on the sieve as represented in Figure 3.3(b) and Figure 3.3(c) respectively. Then the mortar was molded into a 100mm×200mm cylinder.

The transducers and strain gauges were placed in axial and lateral direction along the perimeter of the cylinder to obtain the lateral and axial deformation of mortar. The LVDTs and strain gauges position of mortar cylinders had similar to the LVDTs and strain gauges of concrete cylinders as depicted in Figure 3.2 and Figure 3.3(d). 30 mm strain gauges 1 (SG-1) and 2 (SG-2) were located axially on both side of the cylinder and strain gauges 3 (SG-3) and 4 (SG-4) were placed laterally opposite each. The

position of all these strain gauges was half the cylinder height. LVDT-1, LVDT-2, and LVDT-3 were placed to record axial deformation and three LVDTs for lateral deformation (LVDT-4, LVDT-5, and LVDT-6). The LVDTs were located at 120° spacing. Two mortar cylinders were tested one day before prism testing started, and three mortar cylinders were tested after all prism testing was completed.

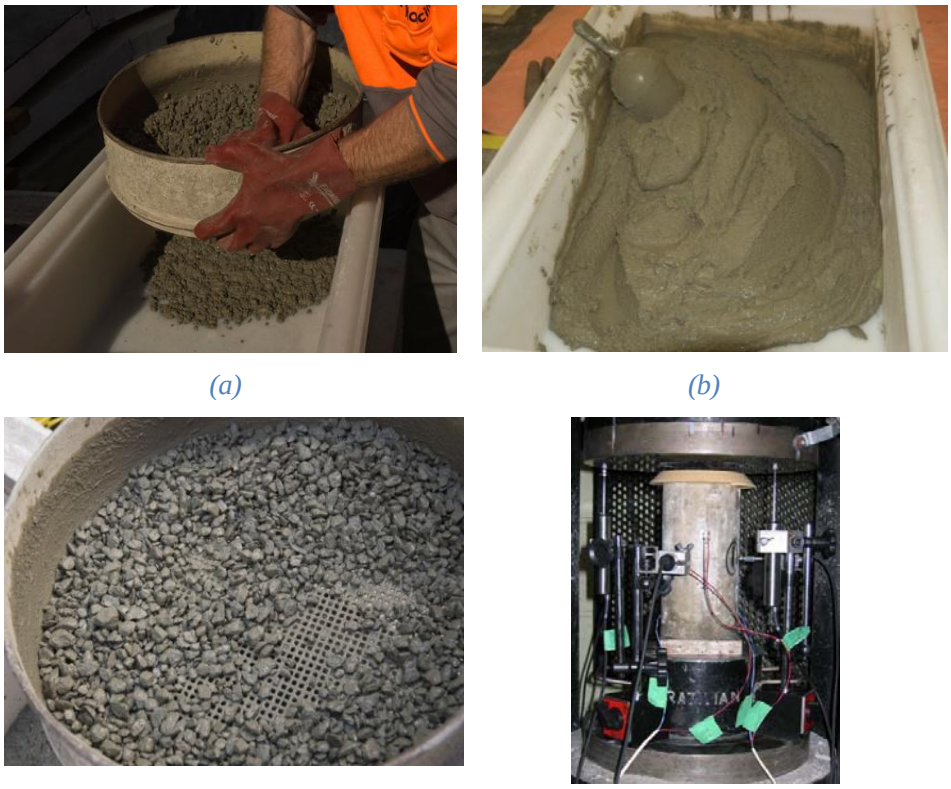

(a) *(b)*

(c) *(d)*

Figure 3.3: (a) how to produce the mortar; (b) fresh mortar; (c) separate aggregate; (d) 100mm×200mm mortar cylinder

3.2.1.3 Aggregate

The mechanical properties of the aggregate were provided by the CEMEX Ready-mix laboratory. Other mechanical properties such as the compressive strength and elastic Young's modulus were quantified by taking core specimens from rock sample as shown in Figure 3.4(a). These tests were conducted at the Rock Mechanics Laboratory, The University of Adelaide. The procedures were used to determine the compressive strength of the aggregate comply to Australian Standard AS 4133.4.3.1-2009. The ratios of length to diameter are 2.5 to 3.0 and the diameter not less than

50mm. Hence, in this research five aggregate core specimens of 150mm length and 58mm diameter were constructed and tested as depicted in Figure 3.4(b).

(a) *(b)* *(c)*

Figure 3.4: (a) rock sample; (b) 58mm diameter and 150mm length core aggregate cylinder; (c) aggregate test set up

Similar to the material tests of the concrete and mortar in the previous section, the axial and lateral deformations were also measured by using LVDTs along with strain gauges attached to the core specimens. The axial and lateral transducers and the strain gauges of these aggregate cylinders used the same location and position as was used for the concrete cylinder test (see again Figure 3.2). The test also used the Seidner Compression Machine with a maximum load of 1500kN. The aggregate cylinder test setup is depicted in Figure 3.4(c), and is identical to that used on the mortar only cylinders [Figure 3.3(d)] and the concrete cylinders [Figure 3.1(b)].

3.2.1.4 The Result of Material Properties

The material properties of the concrete, mortar, and aggregate were obtained from experimental testing, and are described one by one below. In this experimental test, elastic Young's modulus was achieved from strain gauges value readings. The method to determine the elastic Young's modulus using strain gauges can be found in Australian Standard 1012.17-1997.

The first material properties result analysis is concrete. The ultimate load, ultimate stress and elastic Young's modulus of six concrete cylinders are listed in Table

3.1. It can be seen that the average of ultimate stress σ_{ult} and elastic Young's modulus E_c was 37.9MPa and 32,368MPa respectively.

Table 3.1: Material properties of 100mm×200mm concrete cylinders

Specimens	Age (days)	Ultimate Load, Pult (kN)	Ultimate Stress, σult (MPa)	Elastic Young's Modulus,Ec (MPa)
R1	51	291.0	36.7	30,906
R2	51	294.5	37.1	31,534
R3	51	299.0	37.7	34,653
R7	64	306.4	39.0	32,948
R8	64	296.8	37.8	32,897
R9	64	310.1	39.5	31,269
Average			**37.9**	**32,368**

It should be mentioned that the concrete cylinders R4, R5 and R6 have been used to estimate the ultimate stress capacities f_c and therefore used that information to get 40% of that for concrete cylinders R1, R2, R3, R7, R8 and R9.

The stress and axial strain responses of six concrete cylinders are depicted in Figure 3.5. The responses are quite similar on the ascending region, however a little scatter occurred on the descending region. The average curve of these responses is required.

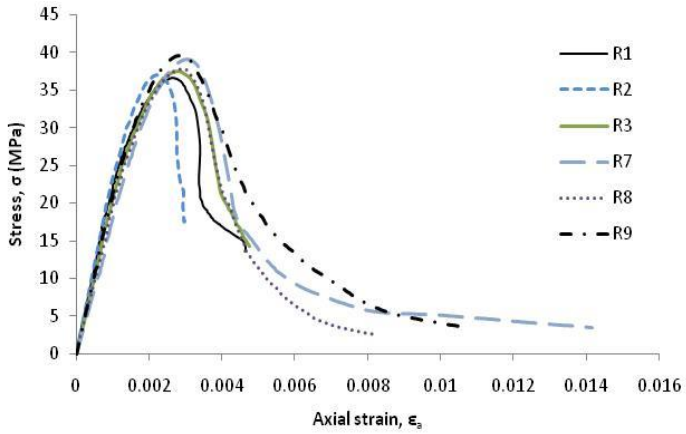

Figure 3.5: Stress-axial strain relationship of six concrete cylinders.

Figure 3.6 shows the average of axial stress-axial strain relationship of concrete. The average value is obtained by making the same interval of axial strain such as 0.0001

of all responses in Figure 3.5. Then the average stress was calculated as $(\sigma_{R1}+\sigma_{R2}+\sigma_{R3}+\sigma_{R7}+\sigma_{R8}+\sigma_{R9})/6$ where σ_{R1}, σ_{R2}, σ_{R3}, σ_{R7}, σ_{R8} and σ_{R9} were the stress of concrete R1, R2, R3, R7, R8 and R9 respectively for a given axial strain. The peak stress, based on the average curve is 37.7MPa corresponding to axial strain of 0.0030.

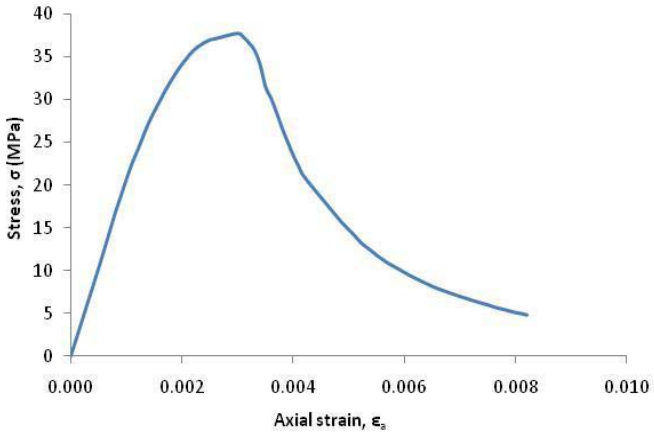

Figure 3.6: The average of the six stress-axial strain relationship curves of concrete cylinders.

The failure pattern of a concrete cylinder subjected to uniaxial compression load is depicted in Figure 3.7. Vertical and incline cracks propagated until the specimens failed.

Figure 3.7: Failure pattern of concrete cylinder

The second material properties result analysis is mortar. The material properties of mortar such as the ultimate load, ultimate stress and elastic Young's modulus are

summarised in Table 3.2. From that table, the average of ultimate stress σ_{ult} and elastic Young's modulus E_c are 41.6MPa and 24,464MPa respectively.

Table 3.2: Material properties of five mortar cylinders

Specimens	Age	Ultimate Load, Pult	Ultimate Stress, σult	Elastic Young's Modulus, Ec
	(days)	(kN)	(MPa)	(MPa)
M1	51	323.8	40.8	24,029
M2	51	322.9	40.7	25,082
M4	64	338.5	43.1	25,029
M5	64	318.1	40.5	23,656
M6	64	336.9	42.9	24,523
Average			41.6	24,464

It should be noted that the ultimate stress capacity of mortar has been determined by using mortar cylinder M3. Then 40% of that ultimate stress capacity is used for specimens M1, M2, M4, M5 and M6 to quantify the elastic Young's modulus.

The axial stress-axial strain response of mortar cylinders is shown in Figure 3.8. The responses are very similar on the ascending and descending branch. However, only mortar cylinder M2 has small scatter on the descending branch of the curve. The mortar cylinders were very brittle. They failed immediately after the peak stress was reached. Only axial strain on the descending branch of cylinder M2 was captured. The average curve is needed.

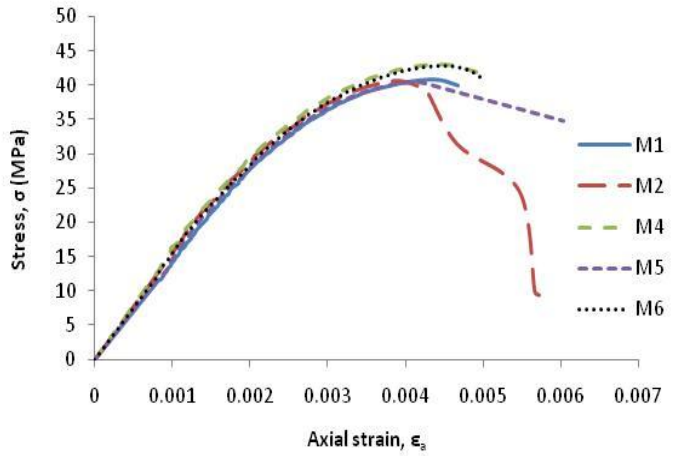

Figure 3.8: Stress-axial strain response of five mortar cylinders.

Figure 3.9 shows the average curve of the stress strain relationship of the mortar cylinders. This curve is the average of the curves in Figure 3.8. The average curve is obtained by using the same method as was used for the concrete cylinders. First the same interval of axial strain of every curve in Figure 3.8 is determined; then the average stress is quantified for a given axial strain. The average stress is $(\sigma_{M1}+\sigma_{M2}+\sigma_{M4}+\sigma_{M5}+\sigma_{M6})/5$ where σ_{M1}, σ_{M2}, σ_{M4}, σ_{M5} and σ_{M6} was the stress of M1, M2, M4, M5 and M6 respectively at the same value of axial strain. Based on the average curve, the ultimate stress is 41.3MPa and the axial strain at the ultimate stress is 0.0041.

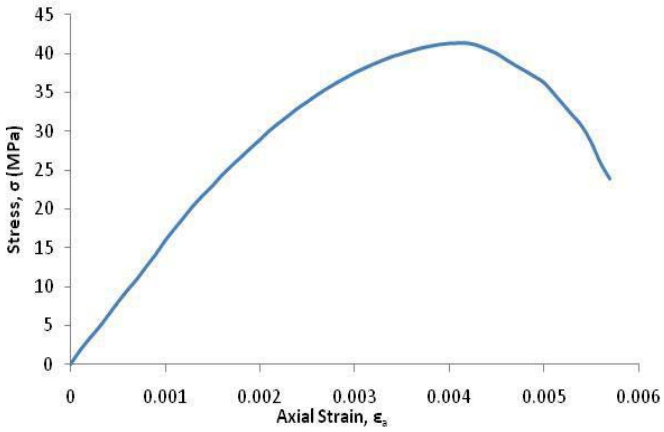

Figure 3.9: The average of stress – axial strain relationship of mortar cylinders.

The failure pattern of mortar cylinders is shown in Figure 3.10. The splitting failure occurred on both mortar cylinders.

Figure 3.10: Failure pattern for mortar cylinders

The third material properties result analysis is aggregate. Table 3.3 summarises the material properties of five core aggregate cylinders. The average ultimate stress is as high as 106.0MPa and elastic Young's modulus is 46,498MPa.

Table 3.3: Material properties of core aggregate cylinders

Specimens	Ultimate Load, Pult (kN)	Ultimate Stress, σult (MPa)	Elastic Young's modulus, Ec (MPa)
A	237.0	88.3	42,803
B	261.5	97.3	43,941
C	269.5	100.4	51,009
D	296.5	110.5	44,435
E	358.5	133.5	50,304
Average		106.0	46,498

The relationship of stress and axial strain of five core aggregate cylinders is depicted in Figure 3.11. The responses of all cylinders are very similar and perfectly linear curves. The graph describes the axial strain increase as the stress increase.

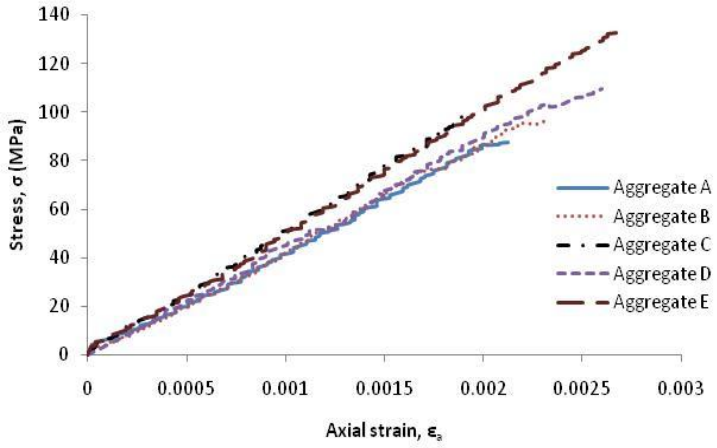

Figure 3.11: Stress–slip wedge response of five core aggregate cylinders.

Figure 3.12 shows the average relationship of the stress-axial strain of core aggregate cylinders. The same method was used to determine the average curve as described previously. The same interval of axial strain of every curve was determined initially and for a given axial strain, the average stress was quantified as

$(\sigma_A+\sigma_B+\sigma_C+\sigma_D+\sigma_E)/5$ where σ_A, σ_B, σ_C, σ_D and σ_E were the stress of aggregate A, B, C, D and E respectively. The ultimate stress based on the average curve was 106MPa relative to the ultimate strain 0.0026.

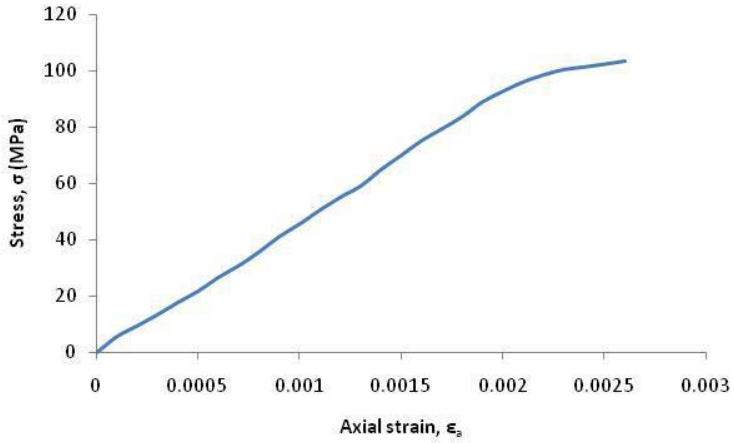

Figure 3.12: The average curve of stress-slip wedge response of core aggregate cylinders.

Figure 3.13 display the failure pattern of three different core aggregate cylinders, all with the same cracking pattern. Splitting failure can be seen clearly on the images in Figure 3.13. The aggregate core was very brittle and an "explosive" failure occurred when the core aggregate reached peak stress. The specimens broke suddenly into two or three pieces parallel to the applied load.

Figure 3.13: Failure pattern of core aggregate cylinders.

The last analysis is comparison of all material. The average curve of concrete, mortar and aggregate is compared and analysed as shown in Figure 3.14. It shows that aggregate has a steeper slope because elastic Young's modulus of aggregate is much higher than the other materials. The ultimate stress of mortar is higher than concrete. The ultimate stress of mortar 41.3MPa with an axial strain of 0.0041, compared to the ultimate stress of concrete 37.7MPa with an axial strain of 0.0030 (Figure 3.6). The difference in the ultimate stress between mortar and concrete is because of the nature of the interfacial transition zone, the zone between mortar and aggregate, which is the weakest region in concrete.

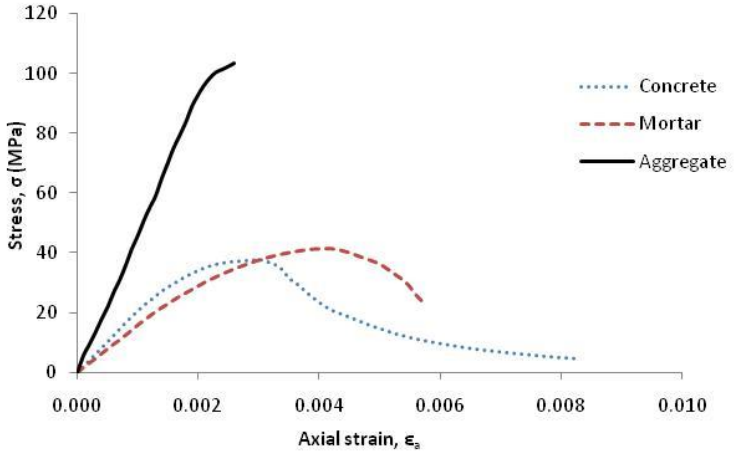

Figure 3.14: Comparison the stress-strain of concrete, mortar and aggregate.

It should be noted that the stress-axial strain relationship for all the individual materials was required and used in a parallel research project at the University of Adelaide. Only the material properties of concrete were investigated in the current research and subsequently repeated in this thesis.

The next section is about specimen details, the test machine and instrumentation which were used in these prism experimental tests. The tests were carried out in order to gather information about the axial and lateral deformation on the long concrete prism under uniaxial compressive load. The cylinder and cube were not chosen as an experimental specimen because the circumferential expansion always occurred along with axial deformation when the specimen was compressed.

3.2.2 Specimens Detail

Uniaxial compression tests were carried out on different sizes of concrete prisms. The geometry of the prism can be seen in Figure 3.15. The long prisms were chosen as specimens in order to avoid the circumferential expansion that always occurs in the cylinder or cube specimens. In addition, the behaviour of the cross section along the length of the prism can be considered as two-dimensional behaviour. The notation of *W*, *H* and *S* in Figure 3.15 are width, height and length of the concrete prism respectively.

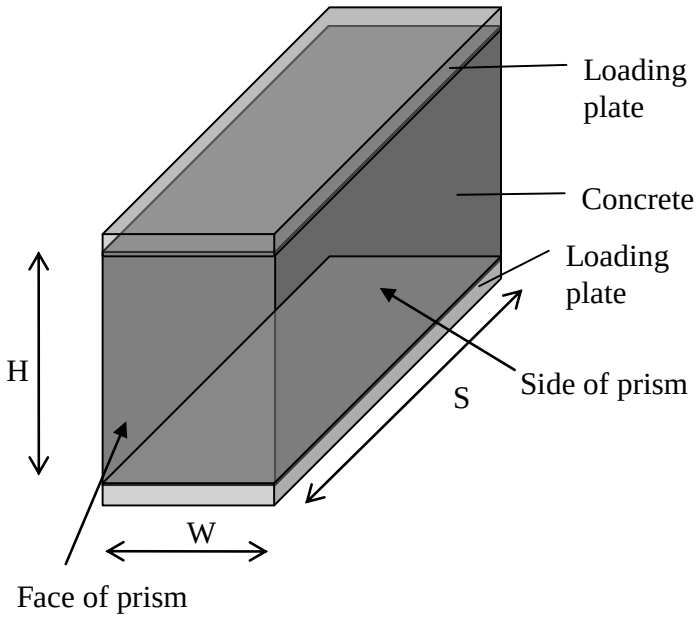

Figure 3.15: The geometry of the concrete prism.

When the prisms were tested, wedge failure occurred along the length of the prism. The maximum length of the concrete prism was limited to 500mm because the size of the loading platen machine on the Amsler Compression Testing Machine that was used in this research was 500mm × 500mm. Thus the length (*S*) in Figure 3.15 was in the range 200mm to 500mm. The width *W* of the prisms was between 50mm to 125mm, and the slenderness ratio of height/width (*H*/*W*) of all prisms was 2.

Shear-friction research on the formation of the wedges suggested that the wedge could be contained within prisms of a height to width ratio of 2:1 (Ali *et al.* 2010). The notation adopted for the four different sized prisms reflected the prism width; Test-125

refers to prisms which are have dimension 125mm width, 250mm height and 500mm long, Test-100 refers to prisms which are have dimension 100mm width, 200mm height and 400mm long, Test-75 refers to prisms which are have dimension 75mm width, 150mm height and 300mm long and Test-50 refers to prisms which are have dimension 50mm width, 100mm height and 200mm long.

There were three prisms of each size except the largest, Test-125 (125×250×500), which had four concrete prisms. The prisms in Test-125 are named Test1-125, Test2-125, Test3-125 and Test4-125. The prisms in Test-100 are named Test5-100, Test6-100 and Test7-100. The prisms in Test-75 are named Test8-75, Test9-75 and Test10-75 and the prisms in Test-50 are named Test11-50, Test12-50 and Test13-50. The details of name and specimen size can be seen in Table 3.4. To assist the load distribution, the specimens were set up with steel loading plates exactly matching the size of the specimens pasted top and bottom as shown in Figure 3.15. The thickness of this steel plate was 10 mm.

Table 3.4: Detail of concrete prism.

Specimen	Size (WxHxS)	Specimens number
Test-125	125x250x500	4
Test-100	100x200x400	3
Test-75	75x150x300	3
Test-50	50x100x200	3

3.2.3 The Test Rig and Instrumentation

The Amsler Compression Testing Machine used for the concrete prism test can apply a maximum load of 5000kN. The testing machine is shown in Figure 3.16. A computer was used to perform data acquisition for the LVDTs and loading cells. When a specimen was ready to be tested, it was placed in the rig as shown in Figure 3.16(a). The load was applied axially to the machine platens and loading plate until failure. These tests were undertaken at the Chapman Laboratory, University of Adelaide.

(a) *(b)* *(c)*

Figure 3.16: Amsler Compression Test Machine.

Four vertical LVDTs were fixed on every edge of the loading platens to measure the axial contraction of the prism (Figure 3.17). These axial LVDTs were placed between the platens machine. These transducers measured the axial deformation of each edge of the concrete prism. The axial deformation of the prism was taken as the average of these four individual axial transducers. The instrumentation of all concrete prisms was identical.

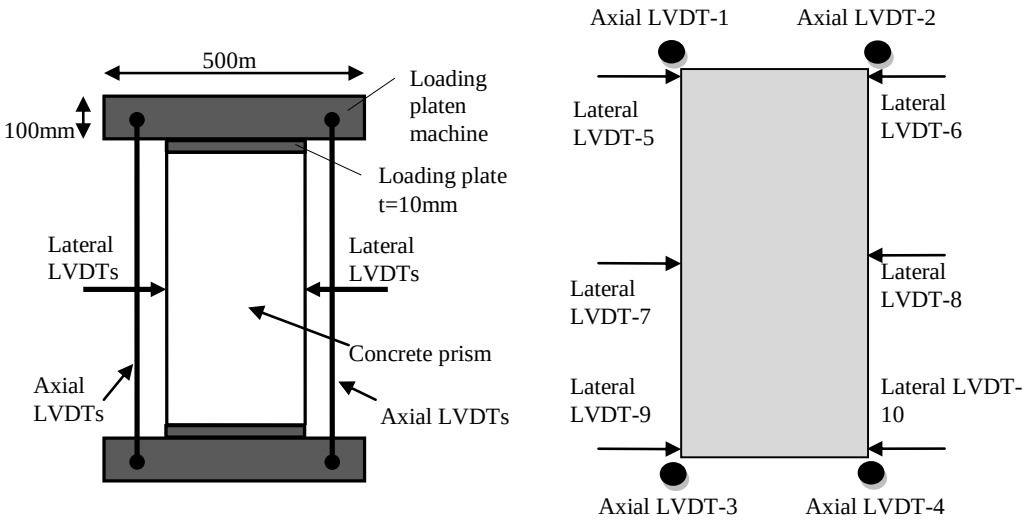

(a) Front view *(b) Plan view*

Figure 3.17: Diagram of axial and lateral transducer layout on prism.

Meanwhile lateral deformations were monitored using three horizontal LVDTs on each side of prism as depicted in Figure 3.17(b) and Figure 3.18. The lateral LVDTs were placed at half the prism height ($H/2$). LVDT-7 and LVDT-8 were placed in the middle of the each side. While LVDT-5, LVDT-6, LVDT-9 and LVDT-10 were placed 10mm from every edge of the prism. These four LVDTs were placed so close to the edges of prism that they were affected by the failure of the face of prism. Hence the lateral deformation result from sensors LVDT-5, LVDT-6, LVDT-9 and LVDT-10 were neglected. Only the data from LVDT-7 and LVDT-8 were used, since it is more reflective of the actual average lateral expansion of the prism.

It is important to note that nine strain gauges were applied axially on each front side of the prism to measure axial deformation as shown in Figure 3.18. The reading values from these strain gauges were not used in this current research, however, since the strain gauge reading values had been obtained during a parallel research project at the University of Adelaide, and were not relevant at this point but were obtained for future research projects.

The 10mm thick steel plates were applied on top and bottom of the specimens to ensure that the applied load was evenly distributed to the prism surface and Kaffir D dental paste was applied between specimens and loading plates.

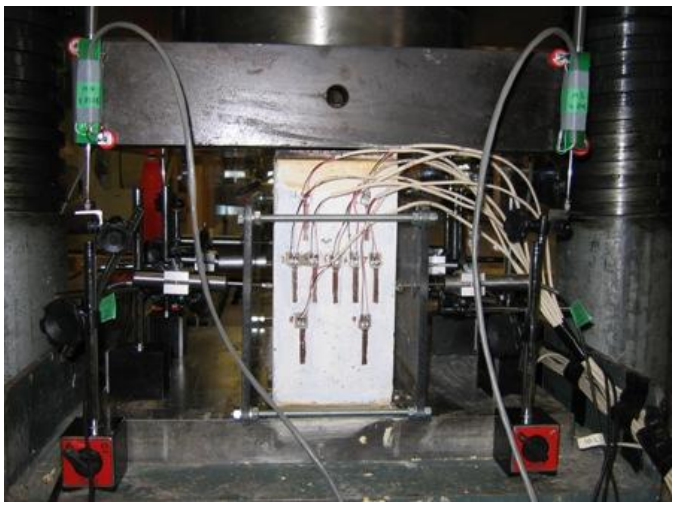

Figure 3.18: Prism uniaxial compression test setup.

The focus of this research was the descending branch of the load-displacement curve in order to evaluate the softening concrete. Displacement control was, therefore, particularly important, and loads were applied steadily and carefully in order to maximise the amount of data captured from the descending branch. Up to peak load, the loads applied on load control to the loading plates were dependent on the size of the specimens. The load rates were 10kN/min, 20kN/min, 30kN/min and 50kN/min for Test-50, Test-75, Test-100 and Test-125 respectively. The loading was switch from load control to displacement control immediately after the peak load reached. Hence a rate of 2×10^{-4}mm/s was applied at post peak load for all concrete prisms.

3.3 Test Results

Raw results of all uniaxial compression tests on the concrete prisms are described in this section. Deformation occurred in axial and lateral directions when an axial load was applied on the top and bottom of the concrete prisms as illustrated in Figure 3.19. The figure shows the front view of a concrete prism with width *W* and height *H*. The load which was applied to the concrete prism is represented by total axial load *L* in kilo Newton (kN). Displacement in the axial and lateral directions is represented by contraction and dilation respectively in millimeters (mm) and shown a $C/2$ and D_1 and D_2 respectively.

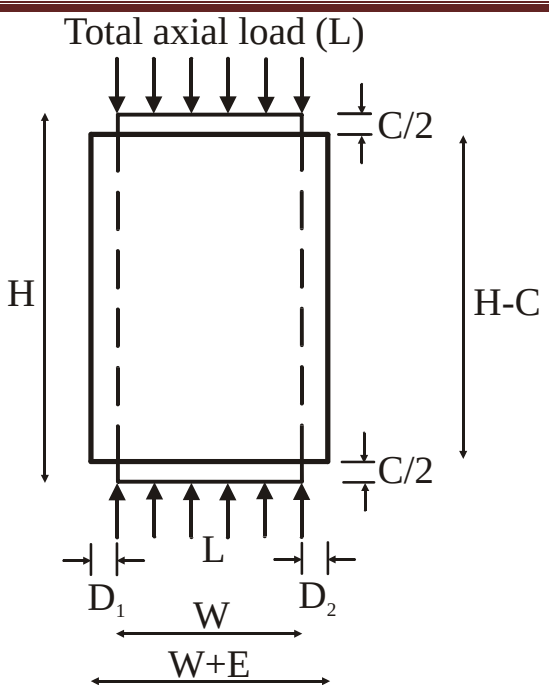

Figure 3.19: Total axial load (L) applied to the prism.

Figure 3.19 depicts the deformation using a thick solid line. Total axial contraction *C* is the contraction of the whole prism, that is, the average contraction from the value of LVDTs reading. Total lateral expansion *E* is the total dilation of the whole prism that is the algebraic sum of the two dilations from the values of lateral LVDT-7 and LVDT-8 readings.

The axial transducer recorded the axial deformation or contraction between the steel platens and therefore included the bedding down and contraction of the dental paste. The experiment result was adjusted to remove this bedding down and dental paste contraction that will be discussed in more detail in Section 3.4.1. While each lateral transducer showed the lateral deformation or dilation on one side of the prism. D_1 was dilation on one side of the concrete prism and D_2 was dilation on the other side (see again Figure 3.17 and Figure 3.19).

A positive LVDTs' reading indicates axial contraction and a negative value indicates axial expansion. When the axial load was applied uniformly to the loading platen machine, sometimes a slight eccentric load application occurred accidently. This was more likely at low load levels.

The dilation as recorded by lateral LVDT is positive, it indicates that the prism expanded on the side where the LVDT was placed or "moved out". A negative dilation value indicates that the prism contracts or "moves in", as shown in a dashed line in Figure 3.20. The position of axial LVDTs-1, -2,-3 and -4 and lateral LVDTs-7 and -8 can be seen again in Figure 3.17.

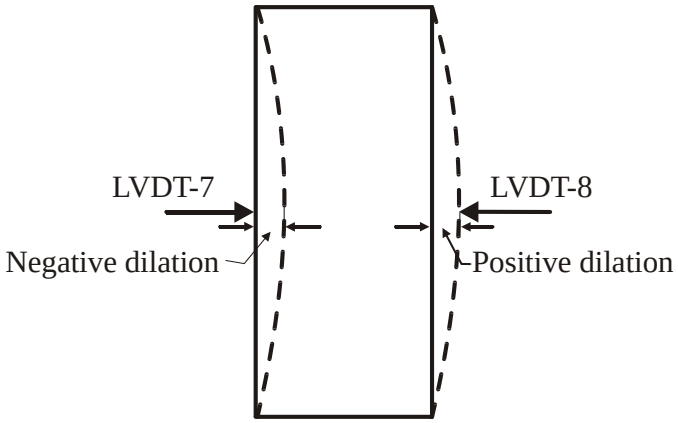

Figure 3.20: The dilation of the prism (top view of prism)

The next 36 sets of images and graphs, Figure 3.21 to Figure 3.56 show the total axial load *L* against contraction graphs, the total axial load *L* versus lateral deformation or dilation graphs and the failure pattern of all concrete prisms is depicted one by one.

TEST1-125

Figure 3.21 shows the values of axial LVDTs' reading for Test1-125. The graph illustrates the fact that the value of LVDT-1 (refer Figure 3.17) has a negative value thus the edge where LVDT-1 was placed is slightly in tension while the other edges of prism are in contraction. This might happen because the axial load being eccentrically accidently at low load. A slight eccentrically load pulls up the platen load a little bit at one edge, where the LVDT-1 was placed, and pushes the platen load at the others edges.

The values of LVDT-1 and LVDT-3, these are on the same side as each other too, are decrease as the load increases until the load approximately 200kN. After that point, contraction at all edges of the prism increases as the load increases, except the edge where LVDT-1 was positioned, which is still in tension. The dial on LVDT-1 becomes positive when the load reaches approximately 2200kN, and LVDT-1 enters a

state of contraction. The contractions on the face where the LVDTs-3 and -4 are placed are higher than the other face of prism.

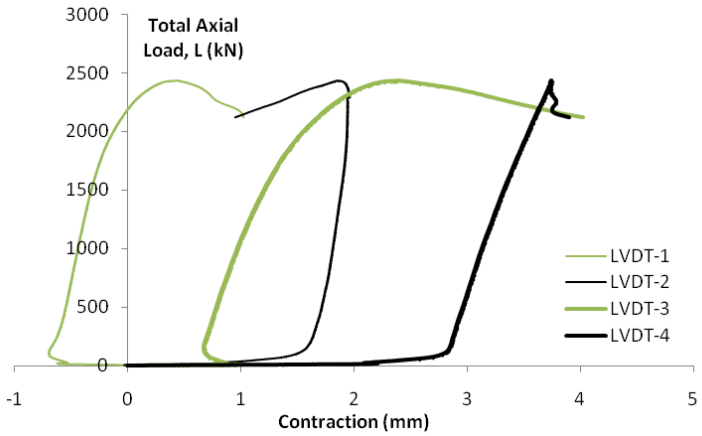

Figure 3.21: Relationship between total axial load and contraction graph of Test1-125.

The response of the total axial load and the dilation of Test1-125 is illustrated in Figure 3.22. The graph indicates the side of prism where lateral LVDT-7 was placed is move out or expands while the value of lateral LVDT-8 reading still around zero. It means that the prism expand only one side until the load is approximately 1800kN. After that point, the both sides of prism expand however dilation of LVDT-7 increases more significantly after peak load.

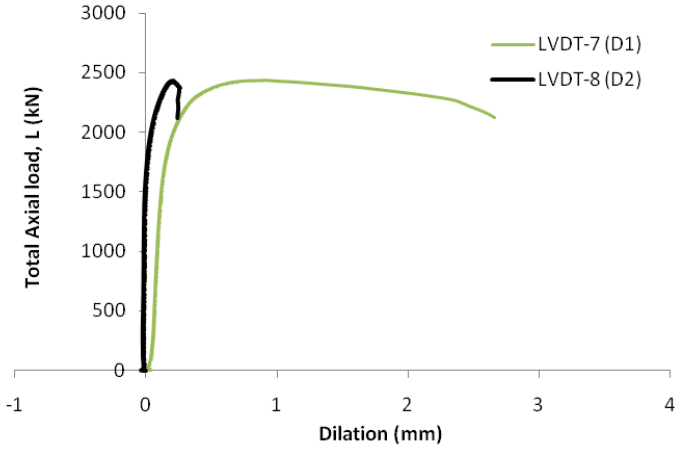

Figure 3.22: Total axial load – dilation response of Test1-125.

The failure pattern of Test1-125 is shown in Figure 3.23. The images show the concrete has softened and fallen away on both sides of prism and the wedges develop almost along the length of prism. The failure occurred just on one face of the prism where LVDTs-3 and -4 are placed [Figure 3.23 (a)]. The contraction on this face is higher than the other face (see again Figure 3.21). An “explosive” failure occurred.

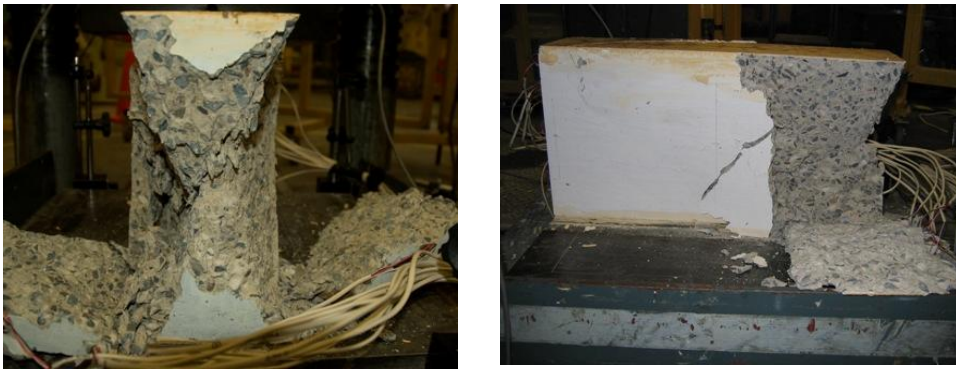

(a) *(b)*

Figure 3.23: Failure pattern of concrete prism Test1-125; (a) failure on one face; (b) side view

TEST2-125

Figure 3.24 shows the relationship between total axial load and contraction of Test2-125. The edges of prism, where LVDT-2, LVDT-3 and LVDT-4 are positioned, are in contraction while the edge, where LVDT-1 is placed, is slightly in tension. Accidentally the eccentrically load occurred at low load. The value of LVDT-1 is in contraction when L is about 2000kN. A large contraction occurred on the face of prism where LVDT-3 and LVDT-4 were placed.

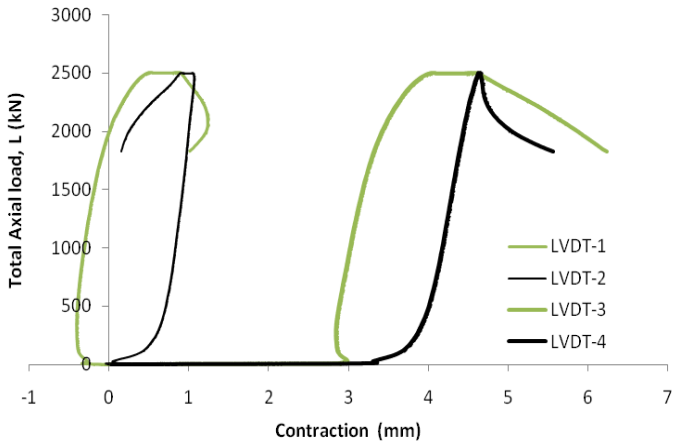

Figure 3.24: The response of total axial load and contraction for Test2-125.

Figure 3.25 illustrates how the prism of Test2-125 expands when the prism is subjected to a uniaxial compression load. The graph indicates that one side of the prism contracts (LVDT-7) while other side of prism moves out or expands (LVDT-8). However, when the load higher than 2,000kN, the both side of the prism move out or expand until the prism failed and the wedge developed.

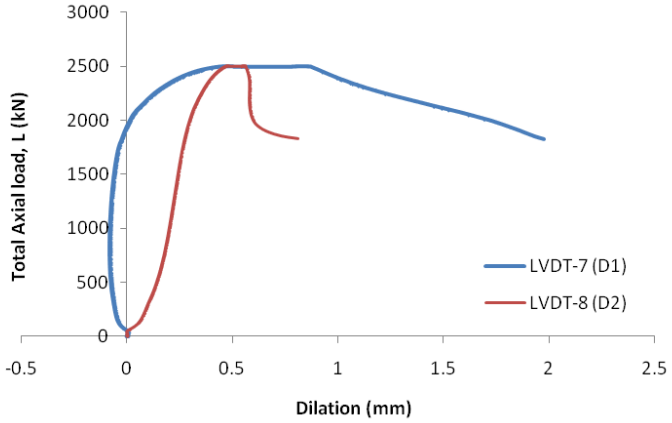

Figure 3.25: Total axial load – dilation response of prism Test2-125.

The failure pattern of prism Test2-125 is shown in Figure 3.26. The failure occurred only in one face where LVDTs-3 and -4 are placed. The wedges can be observed on both sides of the prism in these images. The wedge on the right side of the prism almost broke completely away from the body of the prism. The crack almost occurred along the whole prism. An “explosive” failure also occurred in this prism.

(a) *(b)* *(c)*

Figure 3.26: Failure pattern of concrete Test2-125: (a) front view; (b) side view; (c) top view

TEST3-125

The contraction of Test3-125, as recorded by all axial LVDTs, appears very similar at the beginning of loading (Figure 3.27). Quite slight scatter occurs as the load increases. This pattern means that from the start of the test, the applied load was evenly distributed on the whole prism and the whole prism is in contraction. The contraction of the prism where LVDTS-3 and -4 were placed is higher than the other face.

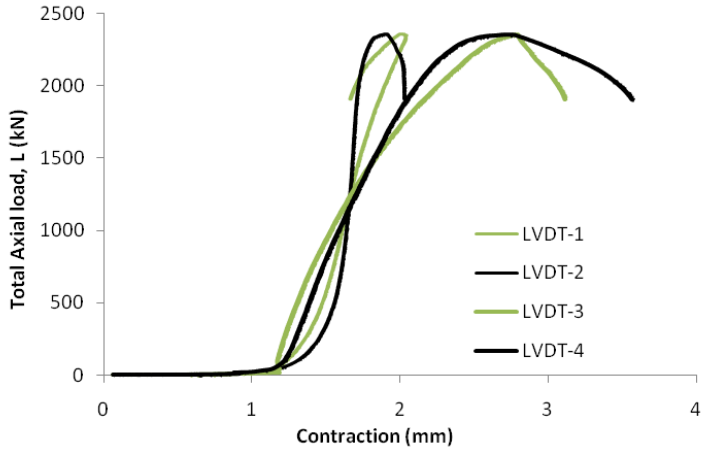

Figure 3.27: Total axial load-contraction response of prism Test3-125.

The relationship total axial load and dilation of Test3-125 is shown in Figure 3.28. The graph indicates both sides of prism expand at the load is approximately 900kN and increase significantly after peak load until the prism failed.

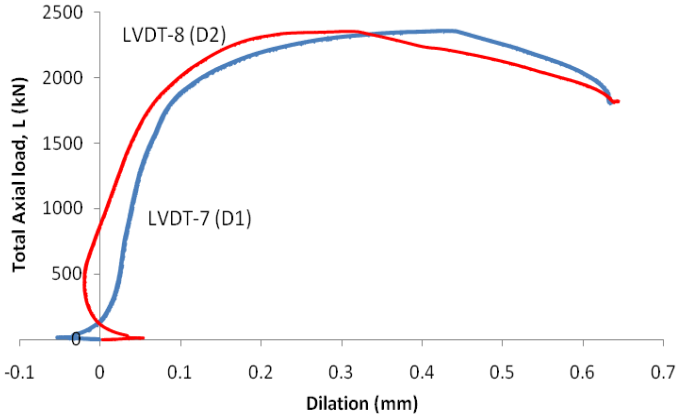

Figure 3.28: Total axial load – dilation response of prism Test3-125.

The concrete prism Test3-125 failed with an "explosive" sound. The concrete prism softened and the wedge developed almost along the whole length on both sides of the prism as depicted in Figure 3.29. The prism failed on the face where LVDTs-3 and 4 were placed.

(a) *(b)*

Figure 3.29: Failure pattern of concrete prism Test3-125; (a) front view; (b) side view.

TEST4-125

The relationship between the total axial load and the contraction of Test4-125 that was obtained when observing the values of the LVDTs is illustrated in Figure 3.30.

From the beginning of loading, the whole prism was in contraction. A large contraction occurred at the edges of prism where the LVDT-2 and LVDT-4 were placed. This means that side where these LVDTs were located failed [see again Figure 3.17(b), as can be observed in Figure 3.32(a) and (b)].

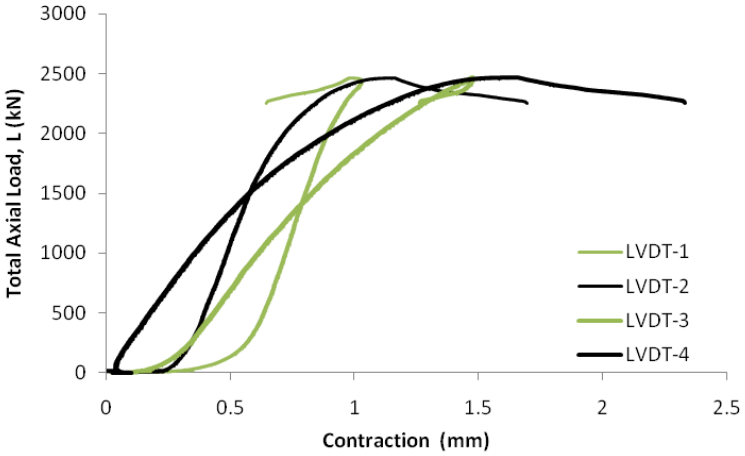

Figure 3.30: Total axial load (L) contraction response of prism Test4-125.

The dilation as recorded by using lateral LVDTs of Test4-125 is depicted in Figure 3.31. The prism start to expand in the both sides when the load 500kN.

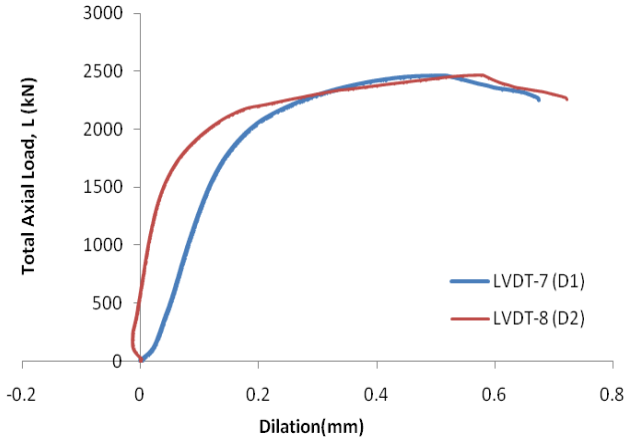

Figure 3.31: Total axial load– dilation response of prism Test4-125.

The concrete prism of Test4-125 failed on both face and the wedges developed along the whole length on both side of prism (Figure 3.32). Only one wedge was fallen away that is the side where LVDT-2 and LVDT-4 placed. The other wedge formed but not fallen away [(Figure 3.32(c)]. An “explosive” failure also occurred.

(a) *(b)* *(c)*

Figure 3.32: Failure pattern of concrete prism Test4-125; (a) front view; (b) side view; (d) top view.

TEST5-100

The total axial load and individual contraction response of prism Test5-100 is shown in Figure 3.33. The contraction is measured by using axial LVDT dials. The graph indicates that the face where LVDT-3 and LVDT-4 were placed failed [see again Figure 3.17(b)]. A large contraction occurred at that face, meaning that more compression had been applied than to the opposite face, accidently the eccentrically load occurred. It is worth noting that this was the same result as in Test4-125.

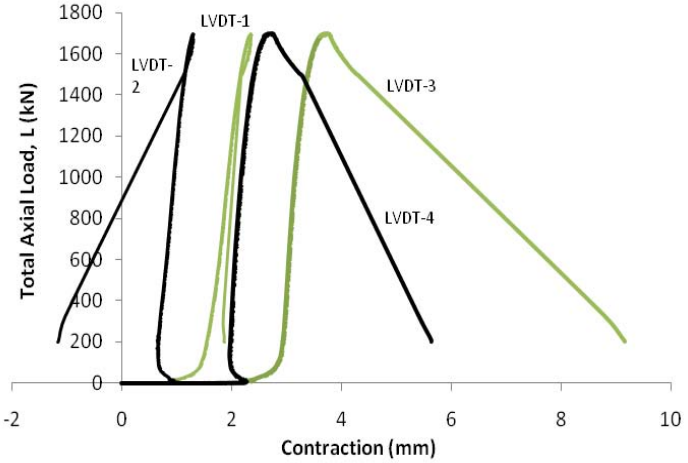

Figure 3.33: Total axial load - contraction response of Test5-100

Figure 3.34 shows dilation response of Test5-100. The graph indicates up to peak load the both side of prism expand slightly up to peak load. However, after this point only the side, where LVDT-7 placed expands significantly as the load decrease.

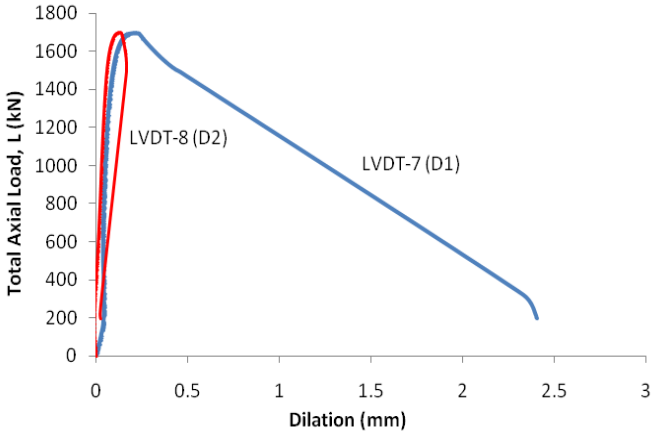

Figure 3.34: Total axial load – dilation response of prism Test5-100

Figure 3.35 shows the failure of concrete prism Test5-100. The diagonal crack occurred on both faces. An "explosive" failure did not occur in this prism. The face [Figure 3.35(a)] was the side where LVDT-3 and LVDT-4 were placed (see also Figure 3.33) while Figure 3.35(b) illustrates the diagonal crack on the face where LVDT-1 and -2 were placed.

(a) *(b)*

Figure 3.35: Failure pattern of concrete Test5-100

TEST6-100

The individual contraction from all LVDTs against the total axial load of Test6-100 is represented in Figure 3.36. From the start the whole prism was under compression. Before peak load the contraction on all four sides was quite similar. After peak load was reached, the contraction on the side where LVDTs-1 and 2 were placed increased as the load decreased, while the contraction on the side where LVDTs-3 and 4 were placed decreased. This result means that after peak load more pressure was applied on the side where LVDTs-1 and 2 were placed because after the side on which LVDT-3 and -4 were placed had cracked, the sound concrete bore the full compressive force of the testing plate. A large contraction, therefore, occurred on that face, followed by failure (see also Figure 3.38).

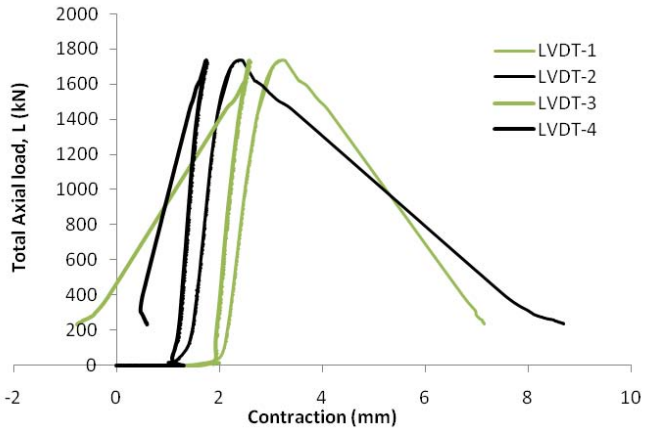

Figure 3.36: Relationship between total axial load and contraction for prism Test6-100.

Relationship dilation and load of Test6-100 is depicted in Figure 3.37. The side where LVDT-8 placed does not expand until load reaches around 1600kN, however, this side expands significantly after peak load reached until the prism failed.

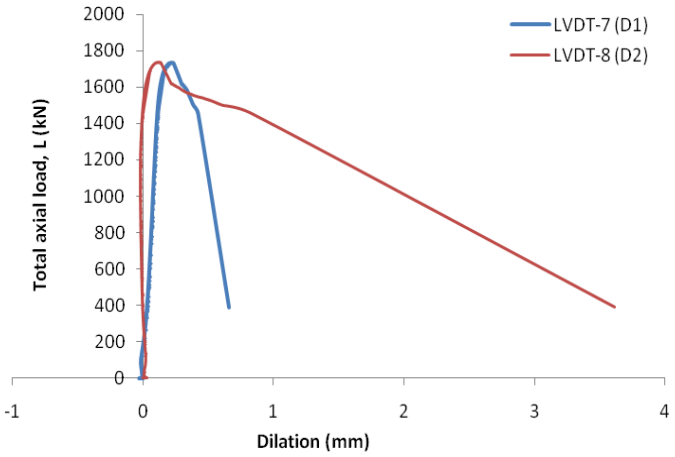

Figure 3.37: Total axial load – dilation response of prism Test6-100.

The failure of the prism in Test6-100 is shown in Figure 3.38. It shows the diagonal crack as well as formation of the wedges but not along the whole prism length. The failure occurred just on one face. The face where LVDTs-1 and 2 placed.

(a) *(b)*

Figure 3.38: Failure pattern of concrete Test6-100; (a) front view; (b) side view.

TEST7-100

The response of total axial load and individual contraction on four edges of the prism Test7-100 is depicted in Figure 3.39. The pattern of the graph is almost same as in Test6-100 described previously. Up to peak load the trend of the response remains quite similar. After peak load, the contraction of LVDT-1 and LVDT-2 increase significantly until it reaches 8mm as the load decreases.

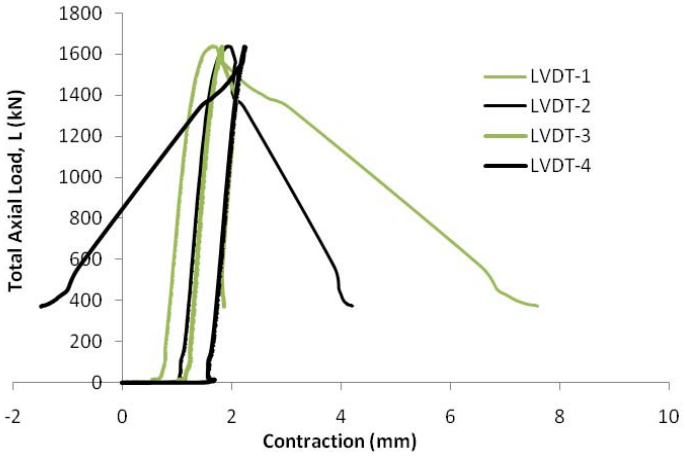

Figure 3.39: The relationship between total axial load and contraction of prism Test7-100

The prism Test7-100 expands just one side that is the side where LVDT-7 were placed (Figure 3.40). The prism expands slightly up to peak load but increase significantly after the peak load reached (see also Figure 3.41).

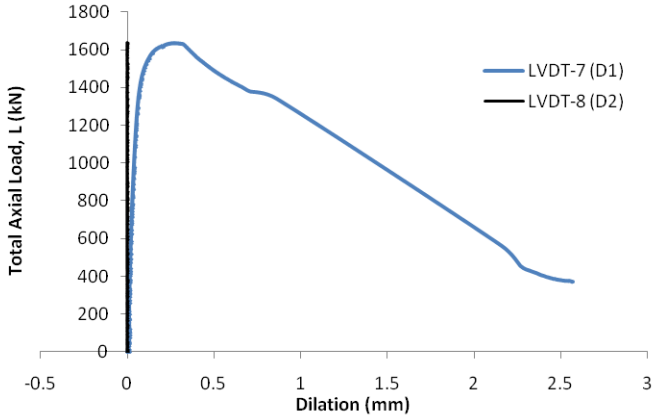

Figure 3.40: Total axial load–dilation response of Test7-100

The failure pattern of prism Test-100 is shown in Figure 3.41. The failure occurred where LVDTs 1 and 2 were placed. The diagonal crack and the wedges are clearly seen. The images show the wedge occurred along the whole length of prism in one side and the other side the wedge occurred along less than half of prism length.

(a) *(b)* *(c)*

Figure 3.41: Failure pattern of concrete prism Test7-100; (a) front view; (b) and (c) sides view

TEST8-75

Figure 3.42 shows that three edges of the prism, where LVDT-1, LVDT-3 and LVDT-4 were set up, are in compression while another edge is in tension. When the load reaches approximately 650kN, all edges are in compression. The value of LVDT-3 and LVDT-4 decreases immediately after peak load is reached. While the value of LVDT-1 and LVDT-2 still increases as the load decreases. Failure continues on this side of the prism as shown in Figure 3.44.

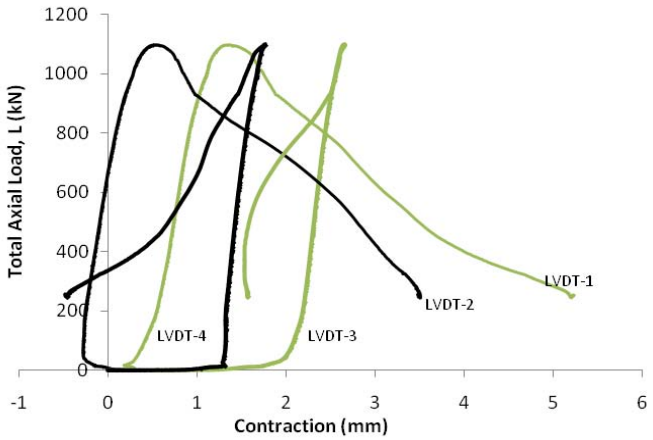

Figure 3.42: Total axial load-contraction response of Test8-75

When the load below 1000kN, one side of prism Test 8-75 is move in and the other side is move out. From that point, both sides of prism expand. The side where LVDT-7 placed expands significantly while the other side expands slightly.

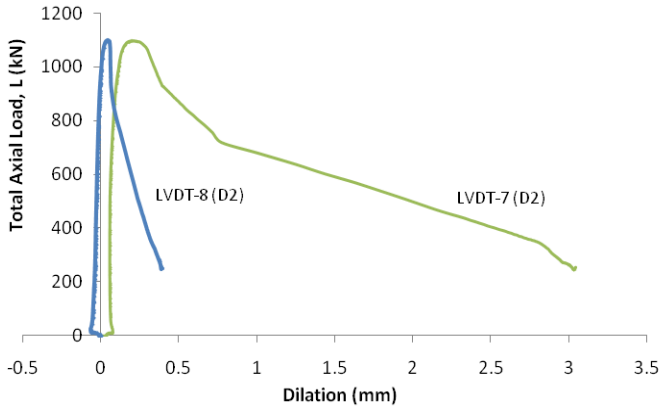

Figure 3.43: Total axial load–dilation response of Test8-75.

Figure 3.44, shows the wedges and the diagonal crack that formed during the test. Significant failure occurred only on one face where LVDT-1 and LVDT-2 were positioned. No visual crack could be seen on the other face.

(a) *(b)*

Figure 3.44: Failure pattern of concrete prism Test8-75; (a) front view; (b) side view

TEST9-75

The values of the contraction of the LVDTs' are shown in Figure 3.45. The graph indicates that the contraction occurred on the whole of prism. The compression

load was distributed uniformly to the whole prism. The values of all LVDTs' are almost the same. After peak load was reached, the contraction increased as the load decreased.

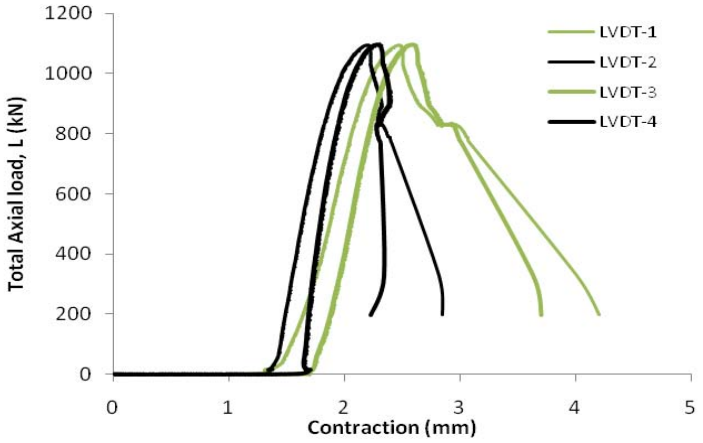

Figure 3.45: Total axial load-contraction response of prism Test9-75.

Similar dilation responses up to peak load are shown in Figure 3.46. The dilation on one side of prism Test9-75 increases significantly (the side of prism where LVDT-7 placed) as the load decrease while the other side of prism increases slightly.

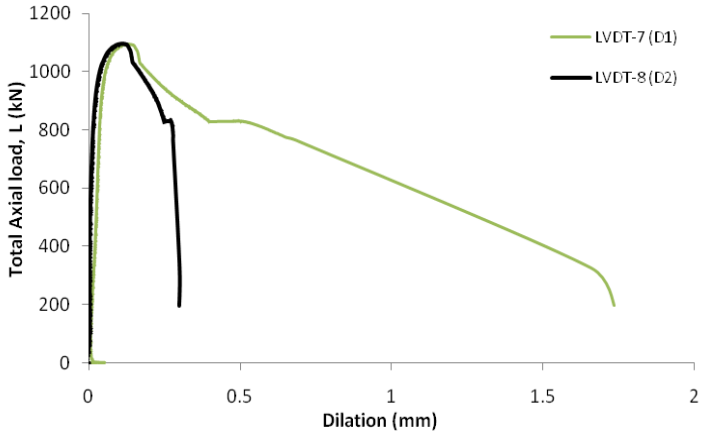

Figure 3.46: Total axial load-dilation response of prism Test9-75.

The failure images of prism Test9-75 are shown in Figure 3.47. The prism failed on both faces. The diagonal crack occurred on one face and the other face, splitting crack occurred clearly.

(a) *(b)* *(c)*

Figure 3.47: Failure pattern of concrete prism Test9-75; (a) and (b) front view; (c) side view

TEST10-75

The graph in Figure 3.48 indicates that contraction occurred on the whole prism as can be seen in the ascending branches up to peak load. After that point, the contraction at the edges where LVDT-1 and LVDT-2 set up, increase with a decrease of the load. While the contraction on other edges of the prism decrease.

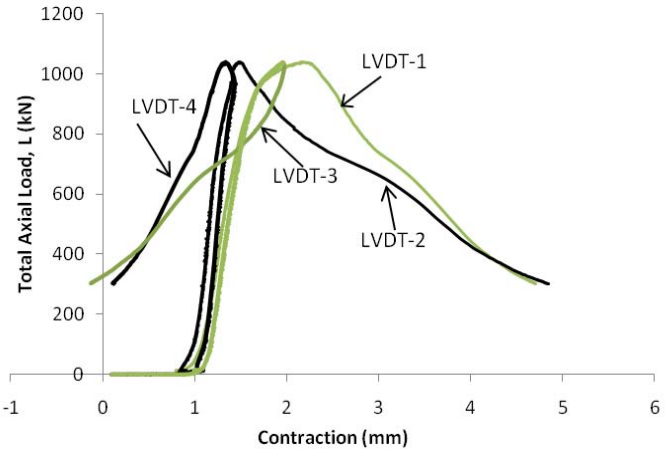

Figure 3.48: The relationship of total axial load-contraction of prism Test10-75

The load and dilation response of Test10-75 (Figure 3.49) is quite similar with the response of Test6-100 (see again Figure 3.37). One side of prism expands slightly since the beginning while the other side does not expand. Dilation the side where the LVDT-8 placed as larger as 1.8mm while the other side just around 1.3mm.

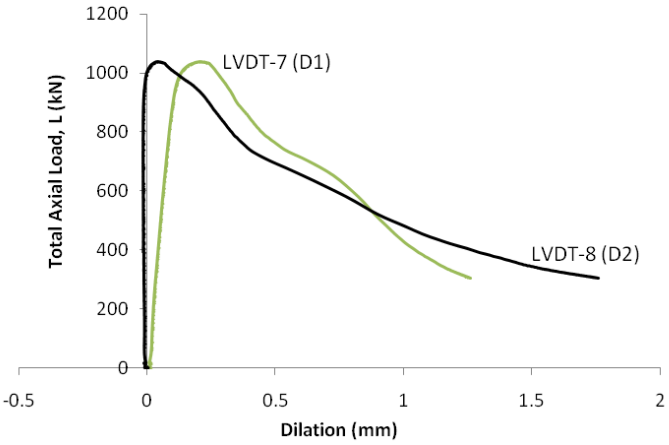

Figure 3.49: Total axial load–dilation response of Test10-75.

The splitting failure occur only one face of prism Test10-75, where LVDT-1 and LVDT-2 placed as shown in Figure 3.50(a). No visual crack seen on the other face.

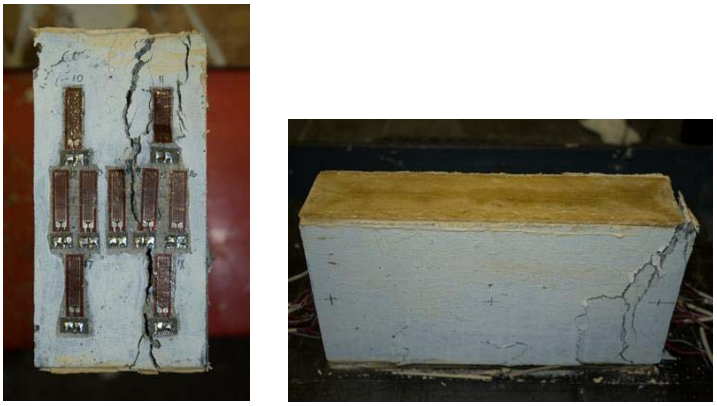

(a) *(b)*

Figure 3.50: Failure pattern of concrete Test10-75; (a) front view; (b) sides view.

TEST11-50

Initially, the edges where LVDT-1 and LVDT-2 applied are in tension while the edges where LVDT-3 and LVDT-4 set up are in compression (Figure 3.51). The eccentrically load occurred on the prism accidently. The dial of LVDT-1 becomes positive when L is around 50kN. The pattern of the curves is almost same. LVDT-2 reading value still in negative until the prism near to fail. The crack occurred on both faces of the prism as shown in Figure 3.53.

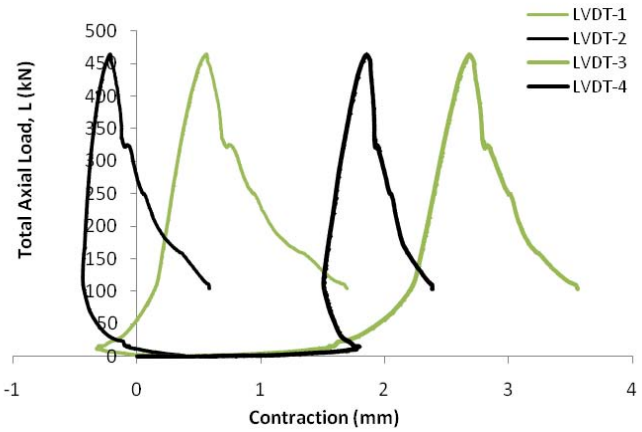

Figure 3.51: Total axial load and contraction response of Test11-50.

Figure 3.52 shows the both sides do not expand until the load is around 300kN. After that point, the side where LVDT-8 placed expands slightly and expands significantly after the peak load reached. While the other side increase slightly on descending branch.

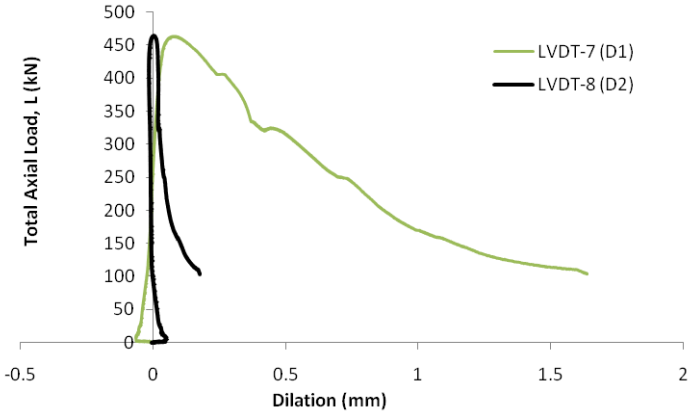

Figure 3.52: Total axial load (L) – dilation response of Test11-50.

Three images in Figure 3.53 show the failure pattern of concrete prism Test11-50. The cracks occurred on both faces of prism. The diagonal and splitting failure occurred.

(a) *(b)* *(c)*

Figure 3.53: Failure pattern of concrete test11-50; (a) and (b) both faces failed; (c) side view.

TEST13-50

Figure 3.54 shows the pattern of total axial load-contraction response of Test13-50 is almost same with response of Test11-50 (see again Figure 3.51). The graph indicates one face in tension at low load, while the other face in compression. When the load reaches 350kN, the whole prism is in compression. The contraction of LVDT-3 and LVDT-4 reading values is larger than the others.

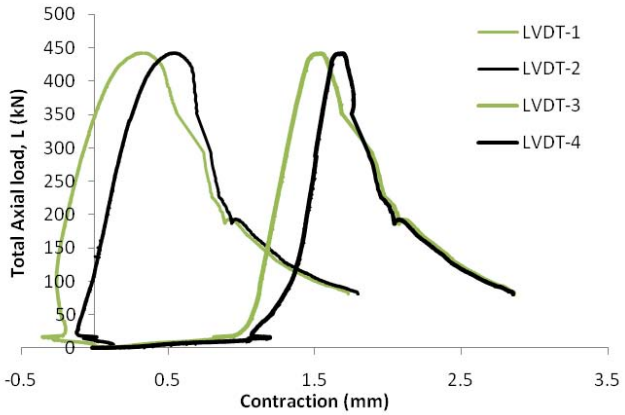

Figure 3.54: Total axial load and contraction response of Test13-50.

One side of prism Test13-50 move in and the other side move out until just before peak load reached around 442kN (Figure 3.55). After that the both sides move out until the prism failed.

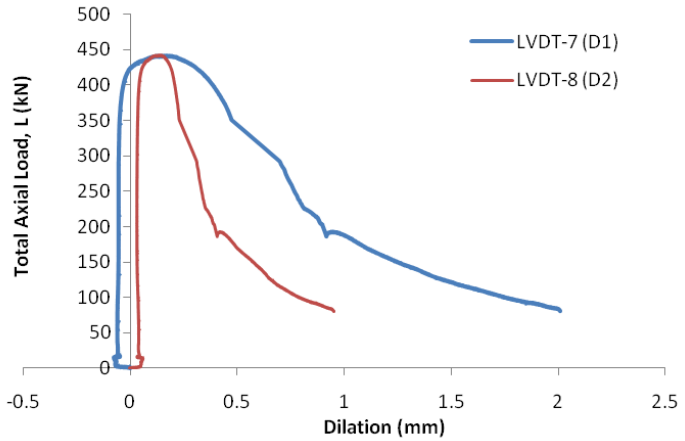

Figure 3.55: Total axial load–dilation response of Test13-50.

Figure 3.56 shows the failure pattern of concrete prism Test13-50. The images illustrates the diagonal cracks occurred on both faces of the concrete prism.

(a) *(b)* *(c)*

Figure 3.56: Failure pattern of concrete Test13-50

It is important to mention that experimental test of prism Test12-50 was failed therefore the results are not presented in this thesis.

The raw data of 12 concrete prisms as recorded by using axial and lateral transducers have been described previously. These raw data are analysed in the next section. The tests data are divided and analysed into two deformation directions: axial

and lateral. The analyses are the same on both directions of deformation. Step by step is explained more detail below.

3.4 Analysis of Test Results

3.4.1 Method of analysis

The raw data in Section 3.3 described the axial contraction and the lateral dilation of every specimen under increasing axial load. In this section the results for every concrete prism that was tested are analysed, first to understand axial deformation or contraction and then lateral deformation or expansion for each prism. The next section of this analysis compares the results across the different sizes of concrete prism in the axial direction, then in the lateral direction in order to determine the influence of prism size on the softening behaviour.

3.4.1.1 Axial Deformation

The technique of analysis in axial deformation is described below. There are 5 steps of the analysis; firstly quantifies the deformation the whole prism for a given applied load; then determines the behaviour of one single wedge only which is the axial load in terms of axial deformation. The non-linear deformation is quantified in the next step. After that the load per millimeter wedge thickness is determined and followed by quantifying the slip wedge for a given stress wedge.

The first step of axial deformation analysis develops the total axial contraction C against total axial load L on each concrete prism. As described previously, L is the total axial load that applied to the prism and C is the total axial contraction of the whole concrete prism. The contraction which is obtained and recorded by axial LVDTs as described previously is contraction that occurred in one edge of prism. Hence total axial contraction of the whole prism C is the average of the individual contraction values recorded by the axial transducers, found using the Eq.3.1

$$C = \frac{LV_{-1} + LV_{-2} + LV_{-3} + LV_{-4}}{4} \qquad \textit{Eq. 3.1}$$

where LV_{-1}, LV_{-2}, LV_{-3}, LV_{-4} are the values in mm recorded by transducer-1, transducer-2, transducer-3 and tranducer-4 respectively. The position of LVDTs-1, -2, -3 and -4 are shown in Figure 3.57.

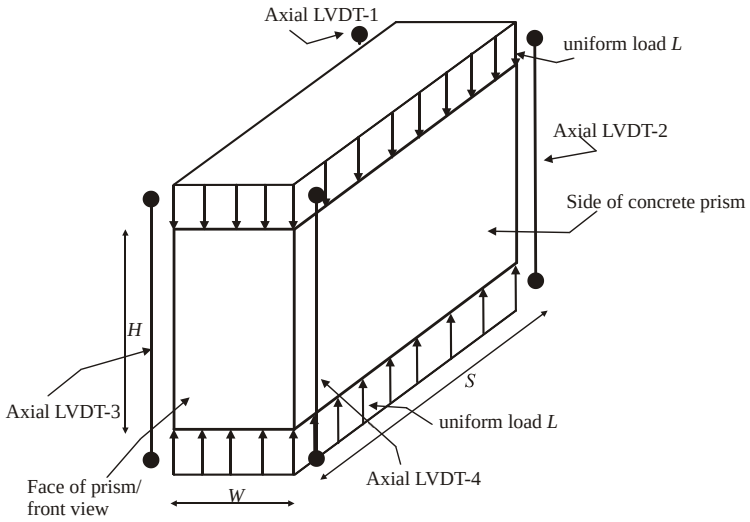

Figure 3.57: The concrete prism under compression load

A typical *L*-*C* response of concrete prism is shown in Figure 3.58. The graph indicates that at initial loading, the "settle down the position" occurred as shown in a dash line. This condition occurred just at low load because the concrete prism surface was not exactly flat thus when the concrete prism is subjected to the load, the prism needed to "settle". As the load increased the whole prism uniform compressed. This means that the prism surface is already flat. To obtain the actual total axial contraction of the prism *C*, the contraction that is caused by "settle down the position" is removed from the *L*-*C* response by determining a new origin point O.

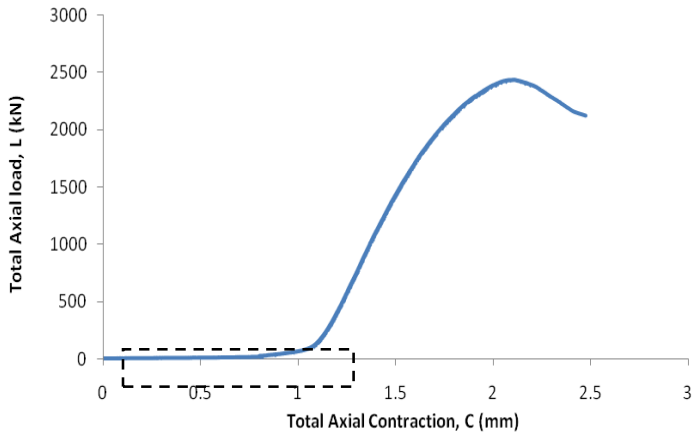

Figure 3.58: A typical of total axial load and total axial contraction of concrete prism

Initially a straight line is extended along the curve, as shown in Figure 3.59. The intercept of this line and the x-axis form the new origin point O (0,0). Then the total axial contraction *C* is subtracted by *m*, where *m* is the distance between O' and new origin point O or the total axial contraction that is caused by "settle down the position" as shown in Figure 3.59. Hence a new x-y axis is obtained. Figure 3.58 is refined into Figure 3.60.

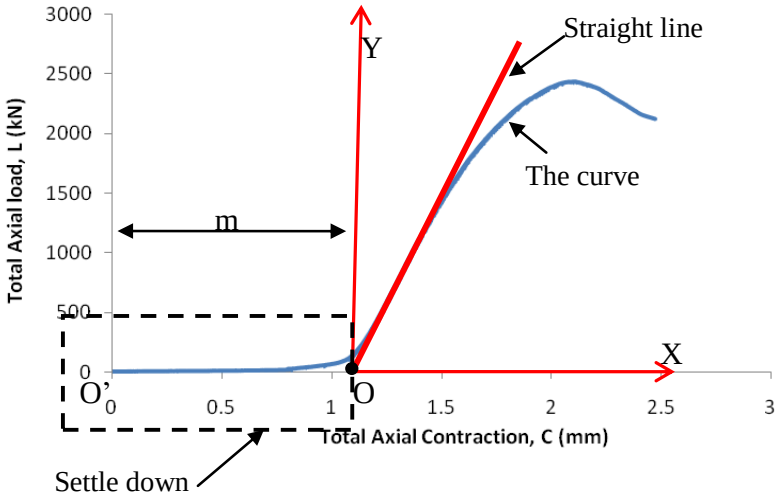

Figure 3.59: The correction of total axial contraction due to settling down

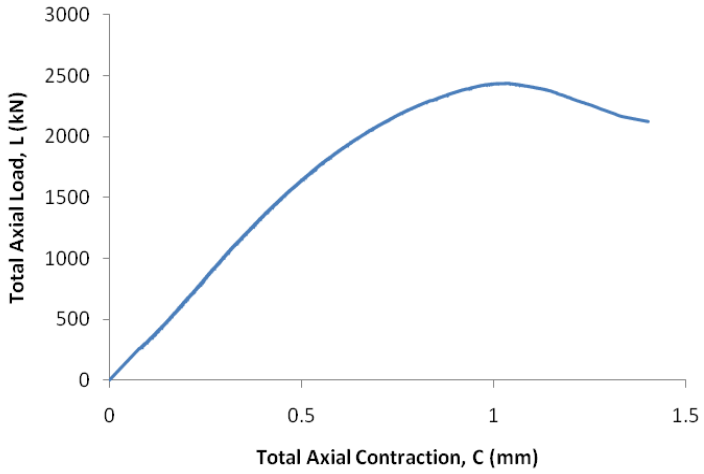

Figure 3.60: A typical of L-C response after correction the x-axis

The second part of the analysis determines the response of load and deformation for one wedge only. The compression concrete wedge and the definition of one single wedge of the prism are explained initially. Let us consider Figure 3.57, the prism with height *H* and width *W* and the length of *S*, which is four times the width, meaning that the behaviour of the prism under pressure can be considered to be two-dimensional. Four axial LVDTs are placed on every edge of prism. The concrete prism is subjected to uniform axial compression load *L* on top and bottom of the prism that cause part of concrete prism softened, crushed and failed as shown shaded in Figure 3.61. This softening region of the concrete prism referred to as the compression concrete wedge. The wedges idealisation is very important to simulate the compression concrete wedges. The wedges form in compression zone of concrete prism is idealised in Figure 3.61. This research analyse what happen after the wedge form not prior to the wedges form.

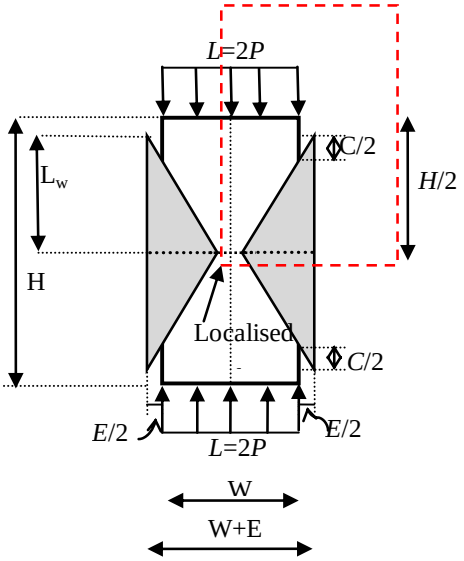

Figure 3.61: Idealised wedges of the prism

Figure 3.61 illustrates that the remaining concrete is referred to body of concrete prism is shown unshaded area and the compression concrete wedges on both sides and along the length of prism *S* are shown shaded area. A typical compression failure also occurrs on cylinder where the remaining concrete has formed a pair of truncated cones and outside these truncated cones has softened (Martinez *et al.* 1984, Mander *et al.* 1988, Xie *et al.* 1995, and Ali *et al.* 2010). However, the compression failure on cylinder

is affected by circumferential expansion. The compression concrete wedge has been observed by many researchers in cylinders (Ali *et al.* 2010), in the eccentrically loaded short prism (Debernardi and Taliano 2001, Daniel *et al.* 2008), in the concentrically loaded FRP confined rectangular prism (Deric *et al.* 2007).

The total axial contraction *C* and total lateral expansion *E* (more detail in lateral deformation in next section) occurred when the total axial load *L* applied to the prism and caused wedges form on both sides of prism. Each wedge expanded *E*/2 and contracted *C* under compression axial load *P* on top and bottom. The axial load, *P* was equal to *L*/2 where *L* referred to total axial load, which was the total load applied to the whole of the concrete prism, and *L*/2 referred to half the load. However, due to the symmetry of the wedges, the half on one wedge was considered to one wedge. Hence a quarter of the prism with a width *W*/2, height *H*/2 and length *S* now referred as a single wedge as shown in Figure 3.62.

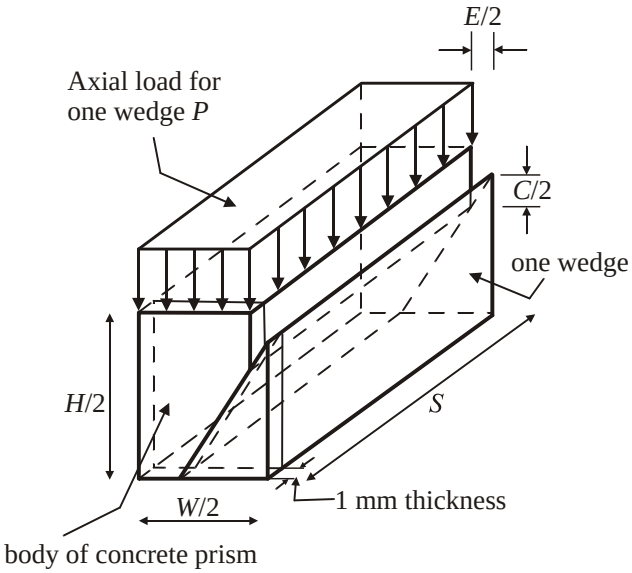

Figure 3.62: Idealised one wedge of prism

Figure 3.62 illustrates one single wedge contracts half of total axial contraction, *C*/2 and expands half of total lateral expansion *E*/2 under compression axial load *P* (more detail about total lateral expansion *E* is discussed in lateral deformation in Section 3.4.1.2.). The axial load *P* versus the total axial contraction for one wedge *C*/2 is

analysed for each prism. Hence this is the behaviour within the concrete zone in which one wedge forms.

The *C* was measured between platens therefore contains bedding down, contraction of the dental paste and the elastic contraction of concrete. This is a single wedge analysis hence *P* is half the applied load *L* and *C*/2 is the deformation of a single wedge as shown in Figure 3.62. Consequently the total axial contraction of one wedge, *C*/2 comprises the slip wedge S_w, the material contraction, bedding down and contraction of dental paste, where the total amount of material contraction, bedding down and contraction of dental paste resulting to *B* as illustrated in Figure 3.63.

Figure 3.63 illustrates that on loading, the load-contraction relationship may be considered to follow a linear path O-D with slope *k* up to a load of αP. Along the line OA, only elastic contraction occurs, the wedge not develops yet. After this point, non-linearity occurs in the ascending portion A-E, where the load peaks as P_p, followed by descending portion E-F which is often referred to as softening. This non-linearity is associated with micro-cracking along inclined wedge shaped plane which allow shearing across the inclined planes to accommodate the non linearity.

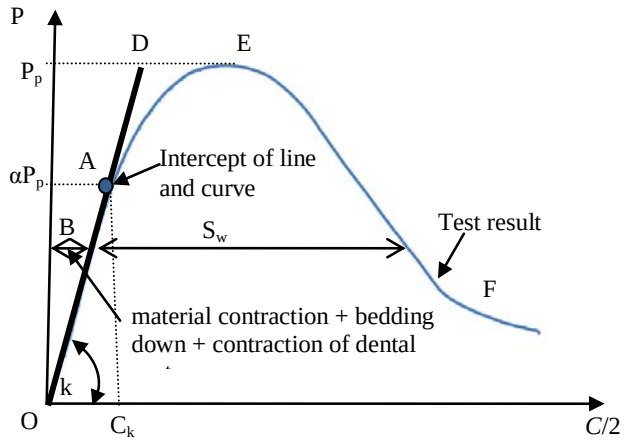

Figure 3.63: The axial load and total axial contraction over one single wedge response

The *P*-*C*/2 response gradually becomes non linear due to the micro-cracking within the prism. Some researchers determined the point where this non-linearity start α that is vary between 45% - 70% of peak load (Park and Paulay, 1975, Palmquist and Jansen 2001). The non-linearity should be occurred over 40% because Elastic Young's

modulus tests always taken up to 40% of peak load that is considered as elastic condition of concrete. In this research, α is considered to be 60%.

The total axial contraction C which was measured experimentally can be converted to the total axial contraction of a single wedge, and referred to as $C/2$ as shown in Figure 3.63. This contraction consists of the material contraction, the bedding down and the contraction of dental paste and that due to the micro-cracking or slip wedge S_w as shown in Figure 3.63, where the elastic deformation B is equal to the total amount of material contraction, dental paste contraction and bedding down.

Up to the load αP_p there is no deformation due to micro-cracking or deformation of the wedge. Only elastic contraction B occurs as shown a straight line O-A in Figure 3.63. The elastic contraction B is the sum of material and dental paste contractions and bedding down that is equal to

$$B = \frac{P\,C_k}{\alpha P_p} \qquad \textit{Eq.3.2}$$

Where B is elastic contraction, P is the applied load of one single wedge, α is a constant when the non-linearity start and in this research equal to 60%, P_p is the peak axial load of one wedge and C_k is the contraction corresponding to αP_p (Figure 3.63).

After the load αP_p, the slip of the wedge S_w starts to develop in ascending portion A-E and in descending portion E-F in Figure 3.63. The slip wedge S_w in mm given by

$$S_w = \frac{C}{2} - B \qquad \textit{Eq. 3.3}$$

Where C is total axial contraction of the whole prism and B is determined by using Eq. 3.2.

After remove the elastic contraction B due to material and dental paste contractions and bedding down, a typical relationship between the slip wedge S_w and the axial load of one wedge P is shown in Figure 3.64.

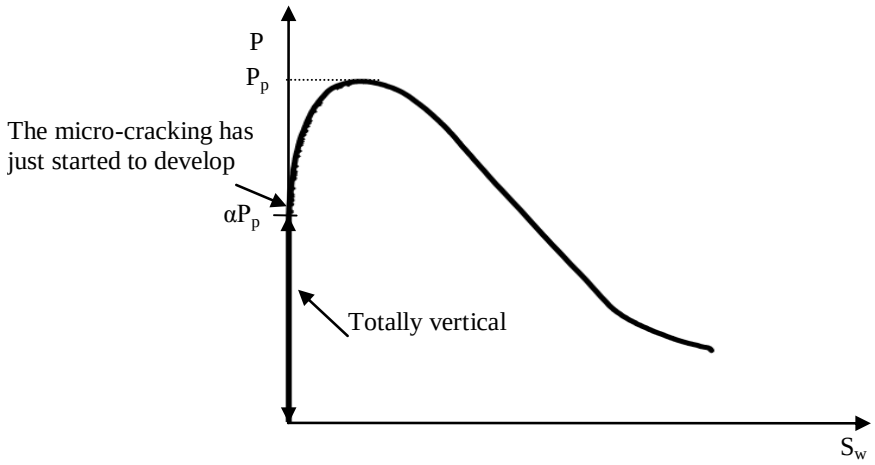

Figure 3.64: A typical of the relationship axial load P and the slip wedge S_w

Figure 3.64 indicates that as expected up to the load αP_p there is no micro-cracking or slip wedge because the wedge deformation has just started to form and the only deformation is elastic deformation due to the material shortening, bedding down, and dental paste contraction.

The response of the slip wedge S_w over the load wedge P_w is presented in the third part of this analysis. Let us see again Figure 3.62, one single wedge with a width $W/2$, height $H/2$ and length S is sliced 1 millimeter thickness as shown. The result shows in Figure 3.65. The figure illustrates a single wedge of height $H/2$, width $W/2$, and 1 mm thickness into the page.

It is assumed when the wedge is fully developed, all the concrete along the localised crushing line in Figure 3.62 is softening. Hence, the depth of the wedge d_w equals to half the width of prism, that is $W/2$. The load which is applied to the 1 mm wedge thickness and the depth of the wedge d_w refers to the wedge load P_w as shown in Figure 3.65. P_w is obtained by dividing axial load P over the length of concrete prism S. S_w is the slip wedge that is occurred in this one wedge in axial direction. A typical curve of the slip wedge S_w against the wedge load P_w is shown in Figure 3.66.

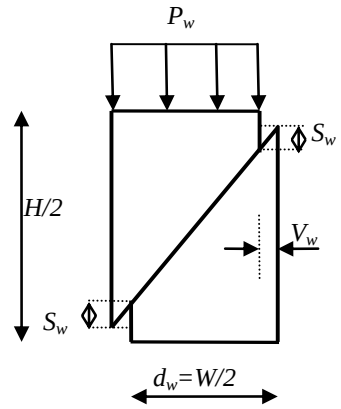

Figure 3.65: Idealised the wedge per 1 millimeter thickness

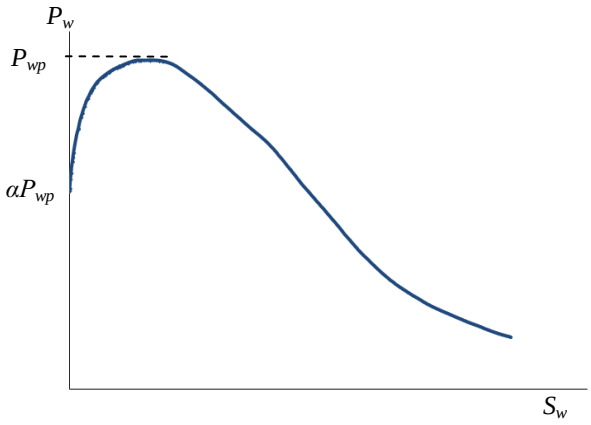

Figure 3.66: A typical response of the wedge load P_w and slip wedge S_w

The last part of the axial deformation analysis determines the relationship between the wedge stress σ_w and the slip wedge S_w as shown in Figure 3.67. The wedge stress is determined by dividing the wedge load P_w by the depth of the wedge d_w given as Eq. 3.4.

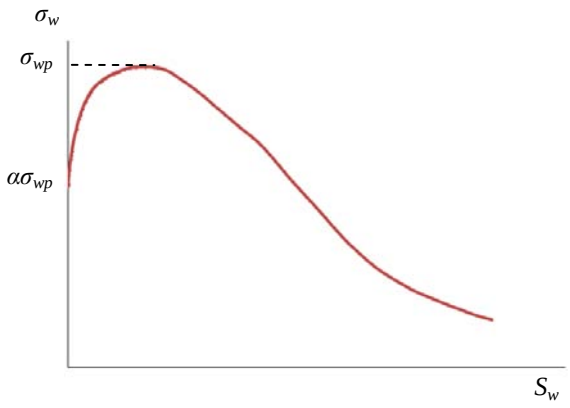

Figure 3.67: The typical of wedge stress – slip wedge response

$$\sigma_w = \frac{P_w}{d_w} \qquad \textit{Eq. 3.4}$$

where σ_w is wedge stress, P_w is the the wedge load and d_w is the depth of the wedge that is half of the prism width, $W/2$.

After finishing analysis in axial deformation, next step is to determine the lateral deformation. The analyses use the same methods that were used in axial deformation previously. More details are described below.

3.4.1.2 Lateral Deformation

The first part of the analysis in lateral deformation quantifies the relationship between the total axial load L and total lateral expansion E on each concrete prism. The total axial load L is the axial compression load that applied to the whole prism and the total lateral expansion E is the total expansion of the whole concrete prism.

The uniform axial compression load L is applied to the concrete prism to on top and bottom of the prism that the prism expands on both sides of prism. Two lateral LVDTs are placed in the middle of every side of prism as shown in Figure 3.20 to record the dilation that was occurred. The dilation which is obtained and recorded by lateral LVDTs as described in Section 3.3 is expansion that occurred in one side of prism. Hence total lateral expansion E is the algebraic sum of the two lateral LVDTs reading value that is given in Eq. 3.5.

$$E = D_1 + D_2$$ *Eq. 3.5*

where E is total lateral expansion, D_1 and D_2 are dilation on each side of prism that are recorded by LVDT-7 and LVDT-8 respectively as explained earlier (see again Figure 3.17 and Figure 3.20).

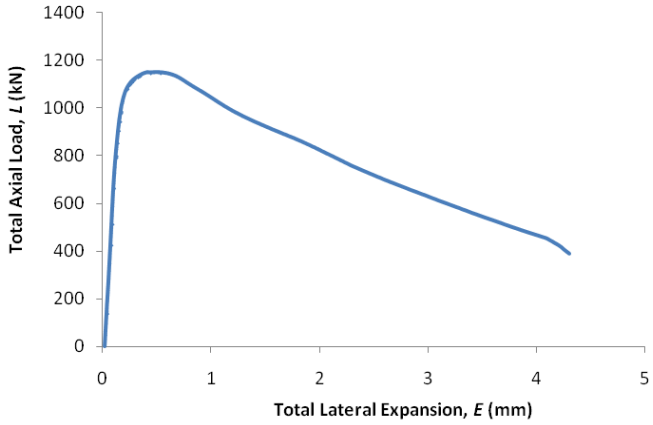

Figure 3.68: A typical total axial load (L) and total lateral expansion (E) response

The second part of the analysis in lateral deformation determines the response of load and lateral deformation for one wedge only. The definition of compression concrete wedge and definition of one single wedge of the prism were explained clearly in axial deformation previously in Section 3.4.1.1.

Let us see again Figure 3.62 that illustrates one single wedge contracts axially and expands laterally under uniform compression load of one single wedge P where P is half of total axial applied load L. The single compression concrete wedge expands half of total lateral expansion of the whole prism refers to as $E/2$. A typical response of P-$E/2$ is shown in Figure 3.69.

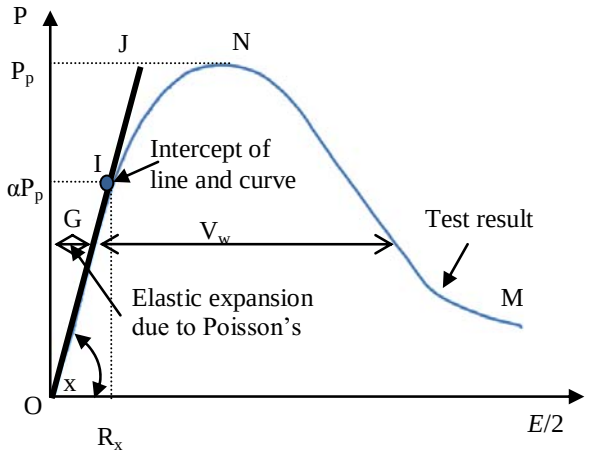

Figure 3.69: A typical response of the axial load and total lateral expansion of one single wedge

The initial of loading, the load and deformation response of one wedge is considered linear as shown a straight line O-I with slope x as depicted in Figure 3.69. Point I corresponds to αP_p, where α is assumed 60% and P_p is the peak of axial load. Up to the load αP_p there is no lateral deformation due to micro-cracking or expansion of the wedge, only elastic expansion G occurred. The elastic expansion G due to Poisson's ratio along the line O-I in Figure 3.69 is equal to

$$G = \frac{P\,R_x}{\alpha\,P_p} \qquad \textit{Eq. 3.6}$$

Where P is applied load of one single wedge, P_p is the peak of axial load of one single wedge. R_x is lateral expansion corresponds to αP_p. However, after the load αP_p, non-linearity gradually occurs in the ascending portion of I-N and continues in the descending portion of N-M. This non-linearity behaviour is due to micro-cracking start to form in lateral direction and the wedge is gradually expands. Hence the total lateral expansion of one single wedge $E/2$ consists of elastic expansion due to Poisson's ratio G and the wedge expansion V_w as shown in Figure 3.70. The lateral expansion due to micro-cracking or wedge expansion V_w is given by

$$V_w = \frac{E}{2} - G \qquad \textit{Eq. 3.7}$$

Where E is total lateral expansion of the whole concrete prism and G is elastic expansion that determines using Eq. 3.6. A typical response of axial load P and wedge expansion

V_w is depicted in Figure 3.70. The graph indicates that the wedge does not expand up to the load αP_p as shown a vertical line up to the load αP_p because only elastic expansion occurs. The wedge expansion occurs just after the load αP_p.

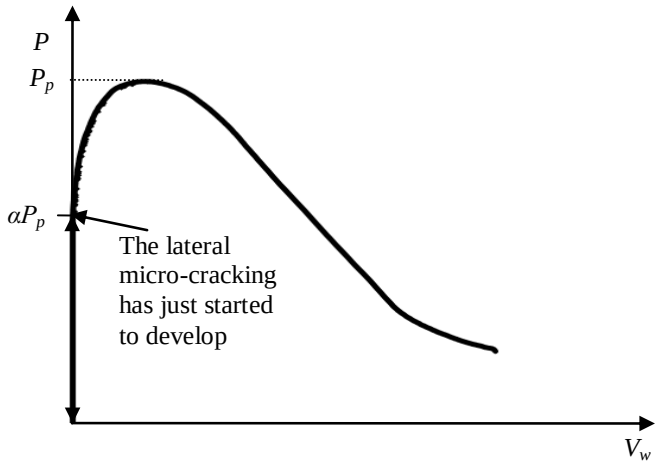

Figure 3.70: A typical of the relationship axial load and the wedge expansion V_w

After analysis one single wedge, the next part of analysis determines the load and the wedge expansion only in one millimeter wedge thickness. A single wedge in Figure 3.62 is sliced 1 millimeter thickness thus the load which applied to 1 mm wedge thickness is referred as the wedge load P_w. P_w equals to the load of one wedge P divided by the prism length S. The wedge expansion V_w occurs when the wedge load P_w applied to 1 mm thickness of the wedge reaches αP_w as shown in Figure 3.65. A typical curve of the wedge expansion V_w against the wedge load P_w is depicted in Figure 3.71.

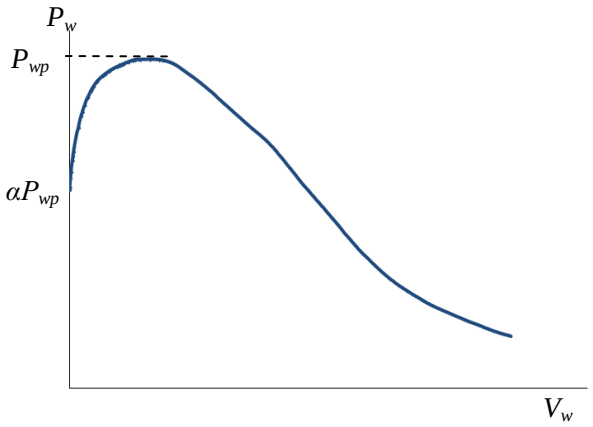

Figure 3.71: A typical response of the wedge load and wedge expansion

The last part of analysis in lateral deformation quantifies the wedge stress σ_w for given the wedge expansion V_w. The stress wedge σ_w is determined by using Eq. 3.4. A typical relationship of stress wedge and wedge expansion is depicted in Figure 3.72.

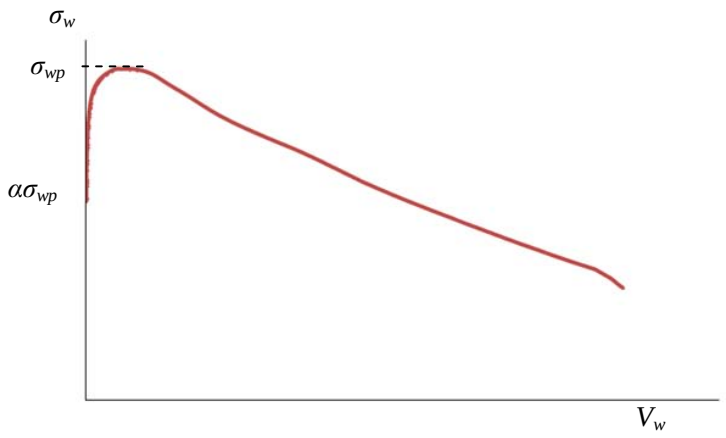

Figure 3.72: A typical response of the stress wedge and wedge expansion

The methods and processes of analysis in axial and lateral deformation have been explained and discussed in detail previously. In the following section, by using those processes the result experiment test of the individual concrete prism is analysed one by one.

3.4.2 Individual tests

3.4.2.1 Tests at 125mm width (125×250×500)

TEST1-125

Following the procedures outlined in Section 3.4.1, the behaviour of an individual wedge was extracted from the behaviour of the prism as a whole. The average of individual contraction as recorded by axial LVDTs is used to obtain the total axial contraction C of Test1-125 by using Eq. 3.1. The relationship between L-C is shown in Figure 3.73. The total axial contraction C increases significantly at low load. The total axial contraction continued to increase as the load increased, however this value is not the real total axial contraction of the concrete prism, as this also includes the setting down of the platens and dental paste contraction.

"Settle down the position" occurred at the early of loading is depicted by using a dash line in Figure 3.73. The concrete prism surface is not exactly flat thus when the concrete prism is set on the loading platen and applied the load, the prism needs to "settle". Therefore correction of the total axial contraction is required to remove the contraction that is caused by "settle down the position".

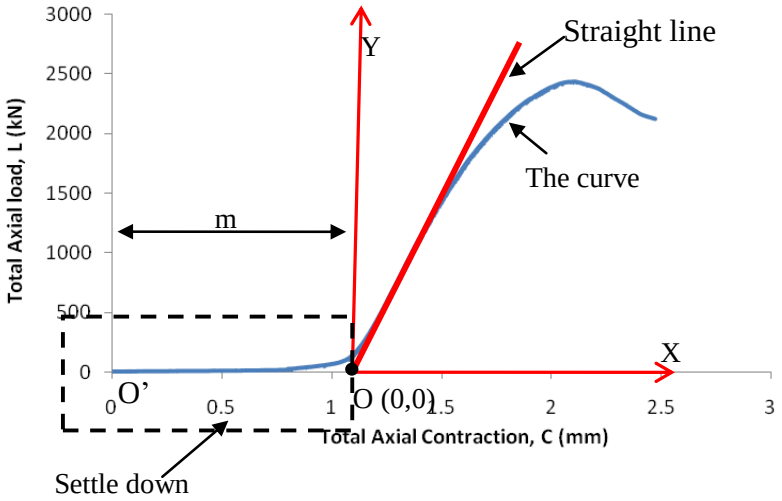

Figure 3.73: The relationship between total axial load and total axial contraction of prism Test1-125.

The curve is refined by determines a new origin point O. Initially a straight line is extended along the curve as shown in Figure 3.73. The intercept of this line and x-axis at a new origin point O (0,0). Then the total axial contraction C is subtracted by m. m is a distance between O' and new origin point O or the total axial contraction that is caused by "settle down the position". Hence a new x-y axis is obtained. Figure 3.73 is refined into Figure 3.74. The graph indicates L_p is the peak of total axial load corresponds to total axial contraction at peak load C_p. L_p is 2436kN at C_p is approximately 1.04mm.

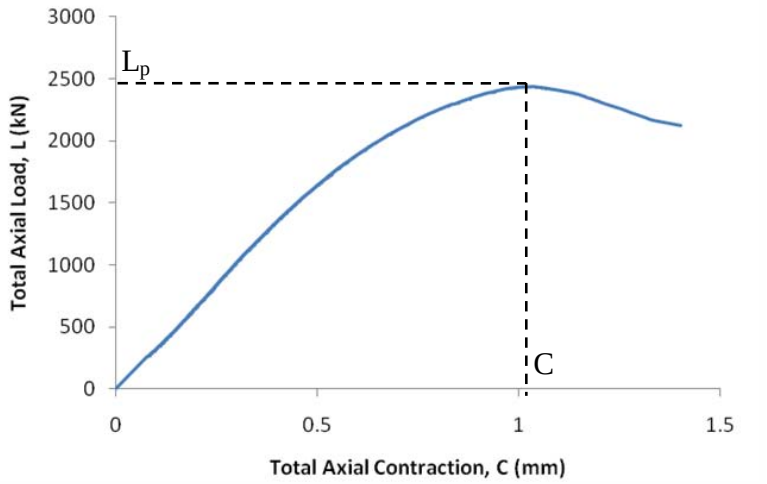

Figure 3.74: The total axial load-total axial contraction response of prism Test1-125 (new axis).

The graph in Figure 3.75 is the graph in Figure 3.74 divided by two because Figure 3.74 shows the responses of load and total axial contraction *L*-*C* of the whole prism that is two wedges form, while Figure 3.75 shows the responses of load and total axial contraction *P*-*C*/2 of one wedge only.

Up to the load αP_p, where α is 60% and P_p is the peak of axial load, only elastic contraction occurred on the prism, the deformation of the wedge not occurs. The elastic contraction is obtained by using Eq. 3.2. After the load αP_p axial micro-cracking starts to form. Hence the slip wedge S_w is obtained by using Eq. 3.3 and shown in Figure 3.75. The graph indicates the peak of axial load of one wedge P_p is 1218kN at the total axial contraction over one wedge $C_p/2$ is 0.52mm. The micro-cracking start to develop when the load αP_p is 731kN at C_k is 0.22mm.

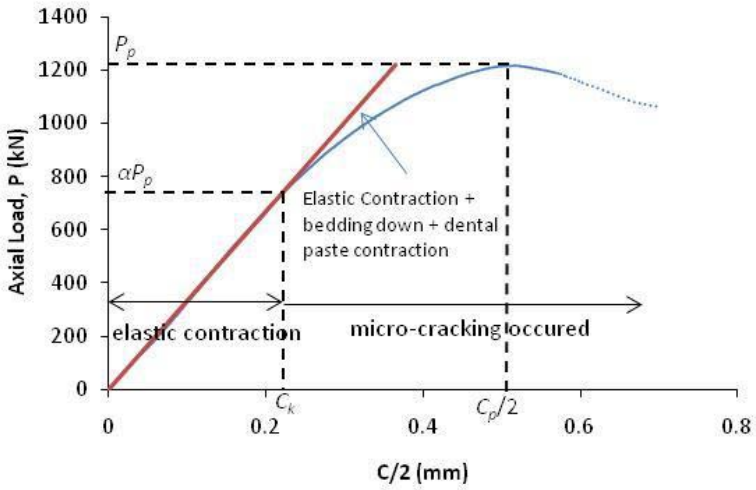

Figure 3.75: The axial load -total axial contraction over a single wedge response of prism Test1-125.

The relationship of axial load of one wedge P and slip wedge S_w is obtained after remove the elastic contraction from the graph P-$C/2$ and only considering the slip of the wedge (Figure 3.75). The result is shown Figure 3.76. The graph indicates there is no deformation due to micro-cracking or slip of the wedge up to the axial load 731kN because all the contraction is in elastic. The slip wedge at peak load S_{wp} is approximately 0.15mm.

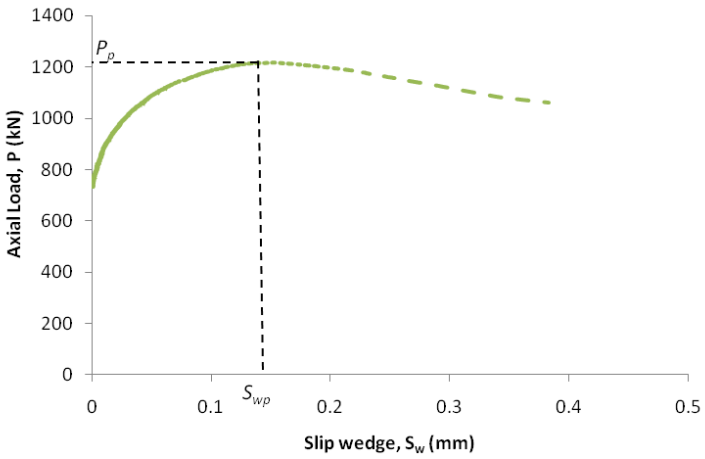

Figure 3.76: Axial load over one wedge-slip wedge response of prism Test1-125.

Figure 3.77 shows the slip wedge S_w against the load wedge P_w. P_w equal to the axial load over one wedge P divided by prism length S, S is 500mm. Figure 3.77 is the

same with Figure 3.76 but the load is per millimeter depth of wedge. The peak of load wedge refers to P_{wp} is 2,44kN/mm. P_{wp} is P_p divided by S.

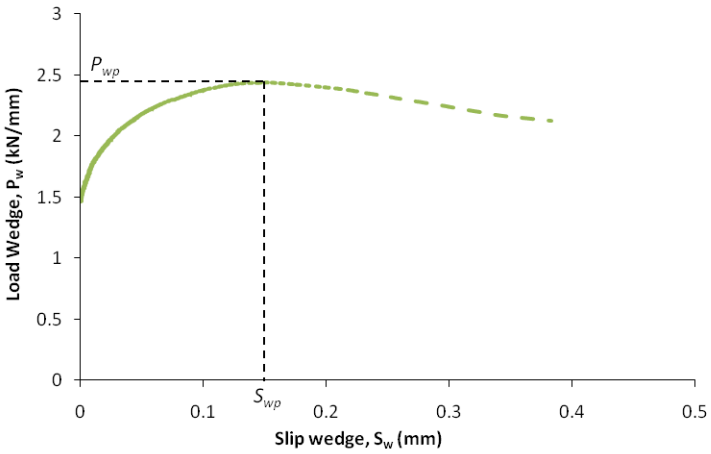

Figure 3.77: Load wedge–slip wedge response of prism Test1-125.

Figure 3.78 illustrates wedge stress-slip wedge response. This is the last analysis in axial deformation. Eq. 3.4 is used to determine the stress wedge. The micro-cracking occurred when stress wedge approximately 23MPa. The micro-cracking propagates as the load increase up to peak of stress wedge σwp is 39MPa.

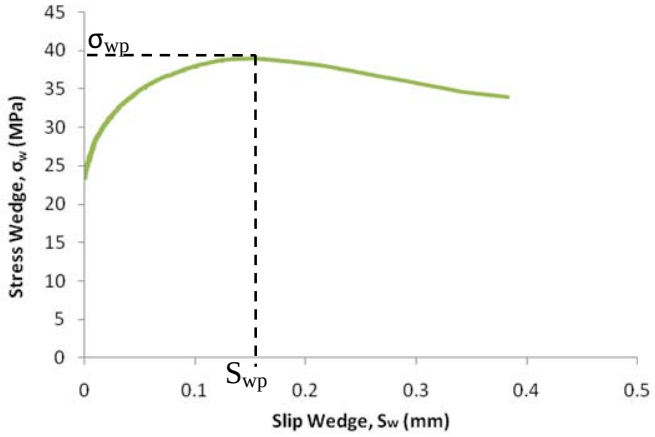

Figure 3.78: The stress wedge-slip wedge response of prism Test1-125.

In lateral deformation analysis, total lateral expansion E is expansion of the whole prism. The total lateral expansion E is obtained from the values of lateral LVDTs-7 and -8 readings and used Eq. 3.5 as shown in Figure 3.79. At peak load, there not

much different between total axial contraction C and total lateral expansion E (see again Figure 3.74). Total lateral expansion at peak load E_p is approximately 1.13mm.

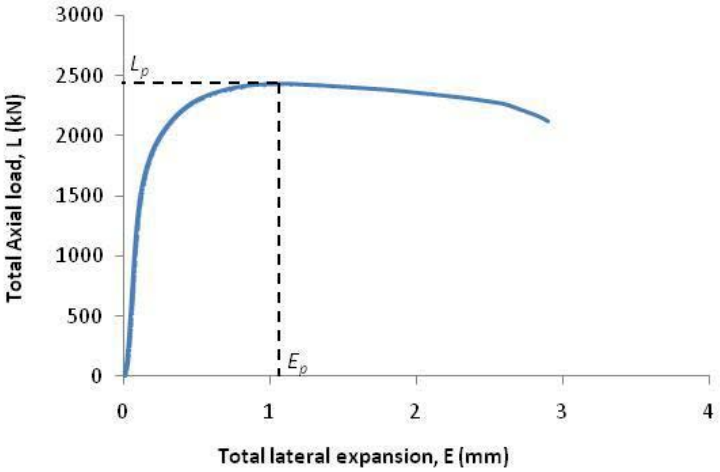

Figure 3.79: Total axial load-total lateral expansion response of prism Test1-125.

Relationship of load and lateral deformation over one wedge is depicted in Figure 3.80. The lateral deformation which is occurred less than R_x is elastic expansion that is obtained by using Eq. 3.6, after this point the deformation due to the micro-cracking developed. Eq. 3.7 is used to determine the expansion that is only caused by micro-cracking or wedge deformation. The graph indicates that the lateral expansion at the micro-cracking starts to form R_x is 0.05mm. At the peak of axial load, the total lateral expansion of one single wedge $E_p/2$ is 0.56mm.

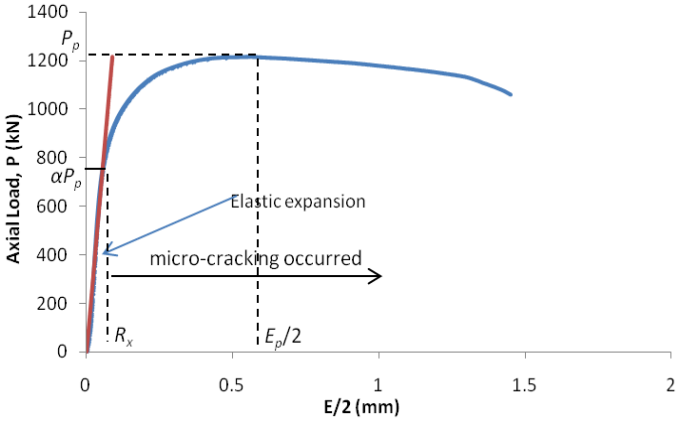

Figure 3.80: The axial load -total lateral expansion over a single wedge response of prism Test1-125

The response of axial load P and wedge expansion V_w is obtained by removing the elastic expansion G from the graph in Figure 3.80 and using Eq. 3.7. The graph in Figure 3.81 indicates deformation due to micro-cracking in lateral direction increase slightly as the load increase up to peak load. The wedge expansion at peak load V_{wp} is 0.47mm. This value is much higher than slip wedge at peak load S_{wp} that is only 0.15mm. After peak load, the wedge expansion increases significantly as the load decrease slightly and the prism failed when V_w is around 1.37mm.

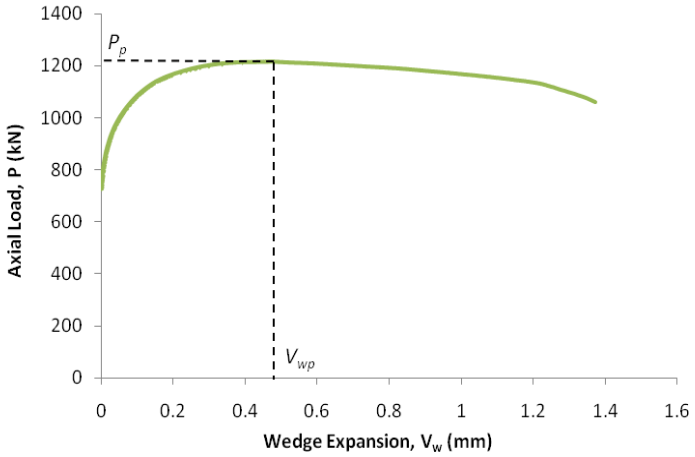

Figure 3.81:Axial load-wedge expansion of prism Test1-125.

The graph in Figure 3.81 shows the load and wedge expansion in a single wedge while the graph in Figure 3.82 illustrates the load and wedge expansion per millimeter depth of wedge. The P in Figure 3.81 is divided by prism length S equal to P_w in Figure 3.82.

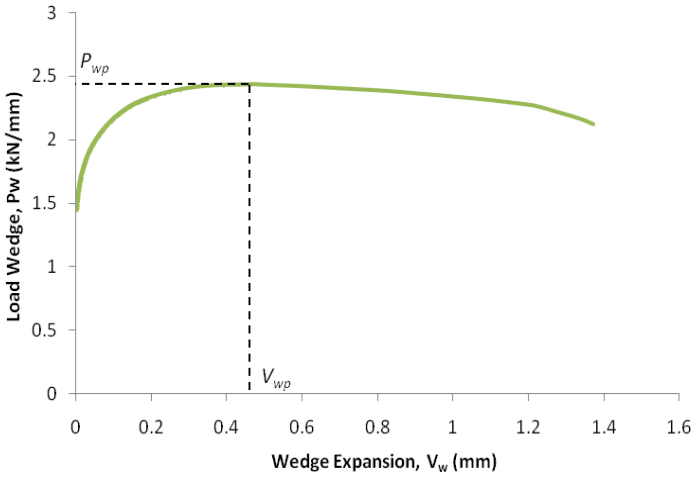

Figure 3.82: The wedge load-expansion per mm thickness of the wedge for Test1-125

The last analysis for prism Test1-125 is stress wedge σ_w and wedge expansion V_w response. The graph in Figure 3.83 indicates the wedge expansion increase slightly as the load increase up to peak load of 39MPa. After this point, the wedge expansion still increase considerably with a decrease of the stress.

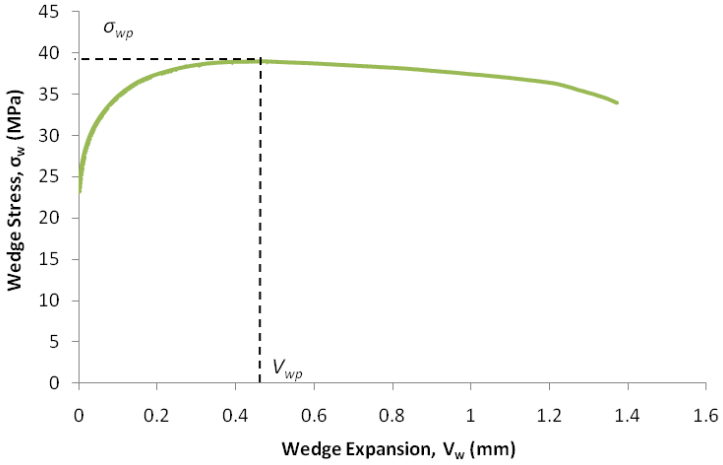

Figure 3.83: Wedge stress - wedge expansion of prism Test1-125. x

The important parameters such as L_p, P_p, P_{wp}, σ_{wp}, C_p, $C_p/2$, S_{wp}, E_p, $E_p/2$, and V_{wp} of prism Test1-125 are clearly explained previously and shown graphically in Figure 3.73 to Figure 3.83. Those parameters are summarised in Table 3.5. It should be noting that the analysis of all others prisms below follows the analysis of Test1-125.

TEST2-125

Figure 3.84 shows the average of contraction of individual axial LVDTs' dial reading. A "settle down the position" shown in a dash line occurred on prism Test2-125 up to total axial contraction *C* reach approximately 1.7mm. After that the actual total axial contraction occurred. Thus Figure 3.84 is refined into Figure 3.85.

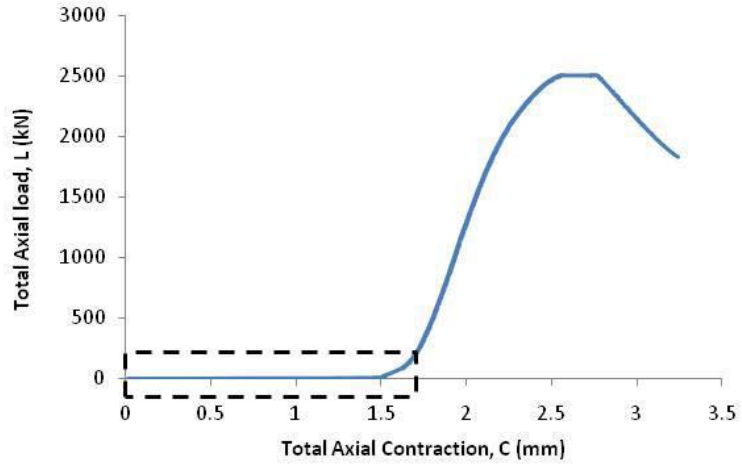

Figure 3.84: Total axial load-total axial contraction response of prism Test2-125.

Figure 3.85 is obtained by removing the "settle down the position" region in Figure 3.84. A new response of *L*-*C* shows a peak of total axial load L_p is 2505kN corresponds to total axial contraction C_p is 1.06mm. This value is almost same with C_p for Test1-125 (see again Figure 3.74).

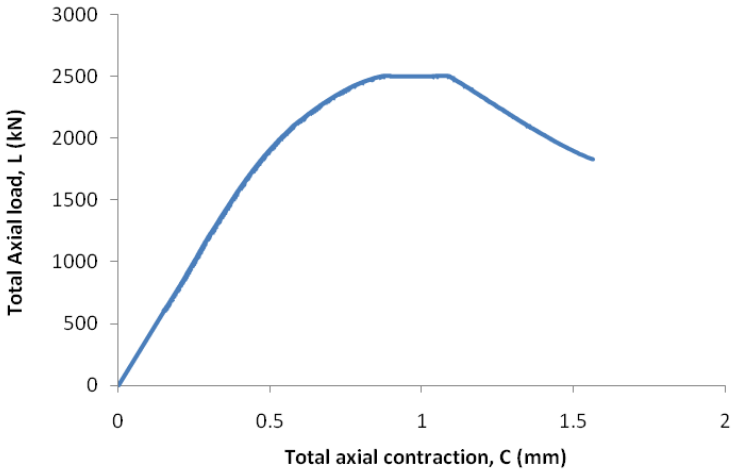

Figure 3.85: Total axial load-total axial contraction of prism of Test2-125 (new axis).

The *P*-*C*/2 graph in Figure 3.86 is the *L*-*C* response divided by 2. Because the *L*-*C* graph is analysis for the whole prism which in terms of two wedges form while the *P*-*C*/2 is analysis for one wedge only. The peak of axial load P_p is 1253kN corresponds to $C_p/2$ is 0.53mm.

The elastic contraction *B* in a single wedge occurred until approximately 0.19mm and the load reach 752kN (Figure 3.86). After this point, the deformation due to micro-cracking occurred in a wedge. The slip of wedge S_w is achieved by removing the elastic contraction *B* from the *P*-***C***/2 graph and by using Eq.3.2 and Eq.3.3. As a result the relationship between axial load *P* and slip wedge S_w of prism Test2-125 is shown in Figure 3.87.

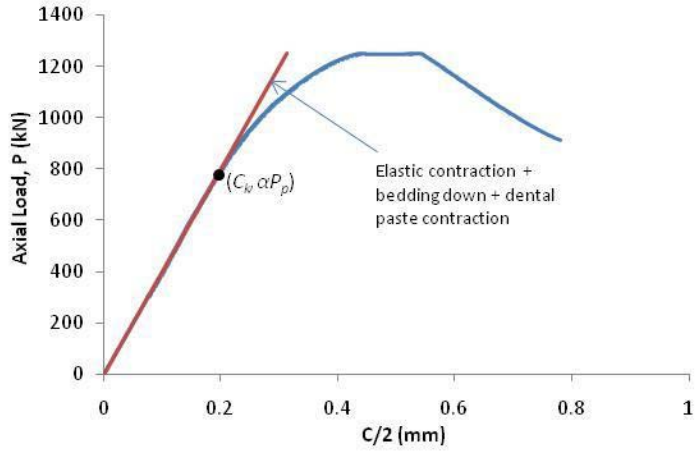

Figure 3.86: The axial load and total axial contraction over one wedge response of prism Test2-125.

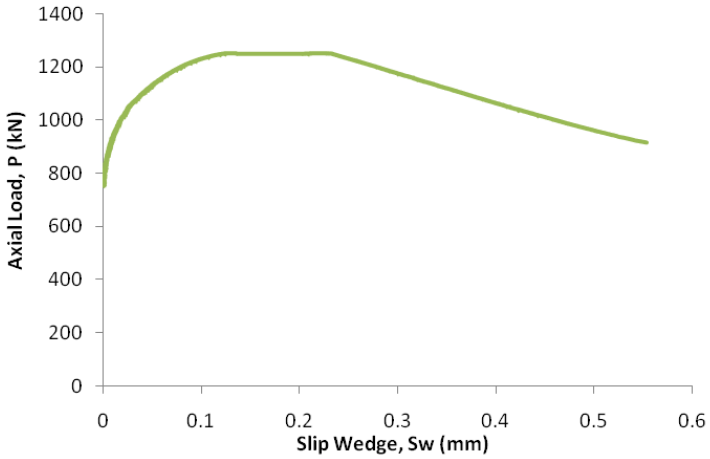

Figure 3.87: Axial load-slip wedge response of prism Test2-125.

Figure 3.87 shows the load and slip wedge for one whole wedge, while Figure 3.88 shows the load and slip for one mm wedge thickness only. The load P_w in Figure 3.88 is P divided by the prism length S. The micro-cracking start to form when load wedge P_w around 1.5kN/mm. When the peak of wedge load P_{wp} reaches 2.51kN/mm, slip wedge S_{wp} is around 0.22mm.

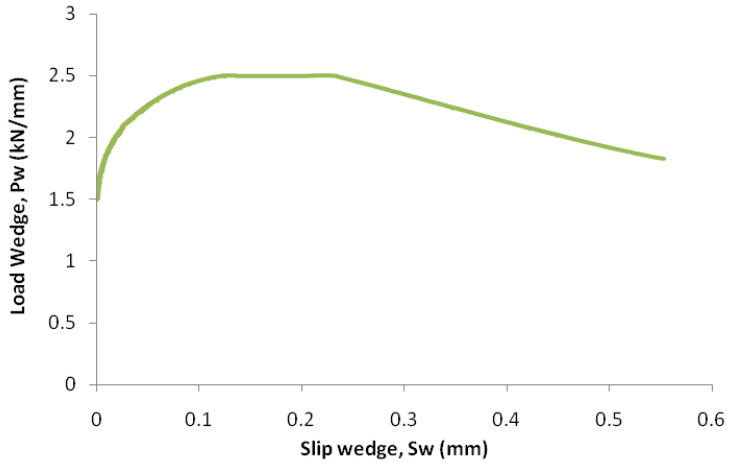

Figure 3.88: Load and slip of wedge response of prism Test2-125

Figure 3.89 illustrates the relationship between the stress wedge and slip wedge of Test2-125. The wedge stress reaches its peak σ_{wp} 40MPa corresponds to slip wedge approximately 0.22mm.

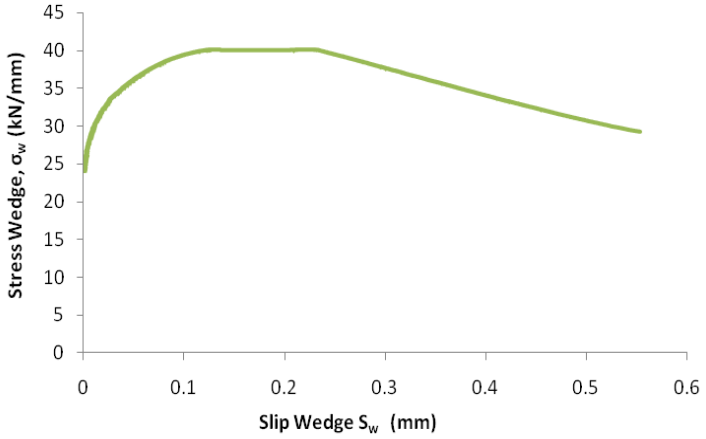

Figure 3.89: Stress wedge-slip wedge response of prism Test2-125

After described the axial deformation, the lateral deformation of prism Test2-125 is described below. The total axial load *L* and total lateral expansion *E* response of prism Test2-125 shows the total lateral expansion of the whole prism at the peak load E_p is 1.39mm (Figure 3.90). This expansion increases considerably as the load decrease until the prism failed at total axial load *L* approximately 1830kN.

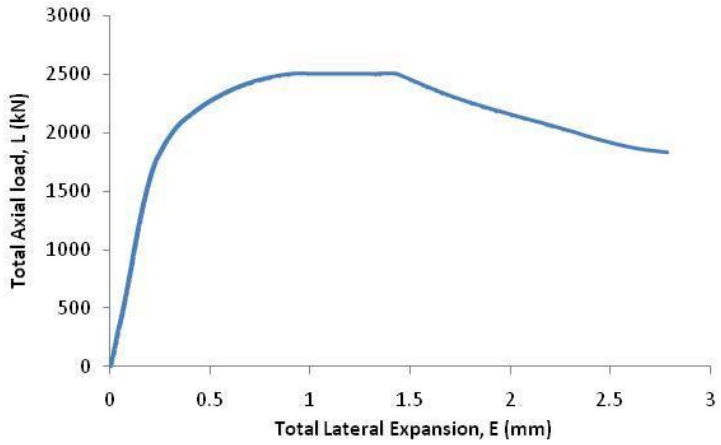

Figure 3.90: Total axial load-total lateral expansion response of prism Test2-125

The analysis of total lateral expansion of one wedge against the axial load is depicted in Figure 3.91. This *P-E*/2 response is *L-E* response divide by 2. Hence at peak load, the total lateral expansion over a single wedge $E_p/2$ is 0.68mm. The micro-cracking start to develop when lateral expansion over one wedge R_x is approximately 0.08mm. Before that point, only elastic expansion *B* occurred.

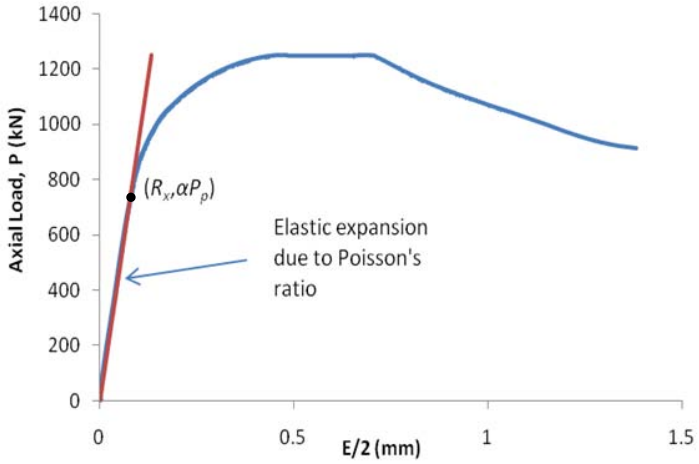

Figure 3.91: Axial load-total lateral expansion over one wedge response of prism Test2-125.

Figure 3.92 shows the axial load P and the wedge expansion V_w response that is obtained by subtracting the elastic expansion from Figure 3.91. Wedge slip S_w and wedge expansion V_w occurred at the same time, when the axial load P reaches 707kN. Wedge expansion at peak load V_{wp} approximately 0.55mm.

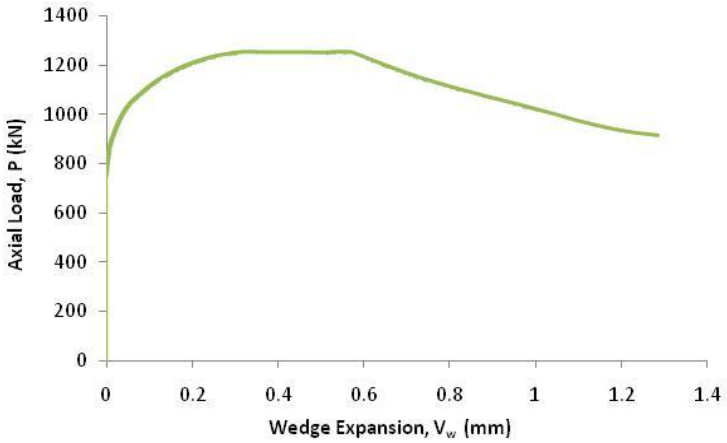

Figure 3.92: Axial load-wedge expansion response of prism Test2-125.

Figure 3.93 shows wedge expansion approximately 0.55mm when the load wedge over 1 mm depth of wedge reached its peak load. This wedge expansion is much higher than slip wedge that is just 0.22mm (see again Figure 3.88). This means that wedge slip and expand at the same time but the wedge expansion increase significantly up to peak load.

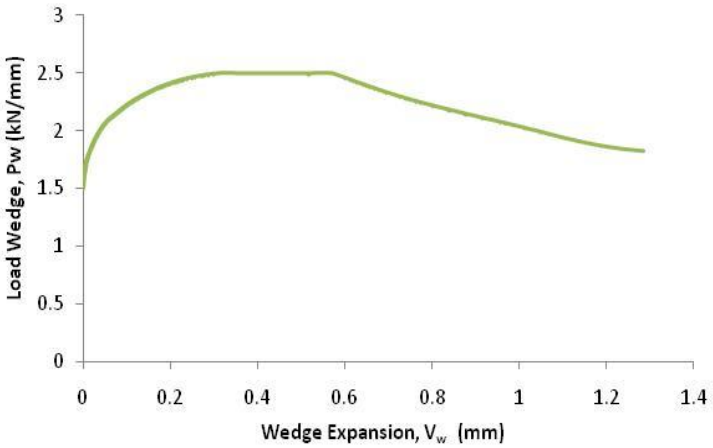

Figure 3.93: Load wedge–wedge expansion response of prism Test2-125.

Figure 3.94 shows the relationship between stress and expansion of wedge. The wedge starts to expand due to micro-cracking when stress wedge approximately 24MPa. Before this point only elastic expansion occurred.

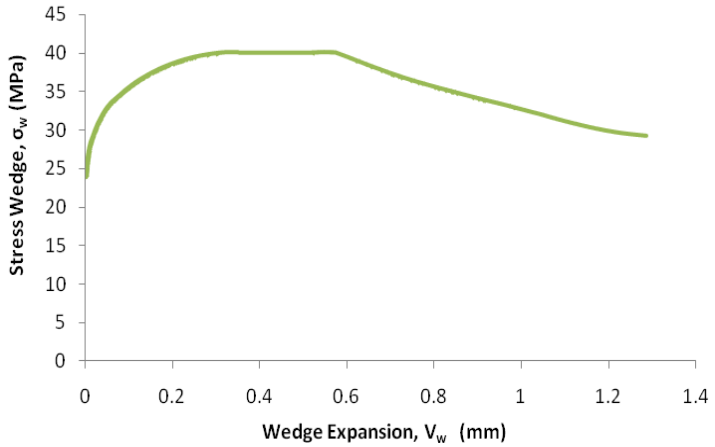

Figure 3.94: Stress wedge – wedge expansion response of Test2-125

The peak values of load, stress, axial and lateral deformations of Test2-125 such as L_p, P_p, P_{wp}, σ_{wp}, C_p, $C_p/2$, S_{wp}, E_p, $E_p/2$, and V_{wp} are clearly described previously. Those parameters are summarised in Table 3.5.

TEST3-125

The next *eleven* graphs illustrate the axial and lateral deformation of concrete prism Test3-125. Initially axial deformation is analised and followed by lateral deformation. The same as the previous prism, the "settle down the position" as shown in a dash line also occurred in prism Test3-125 (Figure 3.95). The total axial contraction *C* of the prism is corrected by subtract as long as 1.27mm. The *L*-*C* graph after the correction is shown in Figure 3.96.

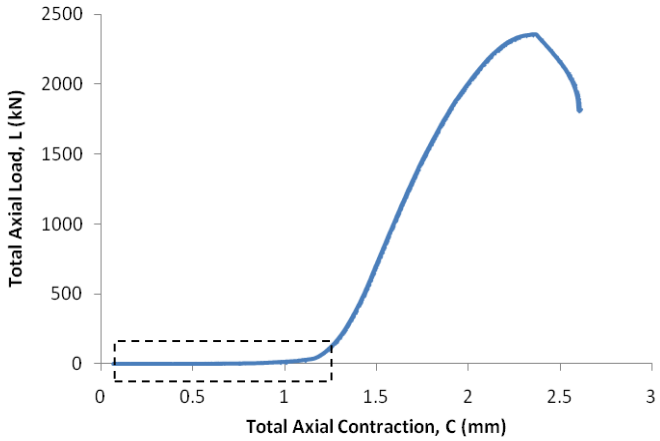

Figure 3.95: Total axial load-total axial contraction response of prism Test3-125.

Figure 3.96 is obtained by removing the "settle down the position" on *L*-*C* graph in Figure 3.95. The peak of total axial load L_p of Test3-125 is 2357kN at total axial contraction C_p is 1.08mm.

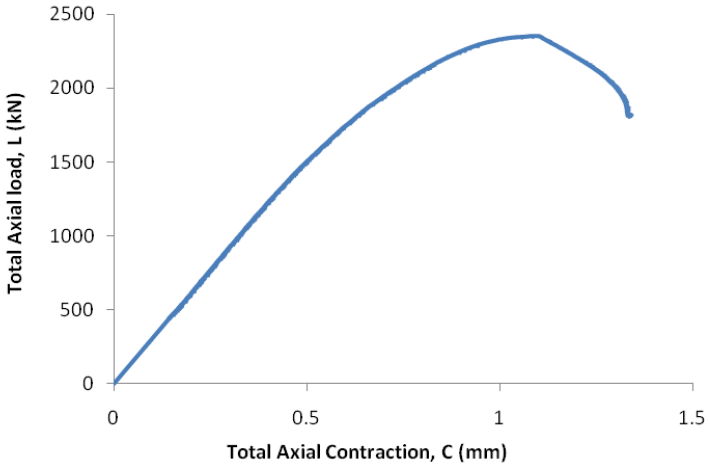

Figure 3.96: Total axial load-total axial contraction response of prism Test3-125

The *L* and *C* values in Figure 3.96 divide by 2 equal to the *P* and *C*/2 values respectively in Figure 3.97. The pattern of those graphs is same with Figure 3.96 but the value is half than Figure 3.96. Hence the peak of axial load P_p is 1179kN and $C_p/2$ is 0.54. The axial load of one wedge around 707kN that is 60% of peak load when micro-cracking begin to develop correspond to C_k is around 0.23mm.

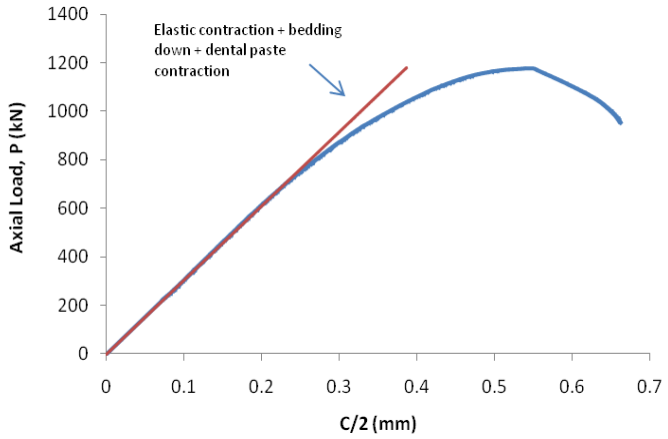

Figure 3.97: Axial load – C/2 slip response of prism Test3-125.

Figure 3.98 shows the slip wedge S_w start to develop when the axial load P around 707kN. The relationship between the load wedge P_w and slip wedge S_w is obtained by dividing P with S where S is 500mm as depicted in Figure 3.99.

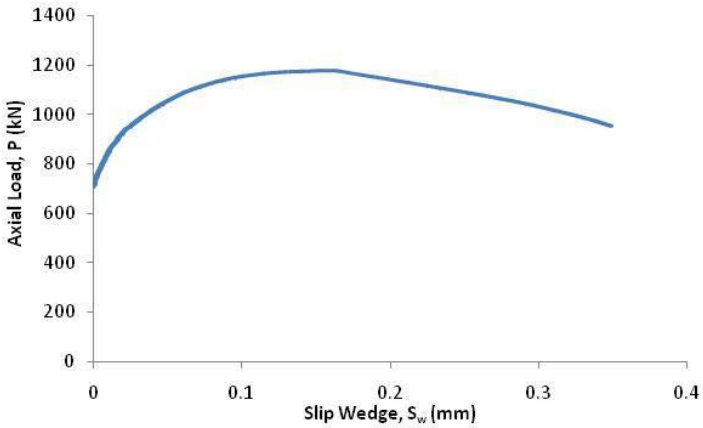

Figure 3.98: Axial load-slip wedge response of Test3-125

Figure 3.99: Load wedge-slip wedge response of prism Test3-125.The graph indicates the micro-cracking starts to form when load wedge is 1.41kN/mm. The peak of wedge load over 1 mm thickness P_{wp} is 2.36kN/mm at S_{wp} is 0.16. The graph in Figure 3.100 indicates that the stress wedge σ_{wp} of Test3-125 is 38MPa at S_{wp} is 0.16.

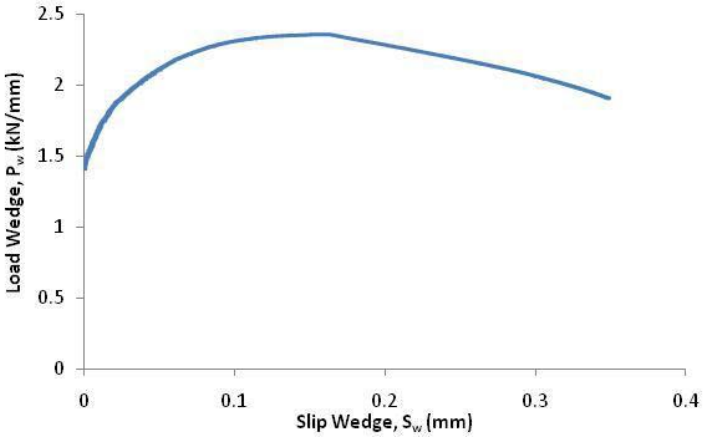

Figure 3.99: Load wedge-slip wedge response of prism Test3-125.

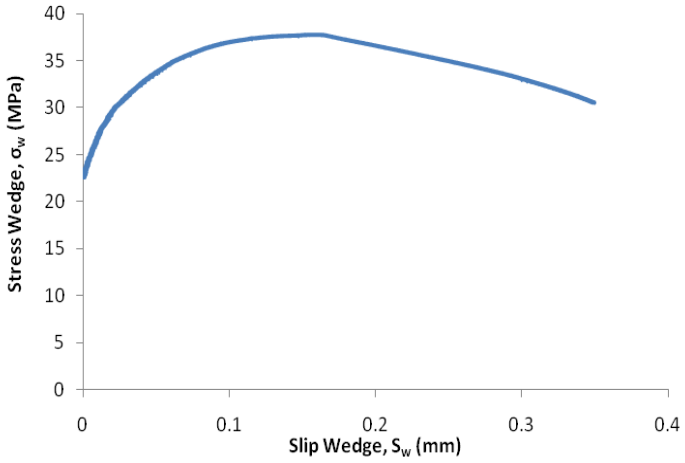

Figure 3.100: Stress wedge-slip wedge response of prism Test3-125

In lateral deformation, the response of total axial load L and total lateral expansion E of Test3-125 is depicted in Figure 3.101. The graph indicates at initial of loading no expansion occurred up to the load approximately 500kN. After that point the prism expand on both sides of prism until the prism failed. The total lateral expansion at the peak total axial load E_p is approximately 0.74mm

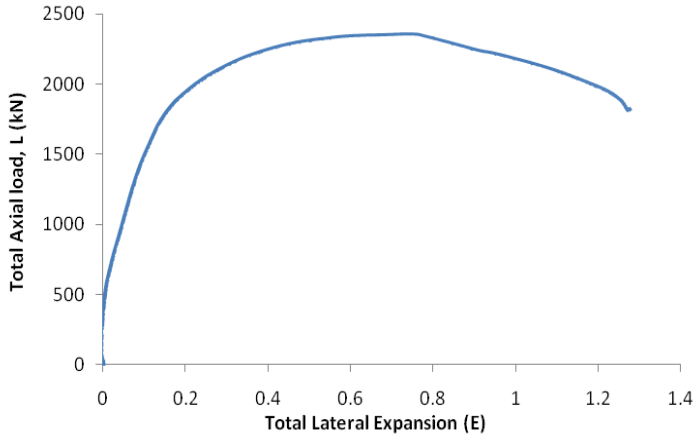

Figure 3.101: Total axial load-total lateral expansion response of prism Test3-125.

The relationship of load and expansion over a single wedge is depicted in Figure 3.102. The straight line is drawn between origin point (0,0) and (R_x,αP_p). The lateral expansion less than R_x is elastic expansion G and more than R_x is wedge expansion V_w. Using this graph and Eqs. 3.2 and 3.3. Hence the wedge expansion V_w is obtained and is shown in Figure 3.103.

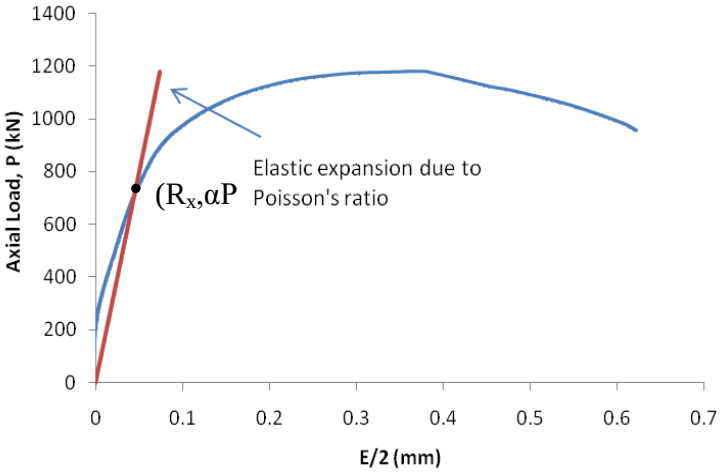

Figure 3.102: Axial load – E/2 response of prism Test3-125

Figure 3.103 shows load and expansion in a single wedge of Test3-125. At peak load the wedge expansion V_{wp} approximately 0.3mm. This value is smaller than other prisms in Test-125 (refer to Figure 3.81 and Figure 3.92).

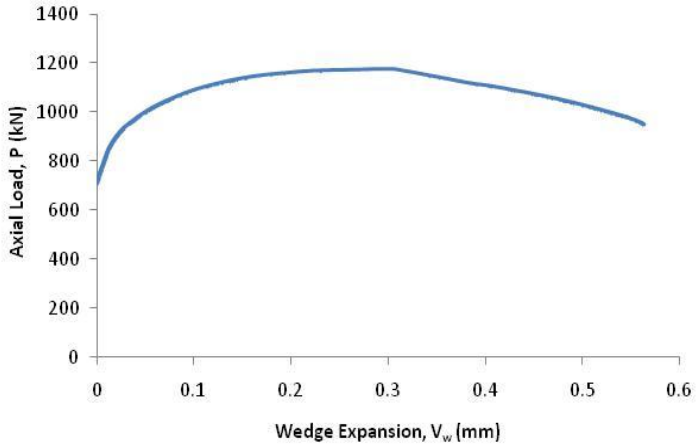

Figure 3.103: Axial load-wedge expansion response of prism Test3-125

The graph in Figure 3.103 is same with the graph in Figure 3.104 but the load in Figure 3.104 is the wedge load in 1 mm wedge thickness P_w. The slip wedge and wedge expansion start to form when P_w is 1.41kN/mm. However at peak load, wedge expansion V_{wp} is higher than slip wedge S_{wp}. This means that after the micro-cracking occurred, the crack propagate in perpendicular to the load direction is higher than in parallel to the load direction. The relationship between wedge stress σ_w and wedge expansion V_w is depicted in Figure 3.105.

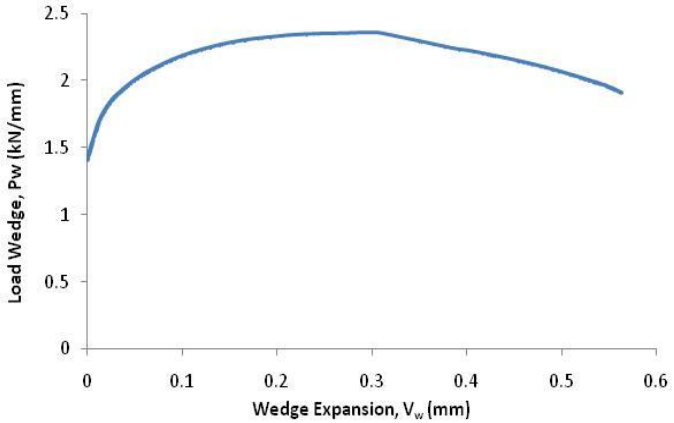

Figure 3.104: Load wedge-wedge expansion response of prism Test3-125

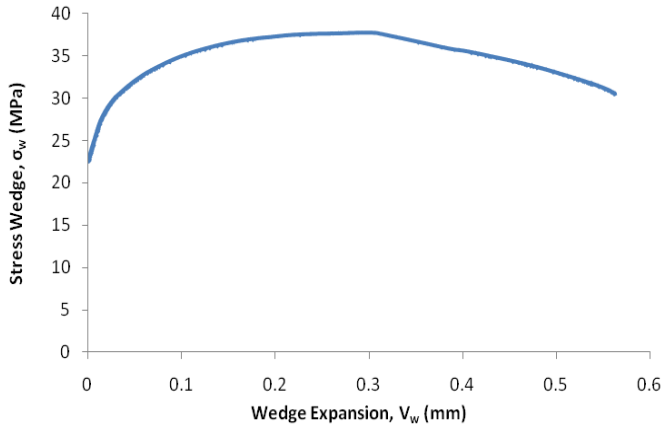

Figure 3.105: Axial stress - wedge expansion response of prism Test3-125

The peak values that are the important parameters of Test2-125 such as L_p, P_p, P_{wp}, σ_{wp}, C_p, $C_p/2$, S_{wp}, E_p, $E_p/2$, and V_{wp} are clearly described previously. Those parameters are also listed in Table 3.5.

TEST4-125

Test4-125 is the last prism in the Test-125. The next eleven figures is described the behaviour of Test4-125. Figure 3.106 illustrates the relationship of *L-C* before refined into Figure 3.107 because of a "settle down the position" occurred in this prism (shown in a dash line). The distance between an origin point O to O' (refer to Figure 3.59) or *m* is approximately 0.27mm. A refined relationship of *L-C* is obtained by subtracting total axial contraction *C* with *m*.

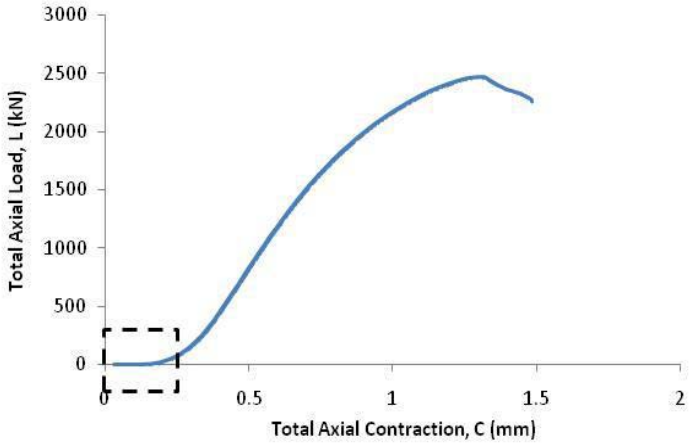

Figure 3.106: Total axial load-total axial contraction response of prism Test4-125

The graph in Figure 3.107 indicates the total axial contraction C_p is 1.04 mm when the total axial load reached the peak L_p of 2,468kN.

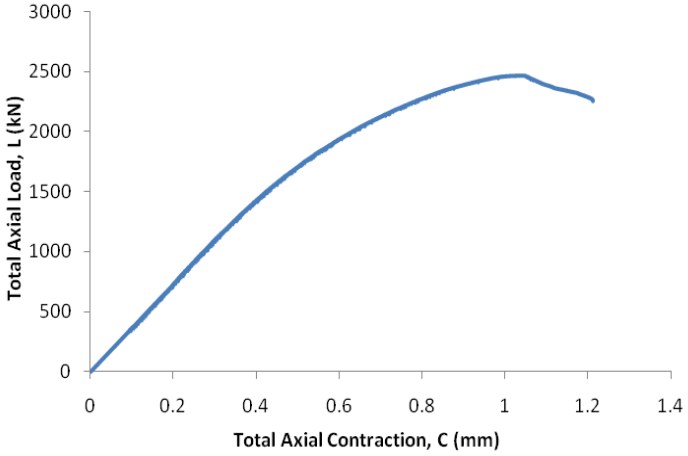

Figure 3.107: Total axial load-total axial contraction response of Test4-125 (new axis)

Figure 3.108 shows how to get the slip of the wedge S_w, 60% of P_p is approximately 740kN corresponding to C_k is 0.21mm. Before this point only elastic contraction occurred. The micro-cracking starts to develop axially when $C/2$ more than 0.21mm. Slip wedge S_w is obtained by using Eqs. 3.2 and 3.3. The slip wedge of Test4-125 is shown in Figure 3.109. The peak of axial load in one wedge *Pp* is 1234kN at slip wedge 0.17mm.

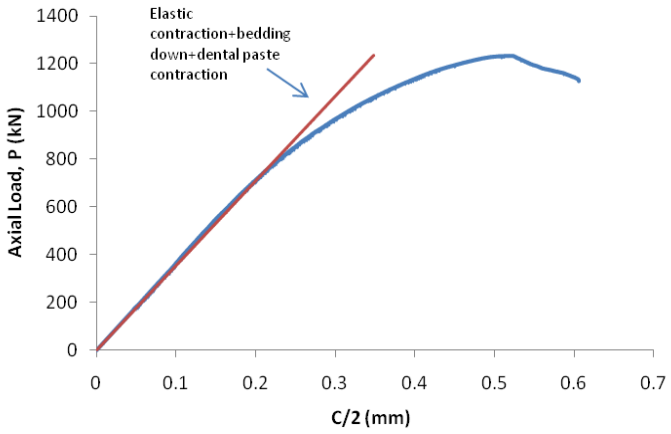

Figure 3.108: Axial load – C/2 response of prism Test4-125

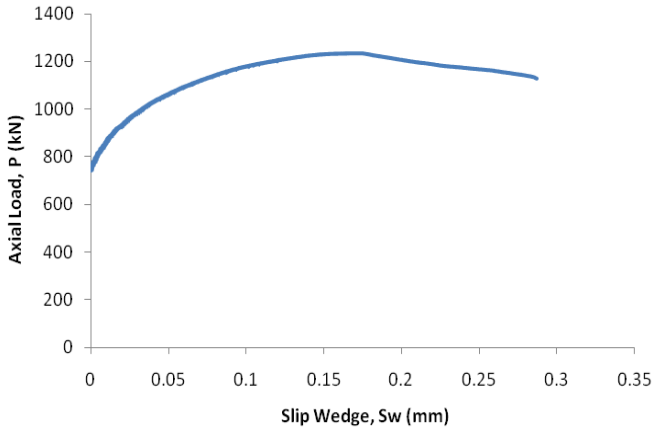

Figure 3.109: Axial load-slip wedge response of Test4-125

The load of wedge P_w *i*s axial load P in Figure 3.109 divided by the prism length S. S for Test4-125 is 500mm thus the relationship of P_w-S_w can be seen in Figure 3.110. The slip wedge starts to form when the load of the wedge P_w is approximately 1.48kN/mm, before this load only elastic contraction occurred. The load increases as the slip increases and peak load P_{wp} reached approximately 2.47kN/mm.

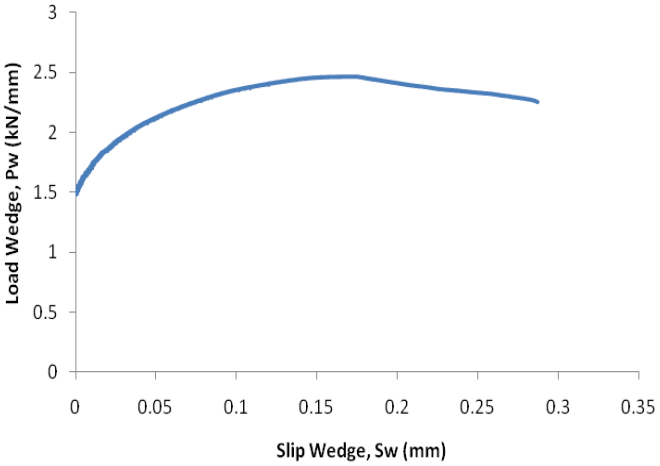

Figure 3.110: Load wedge-slip wedge response of Test4-125

The wedge stress and $_{slip}$ wedge relationship is shown in Figure 3.111. The stress wedge is calculated by using Eq. 3.4. The micro-cracking starts to form when wedge stress is approximately 24MPa. The peak of wedge stress σ_{wp} approximately 40MPa relates to slip wedge S_{wp} is 0.17mm.

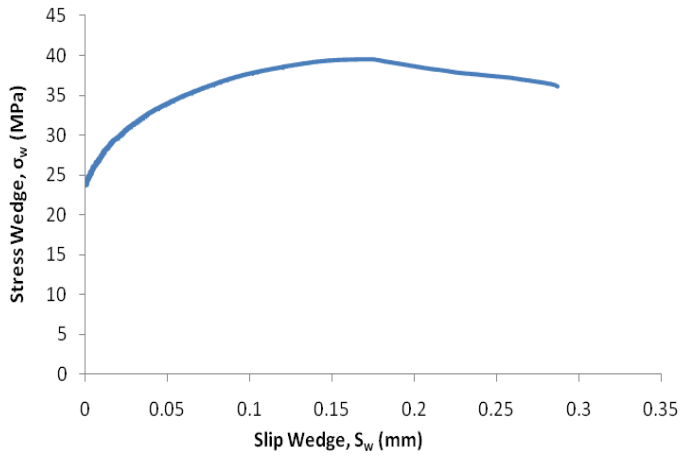

Figure 3.111: Axial stress - slip wedge response of prism Test4-125

In lateral deformation analysis, the total lateral expansion E of Test4-125 is obtained by using Eq. 3.5 as shown in Figure 3.112. At the peak total axial load, total lateral expansion E_p is 1.08mm. This value is almost same with total axial contraction C_p is 1.04mm. (See again Figure 3.107).

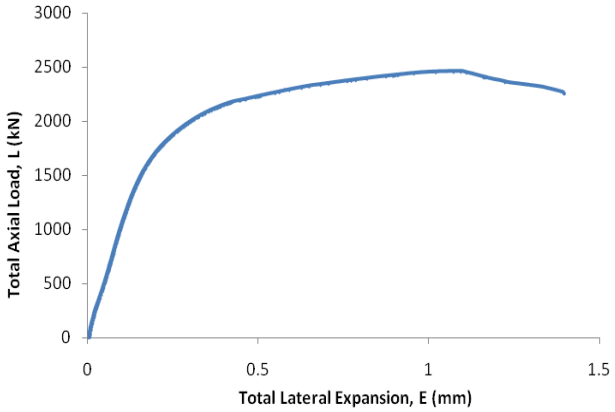

Figure 3.112: Total axial load-total lateral expansion response of prism Test4-125

The lateral micro-cracking starts to develop when $E/2$ more than 0.08mm. Before this point only elastic expansion occurred on Test4-125 as shown in Figure 3.113. $E/2$ at the peak load is approximately 0.54mm. This graph is same with the graph in Figure 3.112 divided by 2 because P-$E/2$ is relationship of load and expansion only for one single wedge.

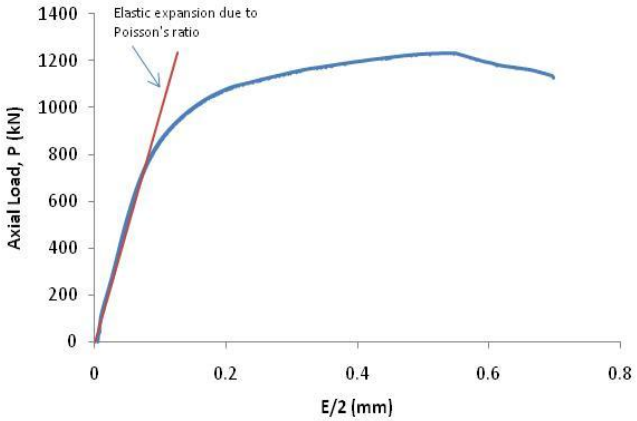

Figure 3.113: Load – E/2 response of prism Test4-125

The wedge expansion V_w is calculated from the graph in Figure 3.113 and used Eqs. 3.6 and 3.7. The wedge expansion of Test4-125 is shown in Figure 3.114. The graph indicates that at peak axial load wedge expansion V_{wp} is 0.41mm. At peak load, V_{wp} is much higher than S_{wp} that is only 0.17mm (see again Figure 3.109). The lateral micro-cracking develop more significant than axial micro-cracking. This means that after micro-cracking formed the crack propagate perpendicular to load direction.

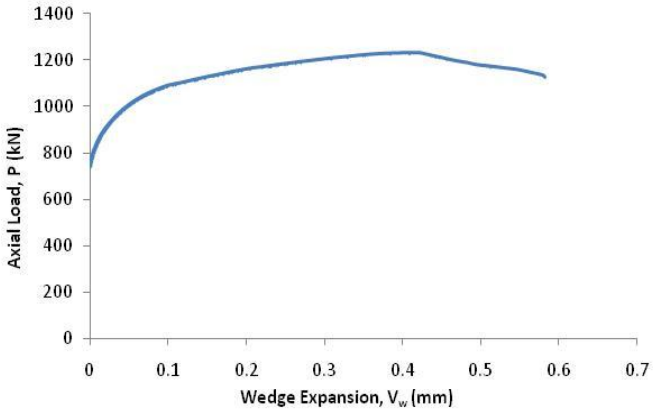

Figure 3.114: Load-wedge expansion response of prism Test4-125

Figure 3.115 shows the relationship between load and expansion in one millimeter of the wedge of prism Test4-125. The graph is same with the graph in Figure 3.114 but the axial load *P* divided by prism length *S* (500mm). Figure 3.116 illustrates the relationship between the stress wedge and the wedge expansion of prism Test4-125.

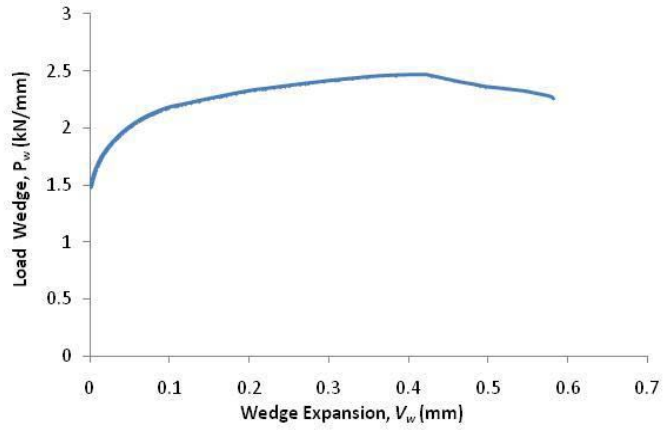

Figure 3.115: Load wedge-wedge expansion response of prism Test4-125

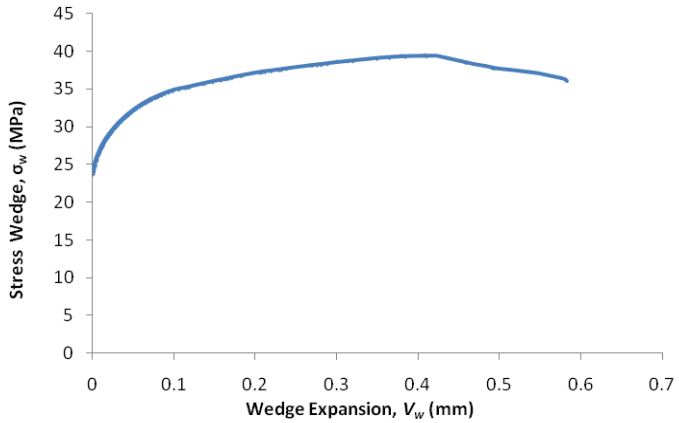

Figure 3.116: Axial stress - wedge expansion response of prism Test4-125

Prism Test4-125 is the last prism in Test-125. All the results of all individual tests in Test-125 are listed in Table 3.5. The average values of all parameters of Test-125 is calculated based on those individual results test and listed in Table 3.5. It should be mentioned that those average values are based on the individual graph of Test1-125, Test2-125, Test3-125, and Test4-125 as described previously. These important parameter is of Test-125 is discussed in detail below. The results is compared with other sizes and explained graphically in Section 3.4.3 in terms of axial deformation and in Section 3.4.4 in terms of lateral deformation.

Table 3.5: The important parameters of prism Test-125 based on individual graph

Prism	L_p (kN)	P_p (kN)	P_{wp} (kN/mm)	σ_{wp} (MPa)	C_p (mm)	$C_p/2$ (mm)	S_{wp} (mm)	E_p (mm)	$E_p/2$ (mm)	V_{wp} (mm)
1	2	3	4	5	6	7	8	9	10	11
TEST1-125	2436	1218	2.44	39	1.04	0.52	0.15	1.13	0.56	0.47
TEST2-125	2505	1253	2.51	40	1.06	0.53	0.22	1.39	0.68	0.55
TEST3-125	2357	1179	2.36	38	1.08	0.54	0.16	0.74	0.37	0.30
TEST4-125	2468	1234	2.47	40	1.04	0.52	0.17	1.08	0.54	0.41
AVERAGE	2442	1221	2.44	39	1.06	0.53	0.17	1.09	0.54	0.43

The data in column 2 and column 6 in Table 3.5 indicates that the peak of total axial load L_p and the total axial contraction at peak load C_p respectively for all prisms in Test-125. The results show the L_p and C_p for Test1-125, Test2-125, Test3-125 and test4-125 are relative the same. The L_p varies between 2357kN to 2505kN while C_p varies in narrow range that is between 1.04mm to 1.08mm. The average values of L_p and C_p are 2442kN and 1.06mm respectively.

The values in columns 3 and 7 in Table 3.5 represent the peak of axial load of one single wedge P_p and total axial contraction of one single wedge at peak load $C_p/2$ respectively. The same behaviour also occurs on P_p and $C_p/2$ because these values are L_p and C_p divided by 2 respectively. The values of parameter P_p and $C_p/2$ are relative the same. The average values of P_p and $C_p/2$ are 1221kN and 0.53mm respectively.

The load wedge P_w is determined by dividing the axial load P with prism length S while slip wedge S_w is quantified by removing the elastic contraction from the P-$C/2$ response. The peak of wedge load P_{wp} and the slip wedge at peak load S_{wp} values of all prisms in Test-125 are listed in columns 4 and 8 in Table 3.5. Those parameter are relative similar, however, small scatter occurs on the slip wedge at peak load S_{wp} of Test2-125. Based on the individual result, the average values of P_{wp} and S_{wp} are 2.44kN/mm and 0.17mm respectively.

The peak of stress wedge σ_{wp} of all prisms in Test-125 is listed in column 5 in Table 3.5. The parameter of σ_{wp} is also quite similar, that varies between 38MPa to 40MPa. The average value based on this individual peak values is 39MPa.

In lateral deformation, the total lateral expansion at peak load E_p of Test-125 is between 0.74mm – 1.39mm. This parameter is represented in column 9 in Table 3.5. A small scatter occurred on Test2-125 and Test3-125. The same pattern also occurred on the total lateral expansion of one wedge $E_p/2$ and wedge expansion at peak load V_{wp} those are listed in columns 10 and 11 in Table 3.5. The average of the total lateral expansion E_p, the total lateral expansion of one wedge $E_p/2$, the wedge expansion V_{wp} at peak load are 1.09mm, 0.54mm and 0.43mm respectively.

3.4.2.2 Tests at 100mm width (100×200×400)

TEST5-100

Test5-100 is the first prism in Test-100. The same behaviour with the previous prisms in Test-125, a "settle down the position" as shown in a dash line in Figure 3.117 also occurred on the total axial load L and the total axial contraction C response on this concrete prism. Figure 3.117 is required to refine. The total axial contraction is subtracted by the length of C that is caused by "settle down the position" and a result shown in Figure 3.118.

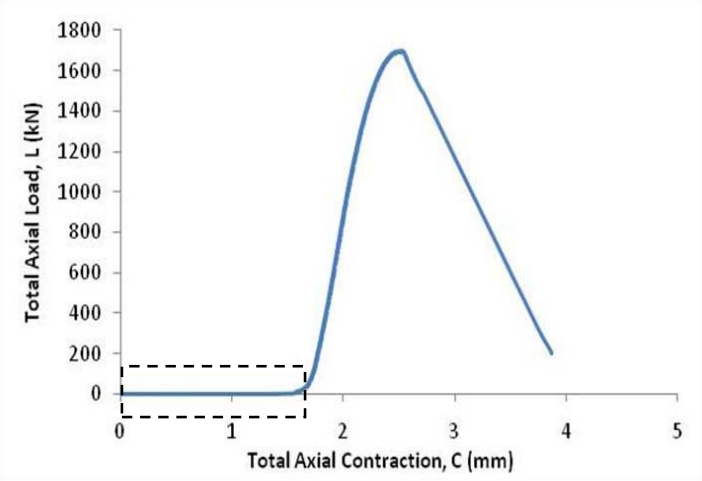

Figure 3.117: Total axial load-total axial contraction response of prism Test5-100

Figure 3.118 depicts *L*-*C* response after correction the axis. The graph indicates the total axial contraction *C* is 0.81 mm when the total axial load reached the peak value of 1,699kN.

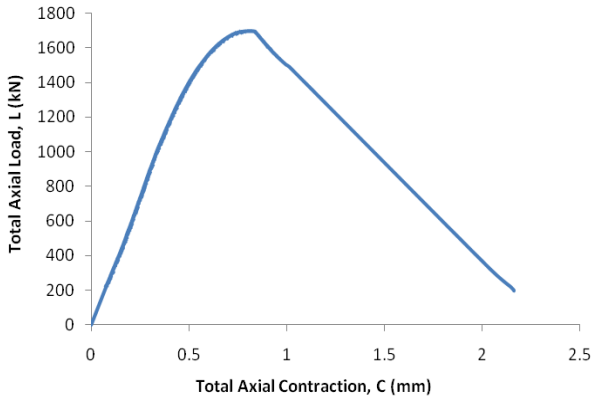

Figure 3.118: Total axial load-total axial contraction response of prism Test5-100 (new axis)

Figure 3.119 shows the relationship between axial load and total axial contraction of one wedge. This graph is obtained by divide the graph in Figure 3.118 with 2. The graph indicates when the load for a single wedge approximately 510kN corresponds to *C*/2 is 0.17; the deformation due to micro-cracking starts to develop. Before this point elastic contraction occurred. The prism reaches the peak of axial load P_p of 849kN at C_p/2 approximately 0.40mm.

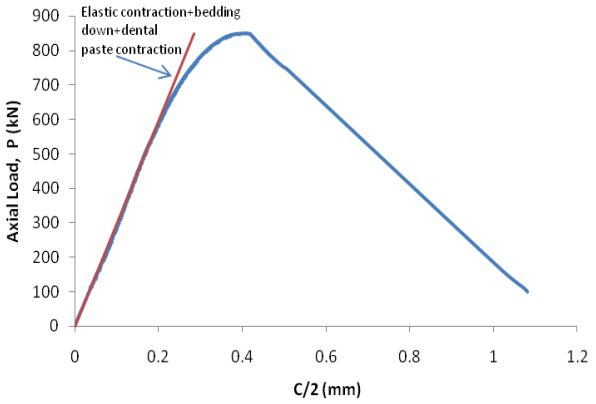

Figure 3.119: Axial load – C/2 response of prism Test5-100

To evaluate the slip of the wedge, elastic contraction *B* in Figure 3.119 should be removed from the *L*-*C*/2 response. Eqs. 3.2 and 3.3 are used to remove the elastic

contraction from total axial contraction. As a result, the relationship between axial load and slip wedge of Test5-100 is obtained and shown in Figure 3.120.

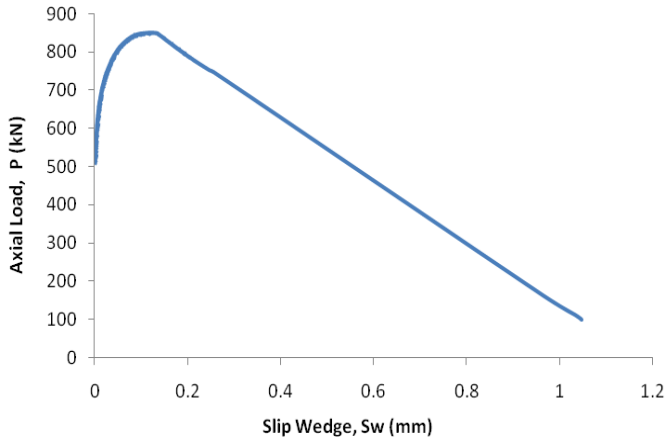

Figure 3.120: Axial load-slip wedge response of prism Test5-100

Figure 3.120 shows the relationship between axial load P and slip wedge of one single wedge S_w, while Figure 3.121 shows the relationship between load wedge and slip wedge P_w- S_w hence the axial load in Figure 3.120 is divided by prism length S. Prism length of Test5-100 is 400mm. The prism reaches the peak of load wedge P_{wp} of 2.12kN/mm at slip wedge S_{wp} approximately 0.12mm.

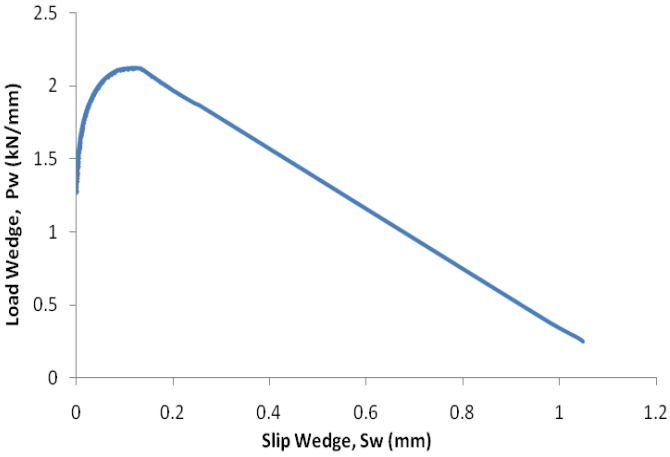

Figure 3.121: Load wedge-slip wedge response of prism Test5-100

The relationship of stress wedge σ_w and slip wedge S_w is depicted in Figure 3.122. The graph indicates that the slip wedge is 0.12 when stress wedge reached the peak σ_{wp} of 43MPa.

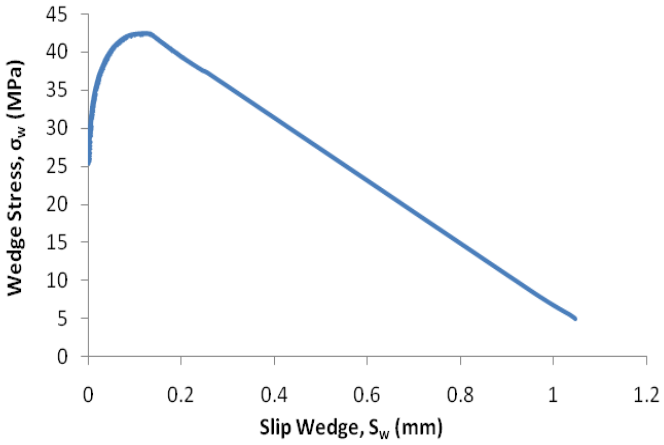

Figure 3.122: wedge stress - wedge expansion response of prism Test5-100

The next four graphs illustrated the lateral deformation analysis. The total lateral expansion is expansion of the whole prism which is obtained by using Eq. 3.5. The relationship between total axial load L and total lateral expansion E of Test5-100 is depicted in Figure 3.123. The graph indicates that as the peak load reached, the total lateral expansion E_p occurred in this test was 0.34 mm. This value is much lower than total axial contraction C_p of 0.81mm (see again Figure 3.118).

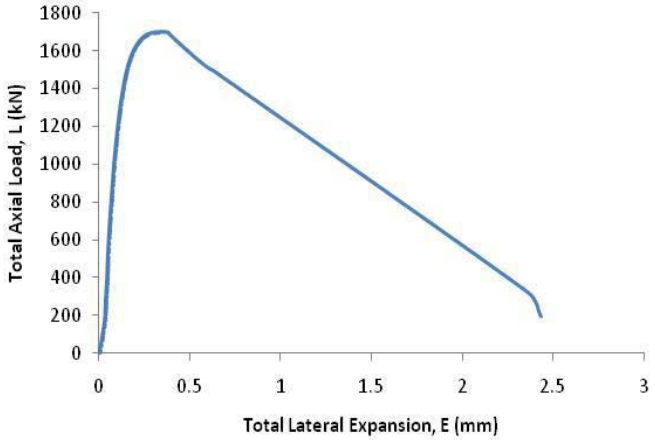

Figure 3.123: Total axial load-total lateral expansion response of prism Test5-100

The total lateral expansion of a single wedge $E/2$ is total lateral expansion divided by 2. Thus the graph in Figure 3.123 divided by 2 is the graph in Figure 3.124. $E/2$ at the peak load is approximately 0.17mm. When $E/2$ is 0.04mm and relates to axial load P 510kN, the deformation due to micro-cracking occurred in lateral direction. The wedge expansion starts to develop. To obtain the expansion of the wedge V_w, the elastic expansion is removed from P-$E/2$ response and Eqs. 3.6 and 3.7 are used. The result is shown in Figure 3.125. The wedge expansion at peak load V_{wp} is approximately 0.1mm.

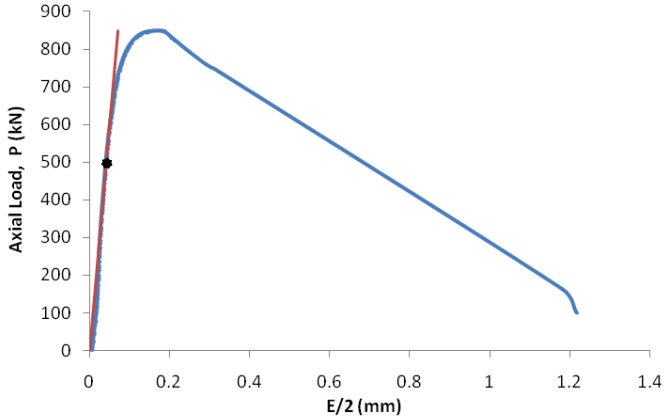

Figure 3.124: Axial load – E/2 response of prism Test5-100

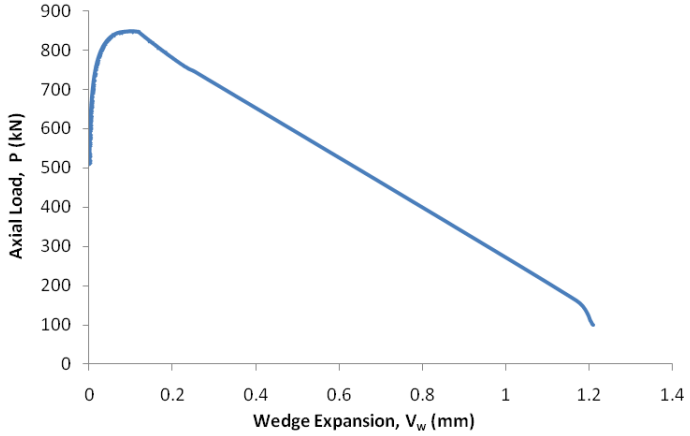

Figure 3.125: Axial load-wedge expansion response of prism Test 5-100

Figure 3.126 shows the relationship between load wedge P_w and expansion over per millimeter thickness of the wedge. P_w is P in Figure 3.125 divided by prism length S. Meanwhile Figure 3.127 shows the stress of the wedge σ_w and wedge expansion V_w of

Test5-100. The wedge expansion V_{wp} is 0.1mm at peak of the wedge stress σ_{wp} is 43MPa.

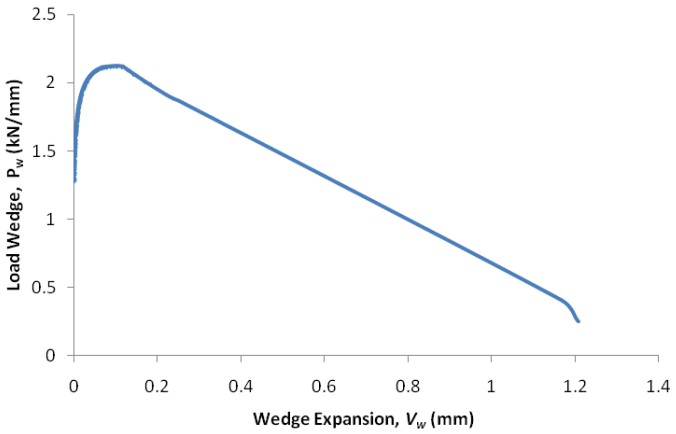

Figure 3.126: Load wedge – wedge expansion response of prism Test5-100

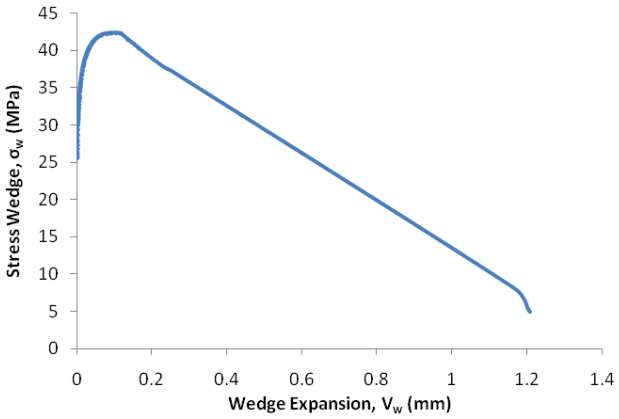

Figure 3.127: Stress wedge – wedge expansion response of prism Test5-100

The individual results of Test5-100 are described previously. The important parameters that are the peak values such as L_p, P_p, P_{wp}, σ_{wp}, C_p, $C_p/2$, S_{wp}, E_p, $E_p/2$, and V_{wp} of Test5-100 are listed in Table 3.6.The second prism in Test-100 is described next.

TEST6-100

The first five graphs illustrate the axial deformation analysis of prism Test6-100. The concrete prism required to settle its position as shown in Figure 3.128. The total axial contraction which is caused by "settle down the position" (shown in a dash line)

required to remove in order to find the actual total axial contraction *C*. The length of the total axial contraction have to remove is approximately 1.6mm. The behaviour the prism after correction the axis was depicted Figure 3.129.

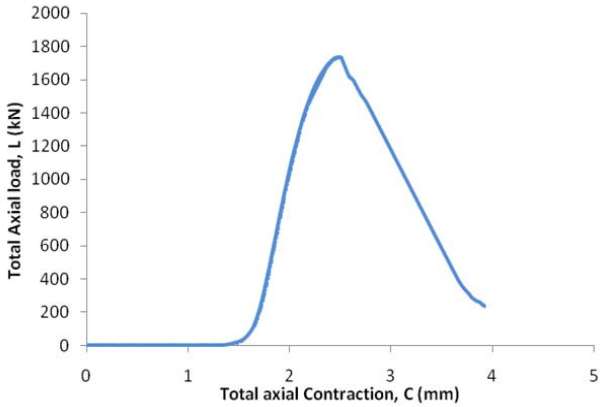

Figure 3.128: Total axial load-total axial contraction response of prism Test6-100

Figure 3.129 illustrates the relationship between total axial load *P* and total axial contraction over the whole prism *C* Test6-100. The graph indicates the total axial contraction is 0.85 mm when the total axial load *L* reached the peak value of 1,737kN.

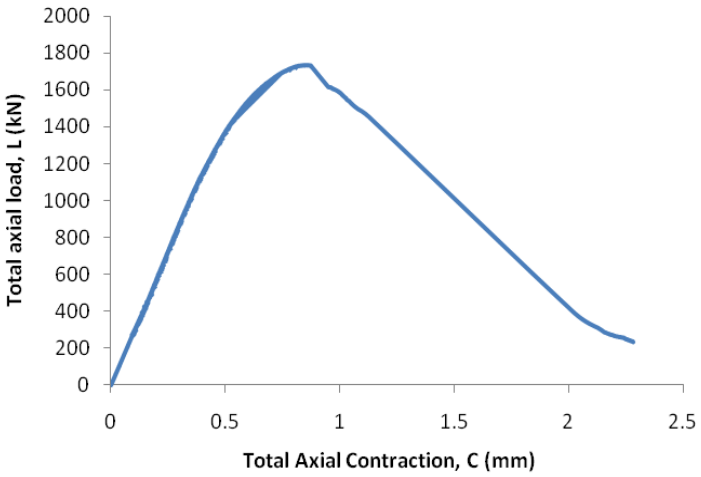

Figure 3.129: Total axial load-total axial contraction response of prism Test6-100 (new axis)

Figure 3.130 illustrated the relationship between axial load and total axial contraction over one wedge that is equal to the *L*-*C* graph (Figure 3.129) divided by 2. Thus the total axial contraction for one single wedge at the peak load of 868kN is approximately 0.43mm.

The graph indicates up to αP_p (520kN) only elastic contraction occurred on the prism. After this point the deformation due to micro-cracking start to develop. The slip wedge is obtained by remove the elastic contraction from *P*-*C*/2 response and use Eq. 3.2 and Eq. 3.3. As result, the relationship between axial load and slip wedge is obtained as shown in Figure 3.131.

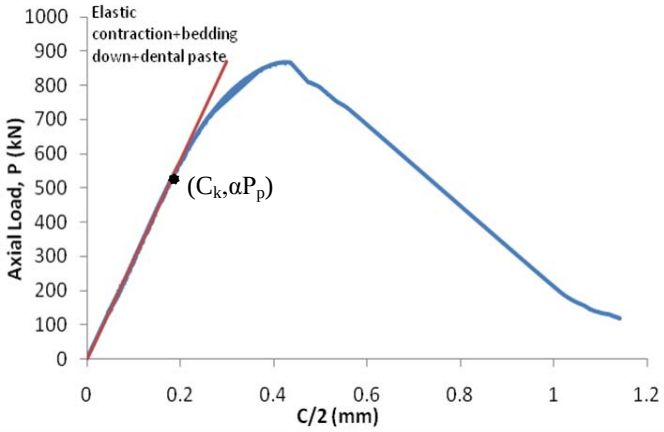

Figure 3.130: Axial load – C/2 response of prism Test6-100

The graph in Figure 3.131 indicates the slip wedge start to develop after the load reaches 520kN. At the peak of axial load P_p of 868kN, the slip wedge S_{wp} approximately 0.13mm.

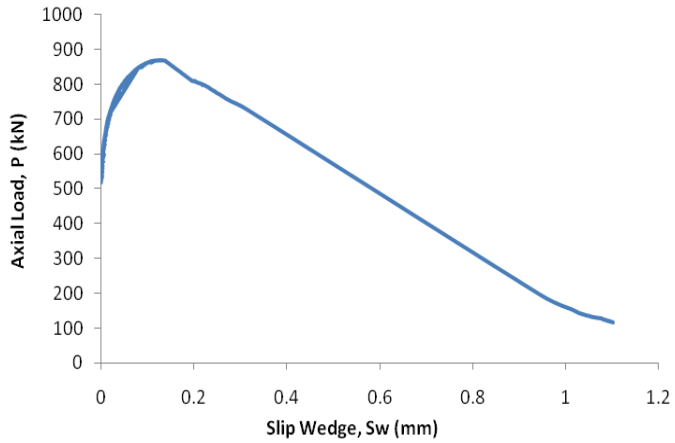

Figure 3.131: Axial load-slip wedge response of prism Test6-100

The load of wedge per millimeter P_w is obtained by divide the axial load P in Figure 3.131 with prism length S (400mm). The micro-cracking starts to occur when the load per millimeter thickness of wedge P_w is 1.3kN/mm. The micro-cracking increases as the load increases up to peak load of 2.17kN/mm and after that point the micro-cracking still increases as the load decreases until the concrete prism failed at slip wedge approximately 1.1mm. While Figure 3.133 shows the relationship between the stress wedge and slip wedge. The slip wedge is 0.13mm when stress reached the peak of 43MPa.

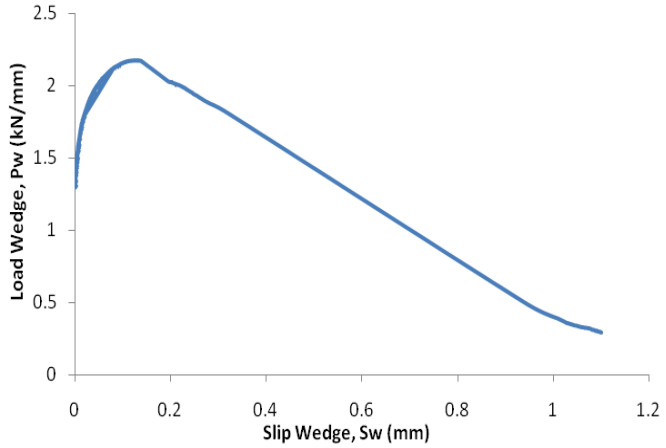

Figure 3.132: Load wedge-slip wedge response of prism Test6-100

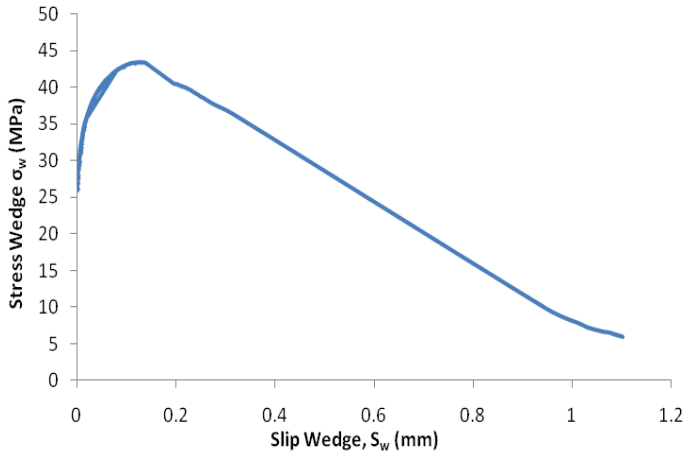

Figure 3.133: Stress wedge – slip wedge response of prism Test6-100

The next five graphs illustrate the lateral deformation analysis. Figure 3.134 illustrates the relationship of *L-E* which is the total lateral expansion of the whole prism. At peak load, total lateral expansion E_p is 0.34 mm. This value is much lower than total axial contraction at peak load C_p (0.85mm).

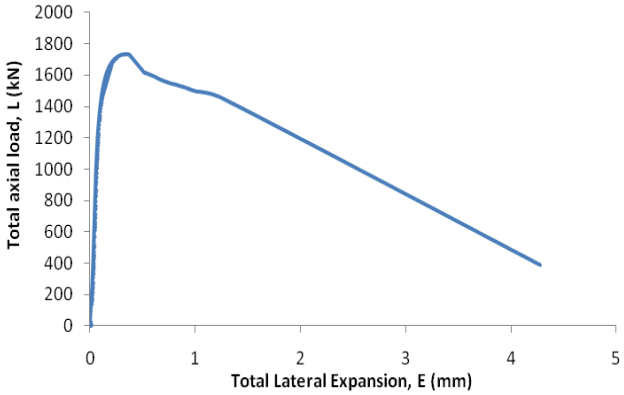

Figure 3.134: Total axial load-total lateral expansion response of Test6-100

The graph in Figure 3.135 is Figure 3.134 divided by 2 because the total lateral expansion *E* is the expansion of the whole prism while Figure 3.135 illustrate the relationship between load and expansion for one wedge only. When *E*/2 is 0.04mm, micro-cracking occurred in lateral direction. The wedge expansion starts to develop. *E*/2 at the peak load is approximately 0.17mm. Eqs. 3.6 and 3.7 are used to obtain the expansion of the wedge, V_w. The result is shown in Figure 3.136. The wedge expansion at peak load V_{wp} is approximately 0.12mm.

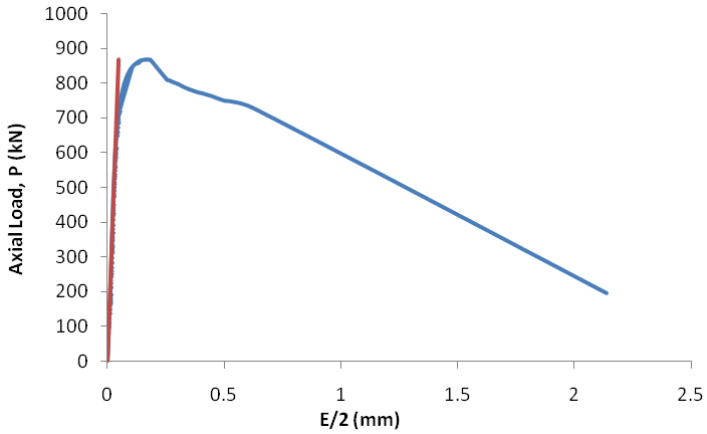

Figure 3.135: Axial load – E/2 response of prism Test6-100

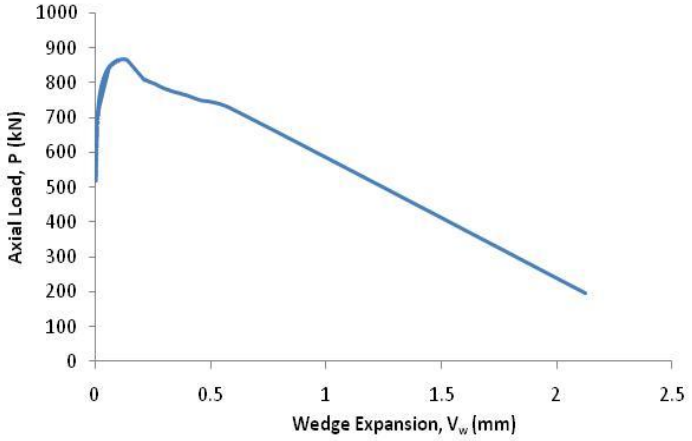

Figure 3.136: Axial load-wedge expansion response of prism Test6-100

Figure 3.137 shows the relationship between load wedge P_w and expansion in one millimeter of the wedge of prism Test6-100. The graph is same with the graph in Figure 3.136 but axial load P divided by prism length S (400mm). Figure 3.138 illustrates the relationship between the stress wedge and wedge expansion of prism Test6-100. The peak stress wedge σ_{wp} is 43MPa corresponds to slip wedge S_{wp} approximately 0.13mm

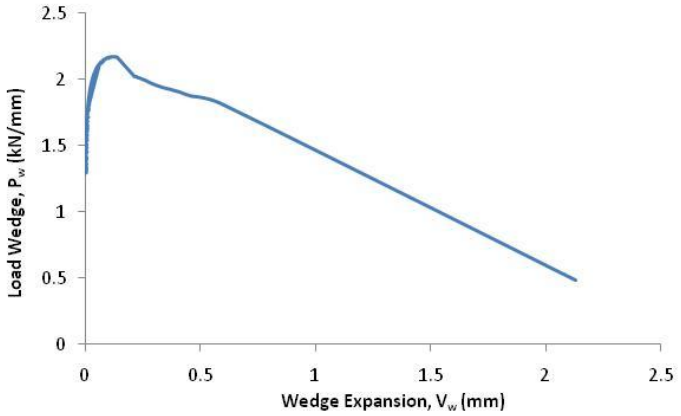

Figure 3.137: Load wedge-wedge expansion response of prism Test6-100

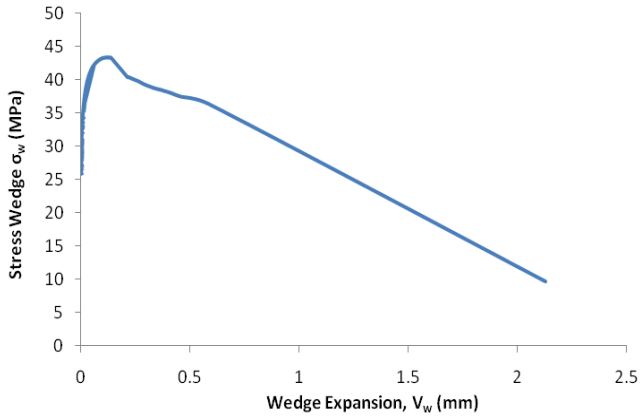

Figure 3.138: stress wedge-wedge expansion response of prism Test6-100

The response of stress wedge and wedge expansion is the last analysis in Test6-100. The important parameters that are the peak values such as L_p, P_p, P_{wp}, σ_{wp}, C_p, $C_p/2$, S_{wp}, E_p, $E_p/2$, and V_{wp} of concrete prism Test4-125 that are described previously, are listed in Table 3.6. The next Section is analysis in Test7-100.

TEST7-100

The first five graphs (Figure 3.139 to Figure 3.144) illustrate the axial deformation analysis. The analysis begin with total axial load – total axial contraction, *L-C* graph as depicted in Figure 3.139 that is required to adjust because the graph shows the "settle the position" (shown in a dash line) of the concrete. After adjustment the position, the total axial contraction is 0.77mm when the total axial load reached the peak load L_p at 1,638kN (Figure 3.140).

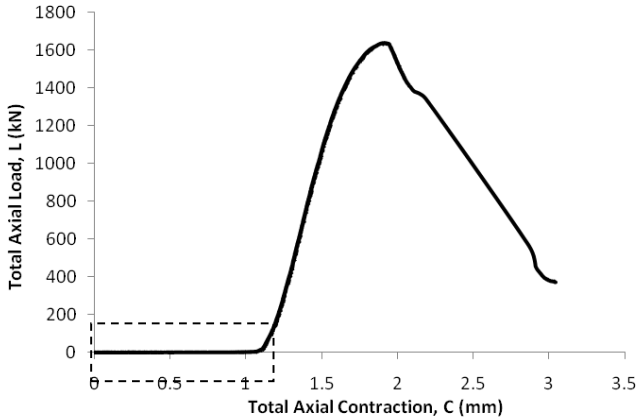

Figure 3.139: Total axial load-total axial contraction response of prism Test7-100

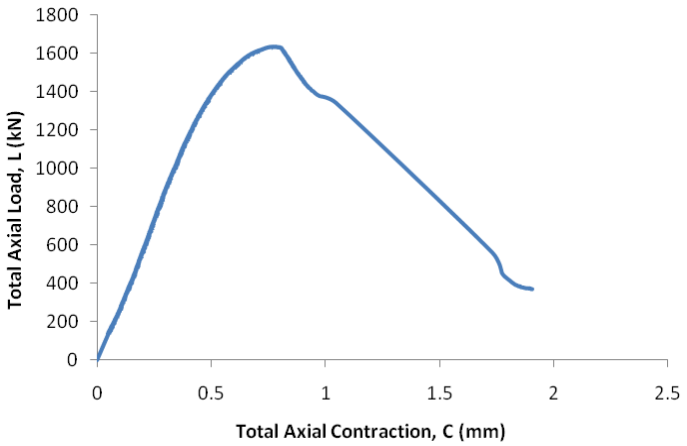

Figure 3.140: Total axial load-total axial contraction response of prism Test7-100 (new axis)

Figure 3.141 shows the total axial contraction over a single wedge $C_p/2$ is 0.39mm as the load of a wedge reaches the peak of 819kN. This graph is the graph in Figure 3.140 divided by 2 because Figure 3.141 illustrates the relationship between load and total axial contraction for a single wedge only while Figure 3.140 illustrates load and total axial contraction for the whole prism. The elastic contraction occurred until $C/2$ approximately 0.17mm that is relates to axial load 491kN, after this point the micro-cracking occurred on the prism. The deformation which is caused by micro-cracking is obtained by remove the elastic contraction from Figure 3.141. The result is shown in Figure 3.142. The slip wedge at peak axial load S_{wp} is 0.11mm (Figure 3.142).

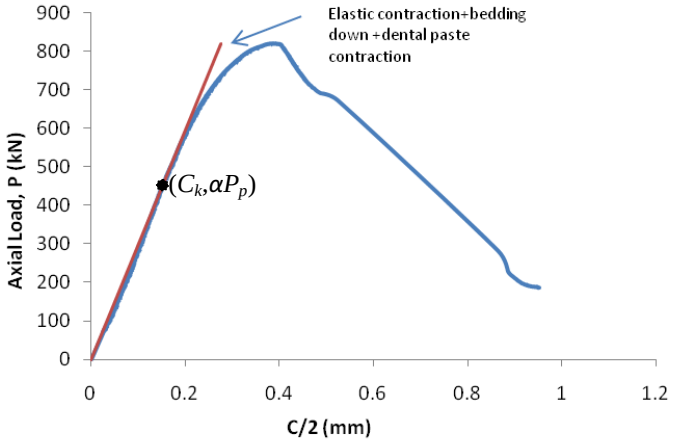

Figure 3.141: Axial load – C/2 response of prism Test7-100

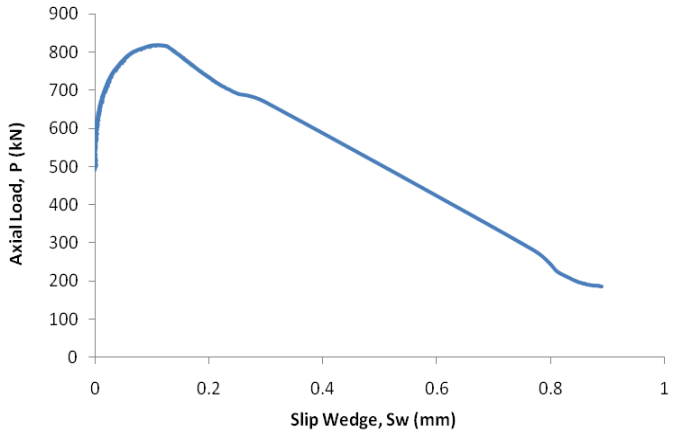

Figure 3.142: Axial load-slip wedge response of prism Test7-100

The relationship between the load wedge and slip wedge for 1 millimeter wedge thickness is illustrated in Figure 3.143. The graph illustrates the slip wedge S_{wp} is 0.11mm when the load wedge reached the peak P_{wp} approximately 2.05kN/mm. The next figure (Figure 3.144) shows the relationship between the stress wedge and slip wedge (σ_w-S_w). The graph indicates that the peak stress wedge is 41MPa at slip wedge 0.11mm

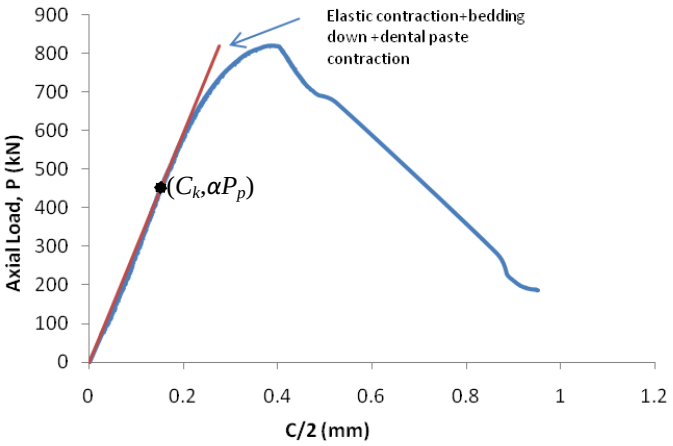

Figure 3.143: Load wedge-slip wedge response of prism Test7-100

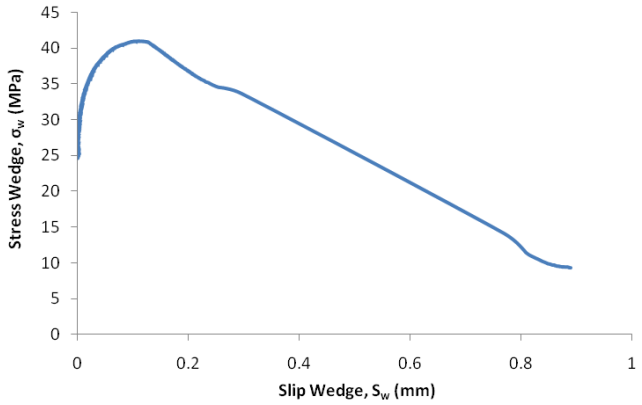

Figure 3.144: Axial stress - slip wedge response of prism Test7-100

The next five graphs show lateral deformation analysis of Test7-100. The graph illustrates total lateral expansion E_p is 0.27 mm when the peak of total axial load L_p reached (Figure 3.145). This load and expansion response is the response of the whole prism while Figure 3.146 illustrates the relationship between the load and expansion for a single wedge only. It can be seen the pattern of these two graphs are the same but the values of axial load P and total lateral expansion of one wedge is half than the load and expansion in Figure 3.145. At peak load $E/2$ is approximately 0.13mm (Figure 3.146). The graph in Figure 3.146 indicates the lateral micro-cracking occurred after the total lateral expansion for one wedge is approximately 0.02mm.

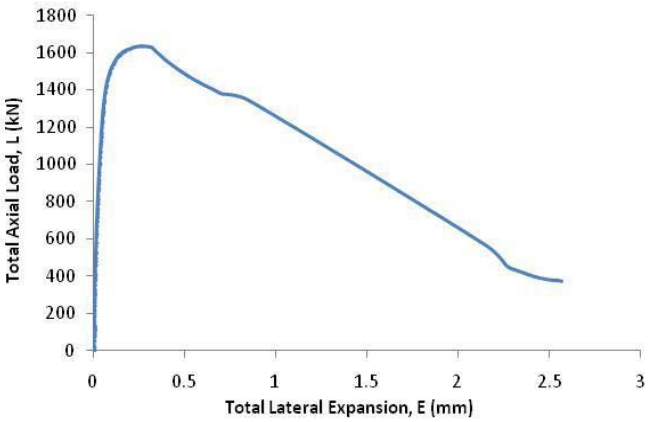

Figure 3.145: Total axial load-total lateral expansion response of prism Test7-100

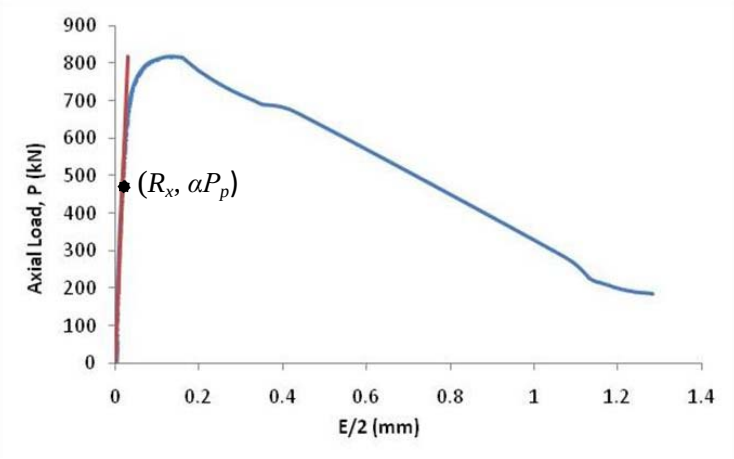

Figure 3.146: Axial load – E/2 response of prism Test7-100

Figure 3.147 illustrates the expansion of the wedge against the axial load over a single wedge. At the peak of axial load P_p of 819kN, the wedge expansion V_{wp} approximately 0.1mm. This value is almost the same with the slip wedge at peak load S_{wp} is 0.11 (see again Figure 3.142). The load P in Figure 3.147 is divided by the prism length S equal to load of wedge in 1 mm wedge thickness P_w as shown in Figure 3.148.

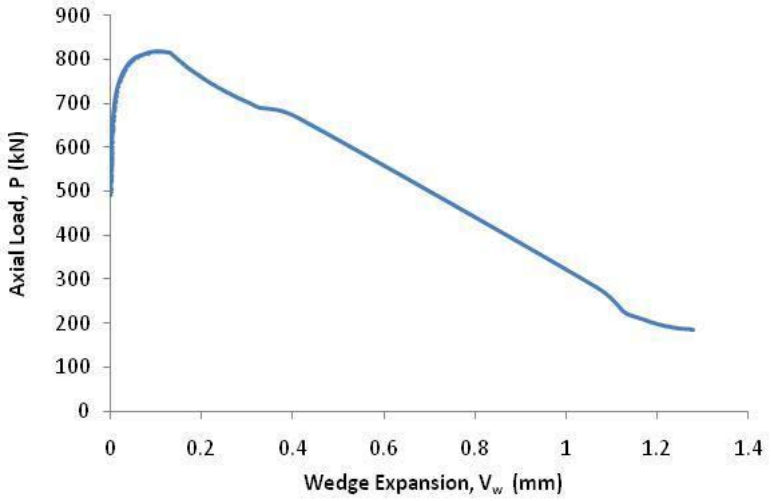

Figure 3.147: Axial load-wedge expansion response of Test7-100

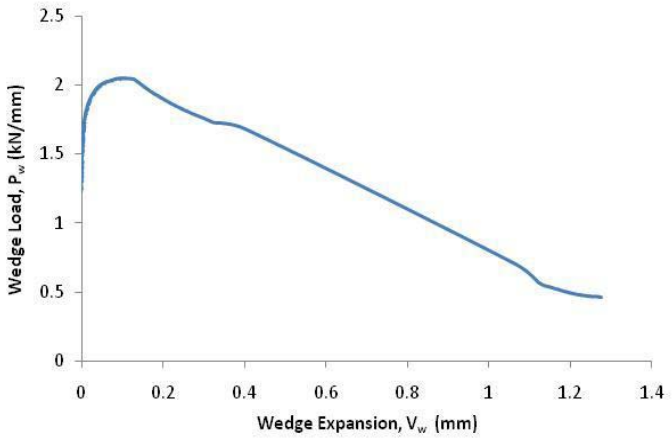

Figure 3.148: Wedge load-wedge expansion response of Test7-100

Figure 3.149 is the last figure in Test7-100. The graph illustrates the relationship of stress wedge and wedge expansion of Test7-100. The micro-cracking starts to form when stress approximately 25MPa. The lateral deformation due to micro-cracking or wedge expansion increases slightly up to peak stress wedge σ_{wp} of 41MPa and increases significantly as the stress wedge decreases until the prism failed.

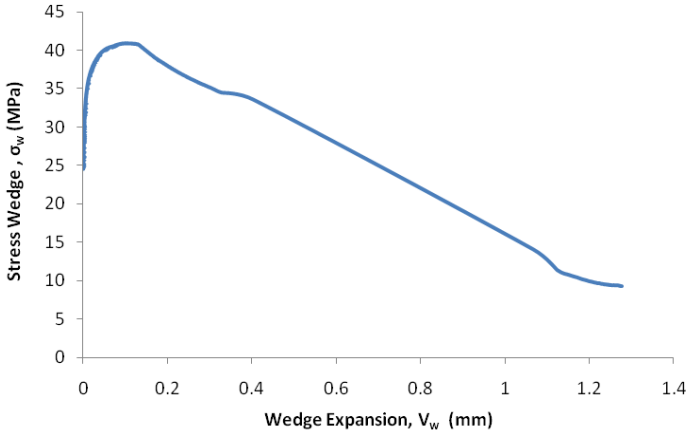

Figure 3.149: Stress wedge – wedge expansion response of prism Test7-100

The individual results of Test7-100 are described previously. The important parameters that are the peak values such as L_p, P_p, P_{wp}, σ_{wp}, C_p, $C_p/2$, S_{wp}, E_p, $E_p/2$, and V_{wp} of Test7-100 are listed in Table 3.6. Test7-100 is the last prism in Test-100.

The all results of concrete prisms Test5-100, Test6-100, and Test7-100 are listed in Table 3.6. The average values of those parameters are also listed in Table 3.6 based

on the individual results graph. The average parameters of Test-100 are also listed in Table 3.6.

It should be noting that the average parameters are based on the individual graph of Test5-100, Test6-100, and Test7-100 as described individually previously. These important parameters of Test-100 are discussed in detail below and explained graphically in Section 3.4.3 for axial deformation and Section 3.4.4 for lateral deformation.

Table 3.6: The important parameters of prism Test-100 based on individual graph

Prism	L_p (kN)	P_p (kN)	P_{wp} (kN/mm)	σ_{wp} (MPa)	C_p (mm)	$C_p/2$ (mm)	S_{wp} (mm)	E_p (mm)	$E_p/2$ (mm)	V_{wp} (mm)
1	2	3	4	5	6	7	8	9	10	11
TEST5-100	1699	849	2.12	43	0.81	0.40	0.12	0.34	0.17	0.10
TEST6-100	1737	868	2.17	43	0.85	0.43	0.13	0.34	0.17	0.12
TEST7-100	1638	819	2.05	41	0.77	0.39	0.11	0.27	0.13	0.10
AVERAGE	1691	846	2.11	42	0.81	0.41	0.12	0.32	0.16	0.11

Table 3.6 shows all parameters in axial and lateral directions of Test-100 are quite similar. The peak of total axial load L_p varies between 1638kN to 1737kN corresponds to total lateral at peak load C_p varies between 0.77mm to 0.85mm. L_p and C_p for all prisms in Test-100 are listed in columns 2 and 6 in Table 3.6 respectively. The average values of L_p and C_p based on the individual results are 1691kN and 0.81mm respectively.

The peak axial load of P_p and total axial contraction of one single wedge at peak load $C_p/2$ is L_p and C_p divided by 2 respectively those are summarised in column 3 and 7 in Table 3.6. The average values of P_p and $C_p/2$ are 846kN and 0.41mm respectively.

The peak of wedge load P_{wp} corresponds to the slip wedge S_{wp} of Test-100 are quite the similar as shown in columns 4 and 8 in Table 3.6. The values of parameter S_{wp} are between 0.11mm to 0.13mm. Based on the individual graph, the average values of P_{wp} and S_{wp} are 2.11kN/mm and 0.12mm respectively. The peak of stress wedge σ_{wp}

(column 5 in Table 3.6) of all prisms in Test-100 is also quite similar, that varies in narrow range between 41MPa to 43MPa. The average value based on this individual peak values is 42MPa.

In lateral deformation, the parameter of E_p (column 9 Table 3.6) of Test5-100 and Test6-100 is exactly the same of 0.34mm while Test7-100 is 0.27mm. The average of the total lateral expansion E_p, the total lateral expansion of one wedge $E_p/2$, the wedge expansion V_{wp} at peak load, those are presented in columns 9, 10 and 11 in Table 3.6 respectively, are 0.32mm, 0.16mm and 0.11mm respectively.

3.4.2.3 Tests at 75mm width (75×150×300)

TEST8-75

As the previous test, the relationship between the total axial load and total axial contraction *L-C* required to adjust as represented in Figure 3.150 because of "settle down the position" occurred on prism Test8-75 (shown in a dash line).

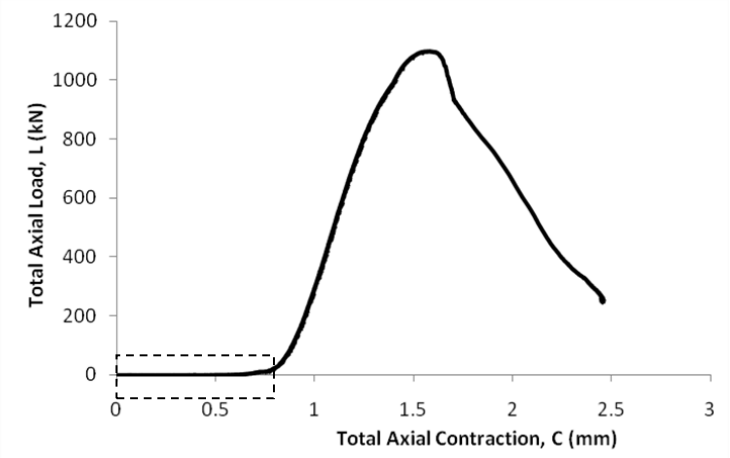

Figure 3.150: Total axial load-total axial contraction response of Test8-75

Figure 3.151 shows the relationship between total axial load and total axial contraction after remove the contraction which is caused by "settle down the position". The contraction increases as the load increases until the peak load reached approximately 1099kN. The total axial contraction at the peak load is 0.74mm. This graph indicates the total axial contraction of the whole prism.

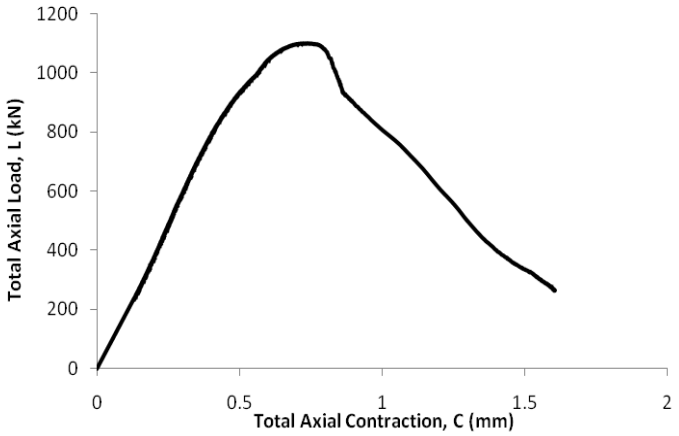

Figure 3.151: Total axial load-total axial contraction response of Test8-75 (new axis)

The total axial contraction of one single wedge is determined by dividing the total axial contraction in Figure 3.151 with 2 and depicted in Figure 3.152. The total axial contraction over one wedge is 0.37 mm when the load reached the peak P_p at 550kN. As the load approximately 330kN the axial micro-cracking start to occur correspond to C_k approximately 0.17mm.

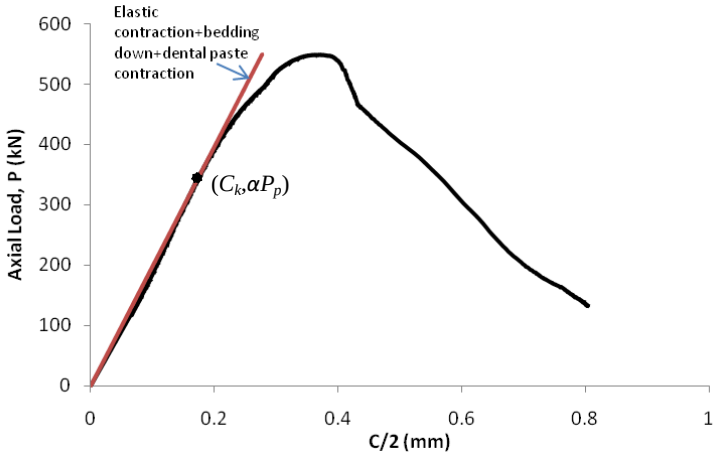

Figure 3.152: Axial load – C/2 response of prism Test8-75

The axial deformation due to micro-cracking is obtained by using Figure 3.152 and Eqs. 3.2 and 3.3 as shown in Figure 3.153. Slip of wedge is 0.09mm when the peak of axial load for a single wedge P_p reached.

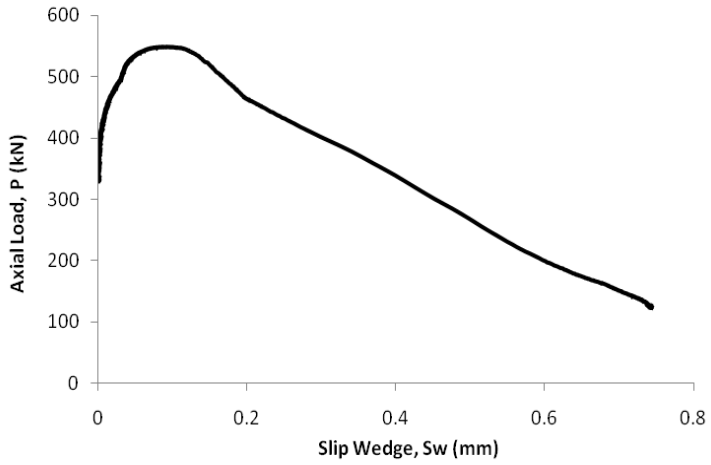

Figure 3.153: Axial load-slip wedge response of prism Test8-75

Figure 3.154 illustrates the relationship between load per millimeter wedge thickness P_w and slip wedge. P_w is P in Figure 3.153 divided by the prism length S (300mm). It can be seen that micro-cracking start to develop when P_w approximately 1.1kN/mm. The last analysis in axial deformation is the relationship between the stress wedge and slip wedge is depicted in Figure 3.155. The graph indicates that the peak of stress wedge of Test8-75 is 49MPa when slip wedge 0.09mm.

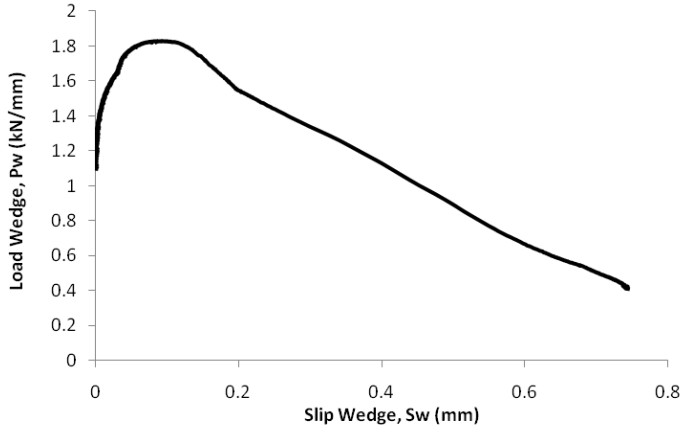

Figure 3.154: Load wedge-slip wedge response of prism Test8-75

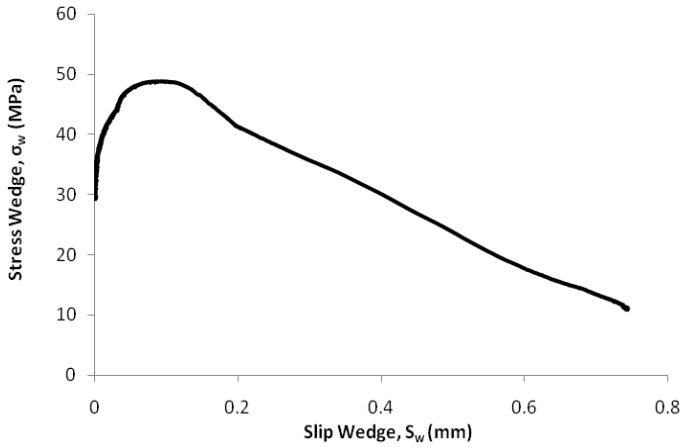

Figure 3.155: Axial stress - slip wedge response of prism Test8-75

Figure 3.156 to Figure 3.160 described the lateral deformation analysis of Test8-75. Figure 3.156 shows the total axial load *L* and total lateral expansion *E*. This total lateral expansion is the algebraic sum of two values of LVDTs reading. The graph indicates the total lateral expansion increases slightly as the load increases. The total lateral expansion at peak load E_p is approximately 0.25mm. After that point the total lateral expansion increases significantly as the load decreases.

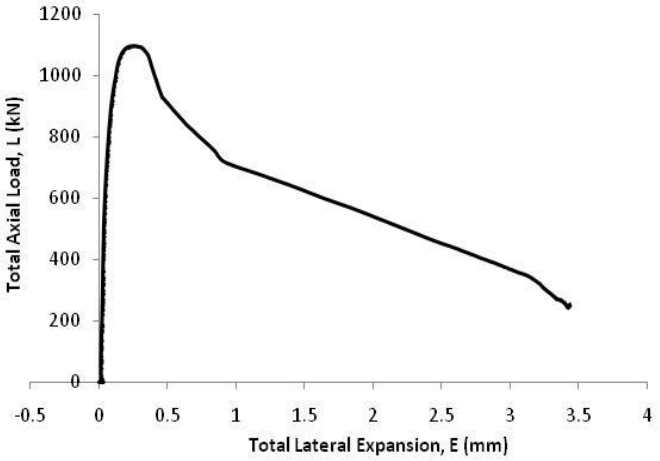

Figure 3.156: Total axial load-total lateral expansion response of prism Test8-75

Figure 3.157 shows the load and total lateral expansion over one single wedge. The graph is half than the graph in Figure 3.156 . Hence at peak load, the total lateral

expansion is half than E is approximately 0.13mm. Micro-cracking starts to develop when $E/2$ is 0.02mm.

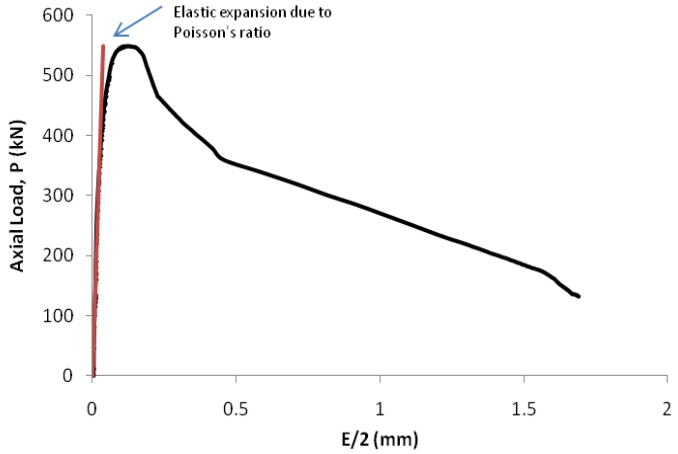

Figure 3.157: Axial load - E/2 response of prism Test8-75

The graph in Figure 3.158 indicates that the lateral micro-cracking start to develop when load over one wedge P is 330kN. The wedges expand very slightly until the load reaches 430kN. After that point the wedges expand slightly up to the peak load. At peak load, wedge expansion V_{wp} is approximately 0.09mm. Then the wedges expand significantly as the load decrease until the prism failed.

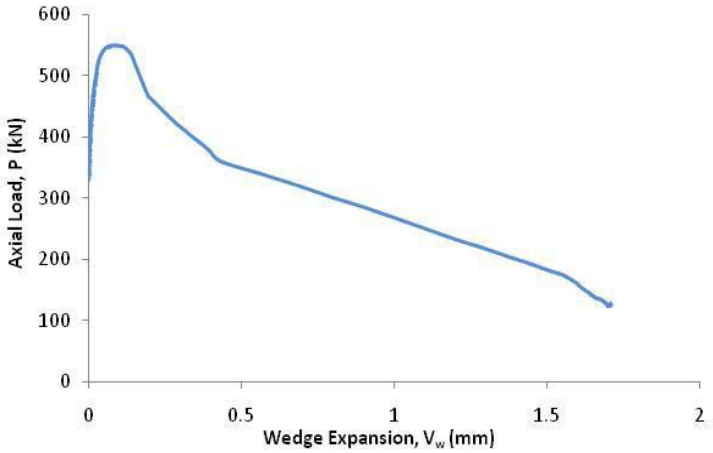

Figure 3.158: Axial load-wedge expansion response of prism Test8-75

Figure 3.159 illustrates the relationship of P_w-V_w. This figure is the same with Figure 3.158 but the load is per millimeter thickness of wedge which is the axial load P

divided by prism length *S*. The last part of analysis Test8-75 is the relationship between stress wedge and wedge expansion as shown in Figure 3.160. The graph indicates the wedge expansion at peak stress wedge is approximately 0.09mm

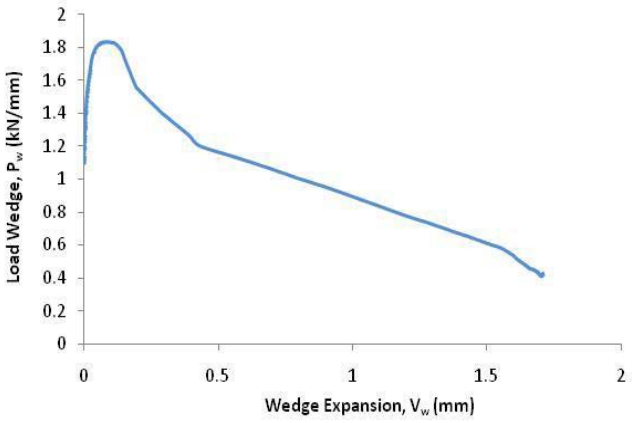

Figure 3.159: load wedge-wedge expansion response of prism Test8-75

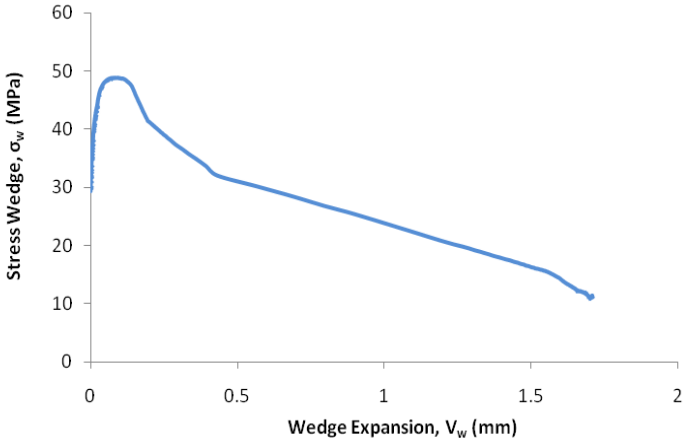

Figure 3.160: Axial stress –wedge expansion response of prism Test8-75

TEST9-75

The relation between the total axial load and the total axial contraction of Test9-75 can be seen in Figure 3.161. It shows that "the settle down the position" as shown in a dash line occurred at early stage of loading. The total axial contraction is required to refine in order to remove "settle down the position ". The distance between a new origin O and O', *m* is 1.53mm (see again Figure 3.59). The total axial contraction in Figure 3.161 is subtracted by *m*. The result is shown in Figure 3.162.

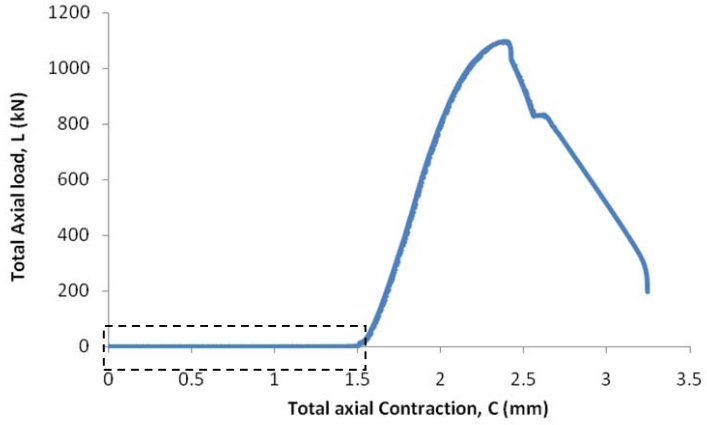

Figure 3.161: Total axial load-total axial contraction response of prism Test9-75

Figure 3.162 illustrates the response of *L-C* after correction the total axial contraction. The graph indicates total axial contraction is 0.86 mm when the peak of total axial load L_p reaches approximately 1,096kN.

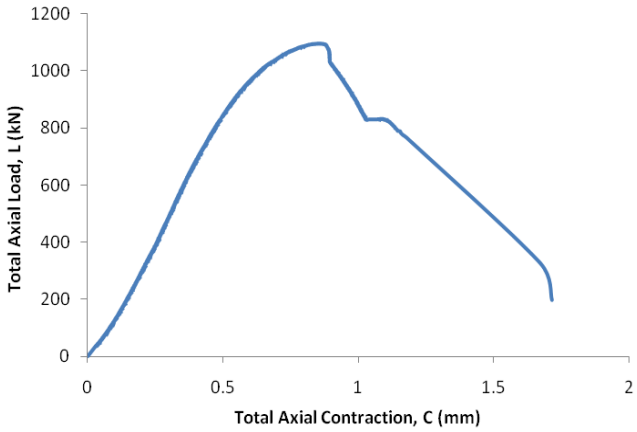

Figure 3.162: Total axial load-total axial contraction response of Test9-75 (new axis)

Figure 3.162 illustrates total axial load and total axial contraction of the whole prism, while Figure 3.163 illustrates axial load and total axial contraction of a single wedge. Thus Figure 3.163 is obtained by dividing Figure 3.162 with 2. The $C_p/2$ is 0.43mm at peak axial load over a single wedge of 548kN. The micro-cracking starts to develop when axial load approximately 329kN at C_k is 0.19mm. Before this point elastic contraction occurred on the prism.

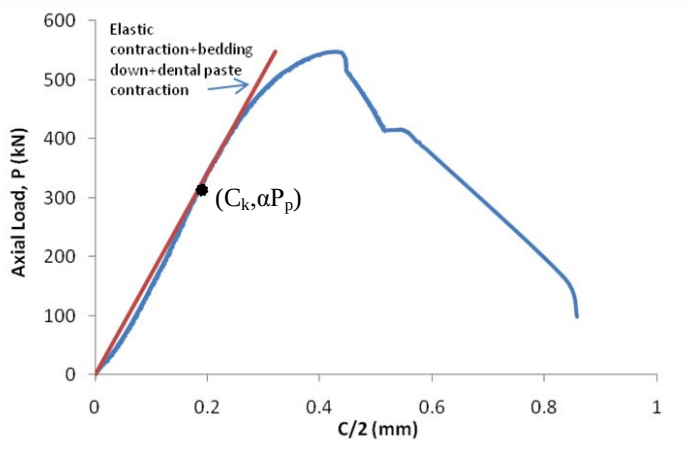

Figure 3.163: Axial load – C/2 response of Test9-75

To analyse one wedge of the prism, axial load and slip wedge is required. Figure 3.164 shows the relationship between axial load and slip wedge which is obtained by using Figure 3.163 and Eqs. 3.2 and 3.3. The graph indicates the axial deformation due to micro-cracking start to form at the axial load P is 329kN.

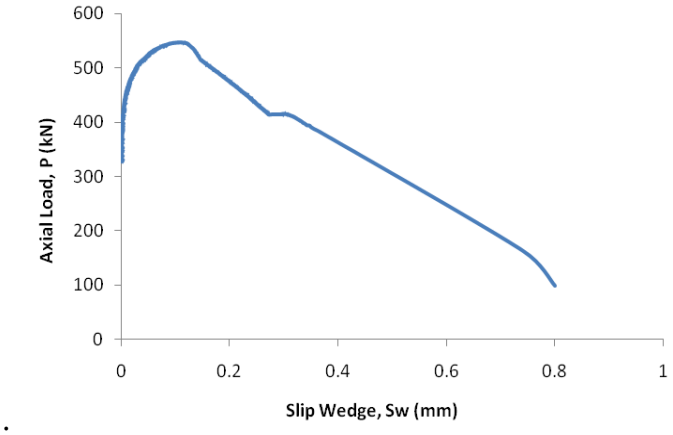

Figure 3.164: Axial load-slip wedge response of Test9-75

The load in 1 mm wedge thickness is obtained by dividing the axial load P in Figure 3.164 with prism length S of 300mm as shown in Figure 3.165. The micro-cracking starts to develop when the load per 1 mm wedge thickness P_w is 1.1kN/mm. The slip wedge is 0.11mm at the peak load P_{wp} of 1.83kN/mm. The last analysis in axial deformation quantifies the relationship of stress wedge and slip wedge is depicted in Figure 3.166. The concrete prism reaches the peak of stress wedge approximately 49MPa corresponds with slip wedge 0.11mm.

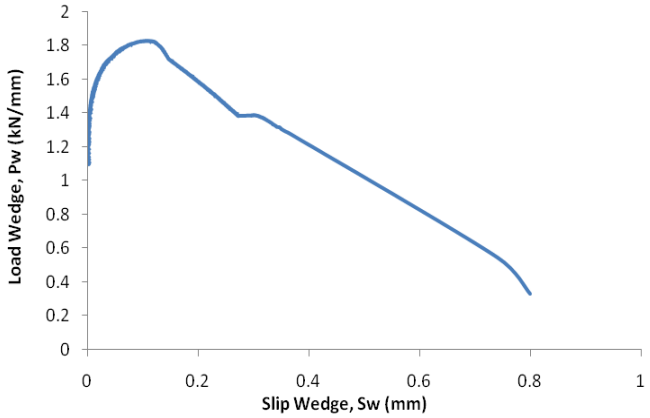

Figure 3.165: Load wedge-slip wedge response of prism Test9-75

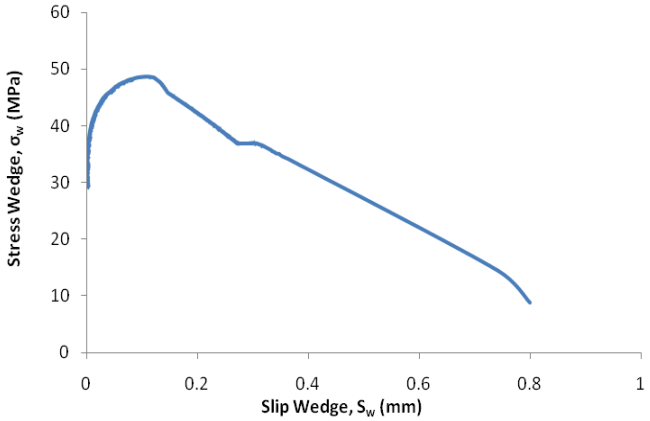

Figure 3.166: Stress wedge – slip wedge response of prism Test9-75

The next five graphs show the analysis in lateral deformation of test9-75. Figure 3.167 illustrates the relationship between total axial load L and total lateral expansion E of Test9-75. Total lateral expansion at peak total axial load E_p is approximately 0.24mm.

Figure 3.168 shows the response of axial load *P* and total lateral expansion over a single wedge *E*/2 that is half of the *L*-*E* response. Thus at the peak of axial load, the total lateral expansion for one wedge is 0.12mm. The graph indicates the lateral micro-cracking occurred when *E*/2 more than 0.02mm. The response of axial load and wedge expansion is quantified by using this graph and Eqs. 3.7 and 3.8. The result is shown in Figure 3.169.

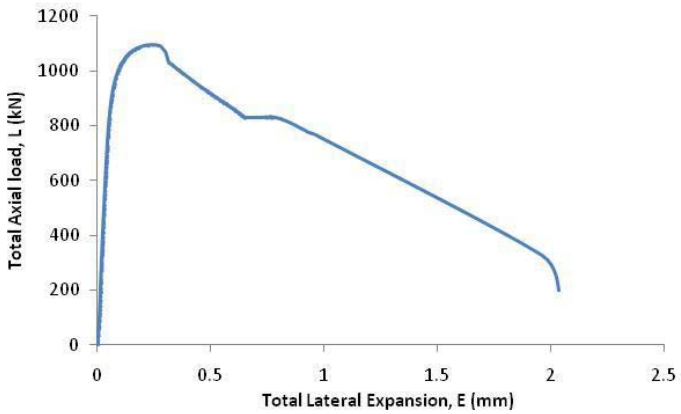

Figure 3.167: Total axial load-total lateral expansion response of Test9-75

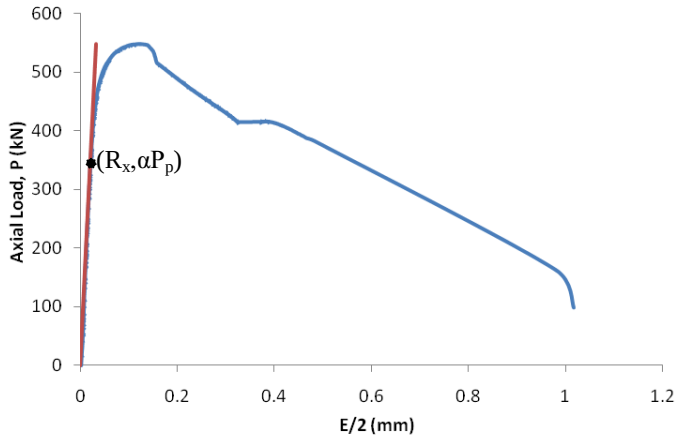

Figure 3.168: Axial load – E/2 response of Test9-75

Figure 3.169 shows the wedge did not expand until the axial load *P* reaches approximately 470kN. After that point the wedge expands slightly until the peak load reached. The wedge increases significantly as the load decreases until the prism failed.

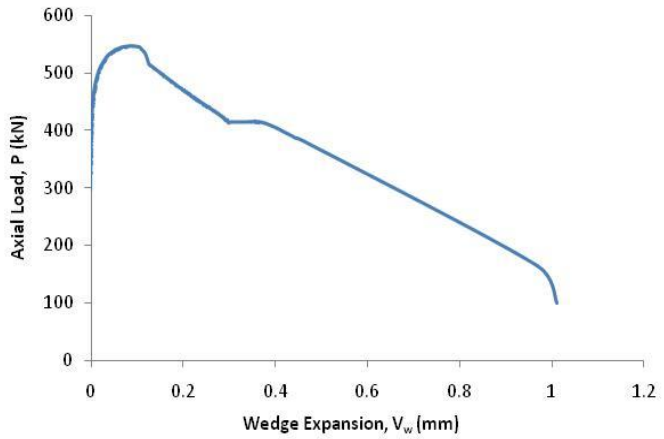

Figure 3.169: Axial load-wedge expansion response of Test9-75

Figure 3.170 illustrated the load per 1 mm wedge thickness. This graph is the graph in Figure 3.169 divided by the prism length *S*. *S* for Test9-75 is 300mm. The lateral micro-cracking starts to develop when the load per 1 mm wedge thickness P_w is 1kN/mm.

The relationship between stress wedge and wedge expansion is depicted in Figure 3.171. At peak of stress wedge the wedge expansion is 0.09mm.

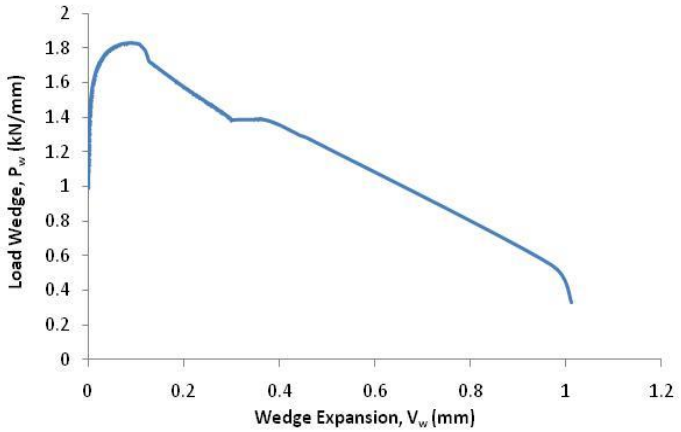

Figure 3.170: Load wedge-wedge expansion response of Test9-75

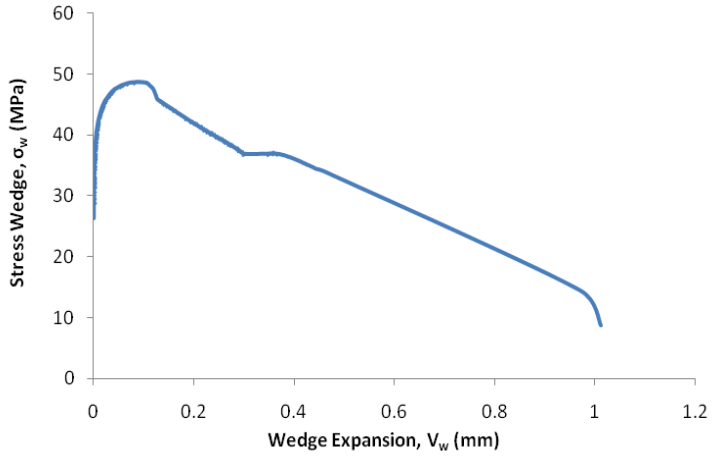

Figure 3.171: Stress wedge – wedge expansion response of Test9-75

TEST10-75

The analysis for Test 10-75 shows at the next eleven graphs. First graph, Figure 3.172 shows the relation between total axial load *L* and the total axial contraction *C* that is occurred on Test1075. The graph shows "the settle down the position" of the specimen also occurred as shown in a dash line. Thus total axial load-total axial contraction in Figure 3.172 is corrected into the second graph (Figure 3.173).

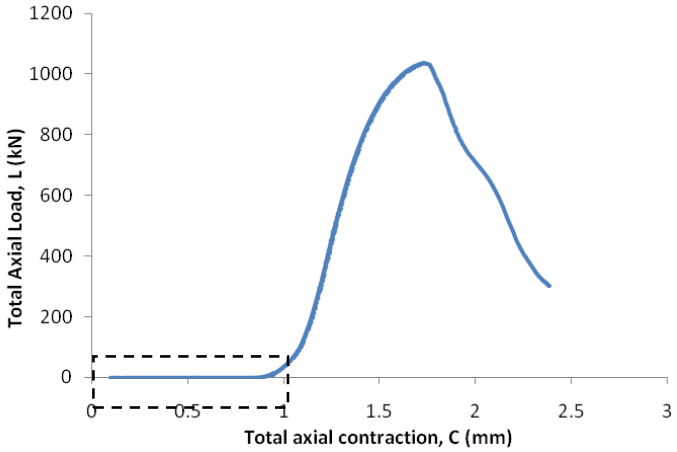

Figure 3.172: Total axial load-total axial contraction response of Test10-75

Figure 3.173 shows the total axial contraction of the whole prism. The total axial contraction is 0.69mm when the peak of L_p reached 1,038kN.

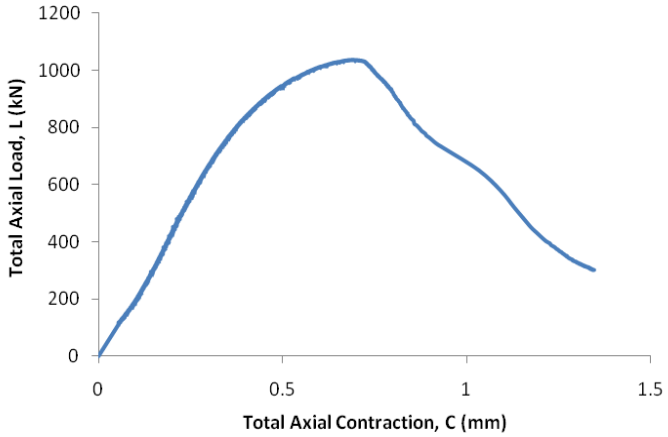

Figure 3.173: Total axial load-total axial contraction response of Test10-75 (new axis)

Figure 3.174 shows the relationship between axial load and total axial contraction of one single wedge. This response is obtained by divide the graph in Figure 3.173 with 2. When the total axial contraction over one wedge $C/2$ 0.14mm and the load reaches of 311kN, the micro-cracking start to form. Before this point material contraction occurred. The slip wedge is obtained by removing the material contraction from Figure 3.174. A result is shown in Figure 3.175.

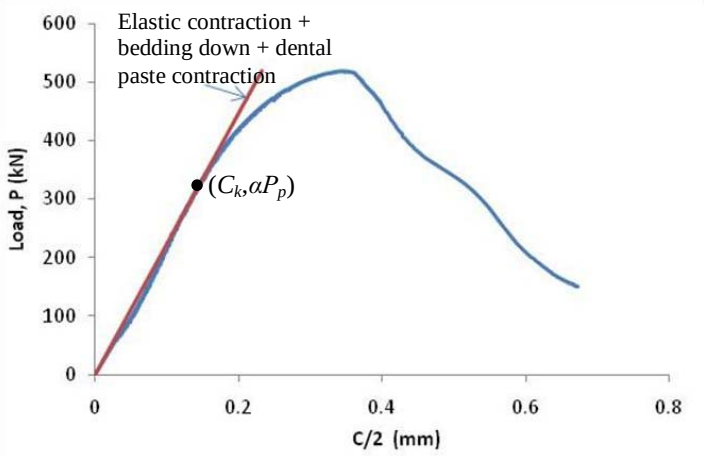

Figure 3.174: Axial load – C/2 response of Test10-75

The axial load and the slip wedge response of prism Test10-75 is shown in Figure 3.175. The graph indicates that the slip wedge at peak load S_{wp} is 0.11mm when the peak load P_p is approximately 519kN.

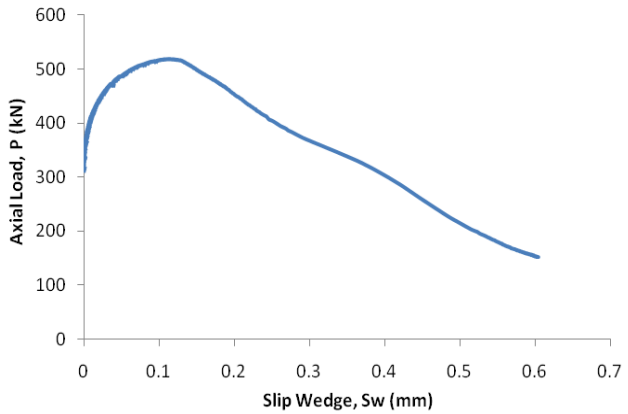

Figure 3.175: Axial load-slip wedge response of Test10-75

The response in Figure 3.176 is the load P in Figure 3.175 divided by S. The micro-cracking starts to develop when the load wedge per mm wedge thickness P_w is approximately 1mm. The last analysis in axial deformation is stress wedge and slip wedge response as depicted in Figure 3.177. The stress wedge reaches the peak value of 46Mpa corresponds to slip wedge 0.11mm.

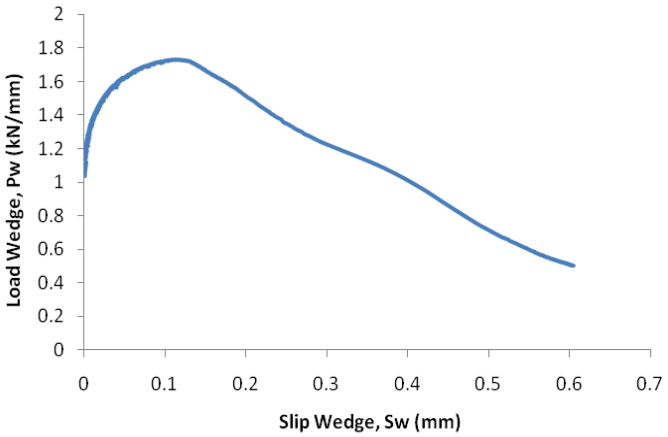

Figure 3.176: Load wedge-slip wedge response of Test10-75

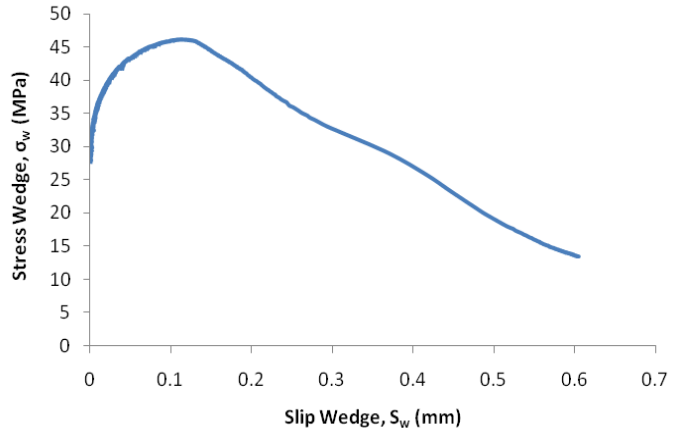

Figure 3.177: Stress wedge – slip wedge response of Test10-75

In lateral deformation analysis, the total lateral expansion is the expansion of the whole prism is shown in Figure 3.178. The graph shows on ascending branch, the total lateral expansion increases slightly until the peak load reached. After that, the prism expands significantly as the load decreases until the prism failed. The total lateral expansion at peak load is approximately 0.25mm.

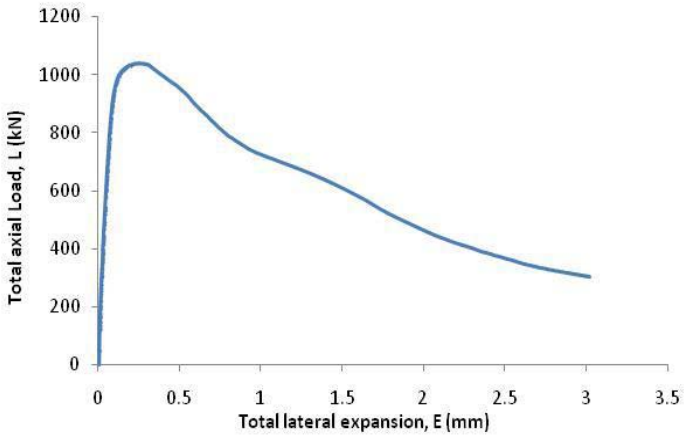

Figure 3.178: Total axial load-total lateral expansion response of Test10-75

Figure 3.179 shows the response of load-expansion of one single wedge which is half than the graph in Figure 3.178. When *E*/2 is equal to 0.03mm, the micro-cracking occurred in lateral direction. The elastic expansion occurred before that point.

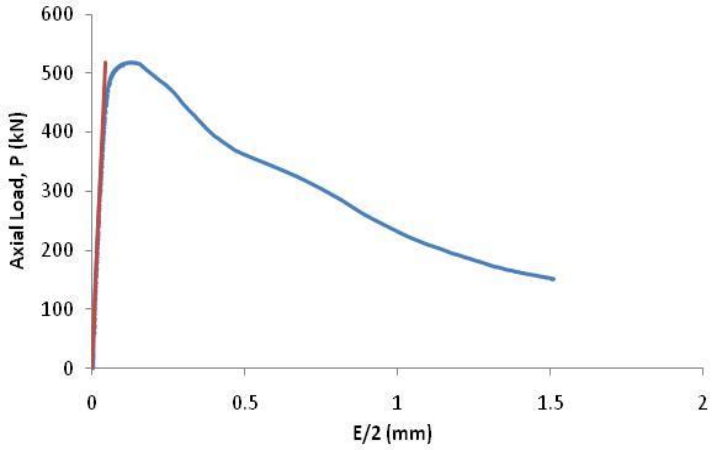

Figure 3.179: Axial load – E/2 response of Test10-75

To analyse the wedge expansion, the elastic expansion is removed from Figure 3.179. The result is shown in Figure 3.180. Wedge expansion at peak load V_{wp} is 0.08mm.

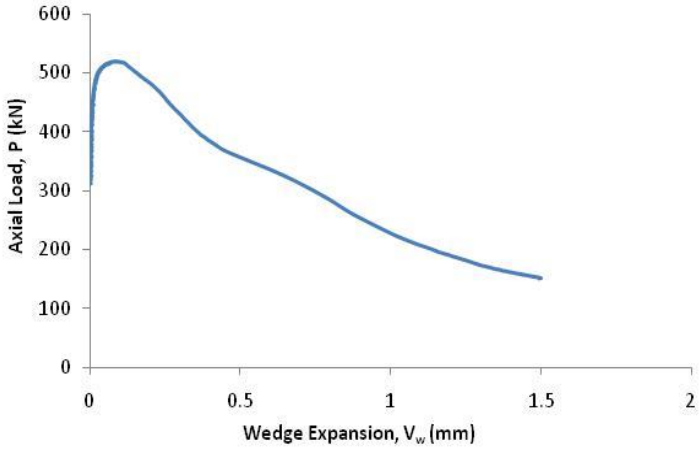

Figure 3.180: Axial load-wedge expansion response of Test10-75

Figure 3.181 shows the relationship between load and expansion over one wedge per millimeter thickness of the wedge. P_w is P in Figure 3.180 divided by prism length S.

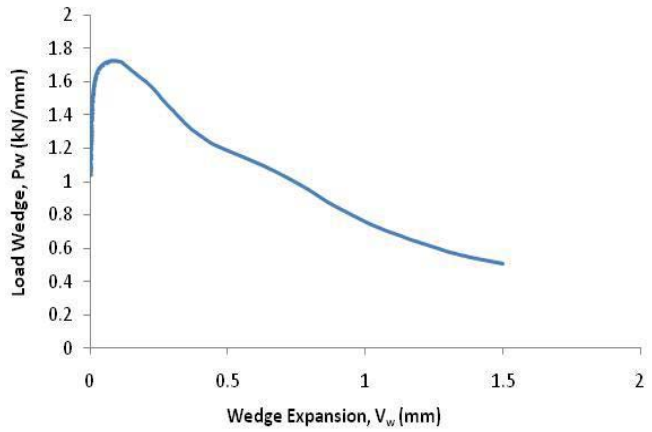

Figure 3.181: Load wedge-wedge expansion response of Test10-75

The last part in analysis the prism Test10-75 is analysis the relationship between stress wedge and wedge expansion. At peak stress, the wedge expansion V_{wp} is 0.08mm.

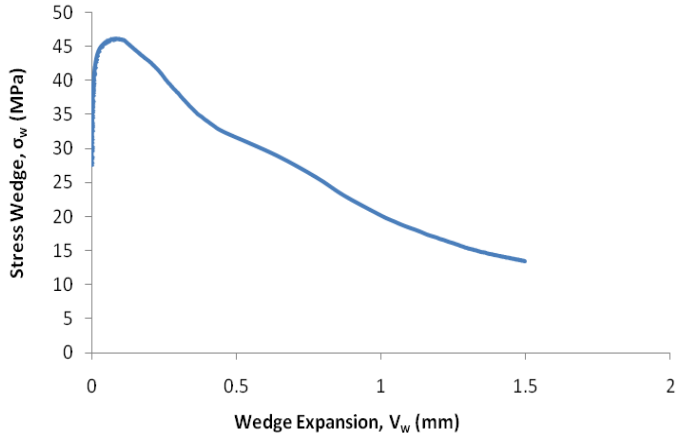

Figure 3.182: Stress wedge – wedge expansion response of Test10-75

The all important parameters of concrete prisms Test8-75, Test9-75 and Test10-75 are listed in Table 3.7. The average values of those parameters based on the individual graph are also listed in Table 3.7.

Table 3.7: The important parameters of prism Test-75 based on individual graph

Prism	L_p (kN)	P_p (kN)	P_{wp} (kN/mm)	σ_{wp} (MPa)	C_p (mm)	$C_p/2$ (mm)	S_{wp} (mm)	E_p (mm)	$E_p/2$ (mm)	V_{wp} (mm)
1	2	3	4	5	6	7	8	10	11	12
TEST8-75	1099	550	1.83	49	0.74	0.37	0.09	0.25	0.13	0.09
TEST9-75	1096	548	1.83	49	0.86	0.43	0.11	0.24	0.12	0.09
TEST10-75	1038	519	1.73	46	0.69	0.34	0.11	0.25	0.13	0.08
AVERAGE	1078	539	1.80	48	0.76	0.38	0.11	0.25	0.13	0.09

Table 3.7 shows the value parameters of L_p, P_p, P_{wp}, and σ_{wp} of Test8-75 and Test9-75 are quite the same while a small scatter occurs on Test10-75. The parameters of S_{wp}, E_p, $E_p/2$, and V_{wp} for all prisms in Test-75 are really similar. A small scatter occurs on parameters C_p and $C_p/2$.

The total axial contraction at peak load C_p of all prisms in Test-75 is higher than total lateral expansion at peak load E_p. The same pattern also occurs on $C_p/2$and $E_p/2$ because these values are half than C_p and E_p respectively. However, the deformation due to micro-cracking in axial and lateral directions is almost the same. S_{wp} varies in small range between 0.09mm-0.11mm and V_{wp} varies between 0.08-0.09mm.

3.4.2.4 Tests at 50mm width (50×100×200)

There are three concrete prisms in Test-50; Test11-50, Test12-50 and Test13-50. It should be noted that Test12-50 is not tested due to fracture.

TEST11-50

The total axial load applied to concrete prism Test11-50 against the total axial contraction that was occurred shown in Figure 3.183. The “settle down the position” of the specimen also occurred (shown in a dash line). Thus total axial load-contraction in Figure 3.183 is corrected into Figure 3.184.

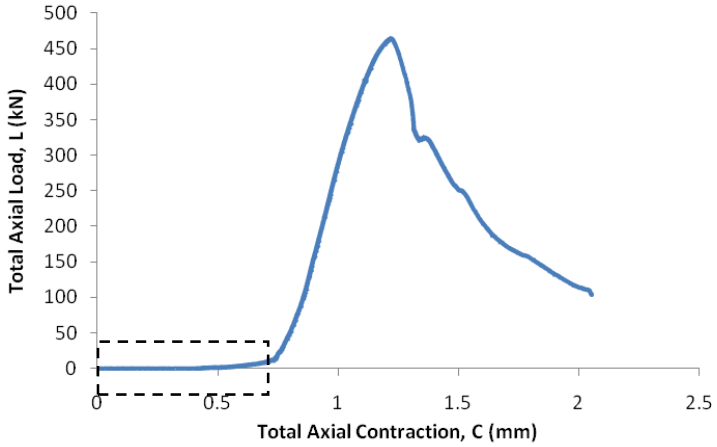

Figure 3.183: Total axial load-total axial contraction response of Test11-50

Figure 3.184 illustrates the total axial load L and total axial contraction C after correction. The total axial contraction C_p is 0.45 mm when the load reached its peak L_p of 464kN.

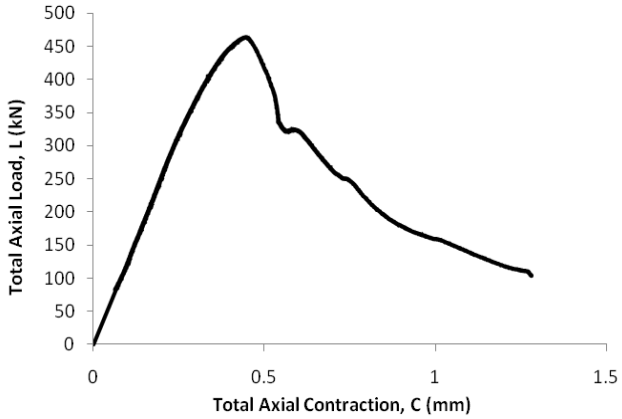

Figure 3.184: Total axial load-total axial contraction response of Test11-50 (new axis)

The relation of load and total axial contraction over a single wedge, P-$C/2$ is depicted in Figure 3.185. Elastic contraction occurred until $C/2$ approximately 0.11mm corresponds to 60% of P_p. After that point the micro-cracking occurred. Axial deformation due to micro-cracking or slip wedge S_w is obtained by using Eqs. 3.2 and 3.3. The slip wedge of Test11-50 is shown in Figure 3.186. The peak of axial load in one wedge P_p is 232kN at slip wedge S_{wp} is approximately 0.04mm.

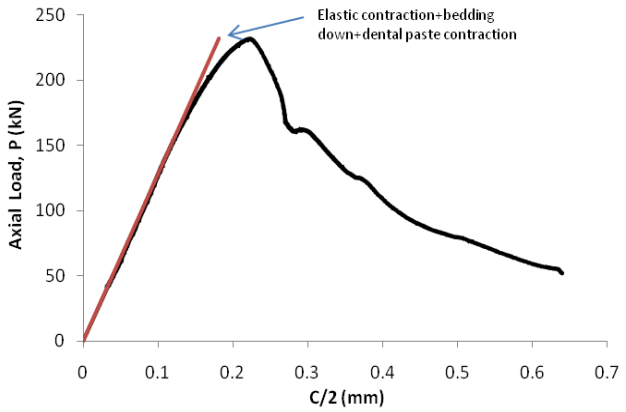

Figure 3.185: Axial load – C/2 response of Test11-50

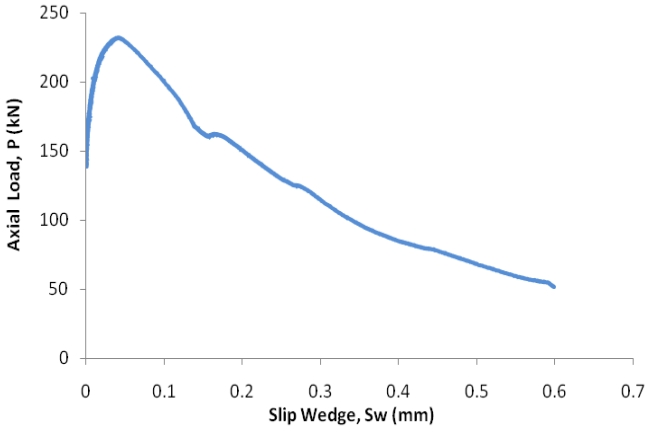

Figure 3.186: Axial load-slip wedge response of Test11-50.

The load wedge P_w *i*s axial load P in Figure 3.186 divided by the prism length S. S for Test11-50 is 200mm thus the relationship of P_w-S_w can be seen in Figure 3.187. The slip wedge starts to form when the load of the wedge P_w is approximately 0.7kN/mm. The load increases as the slip increases and peak load P_{wp} reached approximately 1.16kN/mm.

The stress wedge σ_w and slip wedge S_w response shown in Figure 3.188. To determine the stress wedge Eq. 3.4 is used. The micro-cracking starts to occur when stress wedge is approximately 28MPa. The peak stress wedge is 46MPa relate to slip wedge 0.04mm.

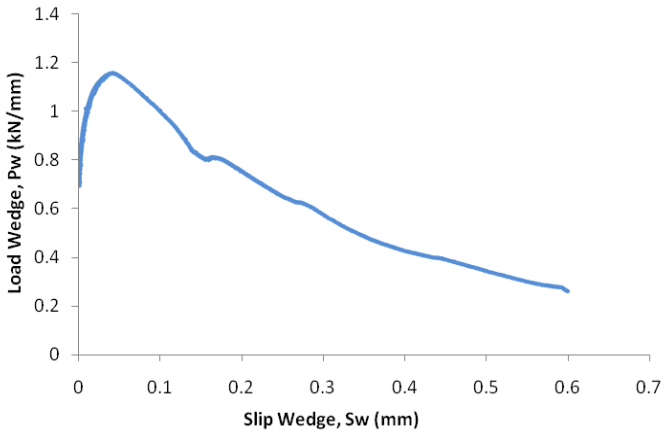

Figure 3.187: Load wedge-slip wedge response of Test11-50

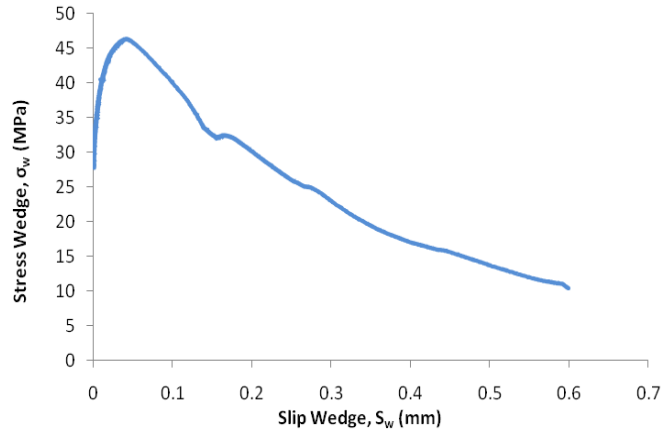

Figure 3.188: Stress wedge – slip wedge response of Test11-50

Figure 3.189 shows total axial load and total lateral expansion of Test11-50. The graph indicates up to the total axial load L 260kN, the prism did not expand. After this point the prism expands very slightly until the peak load reach approximately 464kN corresponds to total lateral expansion E_p is 0.09mm. After that the prism expands significantly as the load decreases.

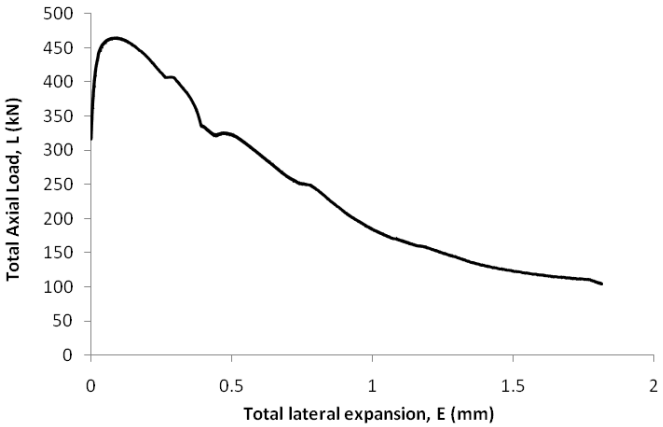

Figure 3.189: Total axial load-total lateral expansion response of Test11-50

Figure 3.190 shows the axial load and wedge expansion over one single wedge of Test11-50. This graph is the *L-E* response divided by 2. The graph indicates that the wedge not expand up to the axial load 130kN which is approximately 56% of peak axial load P_p of 232kN. As assumed previously at 60% P_p, the deformation due to micro-cracking or slip wedge occurred. This means that the prism not expand up to 56% of P_p and it followed by wedge expansion. The total lateral expansion of one single wedge at peak load, $E_p/2$ is 0.04mm.

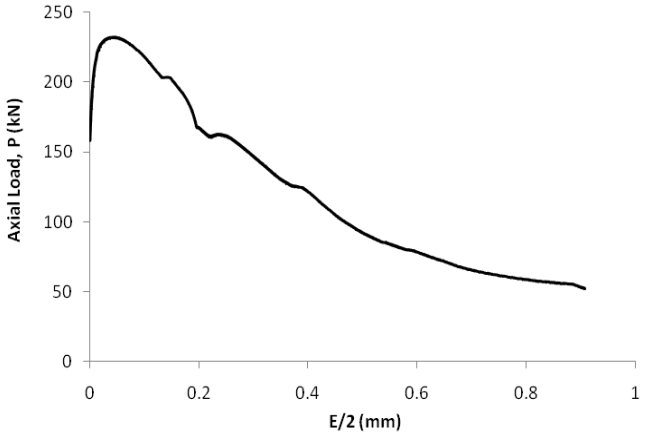

Figure 3.190: Axial load - E/2 response of Test11-50

Figure 3.191 illustrates the load and wedge expansion. It shows at peak load, wedge expansion V_{wp} is 0.04mm. This value is the same with the total lateral expansion of one single wedge at peak load, $E_p/2$ and slip wedge at peak load S_{wp}.

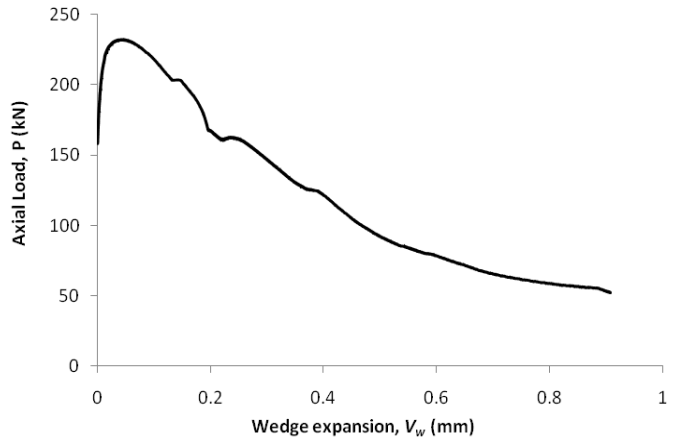

Figure 3.191: Axial load-wedge expansion response of Test11-50

Figure 3.192 shows the load and wedge expansion per 1 mm wedge thickness, while Figure 3.193 illustrates the stress wedge and wedge expansion of prism Test11-50.

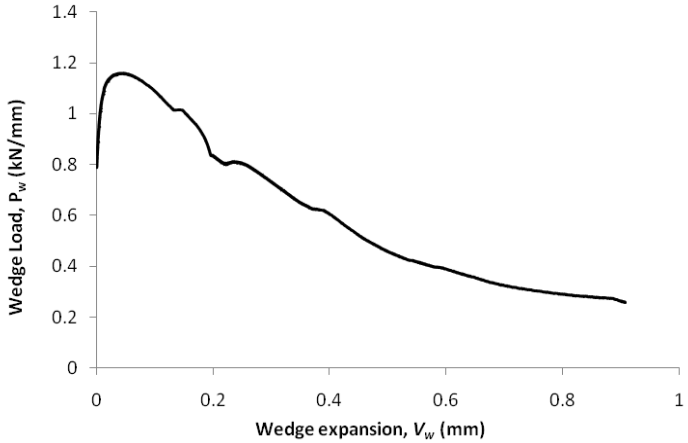

Figure 3.192: Load wedge-wedge expansion response of Test11-50

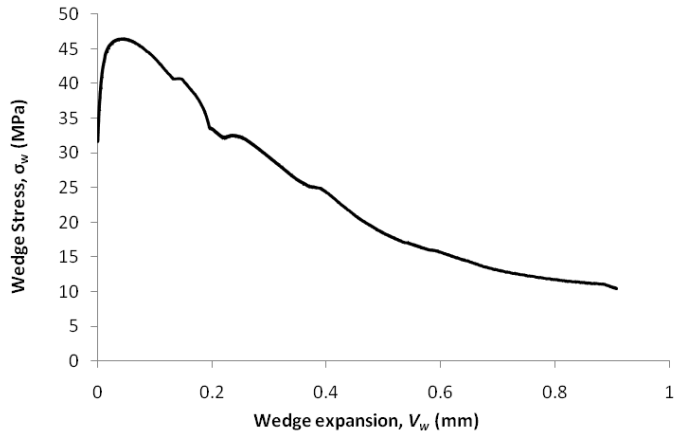

Figure 3.193: Stress wedge-wedge expansion response of Test11-50

After described the analysis of axial and lateral deformation of Test11-50, the next analysis is for Test13-50.

TEST13-50

The relationship between total axial load *L* that applied to concrete prism Test13-50 and the total axial contraction *C* is shown in Figure 3.194. The "settle down the position" of the specimen also occurred. Thus the *L*-*C* graph is required to refine. The result after correction is shown in Figure 3.195.

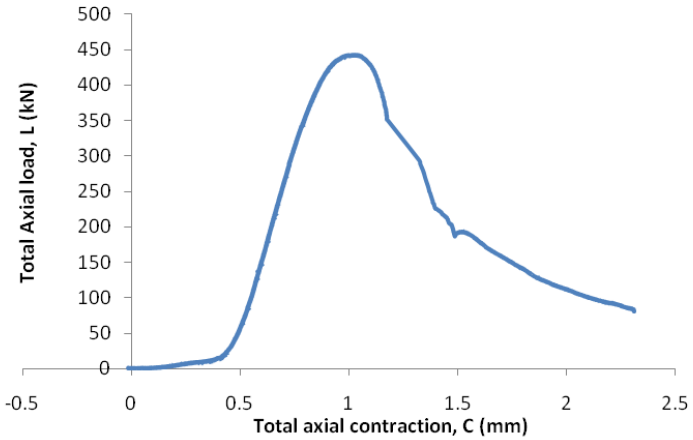

Figure 3.194: Total axial load-total axial contraction response of Test13-50

Figure 3.195 illustrates the *L*-*C* after correction. The C_p is 0.57mm when the peak of total axial load L_p reached of 442kN.

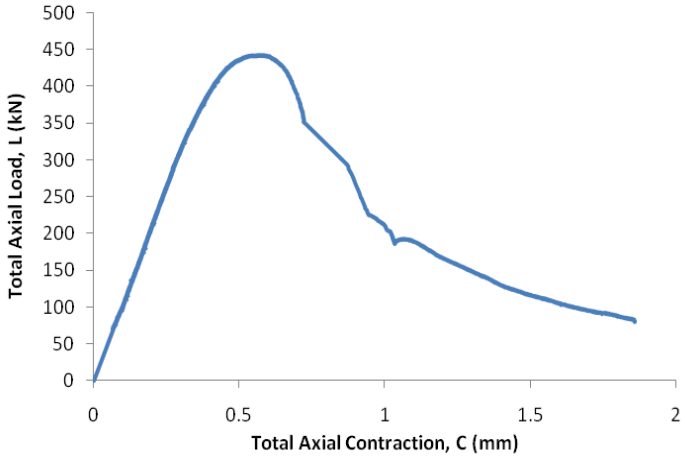

Figure 3.195: Total axial load-total axial contraction response of Test13-50 (new axis)

Figure 3.196 shows the relationship between axial load and total axial contraction over one wedge *P*-*C*/2. This graph is obtained by divide the graph in Figure 3.195 with 2. The graph indicates when the load for a single wedge approximately 132kN corresponds to *C*/2 is 0.13; micro-cracking starts to develop. Before this point elastic contraction occurred. The prism reaches the peak load P_p of 221kN at C_p/2 approximately 0.28mm.

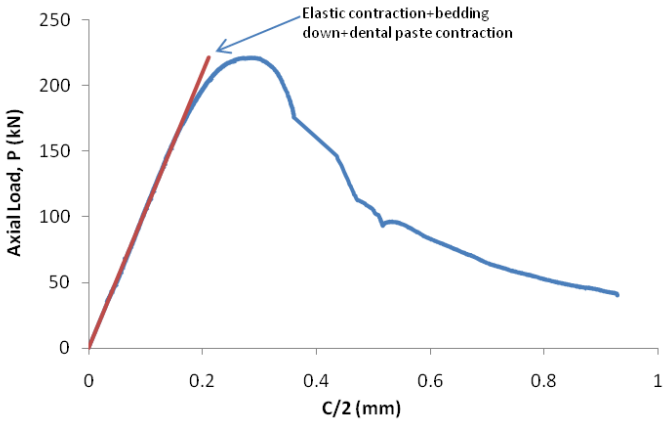

Figure 3.196: Axial load – C/2 response of Test13-50

The contraction due to micro-cracking is obtained by remove the elastic contraction from Figure 3.196. The result is shown in Figure 3.197. At peak load slip wedge S_{wp} is 0.07mm.

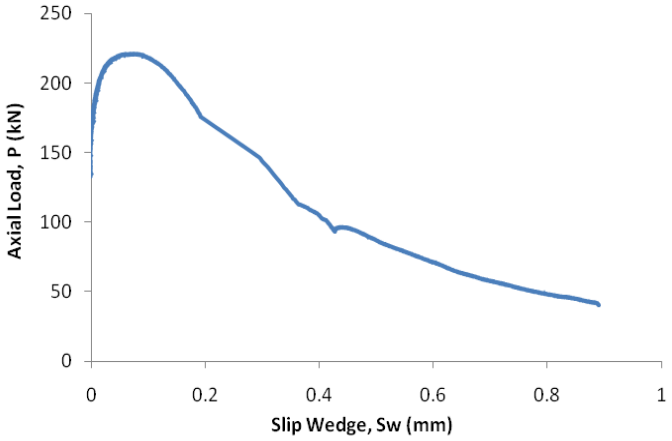

Figure 3.197: Axial load-slip wedge response of Test13-50

The load wedge is load per 1 mm wedge thickness P_w in Figure 3.198 is axial load P in Figure 3.197 divided by prism length S. Thus the pattern of the response is the same but different load. Figure 3.199 shows the relationship between the stress wedge and slip wedge, σ_w - S_w The peak stress wedge is 44MPa corresponds to slip wedge S_{wp} 0.07mm.

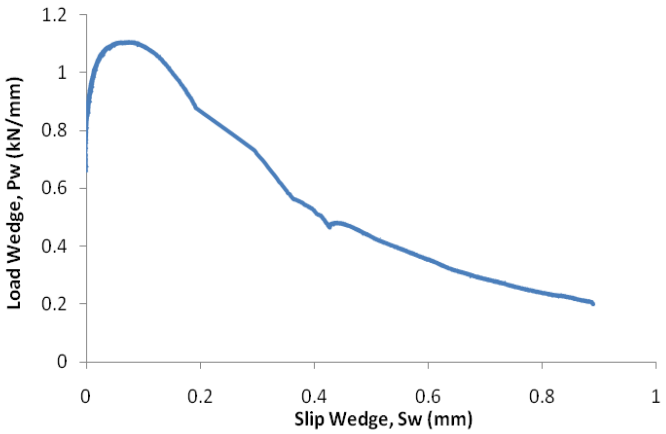

Figure 3.198: Load wedge-slip wedge response of Test13-50

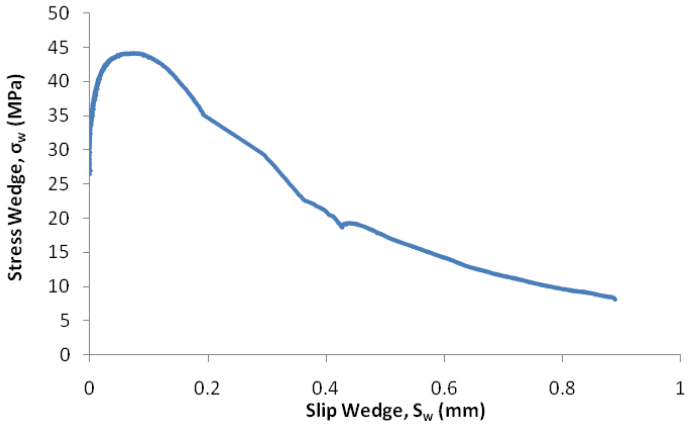

Figure 3.199: Axial stress - slip wedge response of Test13-50

The next explanation is about lateral deformation. Figure 3.200 shows the total axial load *L* and total lateral expansion *E* of Test13-50. This total lateral expansion is the algebraic sum of two values of LVDTs reading. The graph indicates the prism start to expand when the total axial load *L* is 370kN and then the prism expands slightly until reaches the peak load of 442kN. After that point, the prism expands significantly. The total lateral expansion at peak load E_p is approximately 0.3mm. This value is much larger that Test11-50 that is only 0.09mm.

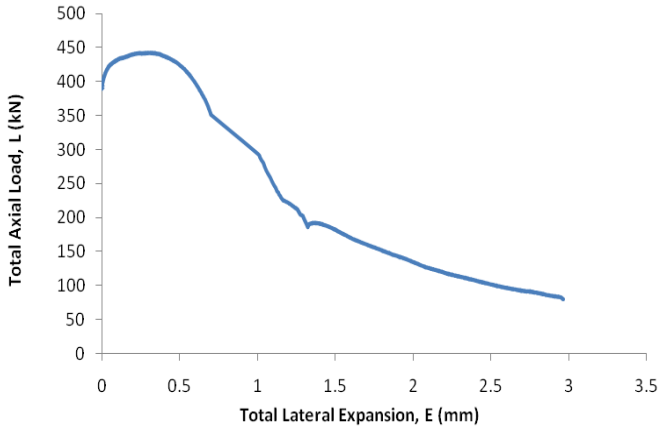

Figure 3.200: Total axial load-total lateral expansion response of Test13-50

Figure 3.201 shows the axial load and wedge expansion over one single wedge of Test13-50. This *graph* is the *L-E* response in Figure 3.200 divided by 2. In analysis one single wedge, the wedge expands when the axial load of one wedge *P* reaches185kN

that is almost 84% of peak load P_p. This means that there is no deformation before 84% P_p. The total lateral expansion of one single wedge at peak load $E_p/2$ is approximately 0.15mm.

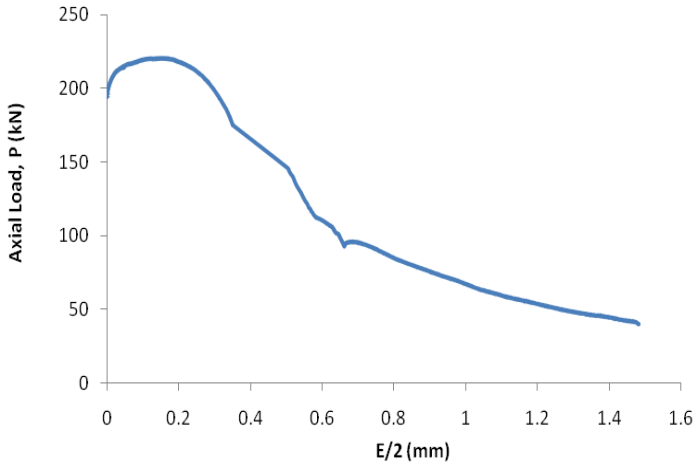

Figure 3.201: Axial load - E/2 response of Test13-50

The graph in Figure 3.202 indicates that the deformation due to micro-cracking or wedge expansion start to develop when load over one wedge P is 185kN that is approximately 85% P_p. The peak of axial load P_p is 221kN and wedge expansion at peak load V_{wp} is approximately 0.15mm.

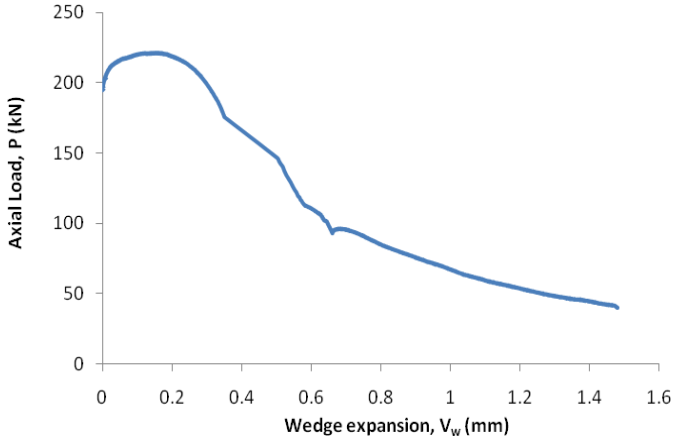

Figure 3.202: Axial load-wedge expansion response of Test13-50

Figure 3.203 shows the relationship between load and expansion per millimeter thickness of the wedge. P_w is P in Figure 3.202 divided by prism length S. S for Test13-

50 is 200mm. Figure 3.204 shows the relationship stress wedge and wedge expansion of Test13-50. The peak stress wedge is 44MPa corresponds to wedge expansion V_{wp} 0.15mm.

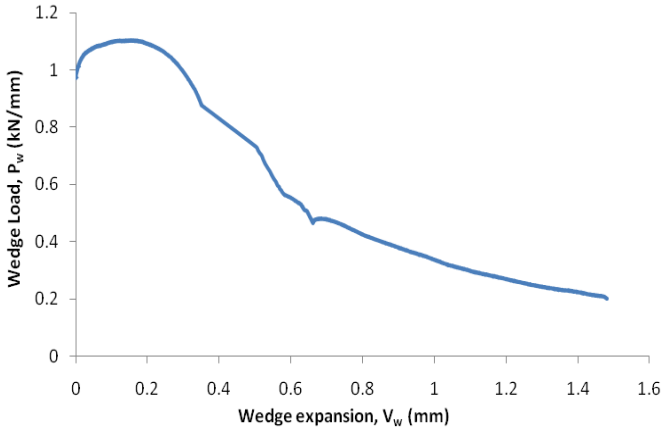

Figure 3.203: Load wedge-wedge expansion response of Test13-50

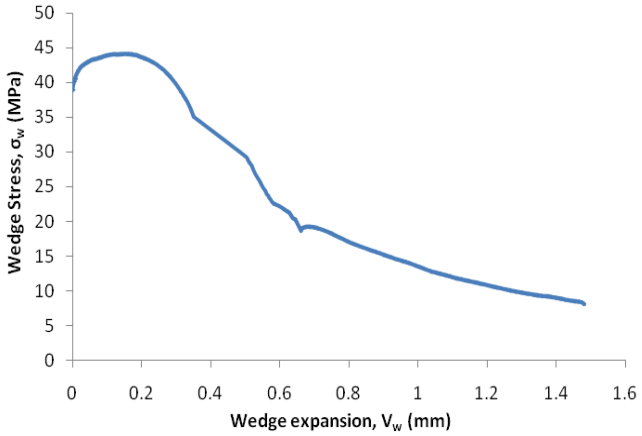

Figure 3.204: Stress wedge-wedge expansion response of Test13-50

The parameters of concrete prisms Test11-50 and Test13-50 such as L_p, P_p, P_{wp}, σ_{wp}, C_p, $C_p/2$, S_{wp}, E_p, $E_p/2$, and V_{wp} and the average values of those parameters are listed in Table 3.8.

The important parameters of Test-50 are discussed in detail below and explained graphically in Section 3.4.3 for axial deformation and Section 3.4.4 for lateral deformation.

Table 3.8: The important parameters of prism Test-50 based on individual graph

Prism	L_p (kN)	P_p (kN)	P_{wp} (kN/mm)	σ_{wp} (MPa)	C_p (mm)	$C_p/2$ (mm)	S_{wp} (mm)	E_p (mm)	$E_p/2$ (mm)	V_{wp} (mm)
1	2	3	4	5	6	7	8	10	11	12
TEST11-50	464	232	1.16	46	0.45	0.22	0.04	0.09	0.04	0.04
TEST13-50	442	221	1.10	44	0.57	0.28	0.07	0.30	0.15	0.15
AVERAGE	453	226	1.13	45	0.51	0.25	0.06	0.20	0.10	0.10

Table 3.8 compares the parameters between Test11-50 and Test13-50. The table shows there is a small scatter on the peaks values of total axial load L_p, axial load per one single wedge P_p, the load wedge P_{wp}, the stress wedge σ_{wp}, the total axial contraction C_p, the total axial contraction of one single wedge $C_p/2$, and the slip wedge at peak load S_{wp}. While a big scatter the peak values of total lateral expansion E_p, total lateral expansion of one single wedge $E_p/2$, and wedge expansion V_{wp}. This indicates that a big scatter occurs on lateral deformation.

After described the individual graph of all prisms and compared the all parameters on the same size of prism. The next section compare the results test graphically all prisms on the same size and then compare to other size.

3.4.3 Comparison of Axial Deformation

After analyzing the individual results of all concrete prism tests in both axial and lateral deformations, in this section all analysis of test results in one size are plotted together in order to evaluate the experiment scatter of the results. Then the average curve of every size is determined and compared with other sizes. More details are described below.

3.4.3.1 Total Axial Load – Total Axial Contraction Relationship

The first part of comparison the results is the relationship between the total axial load and the total axial contraction. Figure 3.205 illustrates the total axial load L and the total axial contraction C responses of Test-125. It can be quickly observed that every

concrete prism in Test-125 has similar pattern of *L*-*C* response. The total axial contraction increased gradually until the peak of total axial load L_p reached and followed by decreasing the total axial load *L* with an increase of the total axial contraction *C*. The total axial contraction at the peak total axial loads of all concrete prisms in Test-125 is almost same. The average of L_p is 2442kN and the average of C_p is 1.06 (see again Table 3.5).

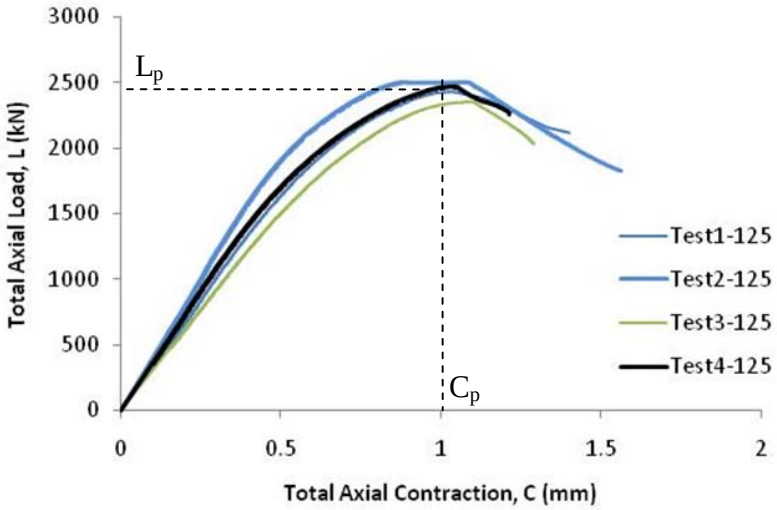

Figure 3.205: Total axial load-total axial contraction responses of prisms Test-125

Figure 3.206 illustrates relationship between the total axial load *L* and the total axial contraction *C* of Test-100. The graphs indicate that the responses of all concrete prisms in Test-100 are very quite similar on ascending and descending portions of the curve. The values of total axial contraction at peak load C_p is almost same for the three prisms in Test-100. The average of L_p is 1691kN and the average of C_p is 0.81mm (see again Table 3.6).

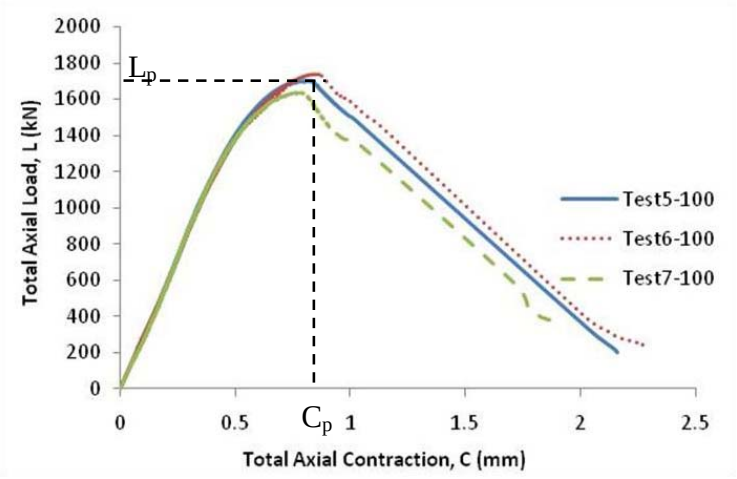

Figure 3.206: Total axial load-total axial contraction response of Test-100

The relationship of *L*-*C* of Test-75 is depicted in Figure 3.207. The pattern of the *L*-*C* response is the same with Test-125 and Test-100 which is described previously. The graphs indicate that all of the concrete prisms in Test-75 show the similar response. However, the small differences of the values of parameter the total axial contraction at peak load C_p for all prisms in Test-100 and the peak total axial load L_p for Test10-75 are occurred. The average of L_p is 1078kN and the average of C_p is 0.76mm (see again Table 3.7).

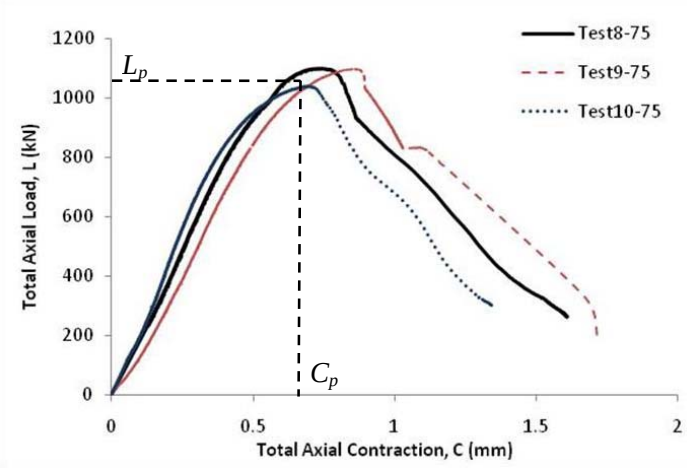

Figure 3.207: Total axial load-total axial contraction response of Test-75

Figure 3.208 shows the *L* - *C* responses of all prisms in Test-50. The two concrete prisms show the similar pattern. However the small scatter occurred in

descending portion of the *L*-*C* response. The small difference of the peak total axial load L_p and total axial contraction at peak load C_p also happened (see again Table 3.8). The average of L_p is 453kN and the average of C_p is 0.51mm.

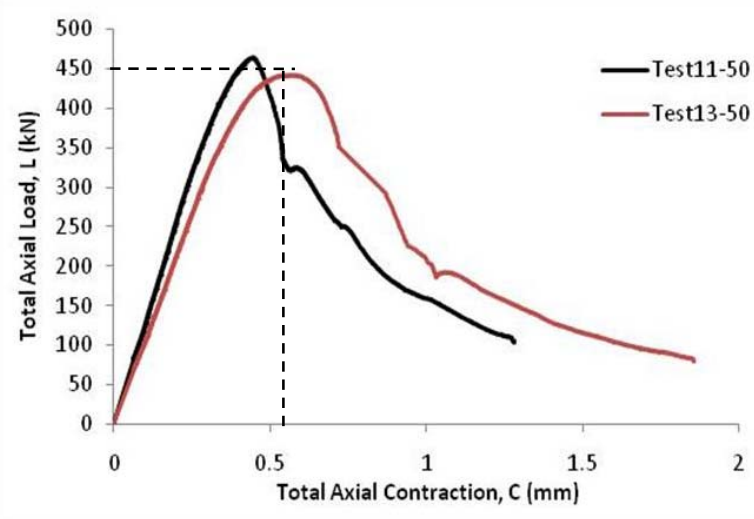

Figure 3.208: Total axial load-total axial contraction response of Test-50

The average curve of every size is required in order to evaluate the size effect on this result. The average curve is obtained by making the same interval of total axial contraction such as 0.0001 of all curves (from Figure 3.205 to Figure 3.208). Then at every size of prism, the average of *L* for a given *C* is calculated. For example to determine the average curve of Test-125. The average of total axial load *L* is $(L_1 + L_2 + L_3 + L_4)/4$ where L_1, L_2, L_3, and L_4 are the total axial load of prism Test1-125, Test2-125, Test3-125, Test4-125 respectively for a given total axial contraction *C*. Then calculate the average curve by using the same method for other sizes of prism.

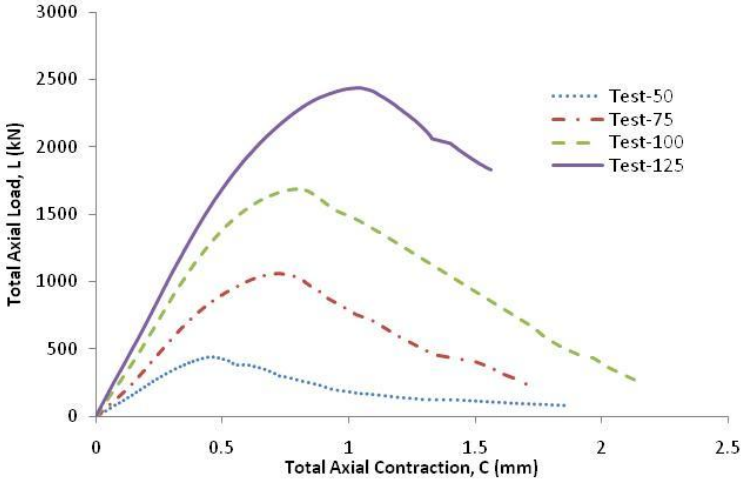

Figure 3.209: The average of total axial load-total axial contraction graph

The result of the average curve of *L*-*C* response is depicted in Figure 3.209. It can be seen that total axial contraction at peak stress C_p increase when size of prisms increase. Bigger prism has steeper curve than smaller prism. It means that axial deformation is influenced by specimen size.

The peak of total axial load L_p corresponding to total axial contraction C_p for average graph of all sizes is listed in Table 3.9. The total axial contraction *C* at failure varies between 1.6mm to 2.2mm.

3.4.3.2 Axial load – Total Axial Contraction of a Wedge

The second part of the comparison is the relationship in one single wedge between axial load and total axial contraction. The *P*-*C*/2 graphs have the same pattern with *L*-*C* graphs because *P*-*C*/2 graphs are *L*-*C* graphs divided by 2 because The *L*-*C* is the response of load and total axial contraction of the whole prism in terms of two wedges while the *P*-*C*/2 is the response of load and total axial contraction over one single wedge.

Figure 3.210 illustrates the relationship of *P*-*C*/2 of all experiment tests in prism Test-125. The average of P_p is 1221kN and the average of $C_p/2$ is 0.53mm.

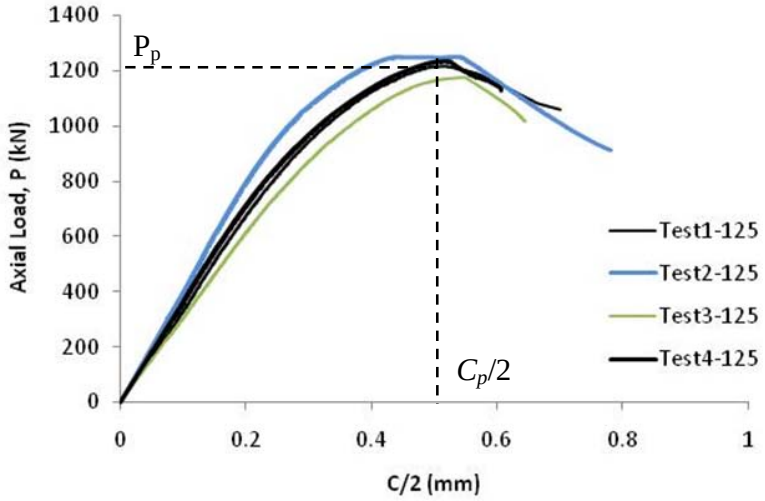

Figure 3.210: Axial load-C/2 response of Test-125

Figure 3.211 shows *P*-*C*/2 response of all prisms in Test-100. The average of P_p is 846kN and the average of $C_p/2$ is 0.41mm.

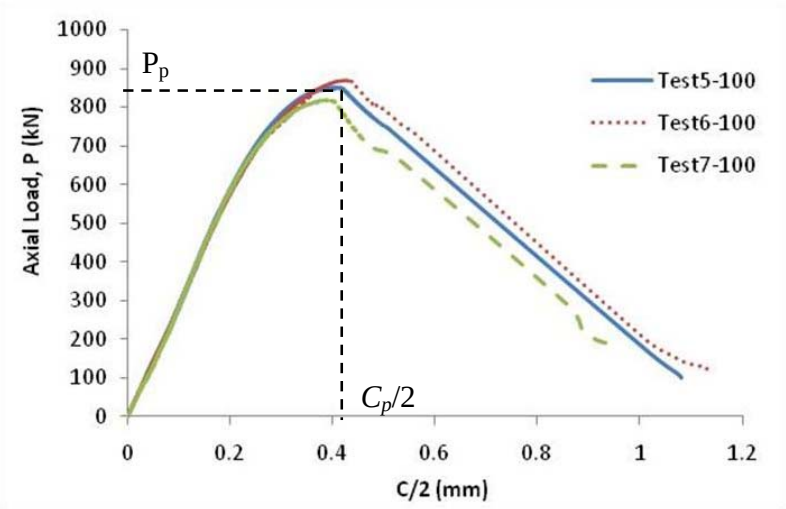

Figure 3.211: Axial load-C/2 response of Test-100

The relationship of *P*-*C*/2 of all prisms in Test-75 is depicted in Figure 3.212. The average of P_p is 539kN and the average of $C_p/2$ is 0.38mm.

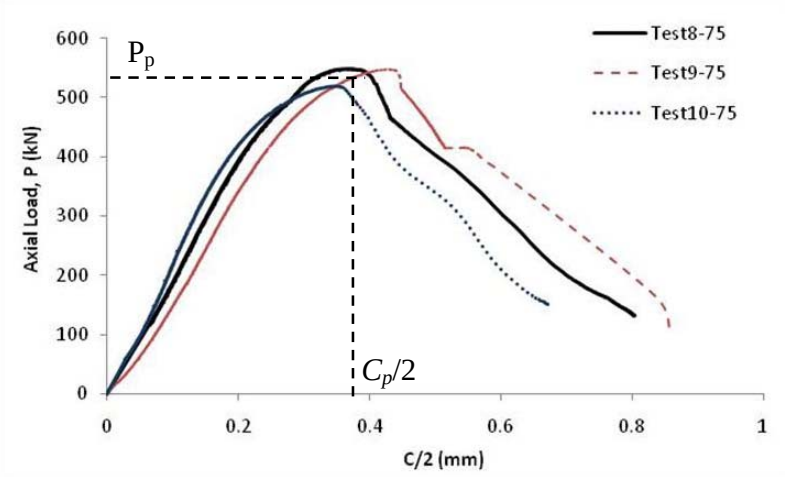

Figure 3.212: Axial load-C/2 response of Test-75

The relationship of axial load and total axial contraction over one single wedge *P*-*C*/2 of all prisms in Test-50 is illustrated in Figure 3.213. The average of P_p is 226kN and the average of $C_p/2$ is 0.25mm.

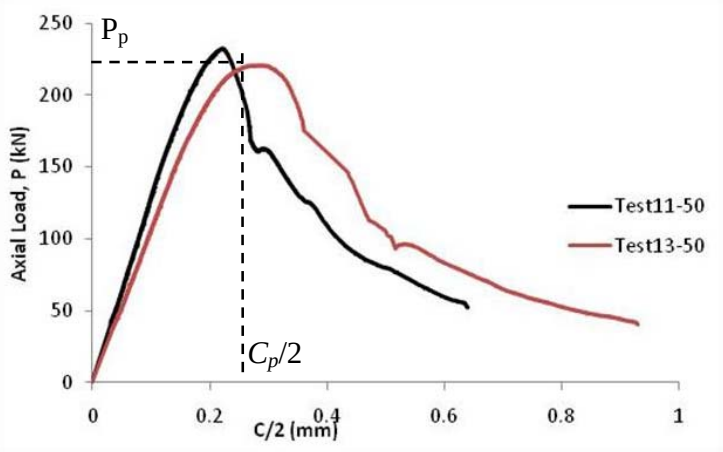

Figure 3.213: Axial load-C/2 response of Test-50

The average curve of *P*-*C*/2 responses of every size of prism is quantified by the same method as was used to determine the average curve of *L*-*C* responses. Figure 3.214 shows the average graphs of every size. First the same interval of *C*/2 is determined for all graphs in Figure 3.210 to Figure 3.213. Then the average of *P* is calculated for a given C/2. For instance quantify the average of *P*-*C*/2 graph of Test-125. The average of P is $(P_1 + P_2 + P_3 + P_4)/4$ where P_1, P_2, P_3, and P_4 are the axial load for one wedge of

Test1-125, Test2-125, Test3-125, Test4-125 respectively for a given *C/2*. The same method is used to others size test and plotted in one graph.

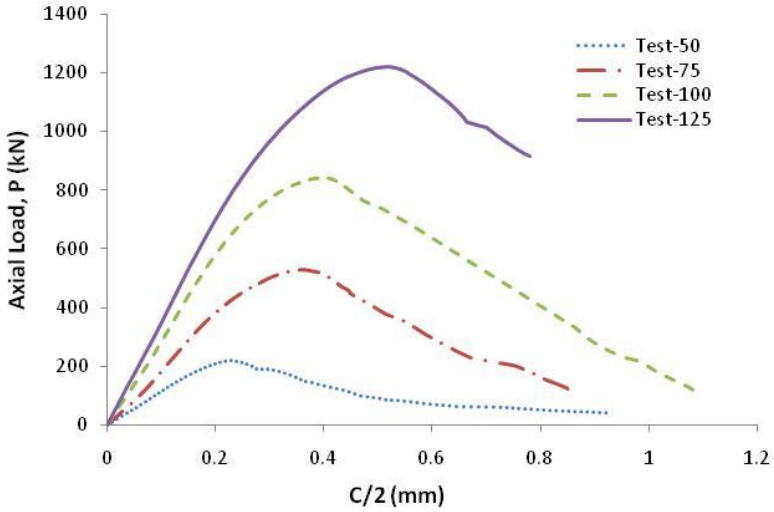

Figure 3.214: The average of axial load-C/2 graph

The behaviour of *P*-*C*/2 response is the same with *L*-*C* response. The total axial contraction of one wedge at peak load, $C_p/2$ increases with an increase of the size of prism. The axial deformation is affected by the specimen size.

The peak of axial load P_p corresponding to total axial contraction over a single wedge $C_p/2$ for average graph of all sizes is listed in Table 3.9. These parameters are obtained from the average curve.

3.4.3.3 Axial Load – Slip of Wedge Relationship

The slip wedge S_w of the concrete prisms is determined by subtracting the elastic contraction from the total axial contraction over one wedge *C*/2 (see again Figure 3.64). The relationship between axial load *P* and slip wedge S_w of Test-125 to Test-50 are depicted in Figure 3.215 to Figure 3.217 respectively.

Figure 3.215 illustrates the axial load *P* and the slip wedge S_w responses of Test-125. The graphs indicate that every concrete prism in Test-125 has similar pattern of *P*-S_w response. The value of the axial load *P* when the micro-cracking starts to develop for all prisms varies in a narrow range between 707kN to 752kN. The slip wedge at the peak axial loads S_{wp} of concrete prisms Test1-125, Test3-125, and Test4-125 is almost the

same but small scatter occurred on Test2-125. It can be seen in Figure 3.215 that Test4-125 has plateau prior to peak load. The average of P_p is 1221kN and the average of S_{wp} is 0.17 (see again Table 3.5).

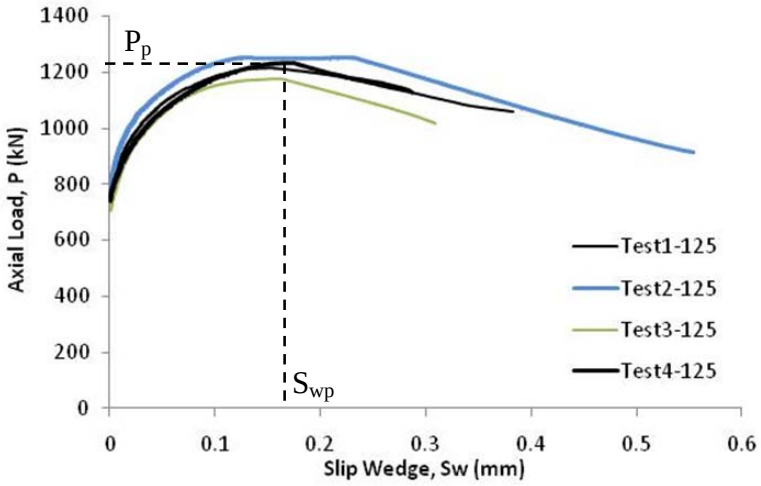

Figure 3.215: Axial load-slip wedge response of Test-125

Figure 3.216 illustrates relationship between the axial load P and the slip wedge S_w of Test-100. The graphs indicate that the responses of all concrete prisms in Test-100 are very similar. The values of slip wedge at peak load S_{wp} is almost same for the three prisms in Test-100. The average of P_p is 846kN and the average of S_{wp} is 0.12mm (see again Table 3.6)

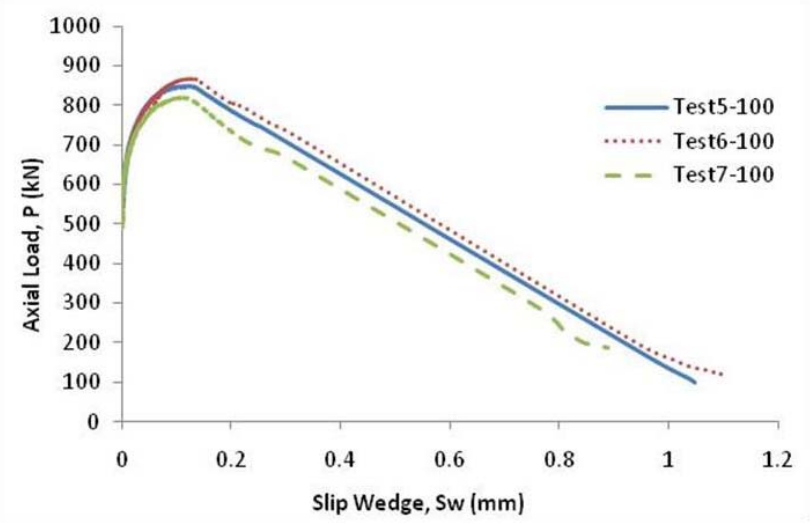

Figure 3.216: Axial load-slip wedge response of Test-100

The relationship of P- S_w of Test-75 is depicted in Figure 3.217.The graphs indicate the similar response all of the concrete prisms in Test-75. The values of slip wedge at peak load S_{wp} for all prisms in Test-75 are quite the same that is between 0.09mm to 0.11mm while a scatter occurred on the parameter of the total axial contraction at peak load C_p (that is between 0.69mm- 0.86mm) and $C_p/2$ (that is between 0.34mm-0.43mm) as described in Section 3.4.3.1 and 3.4.3.2. This means that the scatter on L-C response can be reduced by removing the elastic contraction. The average of P_p is 539kN and the average of S_{wp} is 0.11mm (see again Table 3.7).

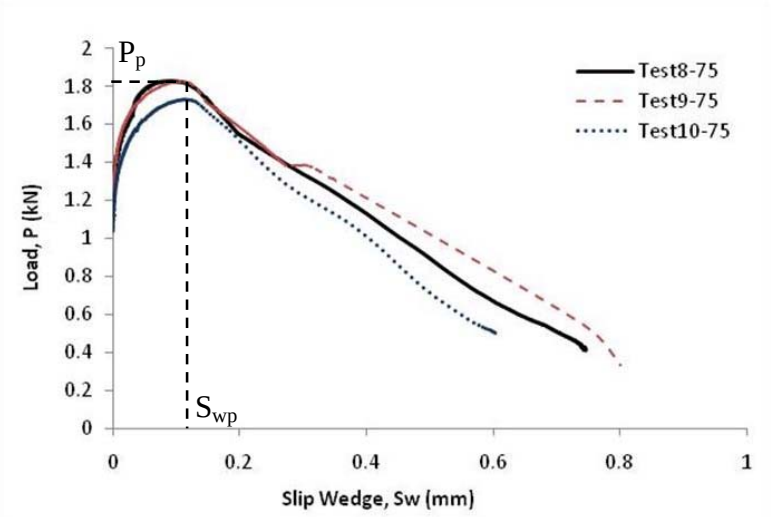

Figure 3.217: Axial load-slip wedge response of Test-75

Figure 3.218 shows the P_p- S_w responses of two prisms in Test-50. The two concrete prisms show the similar pattern. However the small scatter occurred in descending branch of the P_p- S_w response. The small difference of slip wedge at peak load S_{wp} occurred; Test11-50 is 0.04mm and Test13-50 is 0.07mm. The average of P_p is 226kN and the average of S_{wp} is 0.06mm (see again Table 3.8).

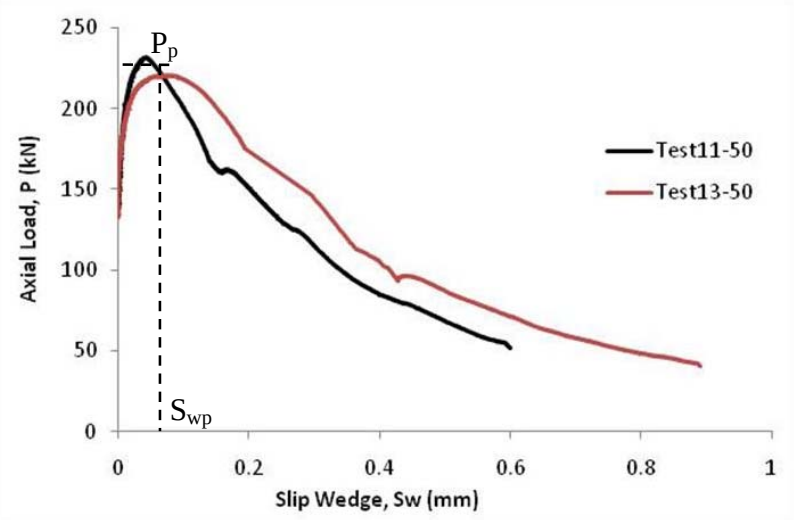

Figure 3.218: Axial load-slip wedge response of Test-50

The average graph of axial load P and slip wedge S_w responses all sizes is determined by using the same method as was used for L-C response previously and compared to others sizes. The average graphs are shown in Figure 3.219. All size shows the same pattern. The deformation due to micro-cracking or the slip wedge S_w started to develop when the loads over one wedge P are 136kN, 322kN, 506kN, and 732kN for Test-50, Test-75, Test-100, and Test-125 respectively. Before this point, there is no slip wedge, only elastic contraction occurred on a wedge. The micro-cracking not occur at lower load for bigger size of prism.

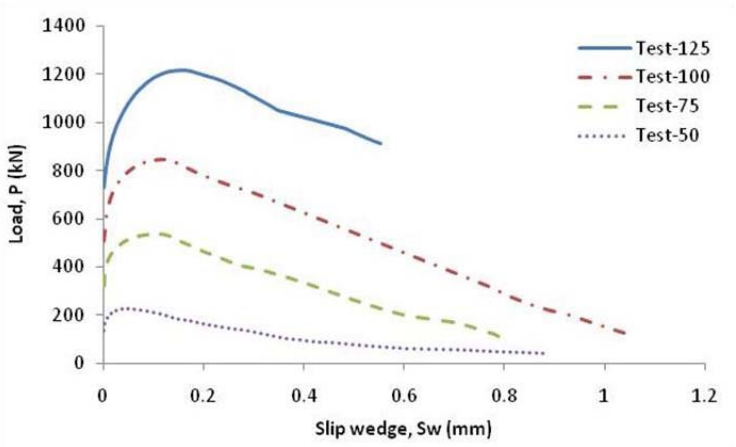

Figure 3.219: The average of axial load-slip wedge graph

The slip wedges at peak load S_{wp} are 0.16mm, 0,12mm, 0.11mm and 0.05mm for Test-125, Test-100, Test-75, and Test-50 respectively. The slip wedges at peak load S_{wp} increases with an increase the size of prism.

The parameter of peak axial load P_p and slip wedge at peak load S_{wp} based on the average curve above are listed in Table 3.9.

3.4.3.4 Load Wedge – Slip of Wedge Relationship

The load wedge P_w is the load per 1 millimeter wedge thickness which is obtained from axial load P divided by the length of concrete prism S. Hence the P_w - S_w graphs have the same pattern with P-S_w graphs.

Figure 3.220 illustrates the relationship of P_w - S_w of all experiment tests in prism Test-125. The average of P_w is 2.44kN/mm and the average of S_{wp} is 0.53mm.

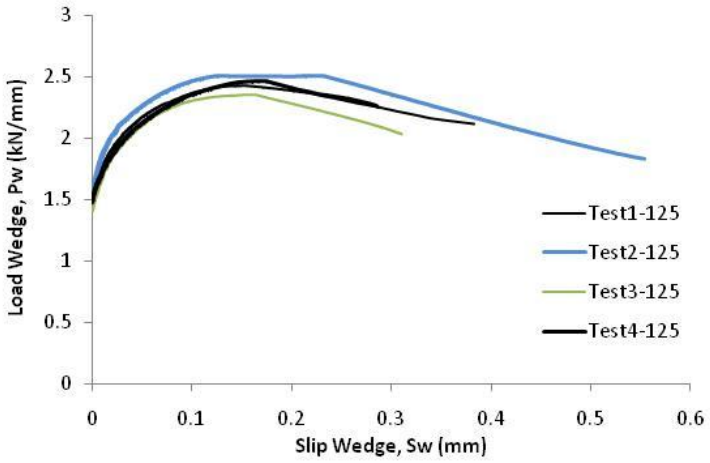

Figure 3.220: Load wedge-slip wedge response of Test-125

Figure 3.221 shows P_w - S_w response of all prisms in Test-100. The average of P_w is 2.11kN/mm and the average of S_{wp} is 0.12mm.

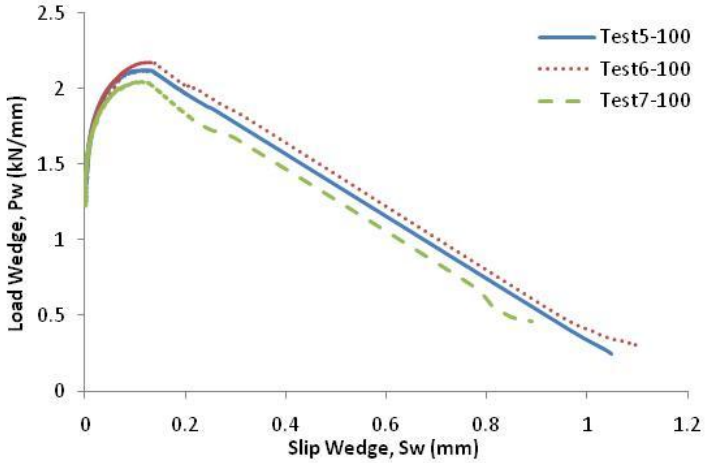

Figure 3.221: Load wedge-slip wedge response of Test-100

The relationship of P_w - S_w of all prisms in Test-75 is depicted in Figure 3.222. The average of P_w is 1.80kN/mm and the average of S_{wp} is 0.11mm.

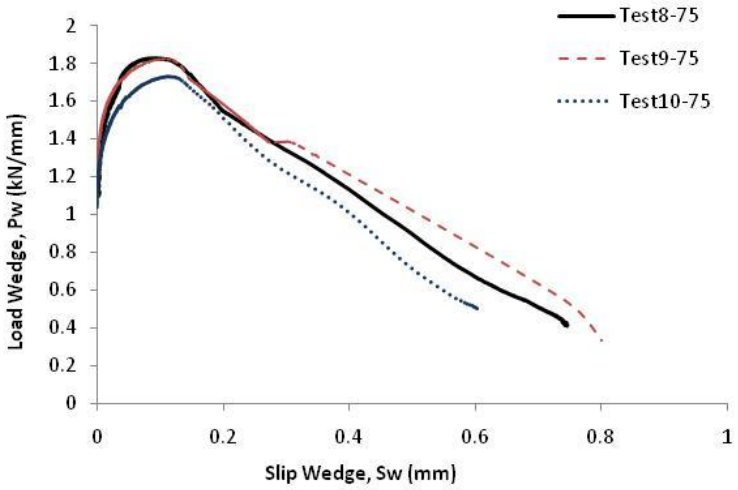

Figure 3.222: Load wedge-slip wedge response of Test-75

The relationship of load per 1 mm wedge thickness and slip wedge P_w - S_w of two prisms in Test-50 is illustrated in Figure 3.223. The average of P_w is 1.13kN/mm and the average of S_{wp} is 0.06mm.

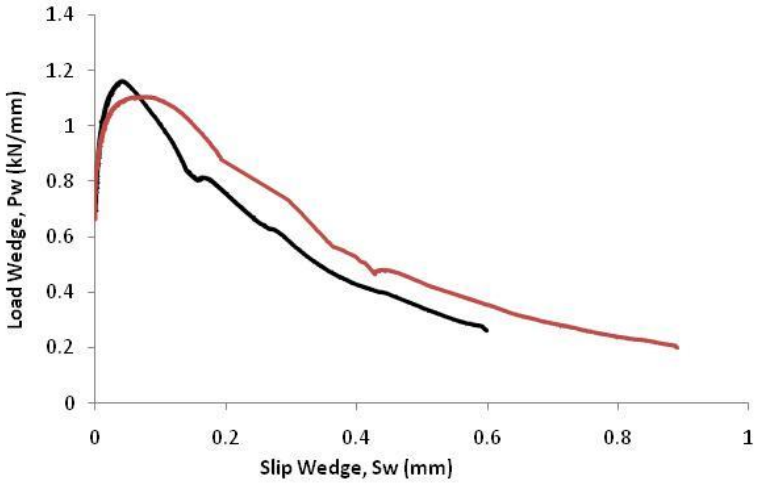

Figure 3.223: Load wedge-slip wedge response of Test-50

The average curves of P_w - S_w response of Test-50, Test-75, Test-100 and Test-125 is determined first then compared to others sizes. To quantify the average curve, the same method is used as was used to determine the average curve of *L-C* earlier in this section. The comparison of the average value of those graphs is depicted in Figure 3.224.

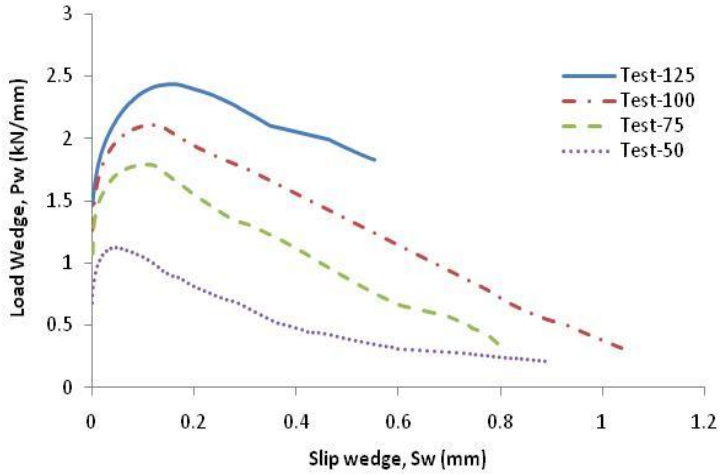

Figure 3.224: The average of load wedge-slip wedge graph

The loads wedge were 0.7kN/mm, 1.1kN/mm, 1.3kN/mm and 1.5kN/mm when the micro-crack begin to occur on the specimens Test-50, Test-75, Test-100 and Test-125 respectively. The pattern of the curves is similar. The slip wedge increases slightly

up to peak load wedge, and increases significantly after the peak load until the prism failed. The peak of wedge load is represented by P_{wp} of Test-125 is 2.44mm, Test-100 is 2.11mm, Test-75 is 1.79mm and Test-50 is 1.12mm as are listed in Table 3.9.

3.4.3.5 Stress Wedge – Slip Wedge Relationship

The individual stress wedge and slip wedge relationship is plotted in one graph and can be seen in Figure 3.225 to Figure 3.228. Figure 3.225 illustrates the relationship between stress wedge and slip wedge of Test-125. It can be seen that every concrete prism in Test-125 has similar pattern. The slip wedge increases as stress wedge increases until the peak stress wedge reached. The slip wedge still increases with a decrease of stress wedge. The slip of wedges of all prisms Test-125 starts to form when stress wedge between 23MPa-24MPa. The average of peak stress wedge σ_{wp} is 39MPa and the average of slip wedge at peak stress S_{wp} is 0.17mm (see again Table 3.5).

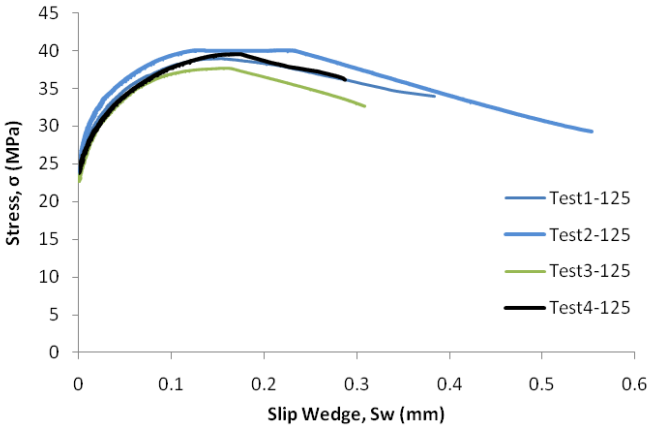

Figure 3.225: Stress wedge-slip wedge response of Test-125

Figure 3.226 illustrates the relationship between the stress wedge σ_w and slip wedge S_w of Test-100. The quite similar pattern of the responses is shown on all concrete prisms in Test-100. The slip wedges or the deformation due to the micro-cracking of all prism in Test-100 start to develop when the stress between 25MPa-26MPa. The peak wedge stress σ_{wp} and the slip wedge at peak stress S_{wp} of all prisms in Test-100 have quite the same values. The average of σ_{wp} is 42MPa and the average of S_{wp} is 0.12mm.

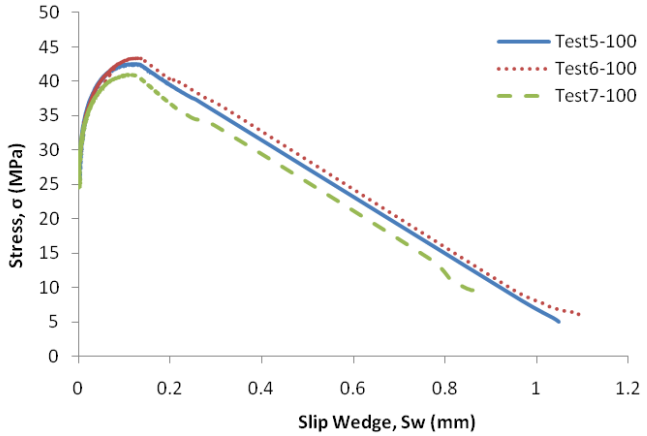

Figure 3.226: Stress wedge-slip wedge response of Test-100

The relationship of σ_w - S_w of Test-75 is depicted in Figure 3.227. The pattern of the σ_w - S_w response is the same with the others sizes test which were described previously. The graph illustrates all prisms in Test-75 show the similar response. However a small scatter occurred on descending branch and the small difference of the values of slip wedge at peak stress S_{wp} is occurred. As the stress reached between 28MPa to 29MPa, the slip wedge of the prisms start to develop. The average of σ_{wp} is 48MPa and the average of S_{wp} is 0.11mm (see again Table 3.7)

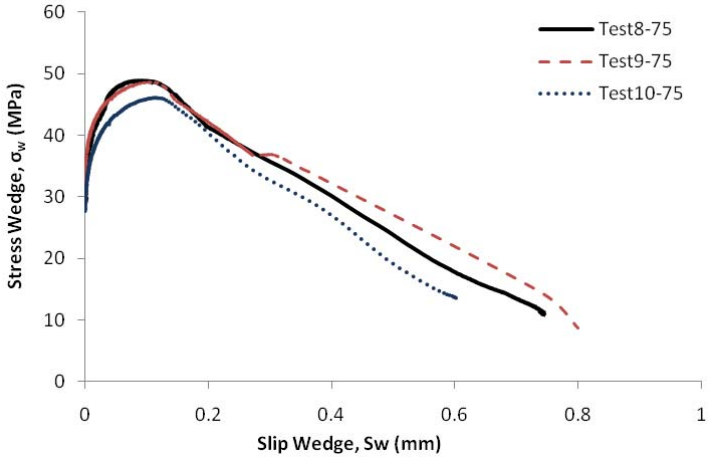

Figure 3.227: Stress wedge-slip wedge response of Test-75

The stress wedge σ_w and the slip wedge S_w responses of all prisms in Test-50 is depicted in Figure 3.228. The concrete prisms in this size show the similar pattern

response. However the small scatter occurred in descending branch of the σ_w - S_w response. The slip wedges start to form when the stress reaches between 27MPa to 28MPa for all concrete prism in Test-50. The average of peak stress wedge σ_{wp} is 45MPa and the average slip wedge at peak stress S_{wp} is 0.06mm (see again Table 3.8).

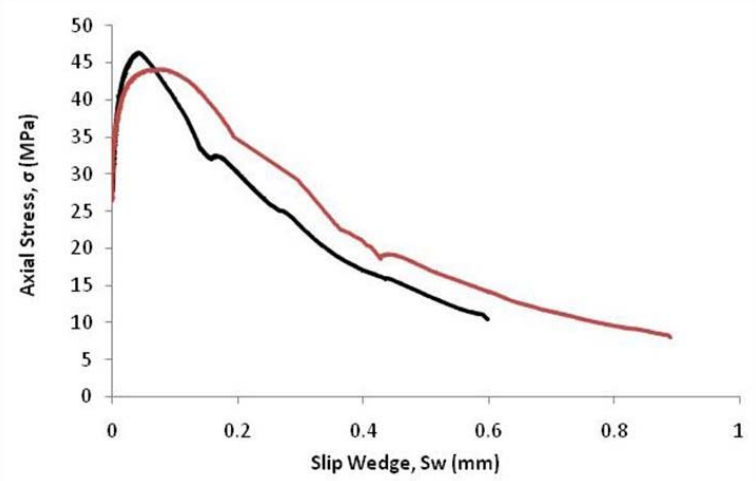

Figure 3.228: Stress wedge-slip wedge response of Test-50

The average curve of every size is required in order to evaluate the size effect on this result. The same method is used to determine the average curve as described previously. The same interval of slip wedge is determined such as 0.001 of all curves (from Figure 3.225 to Figure 3.228). Then the stress wedge is determined for a given slip wedge. For example to determine the average curve of Test-125. The average of stress σ is $(\sigma_1 + \sigma_2 + \sigma_3 + \sigma_4)/4$ where σ_1, σ_2, σ_3, and σ_4 are the stress of Test1-125, Test2-125, Test3-125, Test4-125 respectively for a given slip wedge S_w. Then do the same method for other sizes of prism. Figure 3.229 shows the average graphs of all sizes.

It can be seen that the smaller size of prism has higher peak stress of wedge σ_{wp} than bigger size of prism. It means that the peak stress of wedge increases as the size of prism decreases. Slip wedge corresponding to peak stress S_{wp} increases with an increase of prism size. However peak stress of Test-50 is lower than Test-75. Figure 3.229 indicates that the average of concrete stress of all prisms is 43MPa.

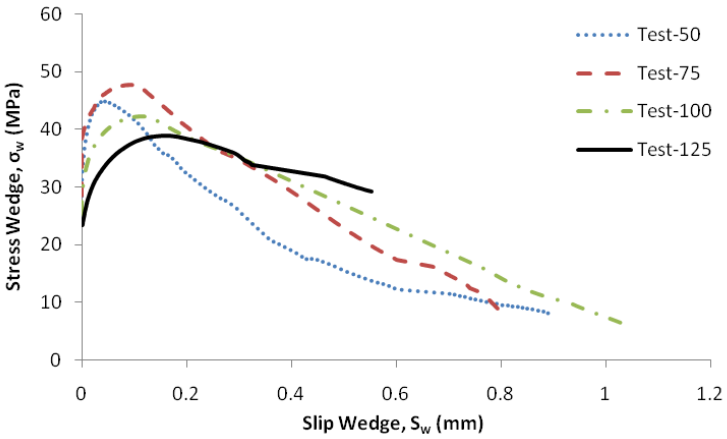

Figure 3.229: The average of stress wedge-slip wedge graph

The peak stress wedge σ_{wp} corresponding to slip wedge S_{wp} are listed in Table 3.9. These peak values are used to develop expression between wedge stress and wedge slip as described next in wedge analysis in Section 3.4.5. It should be noting that the parameters of the concrete prism in Table 3.9 are based on the average curve. More detail about the stress wedge and slip wedge responses is discussed in Section 3.4.5.

After analysed the comparison of axial deformation, the next section comparison in lateral deformation is analysed as describe in detail.

3.4.4 Comparison of Lateral Deformation

Step by step of the analysis to evaluate the test results in lateral deformation use the same method as was described previously in analysis the axial deformation.

3.4.4.1 Total Axial Load – Total Lateral Expansion Relationship

The relationship between the total axial load and the total lateral expansion of Test-125 is shown in Figure 3.230. The graph indicates that the curves of all specimens in Test-125 have similar pattern, no scatter on ascending region of the curve. However small scatter on descending region of the curve and the total lateral expansion at peak load E_p of Test3-125 and Test2-125 has a small difference. The average of total lateral expansion at peak load E_p is 1.09mm (see again Table 3.5)

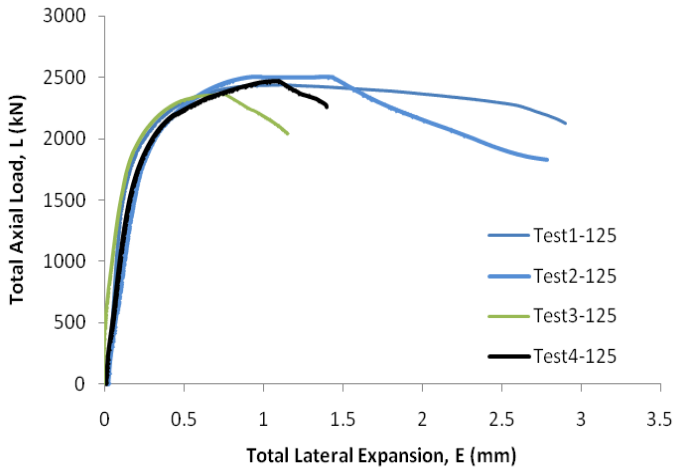

Figure 3.230: Total axial load-total lateral expansion response of Test-125

Figure 3.231 illustrates relationship between the total axial load L and the total lateral expansion E of Test-100. The graphs indicate that the responses of prisms in Test5-100 and Test7-100 are very quite similar. A small scatter occurred on Test6-100 as shown in a dot line in Figure 3.231. The total lateral expansion at peak load E_p of prisms in Test5-100 and Test6-100 is exactly the same 0.34mm but small difference for the prism Test7-100 that is 0.27mm. The average of total lateral expansion of Test-100 at peak load E_p is 0.32mm (see again Table 3.6).

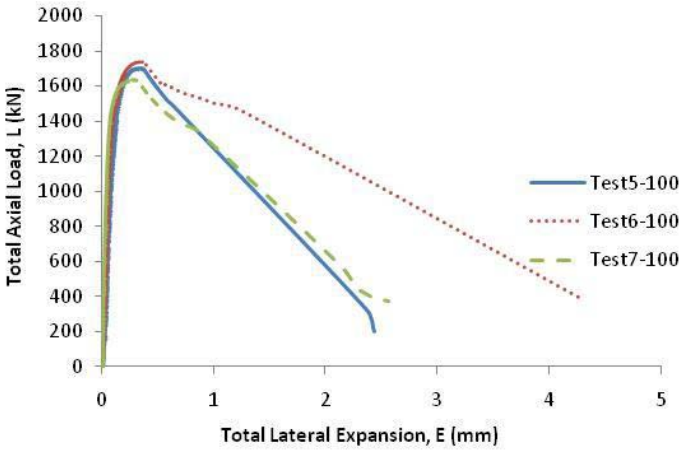

Figure 3.231: Total axial load-total lateral expansion response of Test-100

Figure 3.232 shows the relationship of *L-E* of Test-75. The graph illustrates the pattern of the *L-E* response is quite the same for all test prisms in Test-75, the total

lateral expansion at peak load E_p of all prisms is between 0.24mm and 0.25mm. However a scatter occurs on the peak of total axial load L_p of Test10-75 is 1,038kN as shown in a dot line in Figure 3.232. The average total lateral expansion at peak load E_p is 0.25mm.

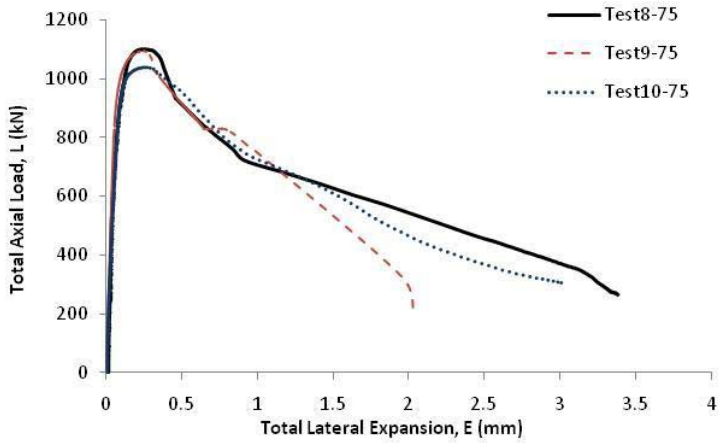

Figure 3.232: Total axial load-total lateral expansion response of Test-75

Figure 3.233 illustrates the relationship between total axial load and total lateral expansion of Test-50. The graph indicates that the two concrete prisms show the similar pattern however the scatter occurred. The small difference of the peak of the total axial load, Test11-50 464kN while Test13-50 442kN. A big scatter occurs on total axial contraction at peak load E_p, Test11-50 is 0.09mm and Test13-50 is 0.30mm (see again Table 3.8). The average of total lateral expansion at peak load E_p is 0.20mm.

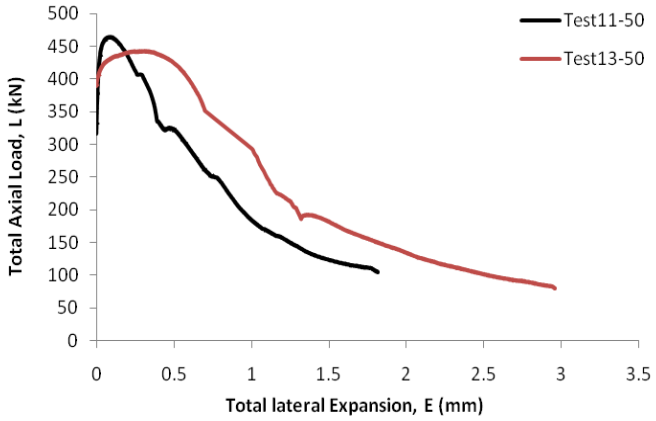

Figure 3.233: Total axial load-total lateral expansion response of Test-50

The average curve of every size is determined and compared as depicted in Figure 3.234. The average curve is obtained by using the same method as was used for another analysis previously. It can be seen that the slope of ascending branch of the curves is the same. Contrary to total axial load-total axial contraction *L*-*C* relationship where the slope of ascending branch depend on the prism size (Figure 3.209). It means that the ascending slope of the total axial load-the total lateral expansion response is not influenced by the size of prism.

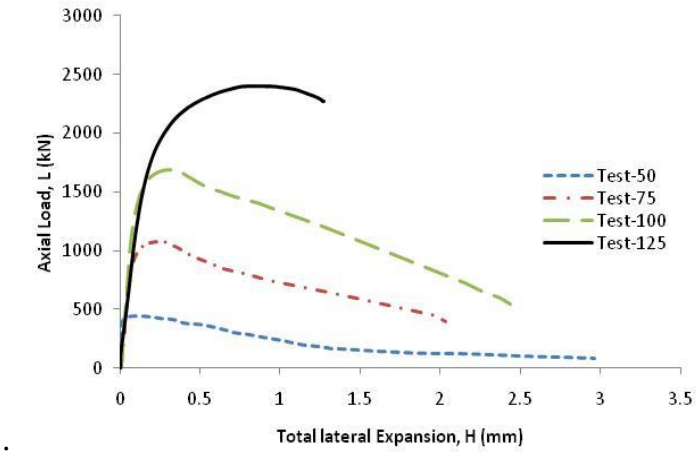

Figure 3.234: The average of total axial load-total lateral expansion graph

The peak of the total axial load L_p corresponding to total lateral expansion E_p of every size of prism is listed in Table 3.9. The next analysis is the response between load and lateral deformation on one single wedge.

3.4.4.2 Axial load – Total Lateral Expansion of a Wedge

Analysis over one wedge in lateral deformation that is relationship between load and total lateral expansion (*P*-*E*/2) is described. The next four figures illustrate the *P*-*E*/2 relationship of every size (Figure 3.235 to Figure 3.238). The *P*-*E*/2 graph has same pattern with *L*-*E* graph because *P*-*E*/2 graph is *L*-*E* graph divided by 2.

Figure 3.235 illustrates the relationship of *P*-*E*/2 of all experiment tests in prism Test-125. The average of total lateral expansion over one single wedge at peak load $E_p/2$ is 0.54mm.

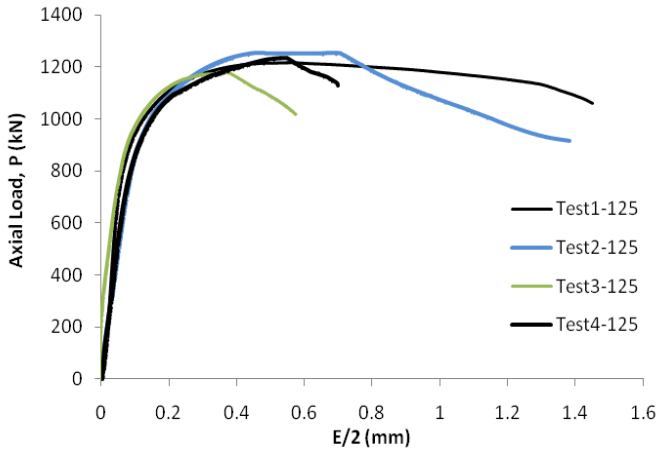

Figure 3.235: Axial load-E/2 response of Test-125

Figure 3.236 shows *P*-*E*/2 response of all prisms in Test-100. The average of total lateral expansion over one single wedge at peak load $E_p/2$ is 0.16mm.

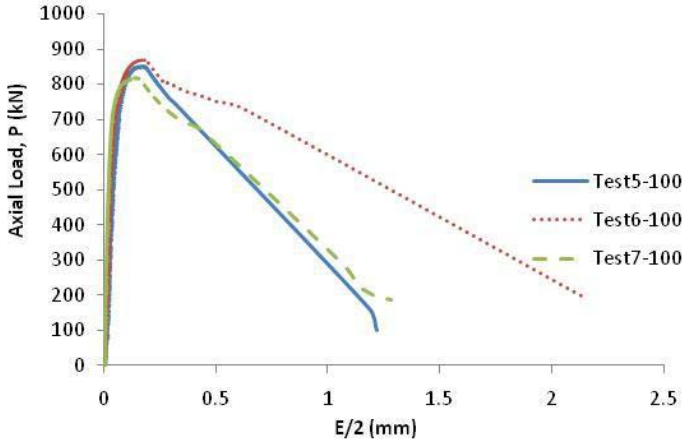

Figure 3.236: Axial load-E/2 response of Test-100

The relationship of *P*-*E*/2 of all prisms in Test-75 is depicted in Figure 3.237. The average of total lateral expansion over one single wedge at peak load $E_p/2$ is 0.13mm.

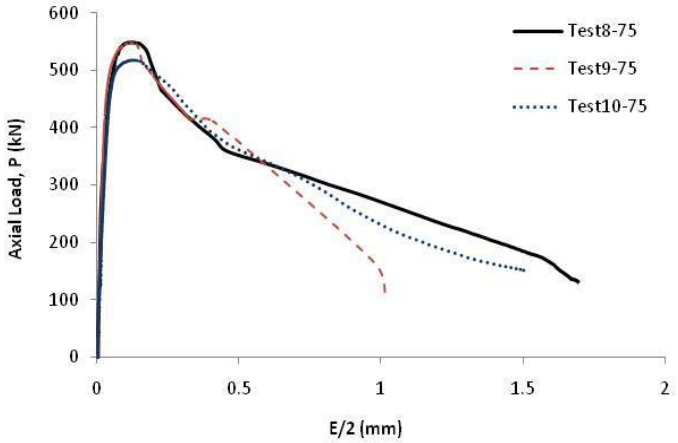

Figure 3.237: Axial load-E/2 response of Test-75

The relationship of *axial* load and total axial contraction over one single wedge *P*-*E*/2 of all prisms in Test-50 is illustrated in Figure 3.238. The average of total lateral expansion over one single wedge at peak load $E_p/2$ is 0.10mm.

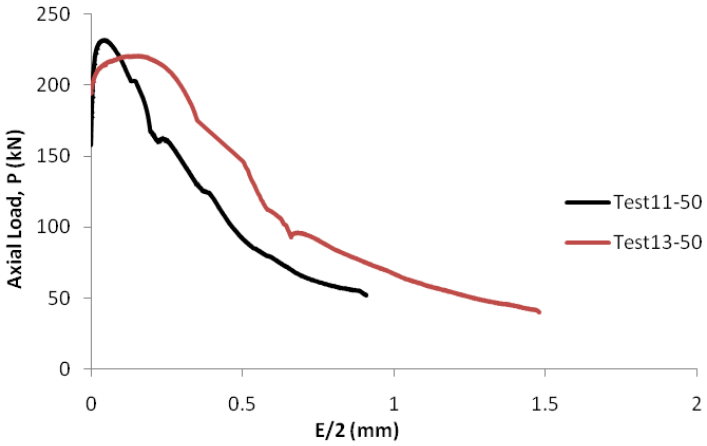

Figure 3.238: Axial load-E/2 response of Test-50

The same method was used to quantify the average graph. The average graphs of all sizes of prism are shown in Figure 3.239. The graph indicates that the pattern of *L*-*E*/2 responses is the same with the pattern of *L*-*E* responses as described previously. Total lateral expansion over one wedge at peak axial load P_p is represented by $E_p/2$. The graph indicates that the $E_p/2$ varies between 0.05mm to 0.42mm. These values are listed in Table 3.9.

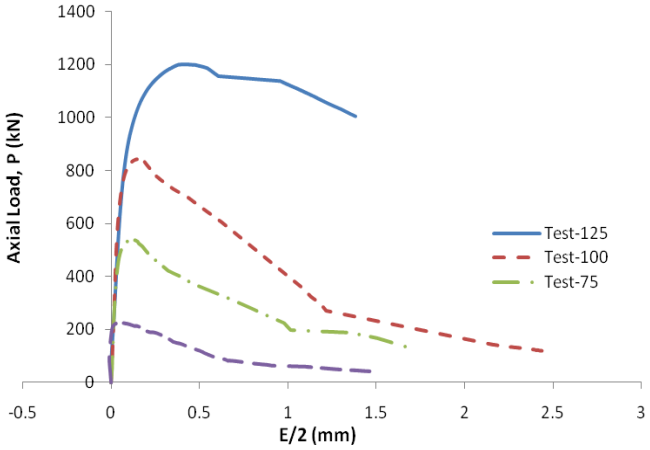

Figure 3.239: The average of axial load-E/2 graph

Figure 3.239 shows the slope of ascending branch of the curves is the same. It means that the ascending slope of the axial load-the total lateral expansion of one single wedge *P*-*C*/2 response is not affected by the size of prism

3.4.4.3 Axial Load – Wedge Expansion Relationship

In analysis over one wedge, total lateral expansion E is composed of wedge expansion that is represented by V_w and elastic expansion G as explained in the beginning of section 3.4 and illustrated in Figure 3.70.

The relationship between axial load P and wedge expansion V_w of individual test are plotted in the same size of prism as shown in Figure 3.240 to Figure 3.243.

Figure 3.240 illustrates the axial load P and the wedge expansion V_w responses of Test-125. The graph shows the responses are quite similar. The axial load when the micro-cracking starts to develop for all prisms is almost same. The small scatter occurred on wedge expansion at the peak axial loads V_{wp}. The average wedge expansion on peak load V_{wp} is 0.43mm. This average value is based on each individual graph in Test-125.

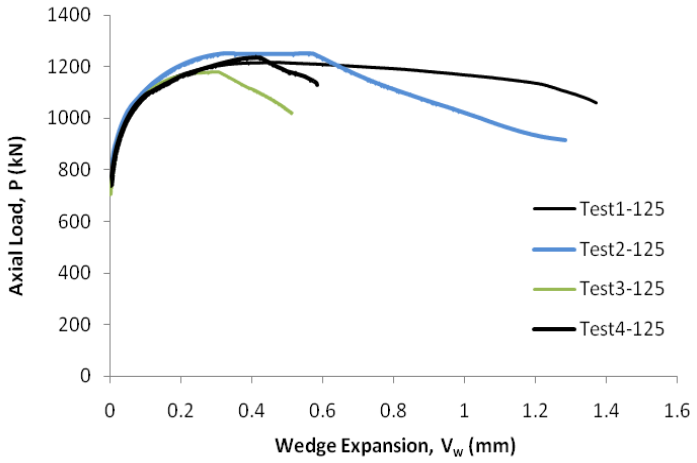

Figure 3.240: Axial load-wedge expansion response of Test-125

Figure 3.241 illustrates relationship between the axial load *P* and the wedge expansion V_w of Test-100. The graph indicates that the responses of prism Test5-100 and Test7-100 are very quite similar while small scatter occurred on Test6-100. The values of wedge expansion at peak load V_{wp} is almost same for the three prisms in Test-100. The average of wedge expansion at peak load V_{wp} is 0.11mm.

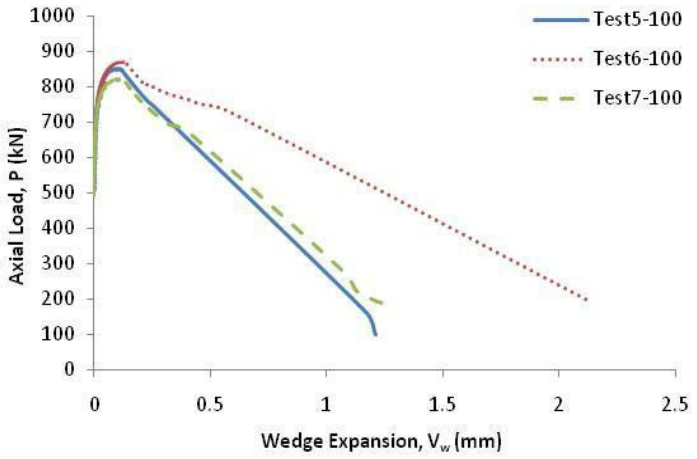

Figure 3.241: Axial load-wedge expansion response of Test-100

The relationship of *P*- V_w of Test-75 is depicted in Figure 3.242.The graphs indicate the similar response all of the concrete prisms in Test-75. The values of wedge expansion at peak load V_{wp} are quite same. The average of wedge expansion at peak load V_{wp} is 0.09mm.

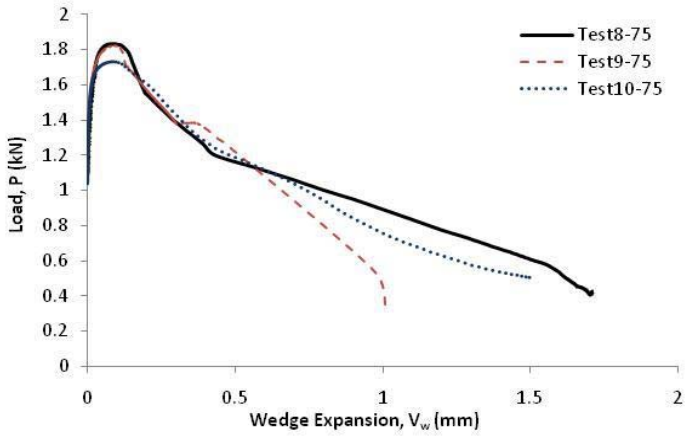

Figure 3.242: Axial load-wedge expansion response of Test-75

Figure 3.243 shows the P_p- V_w responses of Test-50. The graph indicates a scatter occurred on the P_p- V_w response. The wedge expansion on Test11-50 increases very slightly while on Test13-50 increase more significant as the load increases up to peak load. On descending branch, the wedge expansion on both prisms increases significantly as a decrease of the load. The wedge expansion at peak load V_{wp} on Test11-50 is 0.04mm and Test13-50 is 0.15mm. The average of these values is 0.10mm (see again Table 3.8).

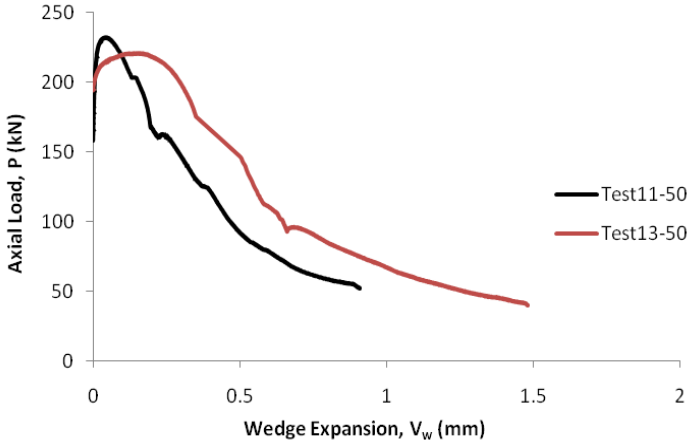

Figure 3.243: Axial load-wedge expansion response of Test-50

The average curve of those figures is determined and illustrated in Figure 3.244. The wedge expansion at peak axial load V_{wp} of each size is summarized in Table 3.9. This table based on the average graph.

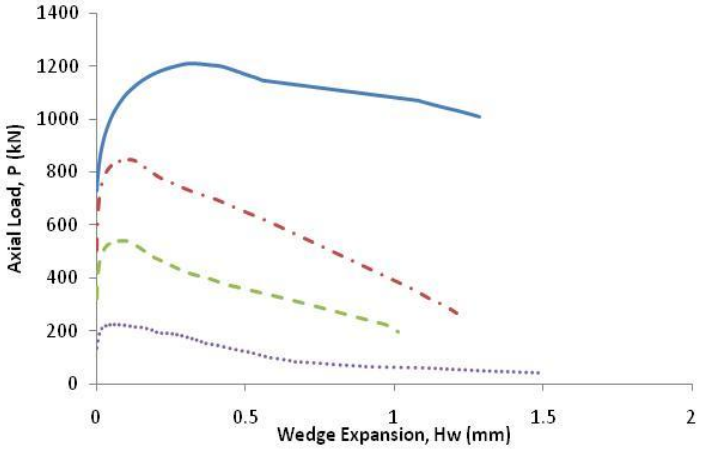

Figure 3.244: The average of axial load-wedge expansion graph

The average values of wedge expansion at peak axial load in Table 3.9 show the bigger size of prism the larger the lateral expansion due to micro-cracking or wedge expansion at peak load.

3.4.4.4 Load Wedge – Wedge Expansion Relationship

The axial load from the previous section is divided by the length of the prism S equal to wedge load P_w in kN/mm. The next four figures (Figure 3.245 to Figure 3.248) present the load wedge P_w against wedge expansion V_w of every prism sizes. The average of individual curves at the same size is compared in the last figure (Figure 3.249). Figure 3.245 illustrates the relationship of P_w - V_w of all experiment tests in prism Test-125. The pattern is same with P-V_w response.

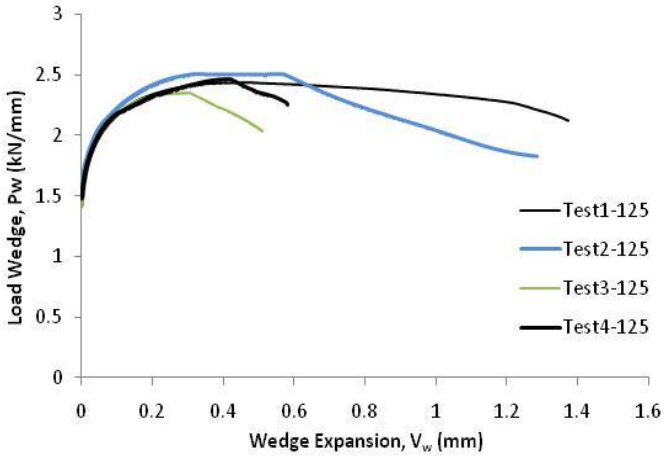

Figure 3.245: Load wedge-wedge expansion response of Test-125

Figure 3.246 illustrates the relationship between load and wedge expansion per 1 mm wedge thickness of Test-100. The similar pattern occurred in this graph with P-V_w response before.

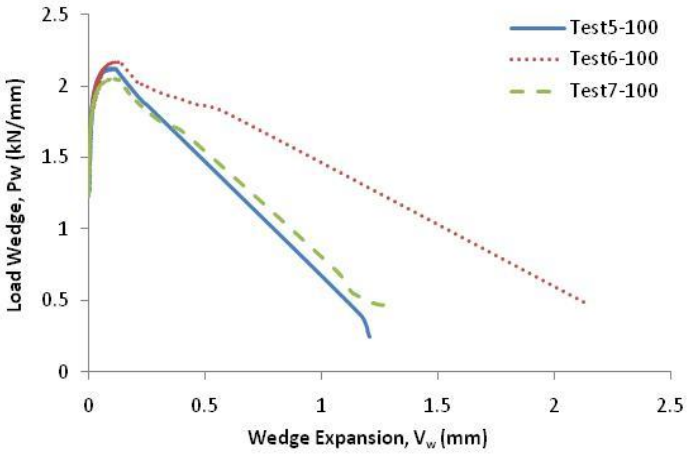

Figure 3.246: Load wedge-wedge expansion response of Test-100

The relationship between load and wedge expansion per 1 mm wedge thickness P_w- V_w of Test-75 is depicted in Figure 3.247. The graph illustrates the same pattern with P-V_w response of Test-75 in Section 3.4.4.3 previously.

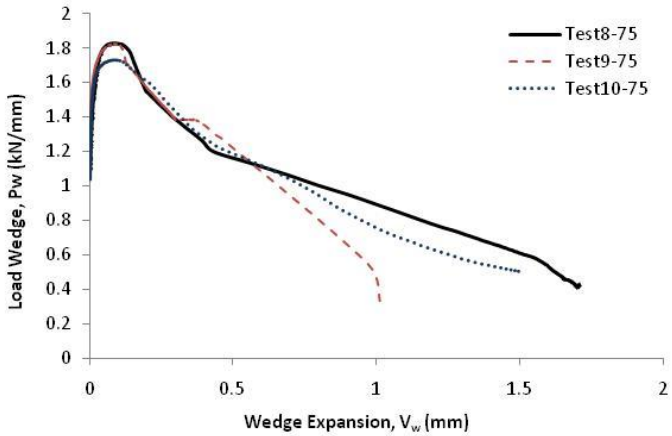

Figure 3.247: Load wedge-wedge expansion response of Test-75

Figure 3.248 shows the response of load and wedge expansion for 1 millimeter wedge thickness. The same pattern is occurred between Figure 3.243 and Figure 3.248.

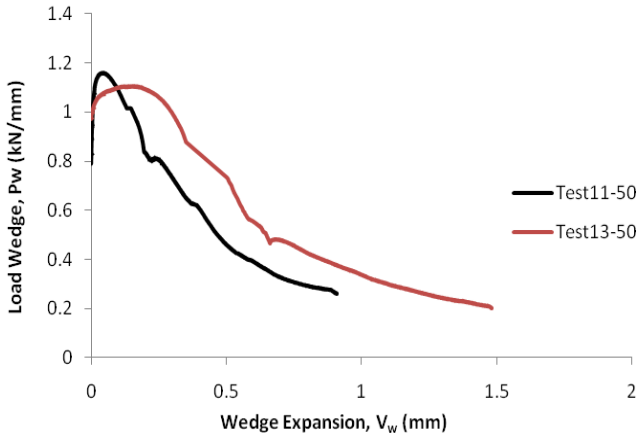

Figure 3.248: Load wedge-wedge expansion response of Test-50

The graphs of each size that were described previously is used to determine the average graph of P_w–V_w response of all size as shown in Figure 3.249. The graph indicated that the micro-cracking start to develop in lateral direction when the wedge load P_w is around 0.7kN/mm, 1,1kN/mm, 1.3kN/mm and 1.5kN/mm for Test-50, Test-75, Test-100 and Test-125 respectively. The values of P_w are same when micro-cracking in axial direction starts to occur (see Section 3.4.3.4). This indicated that micro-cracking occurs in axial and lateral direction at the same time.

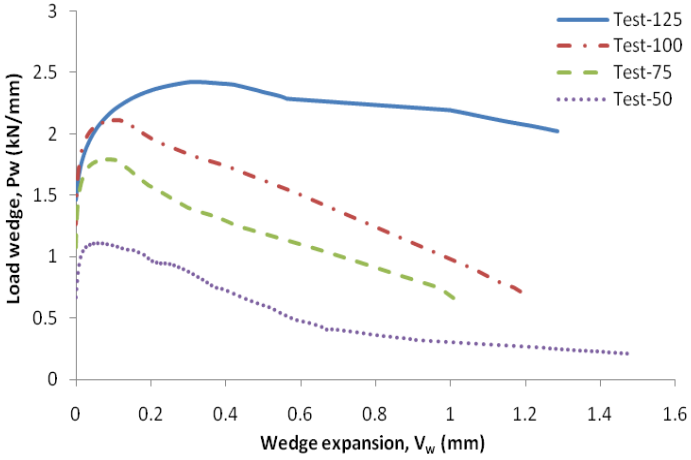

Figure 3.249: The average of load wedge-wedge expansion response of Test-125

The values of the peak of load wedge P_w and the wedge expansion V_w are listed in Table 3.9. The bigger size of prism the higher the peak of load wedge and larger the lateral deformation due to micro-cracking or wedge expansion at peak load.

3.4.4.5 Stress Wedge– Wedge Expansion

The individual stress-wedge expansion relationship of test results of the same size prisms is plotted in one graph to evaluate the trend of the curves which are represented in Figure 3.250 to Figure 3.253.

The relationship between stress and wedge expansion of all prisms on Test-125 is depicted in Figure 3.250. The graph indicates every concrete prism in Test-125 has similar pattern, the lateral deformations due to micro-cracking or the wedge expansion on the prism Test-125 occur almost the same stress wedge that is between 23MPa and 24MPa.

The peak stress wedge σ_{wp} of all concrete prisms in Test-125 is almost the same that is between 38MPa to 40MPa but the wedge expansion at the peak stress V_{wp} has a small scatter that is between 0.30mm to 0.55mm. The average of wedge expansion at peak stress V_{wp} is 0.43mm (see again Table 3.5)

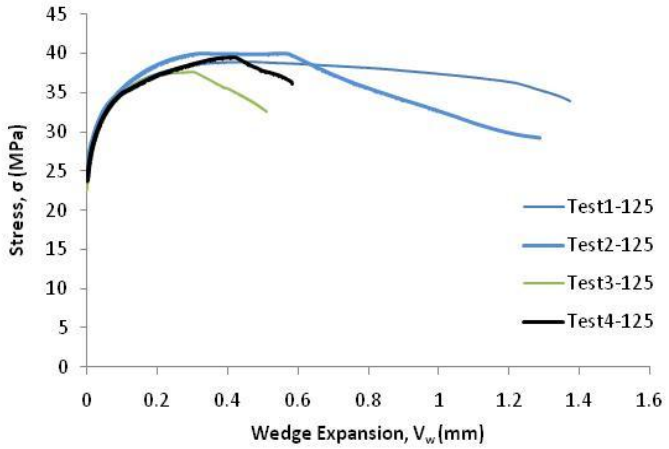

Figure 3.250: Stress-wedge expansion response of Test-125

Figure 3.251 illustrates the relationship between the stress wedge σ_w and the wedge expansion V_w of Test-100. The graph indicate that the responses are quite similar pattern on ascending branch of all prism, however, small scatter occurred on Test6-100

on descending branch. The peak stress wedge σ_{wp} and the slip wedge at peak stress V_{wp} of all prisms in Test-100 have quite the same value that is between 0.10mm to 0.12mm. The average wedge expansion at peak stress V_{wp} is 0.11mm. These important parameters can be seen in Table 3.6.

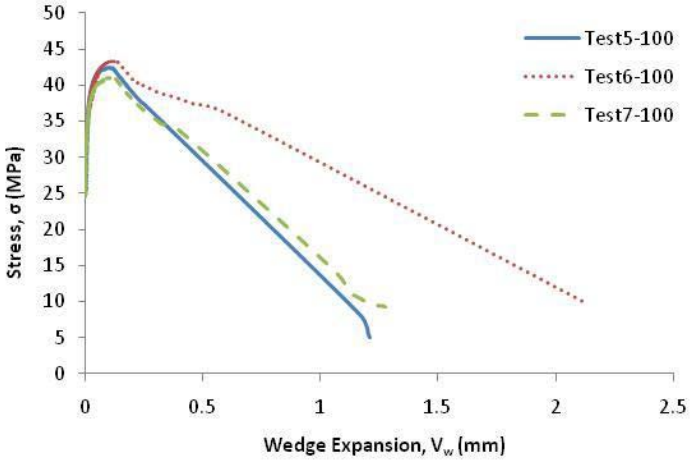

Figure 3.251: Stress-wedge expansion response of Test-100

The relationship of $\sigma_w - V_w$ of Test-75 is depicted in Figure 3.252. The graphs illustrate all prisms in Test-75 show the similar response. The values of wedge expansion at peak stress V_{wp} is quite the same that is between 0.08mm to 0.09mm and the average of V_{wp} is 0.09mm (see again Table 3.7).

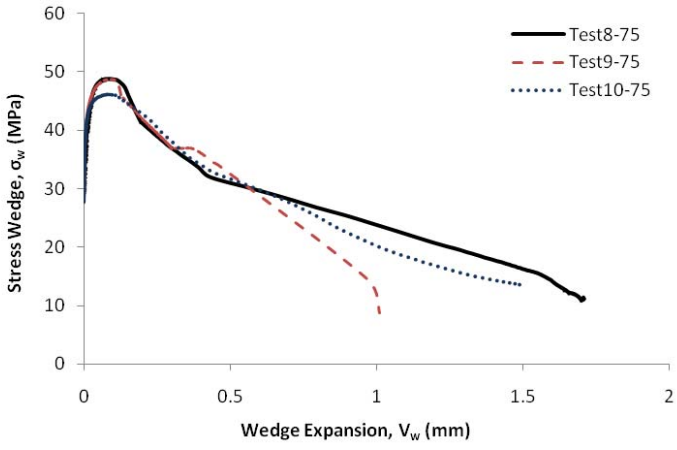

Figure 3.252: Stress-wedge expansion response of Test-75

Figure 3.253 illustrates the σ_{wp}-V_{wp} responses of all prisms in Test-50. The graph indicates the small scatter occurs. There is a big difference wedge expansion at peak stress wedge happened (see again Table 3.8). The average wedge expansion based on each test in Test-50 V_{wp} is 0.10mm.

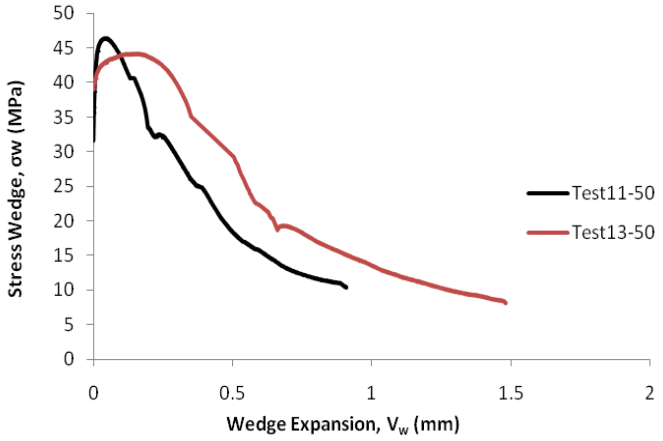

Figure 3.253: Stress-wedge expansion response of Test-50

The average of the results for each size is found out and depicted in Figure 3.254. It shown that wedge expansion at peak stress V_{wp} between 0.06mm to 0.31mm. The wedge expansion at peak stress V_{wp} increases when the prism size increases. It means that wedge expansion is affected by the size of prism. The peak stress σ_{wp} corresponding to slip wedge S_{wp} are listed in Table 3.9.

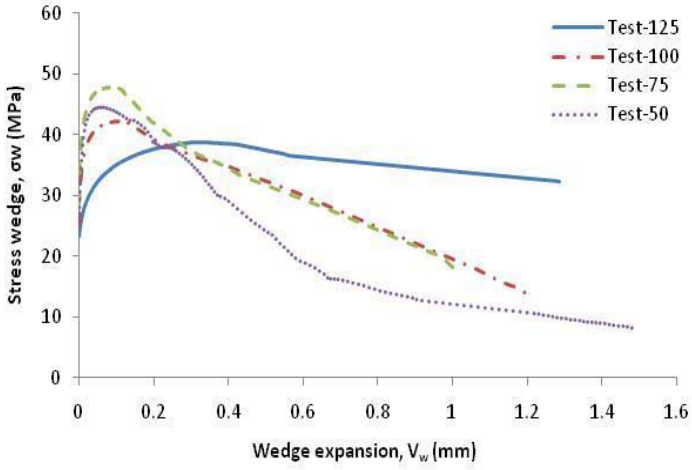

Figure 3.254: The average of stress wedge-wedge expansion graph

The values of V_{wp} are almost same with the values of S_{wp} for all tests. However there is a difference for Test-125. For Test-125, V_{wp} is 0.31mm while S_{wp} is 0.16mm. It means that at peak stress, deformations due to micro-cracking in lateral and axial direction are similar. More detail about the stress wedge and slip wedge responses is discussed in Section 3.4.5.

After analysed the individual result, compared with the other size and evaluated the average graph all the prism, the wedge is analysed more detail in the next section.

Table 3.9: The average of important parameters of all concrete prism based on average curves

Prism	L_p (kN)	P_p (kN)	P_{wp} (kN/mm)	σ_{wp} (MPa)	C_p (mm)	$C_p/2$ (mm)	S_{wp} (mm)	E_p (mm)	$E_p/2$ (mm)	V_{wp} (mm)
1	2	3	4	5	6	7	8	9	10	11
TEST-125	2438	1219	2.44	39	1.04	0.52	0.16	0.84	0.42	0.31
TEST-100	1686	843	2.11	42	0.80	0.40	0.12	0.32	0.16	0.11
TEST-75	1062	531	1.79	47	0.72	0.36	0.11	0.25	0.12	0.08
TEST-50	442	221	1.12	44	0.45	0.23	0.05	0.09	0.05	0.06

The important parameters of Test-125, Test-100, Test-75 and Test-50 from the average graphs are listed in Table 3.9. The parameter L_p corresponds to total axial contraction at peak load C_p. The parameter C_p is listed in column 6 in Table 3.9. The total axial contraction of prism increases as the size of prism increases. The parameters L_p and C_p are the load and contraction of the whole prism. To analyse the behaviour of one wedge, these values are divided by 2.

In analysis one single wedge relates to P_p and $C_p/2$ response. The peak of axial load P_p and total axial load of one single wedge $C_p/2$ are represented in columns 3 and 7 in Table 3.9 respectively. The pattern of P_p and $C_p/2$ are the same with P_p and C_p. The axial load increases and the contraction over one single wedge increases as the size of prism increases.

The total axial contraction consists of elastic contraction and deformation due to micro-cracking or slip wedge. Hence the slip wedge is obtained by subtract the elastic contraction from the total axial contraction of one wedge $C/2$. The parameter of slip

wedge is represented in column 8 in Table 3.9. The slip of the wedge varies and depends on the prism size. The slip wedge increase as the size of the prism increases.

In lateral deformation the same phenomenon also occurs on total lateral expansion E, total lateral expansion over one single wedge $E/2$ and wedge expansion V_w. At peak load total lateral expansion E_p, total lateral of one single wedge $E_p/2$ and wedge expansion V_{wp} are increase as the size of prism increases. They can be seen in columns 9, 10, 11 in Table 3.9.

The load wedge P_w is calculated by dividing the axial load P with the prism length S. The load wedge refers to the load for one millimeter wedge thickness. The peak of the load wedge P_{wp} is represented in column 4 in Table 3.9. The pattern is also same with the total axial load L and axial load for one wedge P. The load wedge increases as the size of the prism increases.

Meanwhile, the peak stress wedge σ_{wp} increases as the size of prism decreases as shown in column 5 in Table 3.9. However, the parameter σ_{wp} in Test-75 is higher than Test-50. Based on individual result, a large scatter occurred in the results of Test-50. As described by Gobbi and Ferrara (1995), the smaller specimens were more difficult to centre in the compression machine.

At peak stress, total axial contraction C_p of all prism size considerable higher than total lateral expansion E_p. This means up to peak stress total deformation in axial direction is much higher than total deformation in lateral direction. However, at peak stress there is no significant difference between axial deformation and lateral deformation due to micro-cracking that is S_{wp} and V_{wp}. This means that elastic contraction give more influence to the axial total deformation. The elastic contraction consists of material contraction, dental paste contraction and bedding down.

3.4.5 Wedges Analysis

After analysed one by one of the results of all concrete prisms in axial and lateral deformation, quantified the average graph of every size and compared to others size of prism, in this section behaviour of the wedges is analysed more detail. Begin with slip wedge and the wedge expansion.

3.4.5.1 Stress Wedges – Slip Wedge Relationship

The average graph of the stress wedge and slip wedge of all sizes prisms in Figure 3.229 is represented again here as shown in Figure 3.255. The focus of this research develops the generic expression to simulate the stress wedge for a given slip. The graph in Figure 3.255 and Table 3.9 clearly seen that the peak of stress wedge σ_{wp} and slip wedge at peak stress S_{wp} are varies. Hence the normalised and non-dimensionalised the stress wedge and slip wedge response is required.

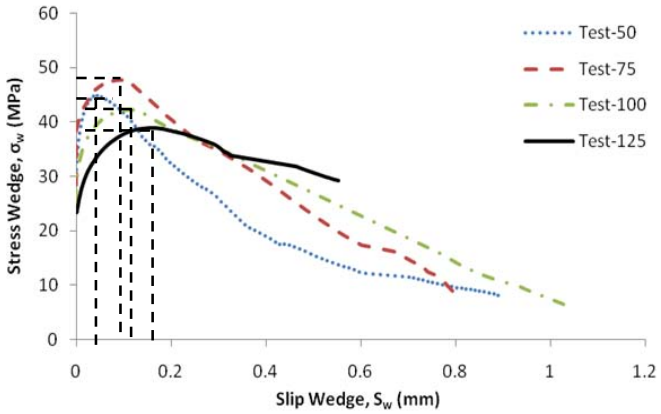

Figure 3.255: The average of stress wedge-slip wedge graph

The normalises and non-dimensionalises of the stress and slip wedge is obtained by dividing the stress wedge and slip wedge with the peak of stress and peak of slip wedge respectively. Figure 3.256 represents the normalized and non-dimensionalised of stress-slip wedge curves for all size. The graph looks very similar, Test-75, Test-100 and Test-125 are in the same line only Test-50 slight outlie (as shown in a dot line) but still appropriate.

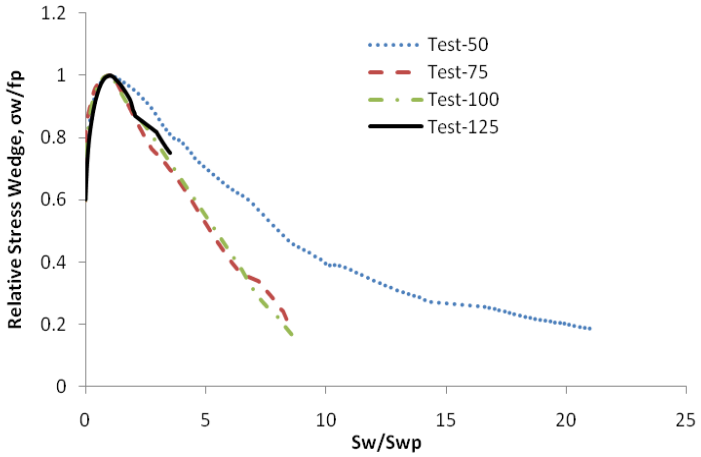

Figure 3.256: Non-dimensionalised stress-slip wedge

Expression the relative normalised stress of the wedge σ_w/f_p in terms of S_w/ S_{wp} is given in Eq. 3.8

$$\frac{\sigma_w}{f_p} = \left[-0.65\left(\frac{S_w}{S_{wp}}\right)^2 + 5.71\left(\frac{S_w}{S_{wp}}\right) + 5.04 \right] \exp\left[0.03\left(\frac{S_w}{S_{wp}}\right)^2 - 0.50\left(\frac{S_w}{S_{wp}}\right) - 1.87 \right] \qquad \textit{Eq. 3.8}$$

where σ_w is the wedge stress, f_p is the average of the peak stress wedge σ_{wp} that is 43MPa, S_w is slip wedge and S_{wp} is slip wedge at peak stress.

The slip wedge at the peak stress S_{wp} varies and depends on the prism size as shown in Table 3.9. It was assumed that the depth of the wedge d_w is half than prism width W. Figure 3.257 illustrates the relationship between S_{wp} and d_w. The graph shows the slip of the wedge at peak load depend on the depth of the wedge d_w. The mathematic expression of the slip wedge S_{wp} for a given depth of wedge d_w as

$$S_{wp} = 0.0025 d_w \qquad \textit{Eq. 3.9}$$

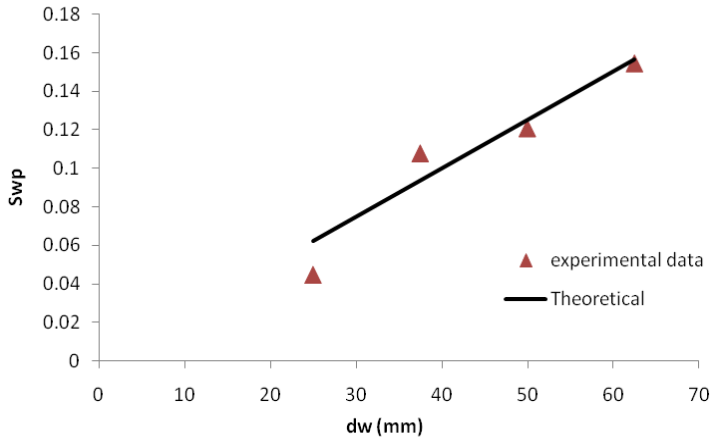

Figure 3.257: Slip wedge at peak stress over depth of wedge graph

The general expression of σ_w/f_p in terms of S_w/S_{wp} in Eq. 3.8 provided an accurate fit to the experimental results, as shown in Figure 3.258, Figure 3.259 and Figure 3.260 for Test-125, Test-100 and Test-75 respectively.

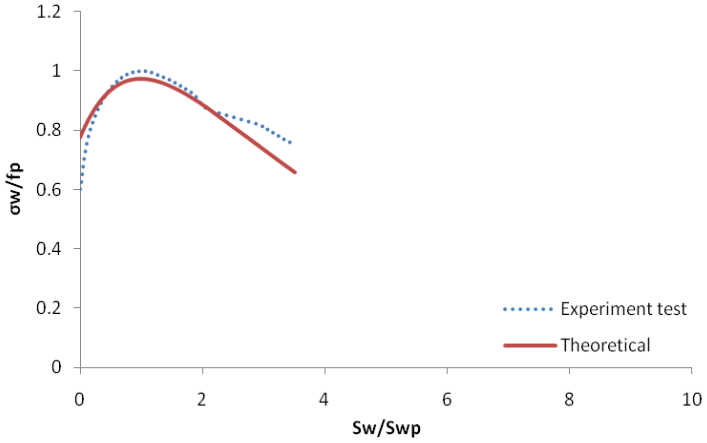

Figure 3.258: Stress-slip comparison response of Test-125

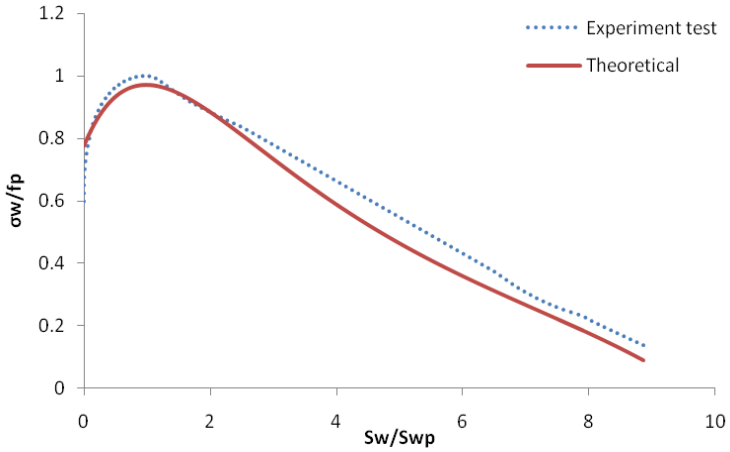

Figure 3.259: Stress-slip comparison response of Test-100

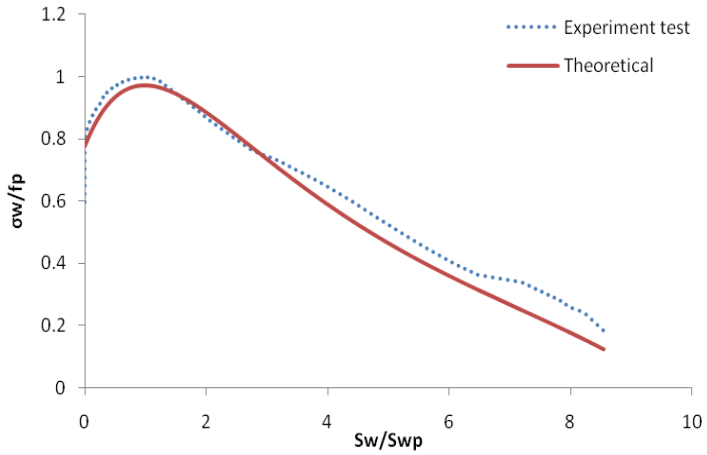

Figure 3.260: Stress-slip comparison response of Test-75

As expected the expression in Eq. 3.8 not too much accurate but still acceptable for Test-50 as shown in Figure 3.261. This is because the response of Test-50 in not the same line as shown in Figure 3.256 and the expression is developed by using that line. Hence the general mathematical expression at Eq. 3.10 can be used.

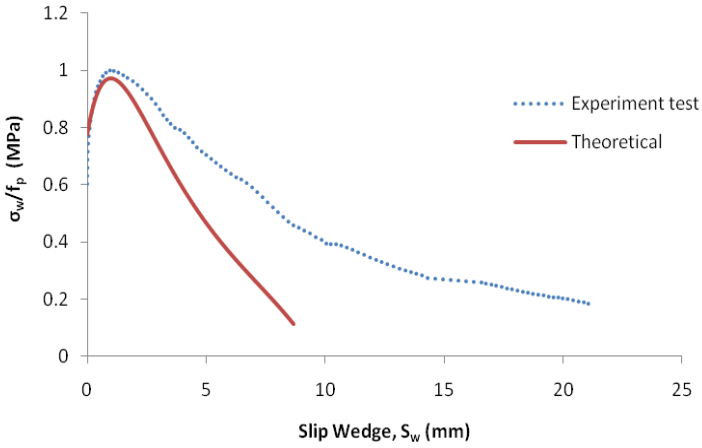

Figure 3.261: Stress-slip comparison response of Test-50

After analyse the response of the stress and the slip of the wedge, the next step analyse the stress and the wedge expansion. The same steps are used as were used in stress-slip wedge analysis.

3.4.5.2 Stress Wedge – Wedge Expansion

Figure 3.262 illustrates the average graph of the stress wedge and wedge expansion of all sizes prisms. The graph indicates that the peak stress of wedge σ_{wp} and wedge expansion at peak stress V_{wp} vary (see again columns 5 and 11 in Table 3.9). The stress wedge σ_{wp} varies between 39MPa to 47MPa and wedge expansion V_{wp} varies between 0.06-0.31mm. As same as in axial deformation, the mathematical expression is developed to simulate the stress wedge for a given wedge expansion. Hence the normalised the stress wedge and wedge expansion response is required. The normalises of the stress and wedge expansion is obtained by dividing the stress wedge and wedge expansion with the peak values of stress and wedge expansion respectively.

Figure 3.263 illustrates the normalized of the stress and the wedge expansion curves for all size. The responses of Test-50, Test-75, Test-100 and Test-125 are in one line and look very similar. The expression of the line that present the relative normalised stress of the wedge σ_w/f_p in terms of V_w/ V_{wp} as given in Eq. 3.10.

$$\frac{\sigma_w}{f_p} = \left[0.12\left(\frac{V_w}{V_{wp}}\right)^2 + 7.68\left(\frac{V_w}{V_{wp}}\right) + 18.18\right]\exp\left[0.01\left(\frac{V_w}{V_{wp}}\right)^2 - 0.30\left(\frac{V_w}{V_{wp}}\right) - 3.01\right] \qquad \textit{Eq. 3.10}$$

where σ_w is the wedge stress, f_p is the average of the peak stress wedge σ_{wp} that is 43MPa, V_w is wedge expansion and V_{wp} is wedge expansion at peak stress.

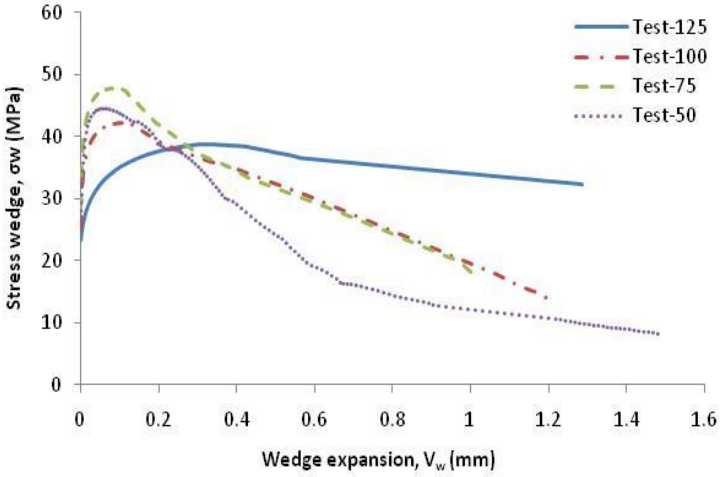

Figure 3.262: The average of stress-wedge expansion graph

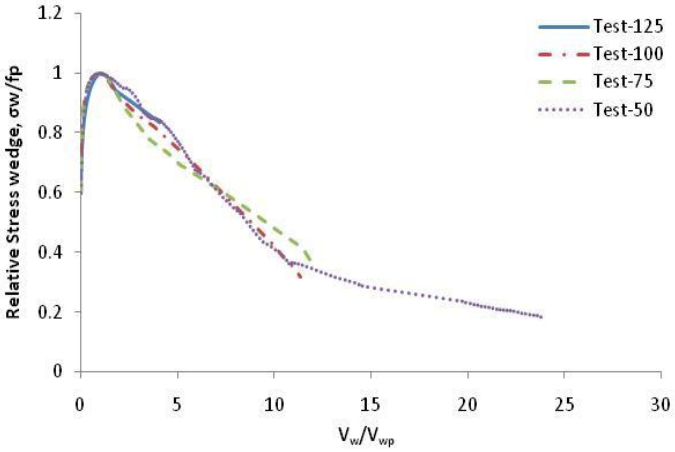

Figure 3.263: Non-dimensionalised stress-wedge expansion

The wedge expansion at the peak stress V_{wp} varies and depends on the prism size as shown in Table 3.9 and Figure 3.262. As shown in Table 3.9, V_{wp} for Test-50, Test-75 and Test-100 are similar while V_{wp} of Test-125 almost three times than other sizes hence V_{wp} of Test-125 is neglected. Figure 3.264 illustrates the relationship between V_{wp} and d_w of Test-50, test-75 and Test-100. The mathematical expression of the wedge expression V_{wp} for a given depth of wedge d_w as

$$V_{wp} = 0.0022 d_w$$ *Eq. 3.11*

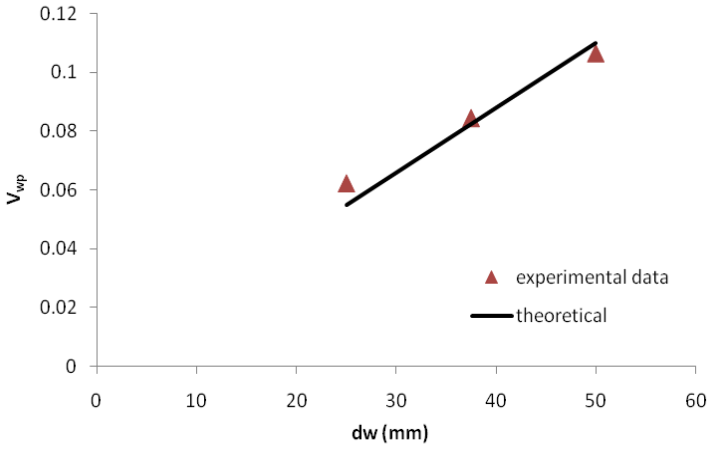

Figure 3.264: Wedge expansion at peak stress over depth of wedge graph

The general expression of σ_w/f_p in terms of V_w/ V_{wp} in Eq. 3.10 provided an accurate fit to the experimental results, as shown in Figure 3.265, Figure 3.266, Figure 3.267and Figure 3.268 for Test-125, Test-100, Test-75 and Test-50 respectively.

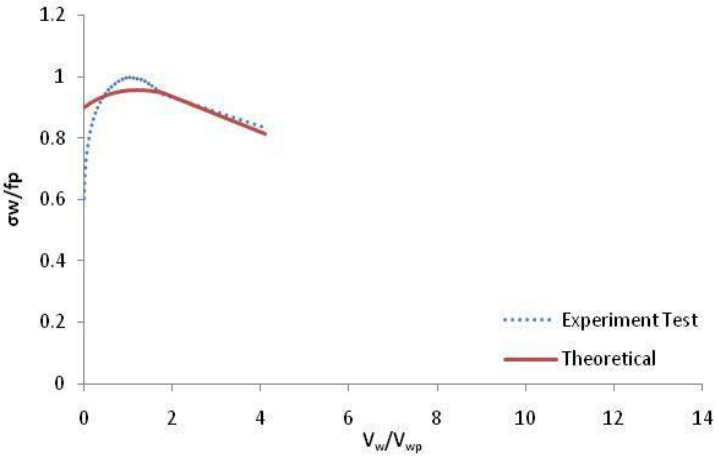

Figure 3.265: Stress-wedge expansion comparison response of Test-125

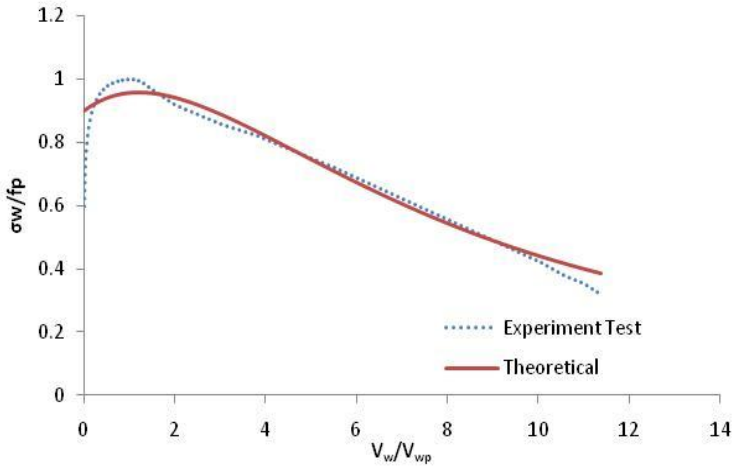

Figure 3.266: Stress-wedge expansion comparison response of Test-100

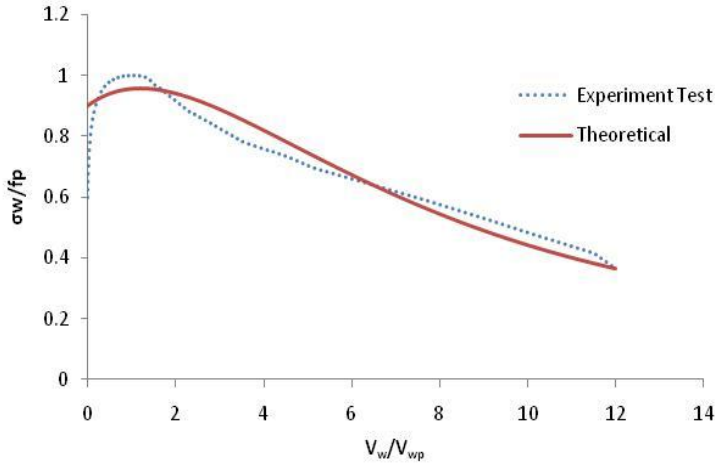

Figure 3.267: Stress-wedge expansion comparison response of Test-75

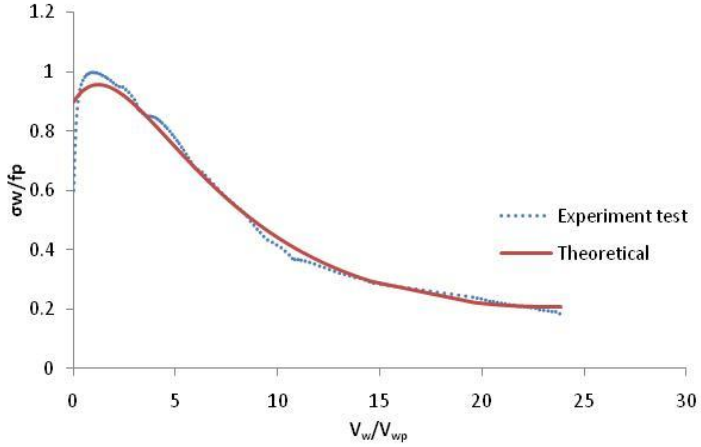

Figure 3.268: Stress-wedge expansion comparison response of Test-50

The generic equations to simulate the deformation due to micro-cracking in axial and lateral direction were developed and those equations were fit with the experimental results.

Chapter 4: PRISM SOFTENING EXPERIMENTS-f_c=23MPa

4.1 Introduction

In this chapter, the second set of experimental tests are described and analysed. This experimental test is same with the first set of experimental test but different concrete strength. The design of specimens is explained initially. It is consists of material properties test details and long concrete prism test details. The raw results of the tests in axial and lateral directions are described next, followed by the analysis of individual concrete prisms. After that the deformation in axial and lateral direction of each prisms are compared. Finally analysis of the wedges in axial and lateral direction is observed.

4.2 Design of Spesimens

Uniaxial compression tests of concrete, mortal and aggregate and tensile tests of concrete and mortar are described initially then the details of concrete block specimens including the test rig and instrumentation are given.

4.2.1 Material Properties

100mm×200mm concrete and mortar cylinders and 58mm×150mm core aggregate cylinders were used in order to determine the material properties of concrete, mortar and aggregate. To complete the results of material properties, in the second set of experiment test, the tensile test was carried out in addition to the uniaxial compression test. Details of the test and the instrumentation are described in the next section.

4.2.1.1 Concrete and Mortar

Nine concrete and nine mortar cylinders were subjected to axial compressive loads to quantify the compressive strength and Young's modulus. Three cylinders were tested one day before prism concrete testing started, three cylinder were tested the same day with prism concrete tested and the last three were tested one day after all prism concrete testing had been finished.

A Seidner compression machine with maximum load of 1500kN also used in the second set of experimental test. The same method was used to produce the mortar as was used in the first set of experiment test.

In the previous experiment test, strain gauges were used to quantify elastic Young modulus but in this test Young modulus rig was used instead of strain gauges as shown in Figure 4.1. The load applied approximately 40% of the maximum load and unloads to zero three times. To obtain the ultimate compressive stress, the cylinder is subjected until failed. Two lateral transducers were placed to measure lateral deformation at the middle of cylinders height up to the ultimate load. Strain softening of stress strain relationship of mortar and concrete was not determined.

By using the same compression mechine, the tensile test was conducted on nine concrete and nine mortar cylinders to obtain the tensile strength. A method to determine indirect tensile strength of concrete follow to Australian Standard AS 1012.10-2000. Apply the load continuously and without shock until failure of the specimens. The concrete and the mortar cylinders were divided and tested in three different of times. One day before the concrete prism testing began, at the time of concrete prism testing dan one day after all conctere prism testing had been completed.

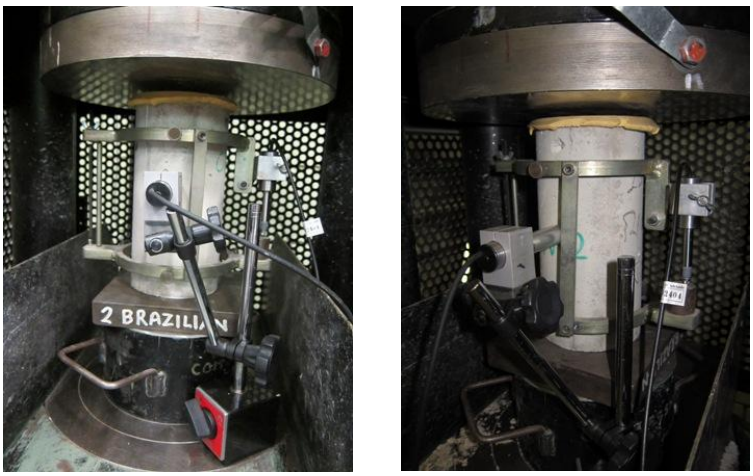

(a) concrete *(b) mortar*

Figure 4.1: Concrete and mortar cylinders test set up.

4.2.1.2 Aggregate

The 58mm×150mm core aggregate cylinders were tested under compression test to quantify material properties of aggregate. The 30mm strain gauge-1 (SG-1) and strain gauge-2 (SG-2) were located axially and two others strain gauges (SG-3 and SG-4) applied laterally to quantify axial and lateral deformation of aggregate up to peak stress as shown in Figure 4.2 (a). The position of all these strain gauges was half of cylinder height as shown in Figure 4.2(b).

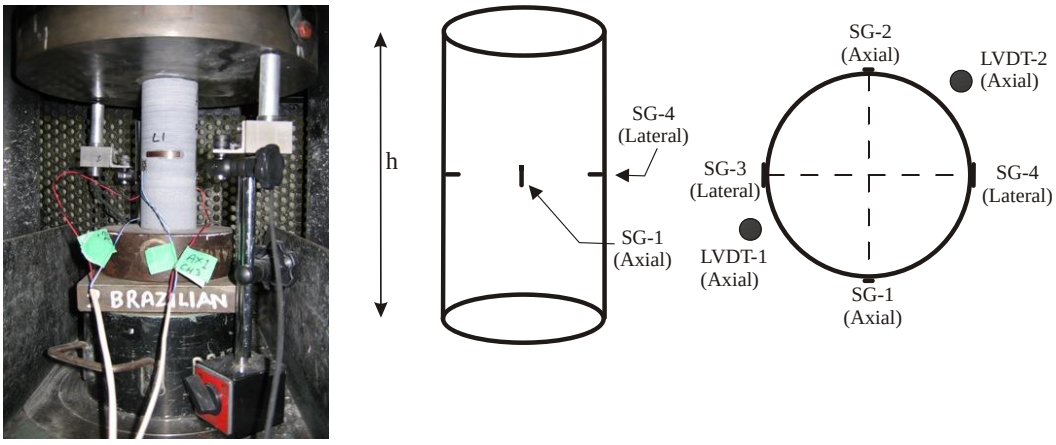

(a) *(b)*

Figure 4.2: (a) Agregate compression test set up; (b) The diagram of transducers and strain gauges layout of aggregate

4.2.1.3 The Result

The results of material properties tests of concrete, mortar and aggregate are summarized in Table 4.1, Table 4.2 and Table 4.3 respectively. On Table 4.1 and Table 4.2 columns 1 to 5 show the result of compression test and Young's modulus while columns 7 and 8 show the result of tensile test.

The average compressive stress of concrete, mortar and aggregate are 23.2MPa, 24.5MPa and 140.5MPa respectively. At low concrete strength, compression stress of mortar is slightly higher than concrete. Meanwhile at higher strength (see again section 3.2.1) compressive stress of mortar is significant higher than concrete.

Table 4.1: Material properties of concrete

Specimens	Age (days)	Compression Load (kN)	Compression Stress (MPa)	Young's modulus (MPa)	Specimens	Tensile Load (kN)	Tensile Stress (MPa)
1	*2*	*3*	*4*	*5*	*6*	*7*	*8*
C1	36	159.6	20.2	23,209	C4	81.8	2.6
C2	36	165.8	21.0	22,725	C5	87.8	2.8
C3	36	159.2	20.1	23,281	C6	88.0	2.8
C7	50	191.0	24.1	22,963	C10	94.0	3.0
C8	50	199.6	25.2	23,421	C11	94.8	3.0
C9	50	195.4	24.4	23,693	C12	103.0	3.3
C13	59	191.8	23.9	23,410	C16	93.8	3.0
C14	59	187.2	23.5	23,280	C17	104.2	3.3
C15	59	209.2	26.2	25,547	C18	111.4	3.5
AVERAGE			23.2	23,500	AVERAGE		3.0

Table 4.2: Material properties of Mortar

Specimens	Age (days)	Compression Load (kN)	Compression Stress (MPa)	Young's modulus (MPa)	Specimens	Tensile Load (kN)	Tensile Stress (MPa)
1	2	3	4	5	6	7	8
M1	36	171.8	21.7	18,574	M4	77.6	2.5
M2	36	173.2	21.8	19,518	M5	67.2	2.1
M3	36	173.2	21.9	18,248	M6	67.0	2.1
M7	50	201.8	25.4	19,286	M10	88.4	2.8
M8	50	207.2	26.2	18,802	M11	80.2	2.5
M9	50	193.4	24.4	17,404	M12	83.2	2.7
M13	59	204.0	25.8	18,655	M16	101.4	3.2
M14	59	214.6	27.2	19,427	M17	110.2	3.5
M15	59	205.2	25.9	18,263	M18	106.8	3.4
AVERAGE			24.5	18,686	AVERAGE		2.8

Table 4.3: Material properties of aggregate

Specimens	Compression		Young's modulus (MPa)
	Load (kN)	Stress (MPa)	
A1	379.0	143.4	62,500
A2	442.4	167.4	69,500
A3	365.3	138.3	59,800
A4	298.7	113.0	49,000
AVERAGE		140.5	60,200

The tensile stress of concrete and mortar were 3.0MPa and 2.8MPa respectively. Tensile stress of concrete depends on compressive stress as given:

$$f_{ct} = 0.6\sqrt{f_c} \quad (\text{MPa}) \qquad \textit{Eq. 4.1}$$

Using Eq. 4.1 tensile stress of concrete f_{ct} was 3.4MPa. This value is almost same with the value was obtained from tensile test. Elastic modulus of concrete, mortar and aggregate are 23,500MPa; 18,686MPa and 60,200MPa respectively. Elastic Young modulus can be determined as

$$E_c = 3320\sqrt{f_c} + 6900 \qquad \textit{Eq. 4.2}$$

Using Eq.2.3, Young's modulus of concrete E_c = 22,800MPa. The results of the experimental test of material properties show the accurate values.

4.2.2 Specimens Detail

The geometry of the concrete prism is the same as was used in the first set of experiment test that can be seen in Figure 3.15. The details of the concrete prism on this second set of experimental test are listed in Table 4.4. The size types of 2, 4, 5 and 6 are the same with the first set of experimental test where the ratio a width to height to length of 1:2:4. While the prisms with ratio a height to width (slenderness ratio) of 3, 2 and 1 were also conducted (size types of 1, 2 and 3 in Table 4.4). This means that varying height and constant cross sectional (A=125×500 mm^2).

The name of the specimen is based on its size. For instance, Test (II)-125×375×500, "II" indicates the second set of experimental test; and the following numbers show the prism size; width *W*=125mm, height *H*=375mm and length

S=500mm. Three each size of prisms are subjected to uniaxial compression load. The first concrete prism in Test (II)-125×375×500 is named Test (II)1-125×375×500; "1" indicates the first prism in the whole numbers of the test, the second prism is named Test (II)2-125×375×500 and the third prism is named Test (II)3-125×375×500. The first prism in the Test (II)-125×250×500 was named Test (II)4-125×250×500; "4" indicate the fourth prism of the set of experiment. The name of the others concrete prism follow this rule.

Table 4.4: Detail of concrete block

Size Type	Specimen	Size (*W*x*H*x*S*)	Specimens number
1	Test II-125×375×500	125×375×500	3
2	Test II-125×250×500	125×250×500	3
3	Test II-125×125×500	125×125×500	3
4	Test II-100×200×400	100×200×400	3
5	Test II-75×150×300	75×150×300	3
6	Test II-50×100×200	50×100×200	3
T O T A L			18

Total number of prism compression test is eighteen prisms. The next section the instrumentation and test rig. There is any the difference instrumentation set up between the first and the second sets of experimental test that is the position of lateral LVDTs.

4.2.3 The Test Rig and Instrumentation

The Amsler Compression Testing Machine is used for concrete prism tests (see again Figure 3.16). The position of four vertical LVDTs (LVDT-1, LVDT-2, LVDT-3 and LVDT-4) is the same with the first set of experimental test was used as shown in Figure 3.17 to record the axial deformation (see also Figure 4.3). Only two lateral LVDTs were used in the first set of experimental test. While in the second set of experimental test, six horizontal LVDTs are placed to measure the lateral deformation,

three of the each side as depicted in Figure 4.3(b) and Figure 4.4. The lateral LVDTs-5, 7 and 9 are placed in one side and LVDTs-6, 8 and 10 are placed in the other side.

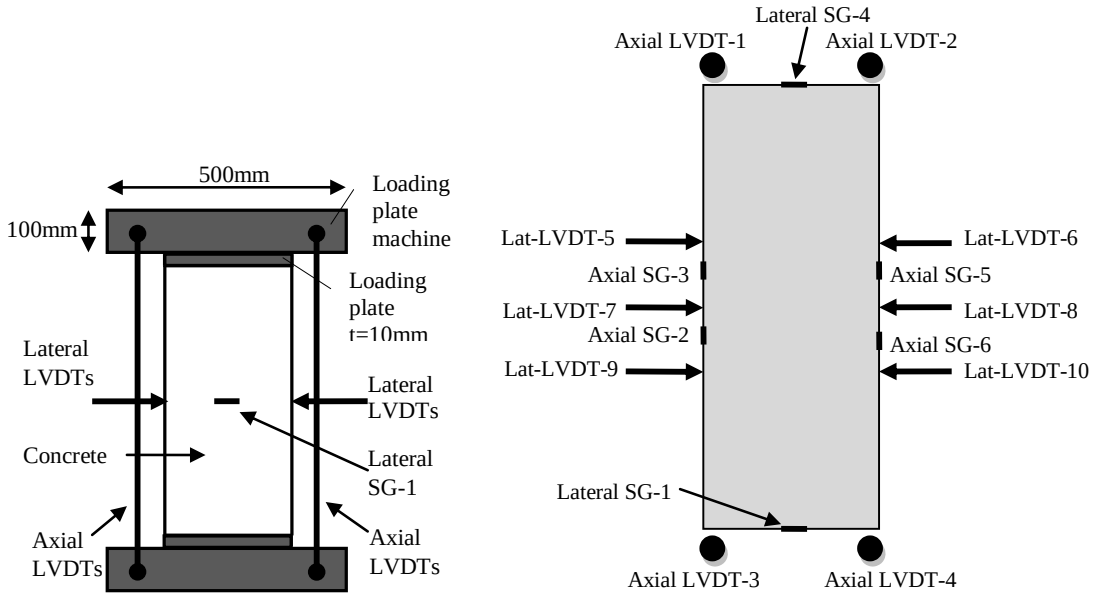

(a) Front view (face prism) *(b)Top view*

Figure 4.3: Layout of the transducers and strain gauges of concrete prism.

A strain gauge is placed laterally in both faces of the prism and two strain gauges are located axially in each side and placed between the transducers as illustrated in Figure 4.3 and Figure 4.4.

A strain gauge is applied laterally on each face/front side of the prism to measure lateral deformation and two strain gauges are applied axially on each side of the prism to measure the axial deformation. It is important to note that the values of axial and lateral deformation as recorded by these strain gauges are not used in this current research, however, since the strain gauge reading values had been obtained during a parallel research project at the University of Adelaide, and are not relevant at this point.

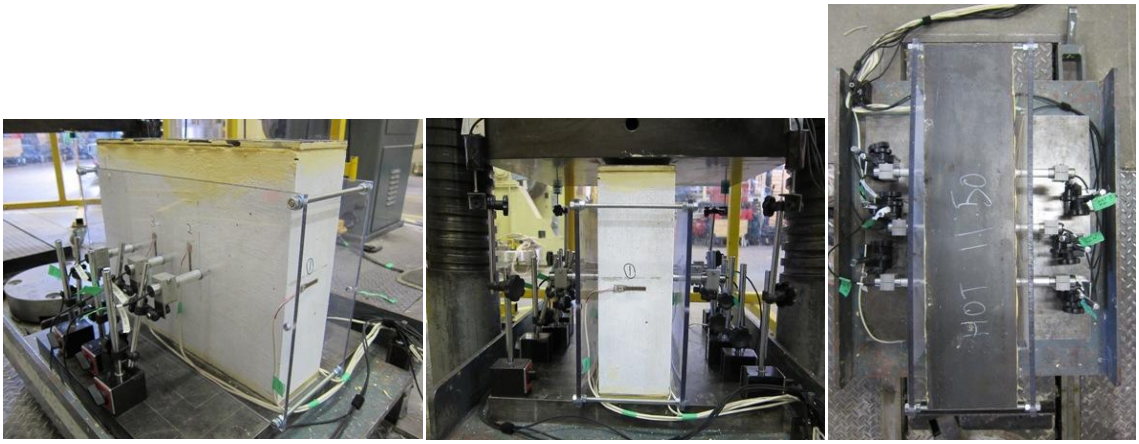

(a) *(b))* *(c)*

Figure 4.4: Concrete prism test set up; (a) side view (b) front view (face prism); (c) top view

The load rates 10kN/min, 20kN/min and 30kN/min were used up to peak stress for Test II-50×100×200, Test II-75×150×300 and Test II-100×200×400 respectively while load rate was 50 kN/min for Test II-125×125×500, Test II-125×250×500 and Test II-125×375×500. After peak stress the loading was changed to displacement control. For all concrete prisms the load rate of 2×10^{-4}mm/s was carried out on post peak stress.

4.3 Test Results

The raw experimental test results of 18 compressed concrete prisms are described below. The deformation in axial and lateral directions which is occurred in the concrete prism is illustrated in Figure 3.19.

The next 54 of images and graphs, Figure 4.5 to Figure 4.58 show the failure pattern of the concrete prism, the relationships between total axial load *L* and contraction and between total axial load *L* and dilation of every concrete prism. The contraction is obtained from the values of the axial LVDT readings which were placed at each edges of concrete prism. The dilation is measured by using six lateral LVDTs.

TEST(II)1-125×375×500

The contraction of each edge of prism Test(II)1-125×375×500 increases similarly as the load increases up to peak load (Figure 4.5). This means the whole prism

under compression. The contraction of the edges of prism where LVDTs-1 and -2 are placed still increase after the peak load reached but contraction of the edges of prism where LVDTs-3 and -4 suddenly dropped.

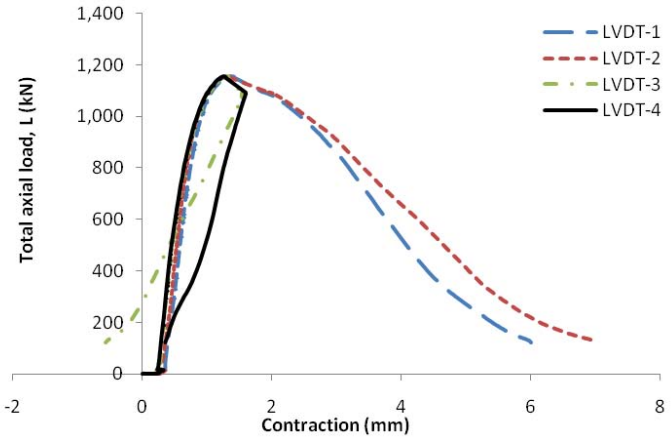

Figure 4.5: Total axial load – contraction response of prism Test (II)1-125×375×500

Figure 4.6 illustrates the response of total axial load and dilation of Test(II)1-125×375×500. The graph indicates the whole prism is expands since the beginning of loading. The responses are similar up to peak load. The values of lateral LVDTs recording are increase slightly as the load increases. After peak load, the dilation on the side of prism where LVDTs-5,-7 and -9 are placed increase significantly as the load decreases.

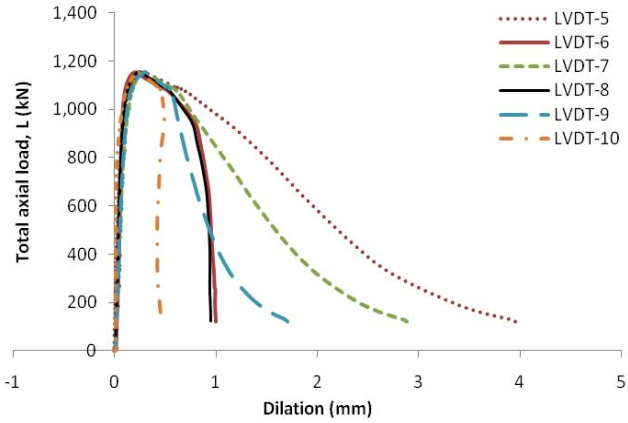

Figure 4.6: Total axial load-dilation response of the prism Test (II)1-125×375×500

Test (II)1-125×375×500 is the first specimen of 125×375×500 prisms. A "non-explosive" failure occurred. Figure 4.7 (a) shows the diagonal crack occurs on the face where the LVDT-1 and LVDT-2 are placed. The localization of damage is occurred in this test prism where the ratio of height to width is 3. Figure 4.7(b) shows the side views of concrete prism. The angle of the crack is recorded around 26°.

(a) face/front view *(b)side view*

Figure 4.7: Failure mode of concrete Test (II)1-125×375×500

The response of contraction and dilation for a given total axial load *L* and the images of the concrete failure for the first prism in Test(II)-125×375×500 have been described. This raw data is discussed more detail in Section 4.4.2.

TEST(II)2--125×375×500

Figure 4.8 shows the edges of prism, where axial LVDTs-1 and -3 were placed, are in compression while the others edges are in tension. The eccentrically load happen accidently at low load. A slight eccentrically load pulls up the platen load a little bit at edges, where the LVDTs-2 and 4 were placed, and pushes the platen load at the others edges. When the load approximately 300kN, the edge of prism of LVDT-2 in compression. The values of contraction as recorded by axial LVDTs-3 and -4 suddenly drop as the peak load reached while LVDTs-1 and -2 increase significantly as the load decreases until the prism failed.

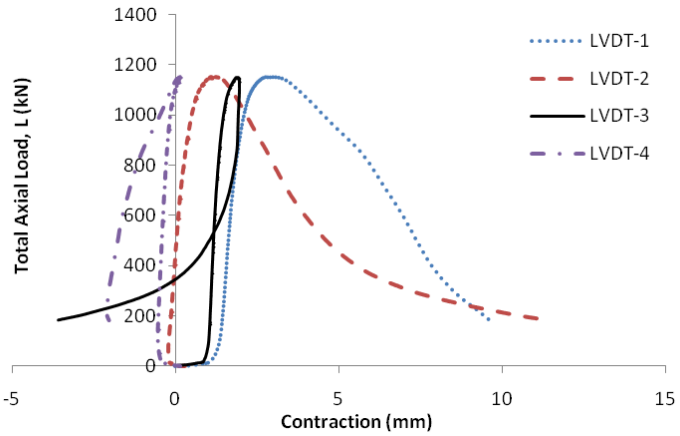

Figure 4.8: Total axial load – contraction response of the prism Test (II)2-125×375×500.

Figure 4.9 illustrates the dilation of Test(II)2-125×375×500 from lateral LVDTs recording. Similar response occurred on all LVDTs recording before the peak load, however, after the peak load LVDT-10 suddenly failed, LVDTs-6,8 and 9 increase slightly and LVDTs-5 and 7 increase significantly until the prism failed.

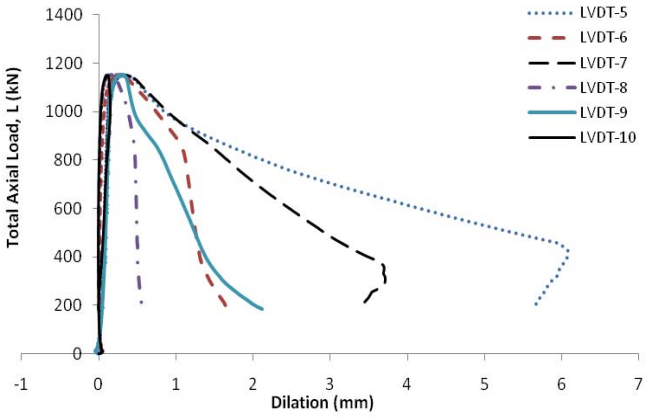

Figure 4.9: Total axial load-dilation response of the prism Test (II)2-125×375×500

Figure 4.10 shows failure occurred on the face of prism Test(II)2-125×375×500 where LVDTs-1 and -2 were placed while only crack surface occurred on the other face. A "non-explosive" failure occurred in this specimen. The wedge formed and the angle of the wedge was measured around 22°.

(a) face/front view *(b) side view*

Figure 4.10: Failure mode of concrete Test (II)2-125×375×500

The relationship between the total axial load *L* against contraction and dilation respectively and the images of the concrete failure of Test(II)2-125×375×500 have been described. This raw data is discussed more detail in Section 4.4.2. Next is raw data of Test(II)3-125×375×500.

TEST(II)3--125×375×500

Figure 4.11 illustrate the contraction response on Test(II)3-125×375×500. The whole prism is in compression. Before the peak load reached, more contraction occurred on the side of prism where LVDTs-1 and -3 were placed than the other side of prism where LVDTs-2 and -4 were placed. The values of LVDTs-3 and -4 readings drop suddenly as the peak load reached while the contractions of LVDTs-1 and -2 increase significantly as the load decreases.

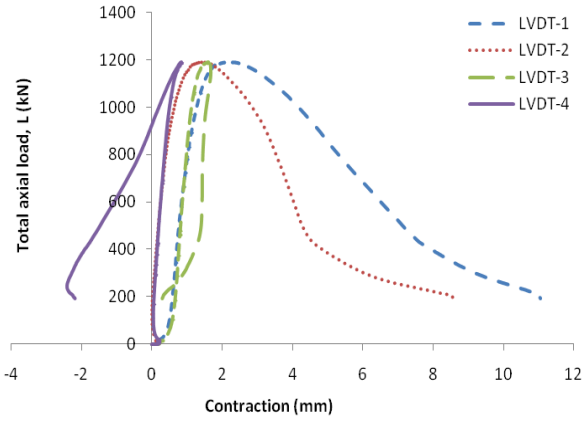

Figure 4.11: Total axial load - contraction response of the prism Test (II)3-125×375×500

The dilation response of prism Test(II)3-125×375×500 is illustrated in Figure 4.12. The graph indicates more dilation (see LVDTs-5 and 6 in Figure 4.12) occurred in the area near the face of prism where axial LVDTs-1 and -2 were placed.

The diagonal crack in the damage zone clearly seen on failure concrete specimen under compression as depicted in Figure 4.13 (a). The angle of the wedge was assessed around 22°. The concrete failed only in one face where LVDTs-1 and -2 were placed, surface crack occurred on the other face.

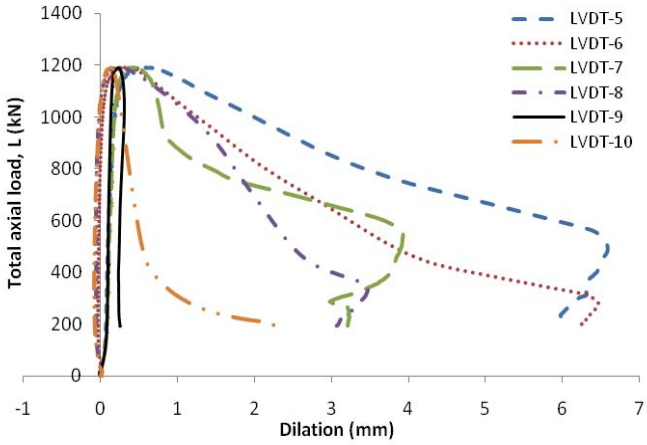

Figure 4.12: Total axial load-dilation response of the prism Test (II)3-125×375×500

(a) face/front view *(b) side view*

Figure 4.13: Failure mode of concrete Test (II)3-125×375×500

The compressive failure results of prisms with ratio height to width is 3 [see again Figure 4.7(a), Figure 4.10 (a) and Figure 4.13 (a)] indicate a localized damage zone developed which is occurred in a portion of prism height.

TEST(II)4--125×250×500

The contraction responses of all edges of the prism are similar up to peak load (Figure 4.14). After this point, the contraction as recorded by the LVDTs-3 and -4 drop quickly while by the LVDTs-1 and -2 increase considerably with a decrease of load. The prism failed at the face where larger contraction occurred.

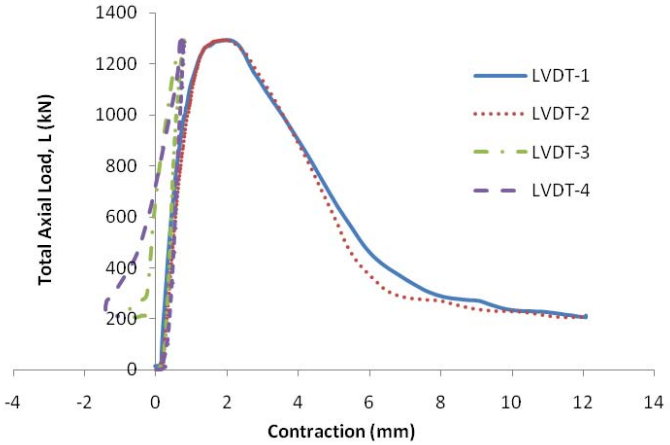

Figure 4.14: Total axial load - contraction response of the prism Test (II)4-125×250×500

At the beginning up to the peak load, the dilation on both sides of prism increases very slowly as the load increases. After reaches the peak load, the values of LVDTs-6,-8 and -10 drop quickly while the values of LVDTs-5, -7 and -9 increase rapidly as the load decreases. The large dilation occurred on the side of prism where LVDTs-5, -7 and -9 were placed.

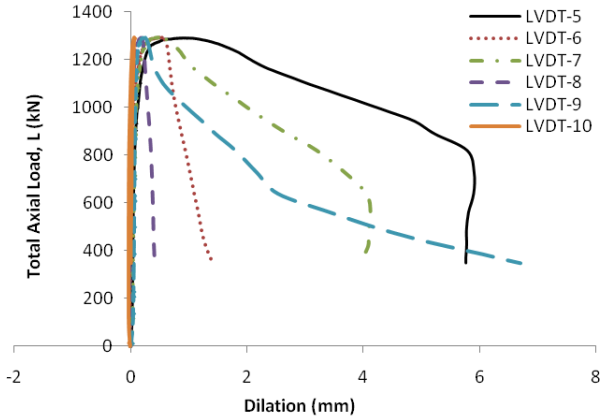

Figure 4.15: Total axial load-dilation response of the prism Test (II)4-125×250×500

A "non-explosive" failure happened in this specimen. The damage zone is occurred on the entire prism height. The wedge formed on the both sides of prism almost along the whole prism length that can be seen in Figure 4.16(a).The angle of the wedge was quantified approximately 22°.

(a) front view *(b)side view*

Figure 4.16: Failure mode of concrete Test (II)4-125×250×500

The raw data of the first prism in Test (II)-125×250×500 have been described. Next the second prism in Test (II)-125×250×500 is described.

TEST(II)5--125×250×500

Figure 4.17 illustrates the contraction which is obtained from axial LVDTs reading. The whole prism is in compression until the peak load reached. The contraction on the edges where LVDTs-3 and -4 were placed increase significantly after the peak

load reached while the contraction on the others edges (where LVDs-1 and -2 set up) suddenly drop and in tension when the prism failed.

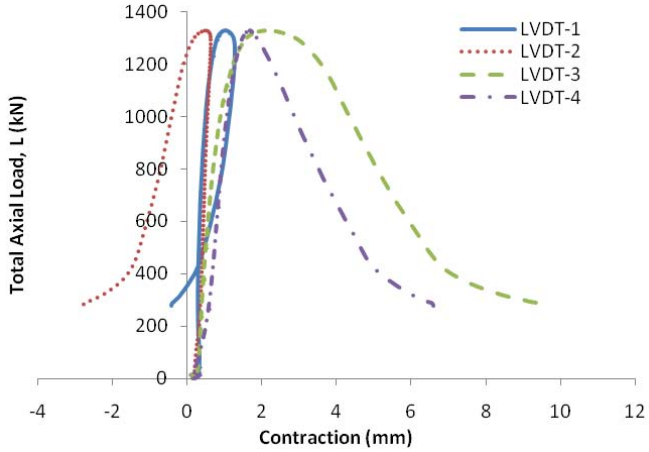

Figure 4.17: Total axial load-contraction response of the prism Test (II)5-125×250×500

The dilation response as shown in Figure 4.18 indicates that the prism did not expand until load is approximately 1200kN. After the peak load reached, the side of prism where LVDTs-5,-7,-9 and -10 expand significantly while the side where LVDTs-6 and -8 expand very slowly until the prism failed.

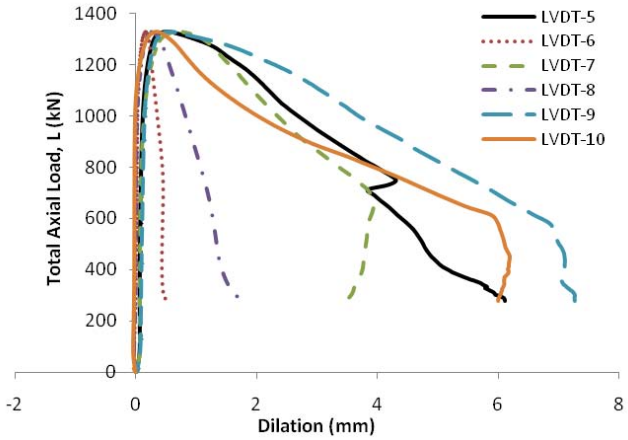

Figure 4.18: Total axial load-dilation response of the prism Test (II)5-125×250×500

Figure 4.19 shows the images of the concrete failure. The compression failure is clearly seen. The concrete prism failed only in one face where LVDTs-3 and -4 were placed (see also Figure 4.17). The angle of the crack was measured around 27° and a "non-explosive" failure occurred.

(a) face/front view *(d) side view*

Figure 4.19: Failure mode of concrete Test (II)5-125×250×500

TEST(II)6-125X250X500

Figure 4.20 illustrates the contraction response as recorded by axial LVDTs. The graph indicate Test(II)6-125×250×500 has similar behaviour with prism Test(II)4-125×250×500 and Test(II)5-125×250×500. Before peak load, the whole prism is in compression. The edges of prism where LVDTs-1 and -2 were placed still in compression after the peak load reached, however, the contraction of the two other edges drop significantly.

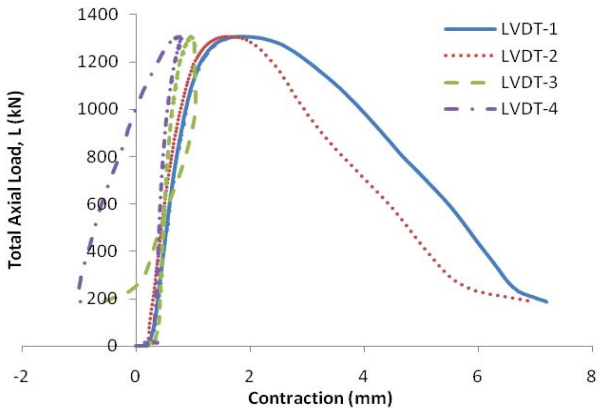

Figure 4.20: Total axial load - contraction response of the prism Test (II)6-125×250×500

The relationship between total axial load and dilation is depicted in Figure 4.21. The graph indicates the prism start to expand when the total axial load is approximately 1200kN and increase slightly up to peak load of 1,309kN. After that point the prism expands significantly.

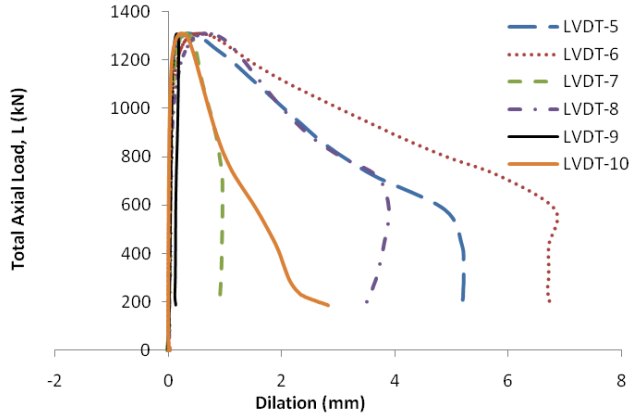

Figure 4.21: Total axial load-dilation response of the prism Test (II)6-125×250×500

A "non-explosive" failure happened and the failure pattern shown in Figure 4.22. The angle of the crack was 25°. The prism failed only in one face where LVDTs-1 and -2 were set up.

The compressive failure of prisms of width 125mm, height 250mm and length 500mm as shown in the images in Figure 4.16(a), Figure 4.19(a) and Figure 4.22(a) indicate the damage zone developed almost the entire of the prism height. This means that the damage zone of short prism (ratio height to width is 2) is the total height of prism test.

(a) front/face view *(b)side view*

Figure 4.22: Failure mode of concrete test Test(II)6-125×250×500

TEST(II)7-125X125X500

The contraction response of prism Test (II)7-125×125×500 shows the whole prism is in compression until the peak load reached (Figure 4.23). The contraction as recorded by LVDT-1 and -2 increases considerably until the prism failed.

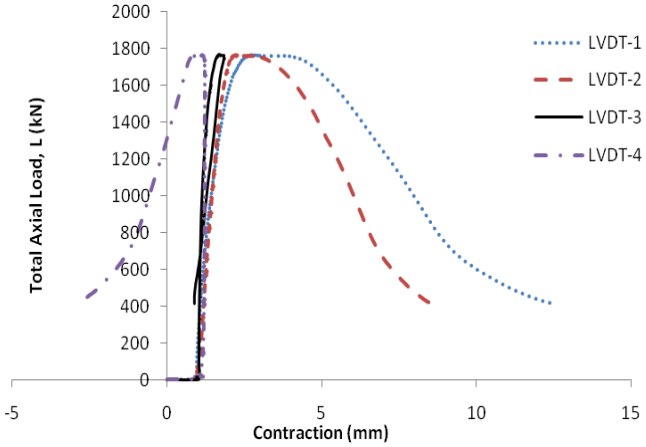

Figure 4.23: Total axial load - contraction response of the prism Test (II)7-125×125×500

The dilation response of prism Test (II)7-125×125×500 is depicted in Figure 4.24. The curve indicates that the prism expand near the peak load. After peak load the prism expand significantly.

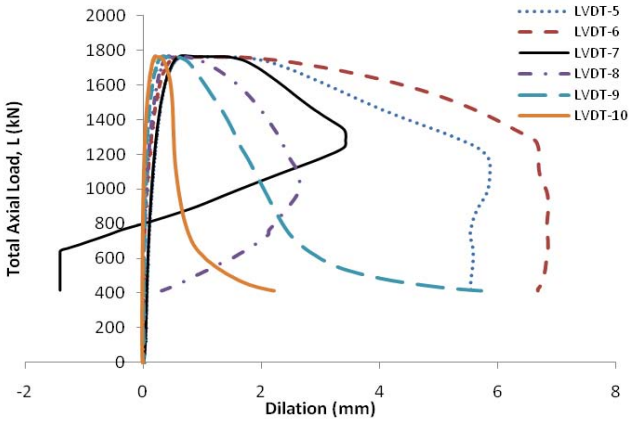

Figure 4.24: Total axial load-dilation response of the prism Test (II)7-125×125×500

The failure pattern of Test(II)7-125×125x500 is difference from other sizes of prism. Let us consider Figure 4.25. The failure occurred only in one face and the wedges

developed on both sides of prism almost the whole of prism length. The angle of upper truncate as big as 38° and the angle of lower truncate around 24°. The localised crushing line placed around one third of prism height from the top of prism.

(a) front/face view *(b)side view*

Figure 4.25: Failure mode of concrete Test (II)7-125×125×500.

TEST(II)8-125X125X500

Figure 4.26 illustrates the whole prism in compression up to peak load. After this point, the edges of the prism, where the LVDTs-1,-2 and -3 were placed, still in compression while LVDT-4 suddenly drops. The values of LVDT-1 and LVDT-2 increase significantly after the peak load reached.

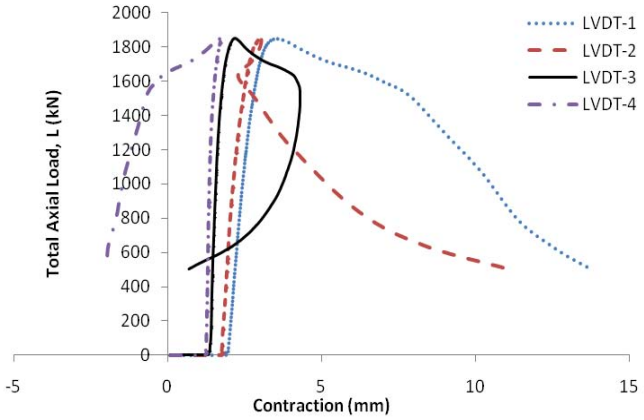

Figure 4.26: Total axial load - contraction response of the prism Test (II)8-125×125×500

Figure 4.27 shows the whole prism starts to expand when load applied to the prism approximately 800kN. After peak load, the both sides of prism expand significantly until the prism failed.

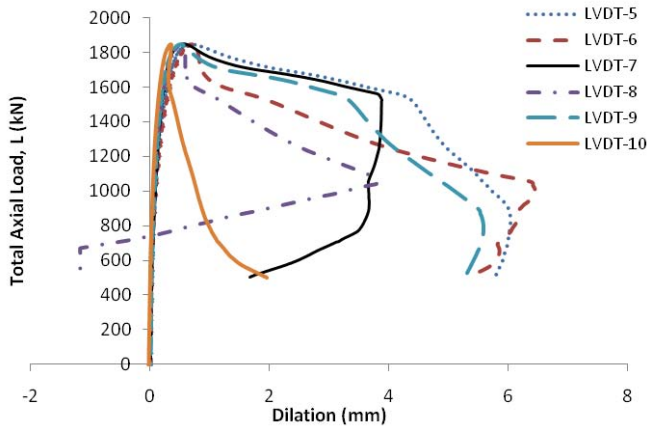

Figure 4.27: Total axial load-dilation response of the prism Test (II)8-125×125×500

The failure pattern of prism Test(II)8-125×125x500 in Figure 4.28 is almost same with the failure pattern of prism Test(II)7-125×125x500 previously. The wedges developed on both sides almost along the whole prism length *S*. The angles of upper truncate as big as 39° and lower truncate just around 27°. The position of the localized crushing line around one third of prism height from the top of prism.

(a) front/face view *(b)side view*

Figure 4.28: Failure mode of concrete Test (II)8-125×125×500

TEST(II)9-125X125X500

The contraction from axial LVDTs readings is shown Figure 4.29. The graph indicates the whole prism in compression until the peak load reached. The contraction of the edges where LVDTs-1 and -3 were placed increases significantly as the load steady at peak load of 1732kN while the contraction of the edges where LVDTs-2 and -4 were placed decreases and finally in tension when the prism failed. This means that before peak load, the compressive load was uniform distributed to the whole prism, however, after peak load more applied load on the side where axial LVDTs-1 and -3 thus more failure occurred on this side.

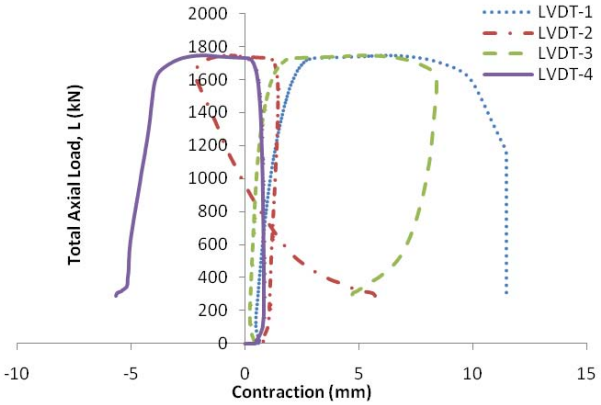

Figure 4.29: Total axial load - contraction response of the prism Test (II)9-125×125×500

The lateral LVDTs recording of prism Test (II)9-125×125×500 is depicted in Figure 4.30. The whole prism starts to expand when the load applied to the prism approximately 700kN. After peak load reached, the side of prism where LVDTs-5,-7 and -9 were placed expands significantly while the side of prism where LVDTs-6,-8 and -10 were placed expand slightly.

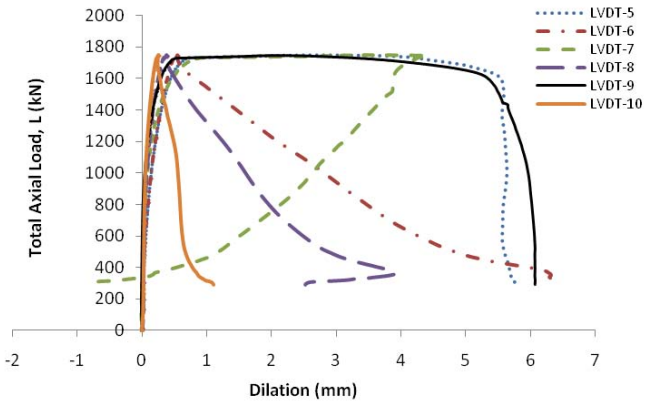

Figure 4.30: Total axial load-dilation response of the prism Test (II)9-125×125×500

The images of failure concrete prism of Test (II)9-125×125×500 is shown in Figure 4.31. It can be seen that the both side of prism has softened and the wedges formed. The wedges occurred along the whole length of prism. The angles of upper truncate as big as 41° and lower truncate just around 28°. The pattern of the failure almost same with the others test on the same size of prism as described previously. The position of the localized crushing line is one third of prism height from the top of prism.

(a) *(b)*

Figure 4.31: Failure mode of concrete Test (II)9-125×125×500.

TEST(II)10-100X200X400

The contractions of the four edges of prism are very similar (Figure 4.32). The contraction increases as the load increases. This means that the applied load is uniform distributed to the whole of the prism. After peak load, the contraction of the edges of the

prism suddenly drop (LVDTs-3 and -4) while the other edges of prism increase slightly (LVDTs-1 and -2).

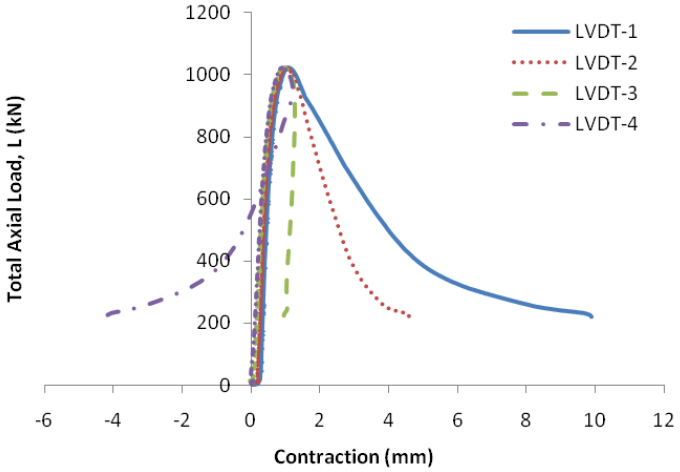

Figure 4.32: Total axial load - contraction response of the prism Test (II)10-100×200×400

The whole prism starts to expand when the applied load is approximately 600kN. After that the prism expands very slightly up to peak load (Figure 4.33). The similar trend is shown on ascending branch of the graph but small scatter occurred on descending branch of the graph.

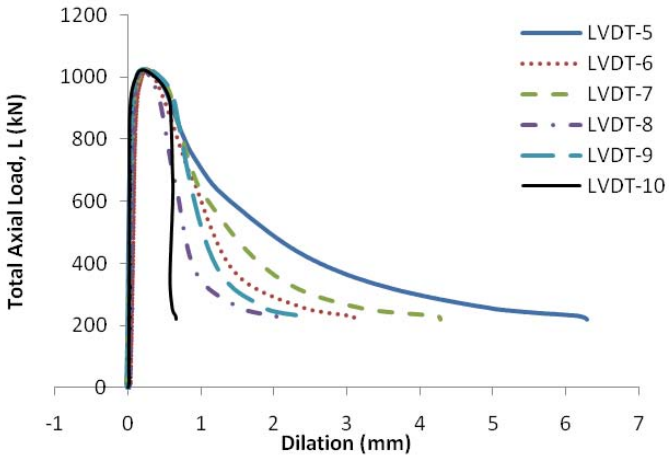

Figure 4.33: Total axial load-dilation response of the prism Test (II)10-100×200×400

Figure 4.34 shows the concrete softened and the wedges clearly formed almost along the both sides of prism. The wedge on the right side broke completely away from the body of the prism. The angle of the wedge was recorded approximately 31°.

(a) front/face view *(b)side view*

Figure 4.34: Failure mode of concrete (II)10-100×200×400

TEST(II)11-100X200X400

The whole prism is in compression after the load reached 300kN (Figure 4.35). The pattern is almost same. After peak load, the contraction values of LVDTs-1 and -2 drop, while the contraction values of LVDTs-3 and -4 increase with a decrease of the total axial load.

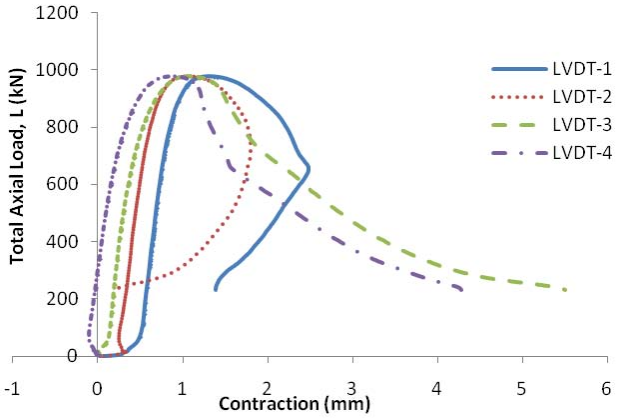

Figure 4.35: Total axial load - contraction response of the prism Test (II)11-100×200×400

Figure 4.36 illustrates the dilation response of Test (II)11-100×200×400 as recorded by using lateral LVDTs. The graph indicates the side of prism where LVDT-6,-8 and -10 were placed expand since the beginning of the loading but after peak load, the dilation on this side of prism suddenly drop. The dilation on the other side of prism

where the LVDTs-5,-7 and -9 were set up still increases with a decrease of the total axial load.

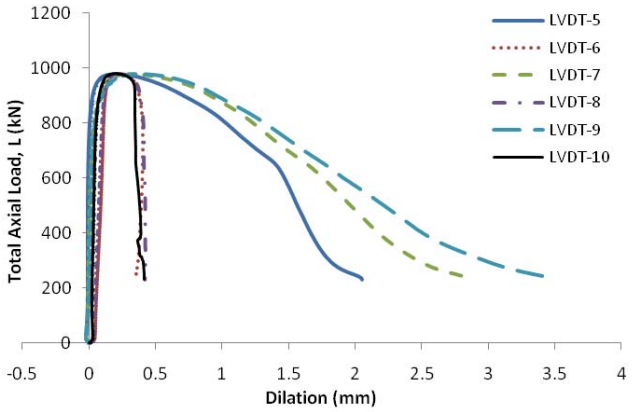

Figure 4.36: Total axial load-dilation response of the prism Test (II)11-100×200×400

The images in Figure 4.37 show the failure of prism Test(II)11-100×200×400. The prism failure occurred just in one face where axial LVDTs-3 and -4 were placed. The angle of the wedge was recorded approximately 29°.

(a) front/face view *(d) side view*

Figure 4.37: Failure mode of concrete prism Test(II)11-100×200×400

TEST(II)12-100X200X400

Figure 4.38 illustrates the contraction as recorded by using axial LVDT. The graph implies that the edges of prism where LVDTs-1,-3 and -4 are in compression while the other edge of prism in tension. When the total axial load is approximately 750kN, the whole prism is in compression. Just after peak load reached, the value of

LVDTs-3 and -4 recording drop suddenly while the two others LVDTs increase as the load decreases.

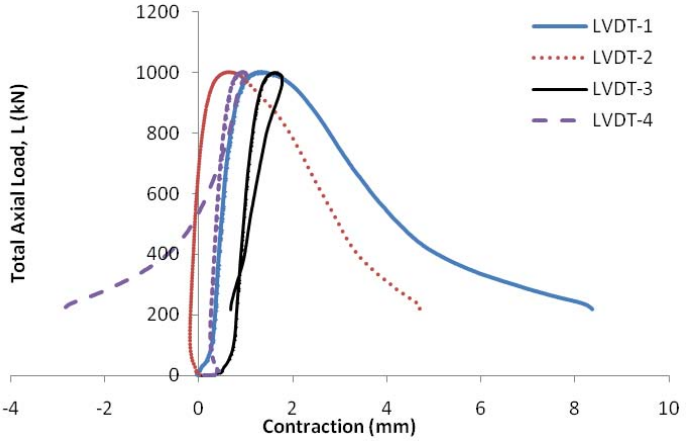

Figure 4.38: Total axial load - contraction response of the prism (II)12-100×200×400

The dilation value from lateral LVDTs reading is depicted in Figure 4.39. The graph indicates the prism more expand in the side of prism where lateral LVDT-5,-7 and -9 were placed.

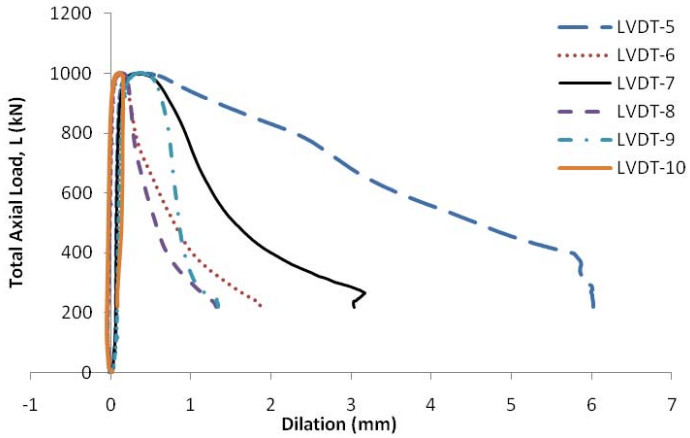

Figure 4.39: Total axial load-dilation response of the prism Test (II)12-100×200×400

Figure 4.40 shows the images of the failure of concrete prism Test(II)12-100×200×400. The prism failed only in one face of prism. The wedge developed on both wide of prism with angle of 22°.

(a) front/face view *(c) side view*

Figure 4.40: Failure mode of concrete prism Test(II)12-100×200×400

TEST(II)13-75X150X300

Figure 4.41 illustrates the whole prism is in compression. The contraction of the four edges of the prism increase as the load increases. After the peak load reached, the contraction of LVDTs-1 and -2 reading decrease while LVDTs-3 and -4 increase as the applied load decreases.

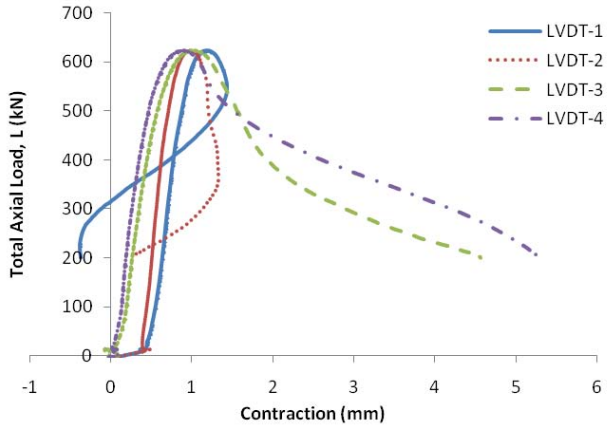

Figure 4.41: Total axial load - contraction response of the prism (II)13-75×150×300

The dilation of Test (II)13-75×150×300 as recorded by lateral LVDTs is depicted in Figure 4.42. The graph indicates that the dilation of LVDT-5,-7 and -9 increases significantly after the peak load reached.

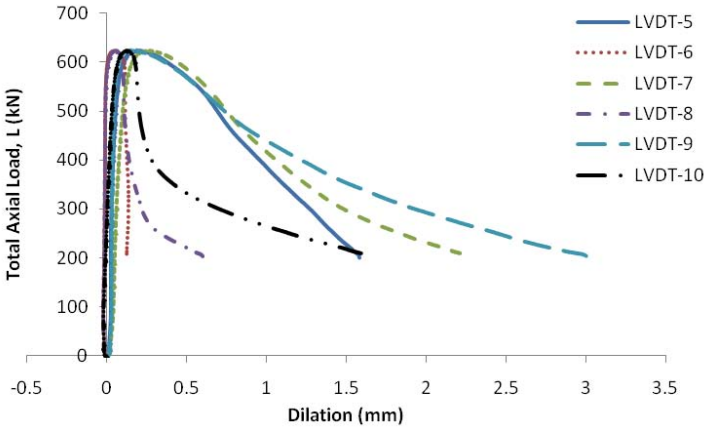

Figure 4.42: Total axial load-dilation response of the prism Test (II)13-75×150×300

Figure 4.43 shows the images of the failure of the prism. The whole prism is failure. More cracks occurred on the face of prism where axial LVDTs-3 and -4 were placed. The angle of the wedge is approximately 24°.

(a) front/face view *(c) side view*

Figure 4.43: Failure mode of concrete Test (II)13-75×150×300

TEST(II)14-75X150X300

Figure 4.44 illustrates the total axial load and contraction response of Test(II)14-75×150×300. The graph indicates that the whole prism compressed since the beginning of loading. The contraction of the four edges of the prism increase as the load increases. After the peak load reached, the contraction of LVDTs-1 and -2 reading increase while LVDTs-3 and -4 drop as the applied load decreases.

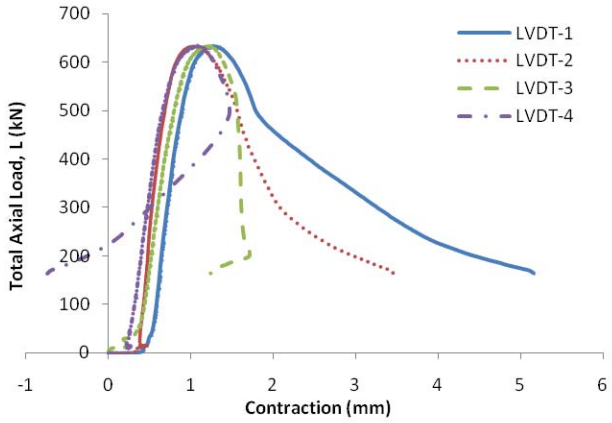

Figure 4.44: Total axial load - contraction response of the prism Test(II)14-75×150×300

Figure 4.45 shows the prism expand very slowly on ascending branch of the curve but after peak load reached, the side of the prism where LVDT-6 and -8 expands significantly until the prism failed while the others LVDTs' value drop.

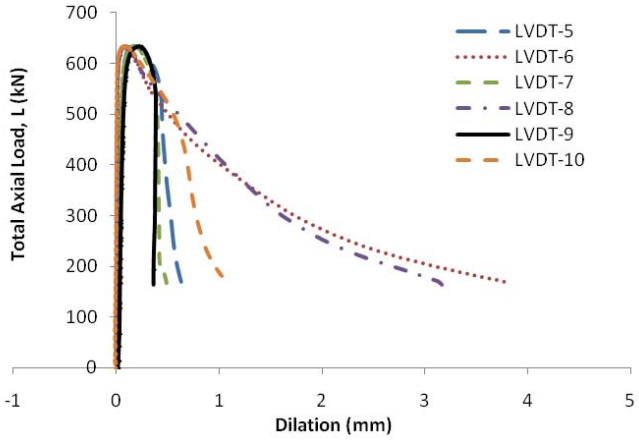

Figure 4.45: Total axial load-dilation response of the prism Test (II)14-75×150×300

The images of the failure of prism Test (II)14-75×150×300 is shown in Figure 4.46. The pattern of crack almost same with Test (II)13-75×150×300 as described previously. The whole prism compressed, the load distributed evenly to the whole prism (see Figure 4.44). After peak load, the contraction on the face of prism where LVDT-1 and -2 were placed increases as the applied load decreases. More failure occurred on this face. The angle of the wedge is approximately 24°.

(a) face/front view *(c) side view*

Figure 4.46: Failure mode of concrete Test (II)14-75×150×300

TEST(II)15-75X150X300

Figure 4.47 illustrates the contraction value from axial LVDTs readings. The graph indicates that the whole prism is compressed. The pattern of the response of all edges of the prism is the similar. This means that the load applied to the prism uniformly. After the peak load the contraction of the edges where LVDTs-3 and -4 set up increase as the load decreases.

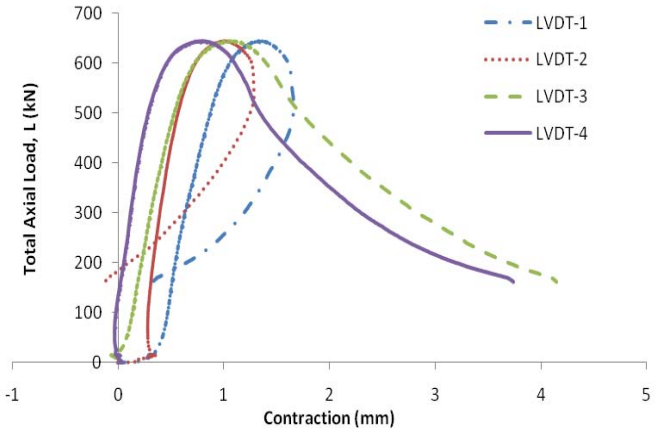

Figure 4.47: Total axial load - contraction response of the prism (II)15-75×150×300

Figure 4.47 shows the prism expand very slightly up to peak load but after peak load reached, the side of the prism where LVDT-5,-7 and -9 expands significantly until the prism failed while the others LVDTs' value drop suddenly.

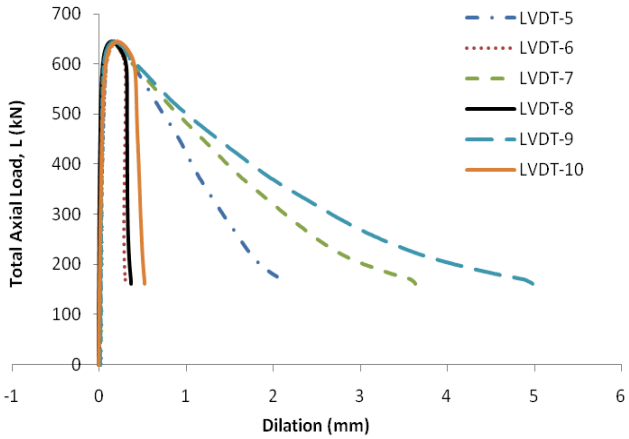

Figure 4.48: Total axial load-dilation response of the prism Test (II)15-75×150×300

The images of failure concrete prism are shown in Figure 4.49. The wedges formed on both side of prism almost along the prism length. The more failure occurred on the face of prism where large contraction occurred. The angle of the wedge was quantified approximately 29°.

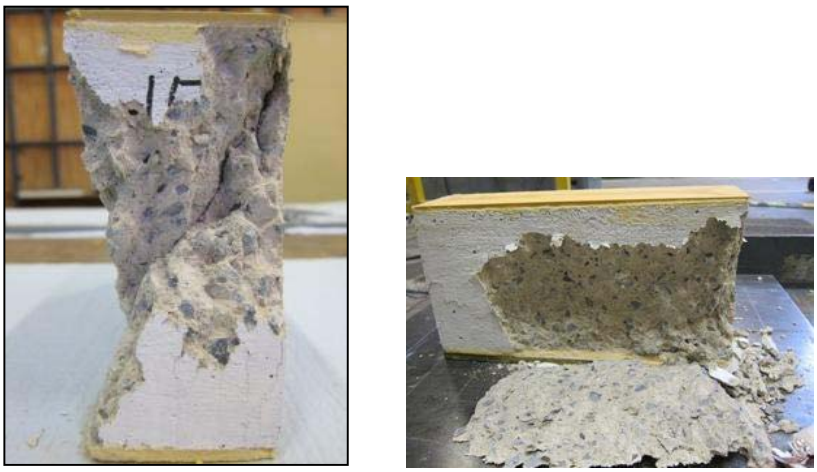

(a) face/front view *(c)side view*

Figure 4.49: Failure mode of concrete Test (II)15-75×150×300

TEST(II)16-50X100X200

Figure 4.50 illustrates the total axial load and contraction response of Test(II)16-50×100×200. The graph indicates that the whole prism compressed evenly since the beginning of loading. The contraction of the four edges of the prism increase as the load

increases. After the peak load reached, the contraction of LVDTs-1 and -2 reading increases while LVDTs-3 and -4 drop as the applied load decreases.

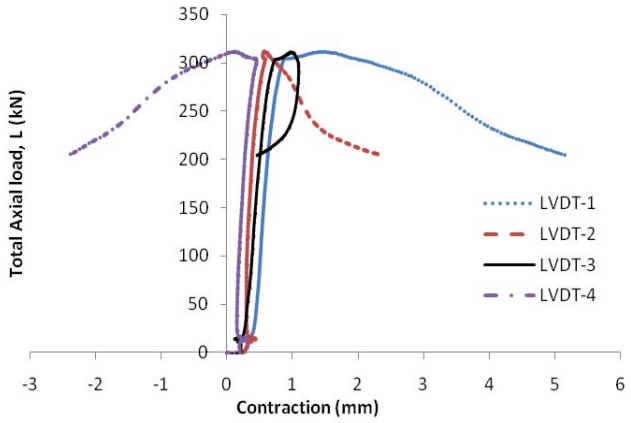

Figure 4.50: Total axial load - contraction response of the prism (II)16-50×100×200

The dilation of Test (II)16-50×100×200 as recorded by lateral LVDTs is depicted in Figure 4.51. The graph indicates that up the peak load, the dilation of the whole prism increases slightly but after that the dilation of LVDT-5 increases significantly until the prism failed.

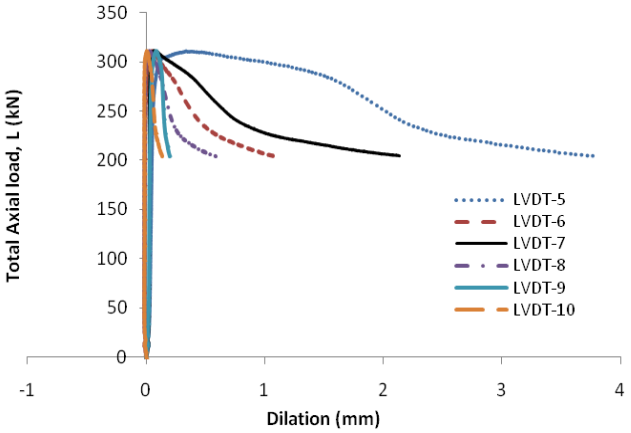

Figure 4.51: Total axial load-dilation response of the prism Test (II)16-50×100×200

Figure 4.52 illustrates the images of the failure of prism Test (II)16-50×100×200. The images show the failure occurs on the whole prism. This means that the whole prism compressed, the load distributed evenly to the whole prism. The angle of the wedge is approximately 32°.

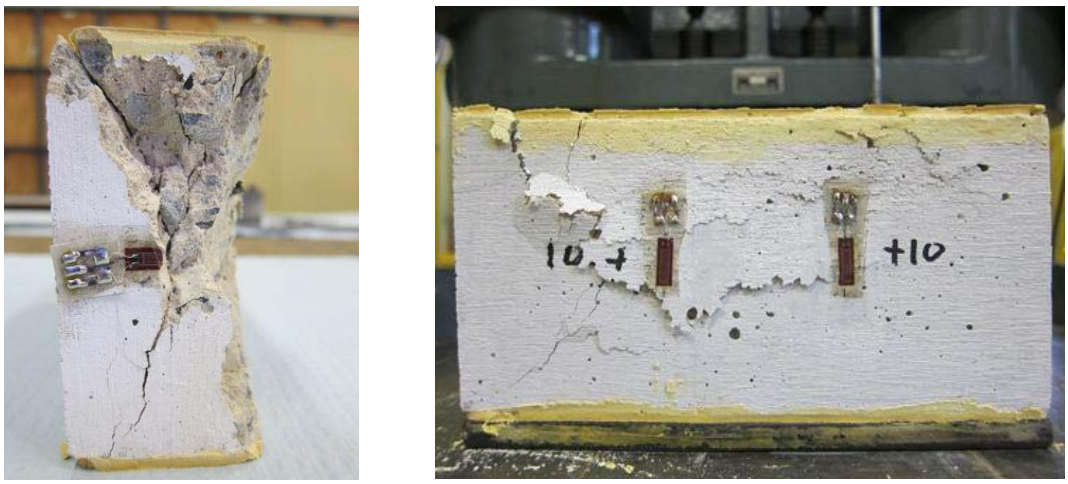

(a) front/face view *(b) side view*

Figure 4.52: Failure mode of concrete Test (II)16-50×100×200

TEST(II)17-50X100X200

Figure 4.53 shows the relationship between total axial load and contraction of Test (II)17-50×100×200. The edges of prism, where LVDT-1, LVDT-2 and LVDT-3 are positioned, are in contraction while the edge, where LVDT-4 is placed, is slightly in tension. Accidentally the eccentrically load occurred at low load. The value of LVDT-4 is in contraction when *L* is about 250kN. A large contraction occurred on the face of prism where LVDT-1 was placed.

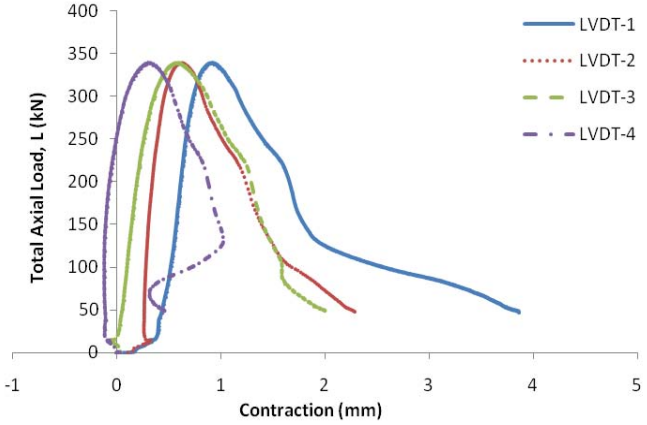

Figure 4.53: Total axial load - contraction response of the prism Test(II)17-50×100×200

Figure 4.54 illustrates how the prism of Test (II)17-50×100×200 expands when the prism is subjected to a uniaxial compression load. The graph indicates that up to peak load the both side of prism expand slightly. However, after this point the both sides expand significantly as the load decrease. The similar response occurs on the three LVDTs -6, -8 and -10 those are placed in one side.

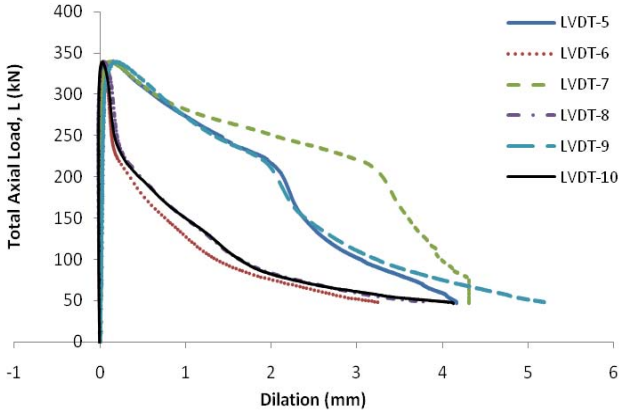

Figure 4.54: Total axial load-dilation response of the prism Test (II)17-50×100×200

Figure 4.55 shows the images of the failure of prism Test (II)17-50×100×200. The images show the whole prism failed. This means that the whole prism compressed evenly, the load distributed to the whole prism. The angle of the wedge is approximately 27°.

(a) front/face view *(c) side view*

Figure 4.55: Failure mode of concrete Test (II)17-50×100×200

TEST(II)18-50X100X200

Figure 4.56 shows the last test in this experimental test. The contraction of LVDTs reading values increases when the load increases at ascending branch of the curve up to peak load then the contraction still increases when the load decreases until the prisms failed. The similar response of all axial LVDTs shown due to the whole prism is compressed uniformly.

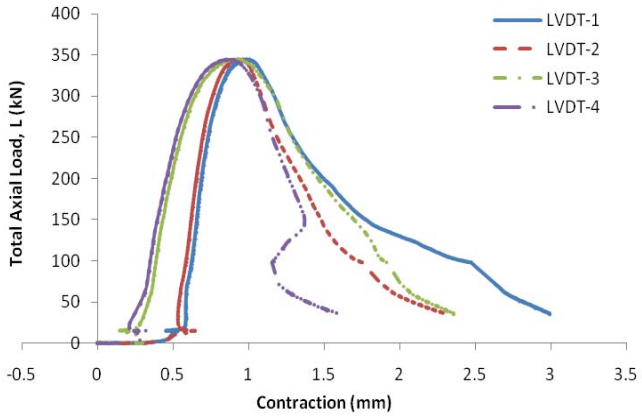

Figure 4.56: Total axial load - contraction response of the prism (II)18-50×100×200

Figure 4.57 illustrates the response of total axial load and dilation of (II)18-50×100×200. The graph indicates the whole prism is expands very slowly since the beginning of loading up to peak load. The responses are similar up to peak load. After the peak load, the dilation on the side of prism where LVDTs-5,-7 and -9 are set up increase significantly as the load decreases.

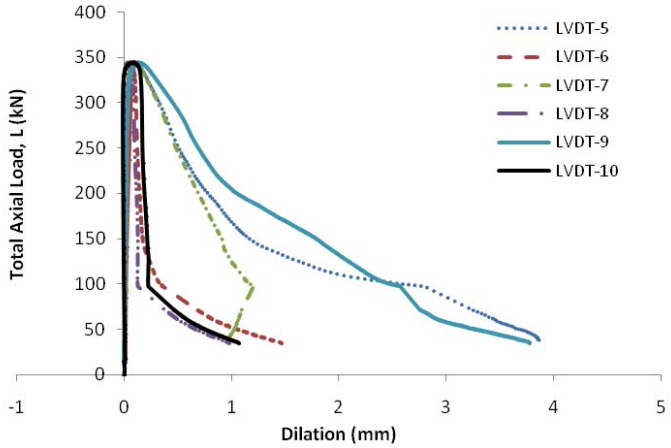

Figure 4.57: Total axial load-dilation response of the prism Test (II)18-50×100×200

The images in Figure 4.58 show the failure of Test (II)18-50×100×200. The images show the whole prism failed in compression. The whole prism compressed evenly, the load distributed to the whole prism. The angle of the wedge is approximately 24°.

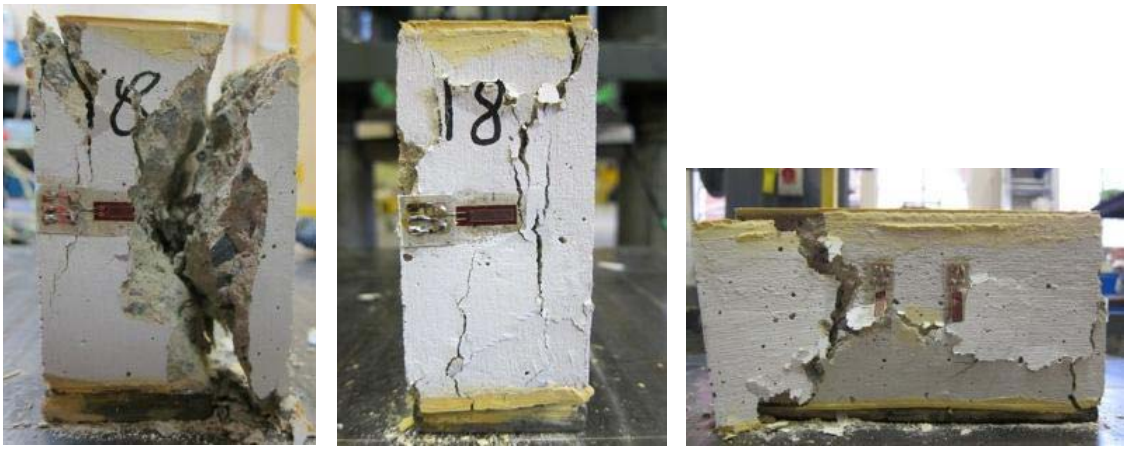

(a) *(b)* *(c)*

Figure 4.58: Failure mode of concrete Test (II)18-50×100×200; (a) and (b) face/front view; (c) side view.

The deformation in axial and lateral directions for a given total axial load and the images of the concrete prism failure for 18 prisms were shown. In the next section this data is analysed, discussed and compared in the same size of prism then the average responses in one size are determined and compared to other prisms size.

4.4 Analysis of Test Results

4.4.1 Method of analysis

The raw data in Section 4.3 described the deformations in axial and lateral directions of every prism under increasing axial load. In this section that raw data results for every concrete prism are analysed. The experimental test analysis follows the analysis as was used in the first set of experimental test in Chapter 3.

The method of analysis in axial deformation is exactly the same as was used in the first set of experimental test at Section 3.4.1; however, there is a difference in lateral deformation. Three lateral LVDTs were used in this experimental test instead of one LVDT in one side of prism. Thus dilation of one side of the prism is average value of these three transducers reading (see also Figure 4.3). Let us consider Eq. 3-6, the average value of LVDTs-5, -7 and -9 recording represent as D_1 and the average value of LVDTs-6, -8 and -10 recording represent as D_2 in that equation. Hence the total lateral expansion E can be quantified using Eq. 3.6. The rest of the analyses used the same method as was applied on analysis in the first set of experimental test.

4.4.2 Individual tests

The individual tests analysis of the second set of experimental test are presented and described in the same size of the prism. Not all prism test is described in details, only the first prism Test (II)1-125×375×500 is analysed step by step and discussed in details. Then this prism is compared to other prisms in the same size in axial deformation and followed by in lateral deformation. Next the similar analyse is carried out in comparison analysis to other next five sets of size of Test (II)-125×250×500, Test (II)-125×125×500, Test (II)-100×200×400, Test (II)-75×150×300 and Test (II)-50×100×200.

4.4.2.1 Tests at 125mm width and 375mm height (125×375×500)

The prism Test (II)1-125×375×500 is described and analysed in detail below. The raw data in Section 4.3 shows the contraction of every edges of the prism thus to obtain the contraction of the whole prism, the average of those contraction as recorded by axial LVDTs is required by using Eq.3.1. As a result, the total axial load *L* and total

axial contraction C is shown in Figure 4.59. The total axial load L is the axial load applied to the whole prism and total axial contraction C is the contraction of the whole prism. The graph indicates that the "settle down the position" occurred on L-C relationship at the early of loading as shown in a dash line. This occurs due to the setting down of the platens and dental paste contraction. The concrete prism surface is not exactly flat thus when the concrete prism is set on the loading platen and applied the load, the prism needs to "settle". This graph is required to refine. Hence Figure 4.59 was corrected into Figure 4.60 by using the same method as was described in Figure 3.59.

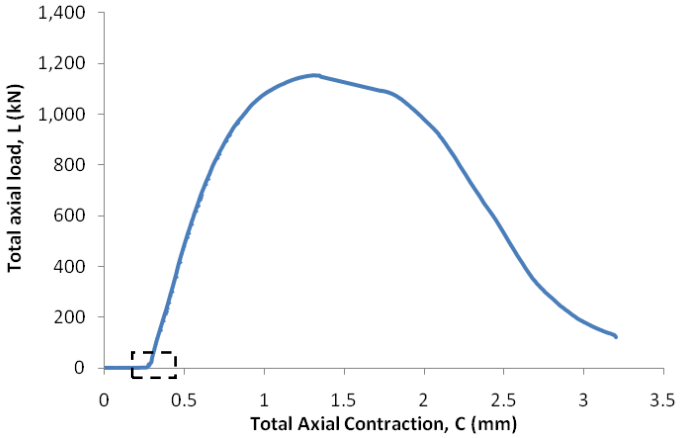

Figure 4.59: Total axial load-total axial contraction for Test (II)1-125×375×500

Figure 4.60 illustrates the response of total axial contraction for a given applied load. The graph indicates when the peak of total axial load L_p reached 1156kN, total axial load C_p approximately 1.04mm.

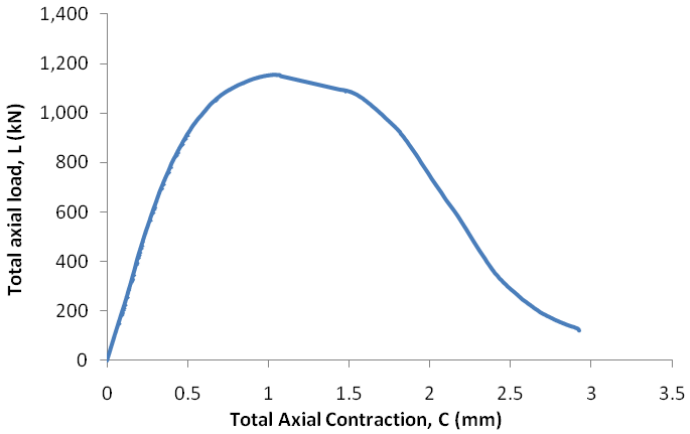

Figure 4.60: Total axial load-total axial contraction for Test (II)1-125×375×500 (new axis)

The next figure shows the relationship between the axial load P and total axial contraction over one single wedge $C/2$ (Figure 4.61). The graph of P-$C/2$ is half of the L-C graph (see again Figure 3.57 and Figure 3.62). Thus $C_p/2$ approximately 0.52mm when the axial load over one wedge reached the peak P_p of 578kN.

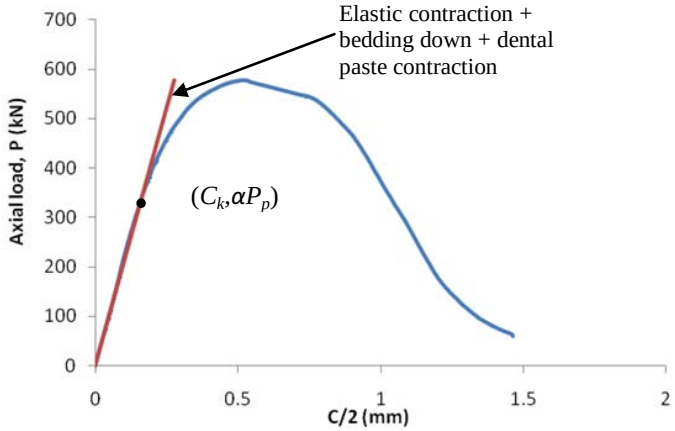

Figure 4.61: Axial load-C/2 response of the prism Test (II)1-125×375×500

Up to αP_p there is only elastic deformation occurs on the prism where α is assumed 60%. Non-elastic deformation due to micro-cracking occurred when axial load P reach 60%P_p approximately 347kN. It corresponds to $C/2$ around 0.17mm (Figure 4.61). Before this point, the elastic contraction occurred. The non-elastic deformation due to micro-cracking or the slip wedge is obtained by removing the elastic contraction from the P-$C/2$ response as shown in Figure 4.62 and using Eqs. 3.2 and 3.3.

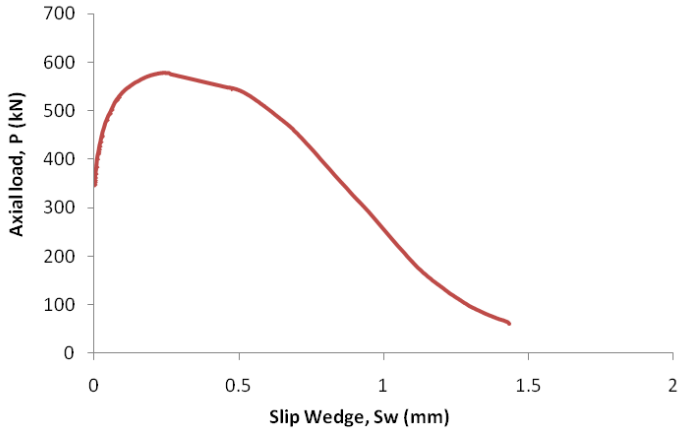

Figure 4.62: Axial load-slip wedge response of the prism Test (II)1-125×375×500

The deformation due to micro-cracking, S_w is shown in Figure 4.62 and Figure 4.63. S_{wp} is approximately 0.24mm at peak of load. Figure 4.62 and Figure 4.63 illustrate the P-S_w and P_w-S_w responses. The graphs indicate the same trend because of P_w is P divided by the prism length S [for Test (II)1-125×375×500, S is 500mm]. P_w is wedge load per millimeter wedge thickness (see again Figure 3.65)

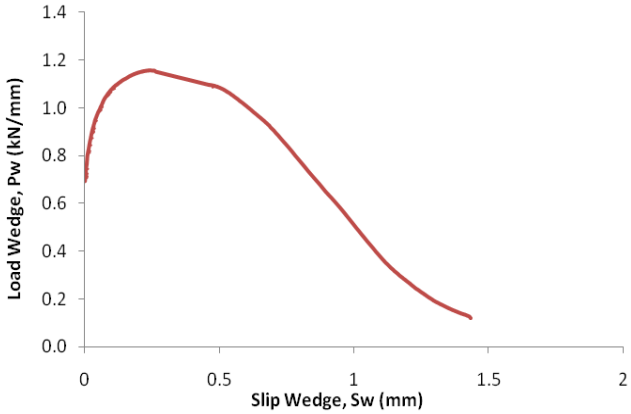

Figure 4.63: Load wedge-slip wedge response of the prism Test (II)1-125×375×500

The main interest of this research is the stress and non-linearity deformation due to micro-cracking σ_w-S_w for prism tests. Eq. 3.4 is used to quantify the stress wedge σ_w. The stress wedge is the load per mm wedge thickness P_w divided by the wedge depth d_w. The stress wedge and slip wedge response of the concrete prism is presented in Figure 4.64. The slip wedge increases as the stress wedge increases until the peak of the stress wedge reached. After that, on descending branch the slip wedge increases significantly with a decrease of stress wedge. The maximum stress wedge is 19MPa relates to slip wedge at peak load S_{wp} at is approximately 0.24mm.

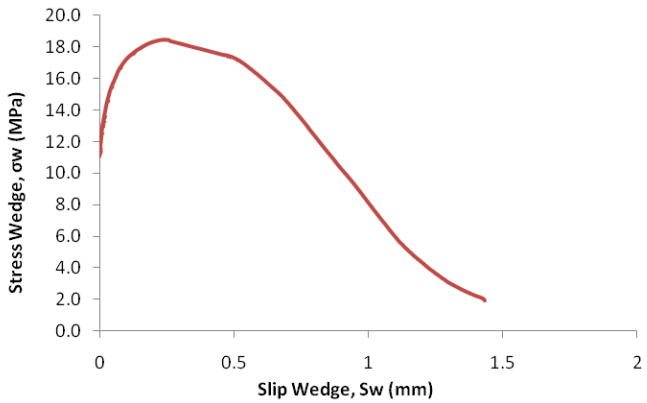

Figure 4.64: The stress wedge-slip wedge response of the prism Test (II)1-125×375×500

After axial deformation now lateral deformation is discussed in detail as describe below. Figure 4.65 illustrates the relationship between the total axial load and dilation. The dilation is obtained by the average value of lateral LVDTs readings at one side of prism. The average value of dilation in one side of prism is represented by D_1 and D_2 in the other side of prism as described previously in Section 4.4.1. D_1 is the average value of LVDTs-5,-7,-9 readings and D_2 is the average value of LVDTs-6,-8,-10 readings (refer to Figure 4.3).

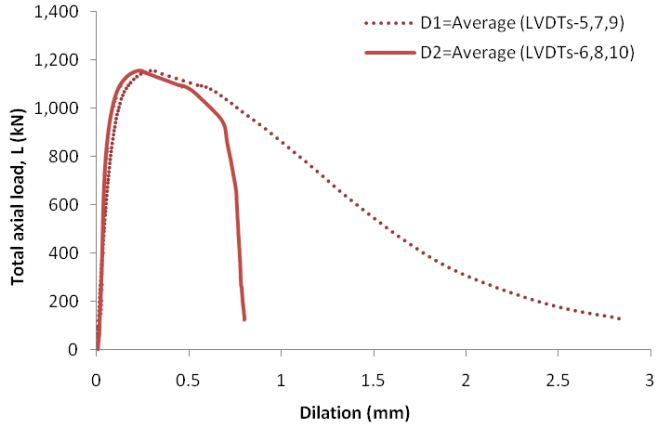

Figure 4.65: Total axial load–average dilation response of the prism Test (II)1-125×375×500

Before peak load the dilation on both sides is similar, the whole prism expands evenly in both sides of prism. After peak load, dilation D_1 is increases considerably and when the prism failed D_1 is approximately 2.8mm, while D_2 increase slowly and when the load reduces to 900kN D_2 drop significantly.

By using Eq. 3.5, total lateral expansion E is obtained as shown in Figure 4.66. When the peak of total axial load L_p reached E_p approximately 0.53mm. The value of E_p is half than total axial contraction at peak load C_p (1.04mm).

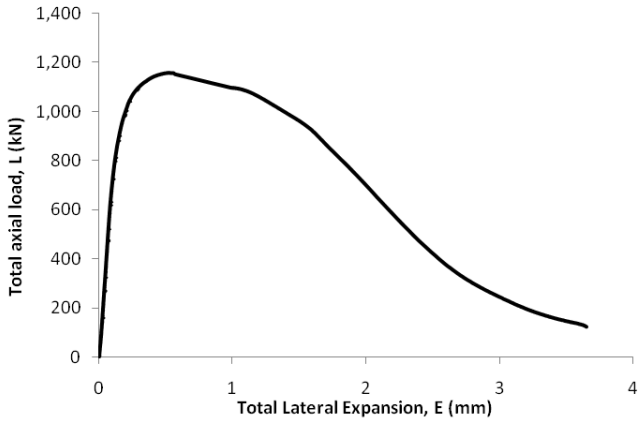

Figure 4.66: Total axial load-total lateral expansion response of the prism Test (II)1-125×375×500

Figure 4.67 shows the axial load and $E/2$ response. This graph is half of L-E response (Figure 4.66). The lateral micro-cracking occurred when $E/2$ approximately 0.05mm, refer to coordinate (R_x, αP_p) in Figure 4.67 where R_x is 0.05 and αP_p is 347kN. Before that point, the elastic expansion due to Poisson's ratio occurred. To analysis the lateral deformation due to micro-cracking, subtract the elastic expansion from the total lateral expansion $E/2$. The result is shown in Figure 4.68.

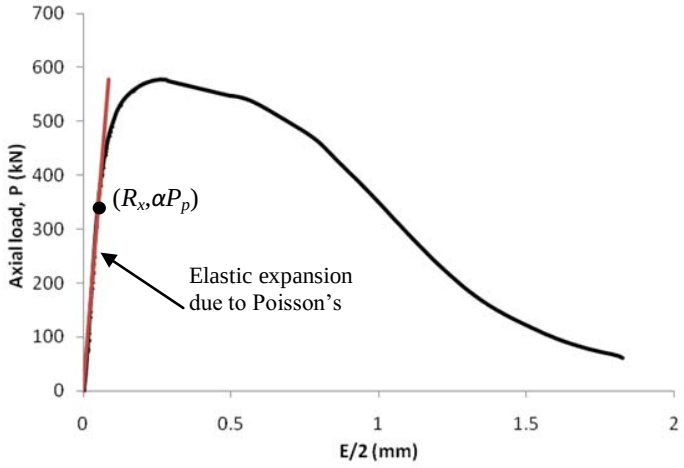

Figure 4.67: Axial load – E/2 response of the prism Test (II)1-125×375×500

Figure 4.68 illustrates the lateral deformation due to micro-cracking V_w. The wedge expansion is obtained by using Figure 4.67 and Eqs. 3.6 and 3.7. The wedge expansion at peak of axial load V_{wp} is 0.18mm.

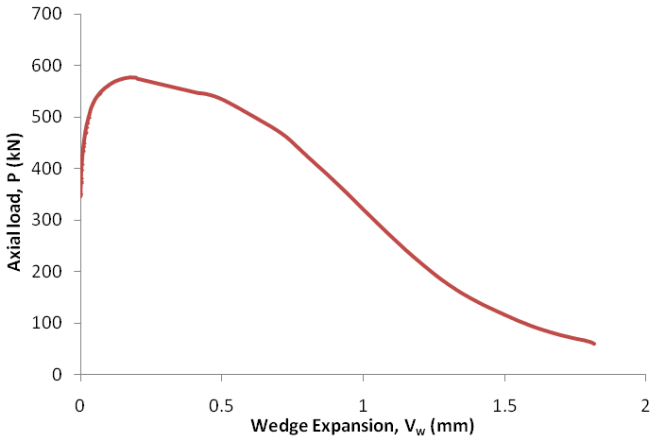

Figure 4.68: Axial load-wedge expansion response of the prism Test (II)1-125×375×500

The response of $P_w - V_w$ as shown in Figure 4.69 is obtained by divide axial load for a single wedge P by prism length S. The wedges expand slowly up to peak load and after peak load reached the wedge expand significantly until the prism failed.

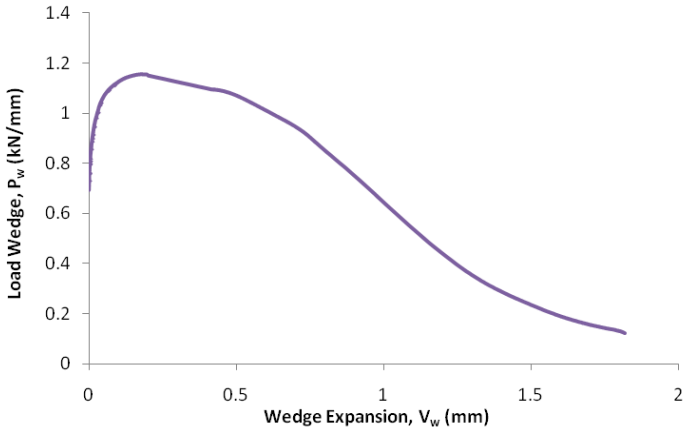

Figure 4.69: Load wedge-wedge expansion response of the prism Test (II)1-125×375×500

Figure 4.70 shows the relationship between stress wedge and wedge expansion of prism of the concrete prism Test(II)1-125×375×500. This relationship is obtained by using Eq. 3.4. The wedge expansion at the maximum stress wedge V_{wp} is approximately 0.18mm. When the prism failed, wedge expansion is 1.85mm.

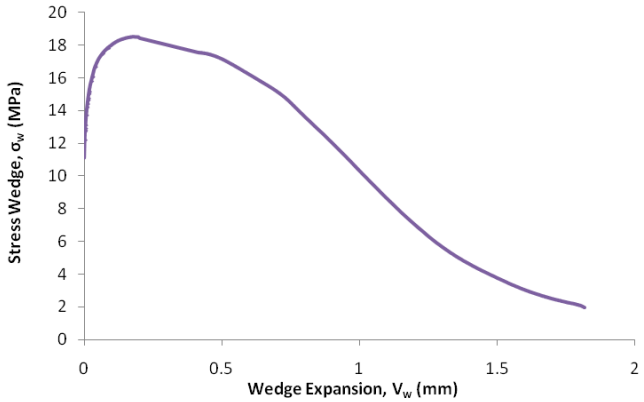

Figure 4.70: The stress wedge - wedge expansion response of the prism Test (II)1-125×375×500

The details and step by step analysis of Test(II)1-125×375×500 have been described previously. The other prisms test in Test(II)-125×375×500 are not analysis in detail one by one like in the first set of experimental test in Chapter 3 but are analysed and discussed in comparison in one size as describe below. The next ten graphs illustrate the comparison analysis in Test(II)-125×375×500 in axial and lateral directions.

First the total axial load and total axial contraction response. The *L*-*C* response of prisms in Test(II)-125×375×500 can be seen in Figure 4.71. The trends of the individual responses are very similar. The peak total axial load L_p and the total axial contraction at peak load C_p of the prisms are very similar those are between 1,151kN to 1,191kN and between 1.04mm to 1.30mm for L_p and C_p respectively (see Table 4.10). The average value of L_p and C_p are 1,166kN and 1.17mm respectively. These parameter values are based on the individual graph.

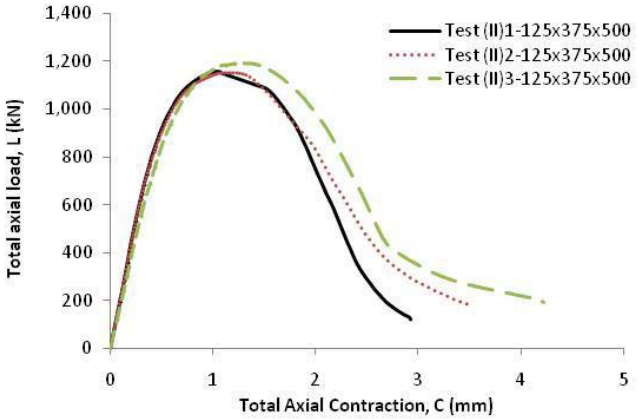

Figure 4.71: Total axial load-total axial contraction response of the prism Test(II)-125×375×500

The next figure illustrates the relationship in one single wedge between axial load and total axial contraction. The *P*-*C*/2 graphs of individual data Test(II)1-125×375×500, Test(II)2-125×375×500 and Test(II)3-125×375×500 are plotted together as shown in Figure 4.72. The *P*-*C*/2 graphs have same pattern with *L*-*C* graphs because *P*-*C*/2 graphs are *L*-*C* graphs divided by 2. The *L*-*C* is the response of load and total axial contraction of the whole prism in terms of two wedges while the *P*-*C*/2 is the response of load and total axial contraction over one single wedge. Hence the values of *P* are between 576kN to 596kN and $C_p/2$ between 0.52mm to 0.65mm (see Table 4.10). The average values of P_p and $C_p/2$ are 583kN and 0.59mm respectively.

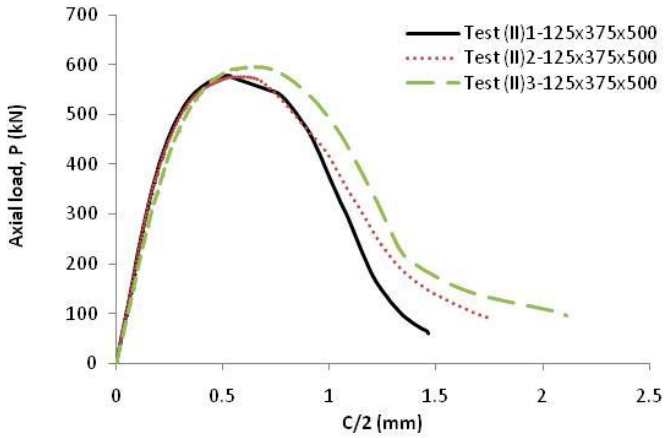

Figure 4.72: Axial load-C/2 response of the prism Test(II)-125×375×500

Up to αP_p the deformation due to micro-cracking is not develop in the prism. After that point the micro-cracking or slip wedge start to develop. The slip wedge S_w of the concrete prisms is determined by subtracting the elastic contraction from the total axial contraction over one wedge *C*/2. The relationship between axial load *P* and slip wedge S_w of Test(II)-125×375×500 depicted in Figure 4.73.

The graphs indicate the responses are very similar. When the axial loads *P* of Test(II)1-125×375×500, Test(II)2-125×375×500 and Test(II)3-125×375×500 are approximately 347kN, 345kN, 357kN respectively, the slip wedge develop in the prism. The slip wedge S_w start to develop almost at the same axial load. Before that point only elastic deformation occurs and there is no non-elastic deformation or deformation due to

micro-cracking. The slip wedges at peak load S_{wp} of Test(II)2-125×375×500 and Test(II)3-125×375×500 are the same of 0.31mm while Test(II)1-125×375×500 is 0.24mm. The average of S_{wp} is 0.29 (see again Table 4.5).

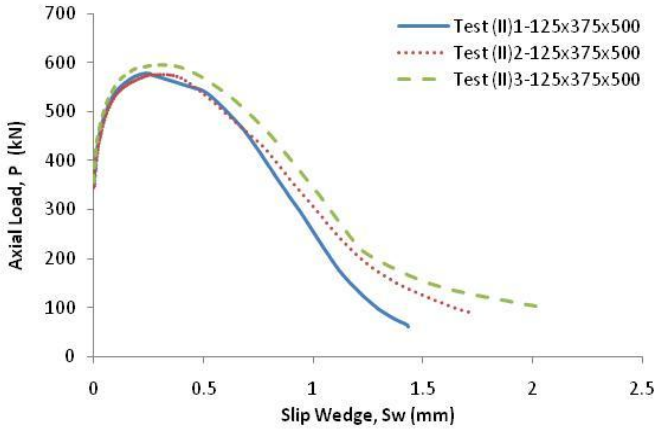

Figure 4.73: Axial load-slip wedge response of the prism Test(II)-125×375×500

Now the axial load P as described previously divided by the length of the prism S. The relationship between the load wedge P_w and slip wedge S_w of Test(II)-125×375×500 is plotted and shown in Figure 4.74. The P_w- S_w graphs are identical with the P- S_w graph in Figure 4.73.

Figure 4.74 indicates the load wedge maximum P_{wp} are varies in the narrow range between 1.15kN/mm to 1.19kN/mm and the average is 1.17kN/mm.

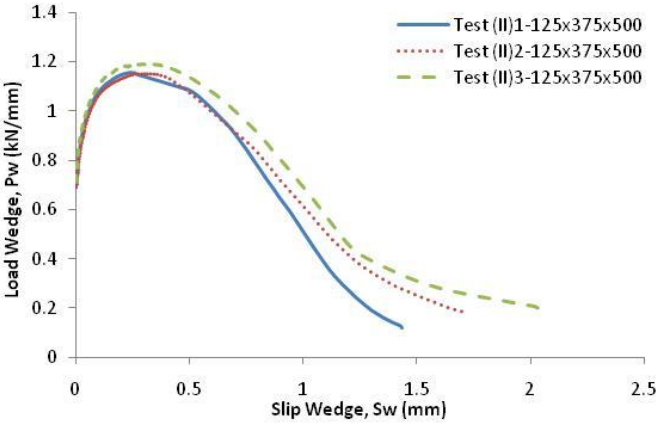

Figure 4.74: Load wedge-slip wedge response of the prism Test(II)-125×375×500

The individual stress wedge-slip wedge relationship of Test(II)-125×375×500 is plotted in one graph as shown in Figure 4.75. The responses of stress wedge-slip wedge were quite similar. The peak wedge stress of Test(II)1-125×375×500 and Test(II)3-125×375×500 are the same 19MPa and Test(II)2-125×375×500 is 18MPa. The average is 19MPa.

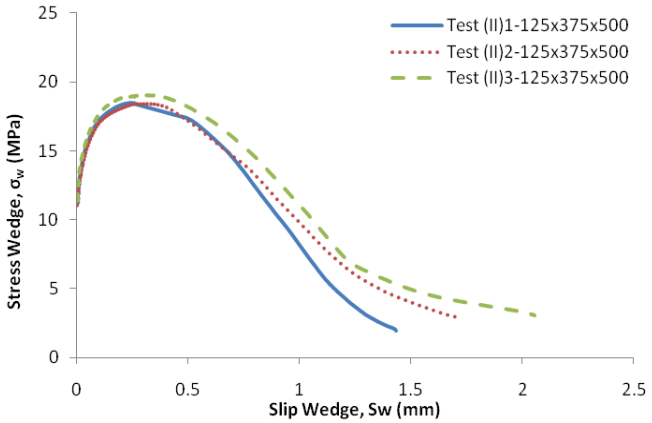

Figure 4.75: Stress wedge-slip wedge response of the prism Test(II)-125×375×500

After analysed the axial deformation, next is the lateral deformation analysis. The next five figures (Figure 4.76 to Figure 4.80) illustrate the deformation of Test(II)-125×375×500 in lateral direction. First the total axial load and total axial expansion *L-E* responses. The graph indicates that the trend of response up to peak load is really identical however the scatter occurred at post-peak region. The total lateral expansion at peak load E_p of Test(II)1-125×375×500, Test(II)2-125×375×500 and Test(II)3-125×375×500 are 0.53mm, 0.49mm and 0.64mm. The average of total lateral expansion at peak load E_p is 0.55mm (see again Table 4.5)

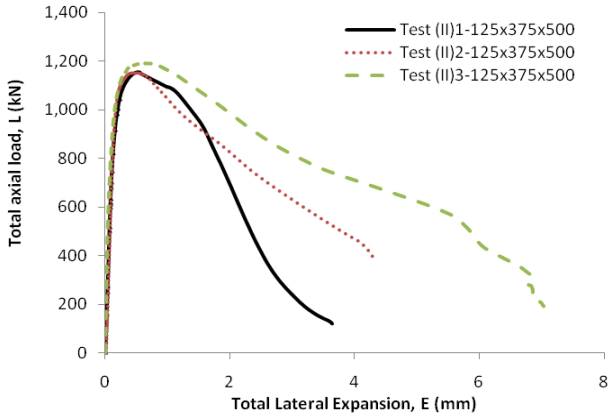

Figure 4.76: Total axial load-total lateral expansion for Test(II)-125×375×500

Analysis over one wedge in lateral deformation that is relationship between load and total lateral expansion (*P*-*E*/2) is described. The *P*-*E*/2 graph has same pattern with *L*-*E* graph because *P*-*E*/2 graph is *L*-*E* graph divided by 2. Figure 4.77 illustrates the relationship of *P*-*E*/2 of all experiment tests in prism Test(II)-125×375×500. The average of total lateral expansion over one single wedge at peak load $E_p/2$ is 0.28mm

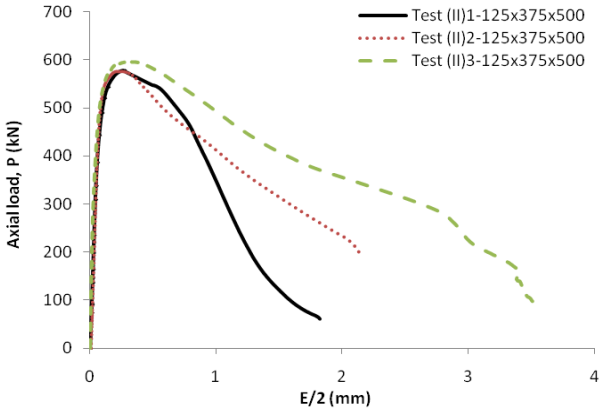

Figure 4.77: Axial load – E/2 response of the prism Test(II)-125×375×500

In analysis over one single wedge, total lateral expansion E is composed of wedge expansion that is represented by V_w and elastic expansion G as explained in the beginning of section 3.4.1 and have been illustrated in Figure 3.69 and Figure 3.70. The relationship between axial load P and wedge expansion V_w of Test(II)-125×375×500 is shown in Figure 4.78. The graph indicates that the responses are quite similar up to peak load and the axial load when the micro-cracking form for all prisms is almost same

approximately 388kN, 399kN and 393kN for Test(II)1-125×375×500, Test(II)2-125×375×500 and Test(II)3-125×375×500 respectively.

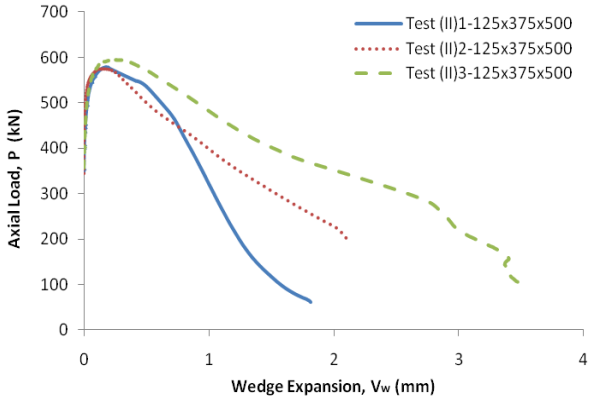

Figure 4.78: Axial load – wedge expansion response of the prism Test(II)-125×375×500

The scatter occurred on the post-peak response. The average wedge expansion at peak load V_{wp} is 0.28mm. This average value is based on each individual Test(II)-125×375×500. The same response is also shown in the Figure 4.79. The graph illustrates the load and wedge expansion per millimeter wedge thickness P_w-V_w. The axial load P in Figure 4.78 is divided by prism length S equal to P_w in Figure 4.79

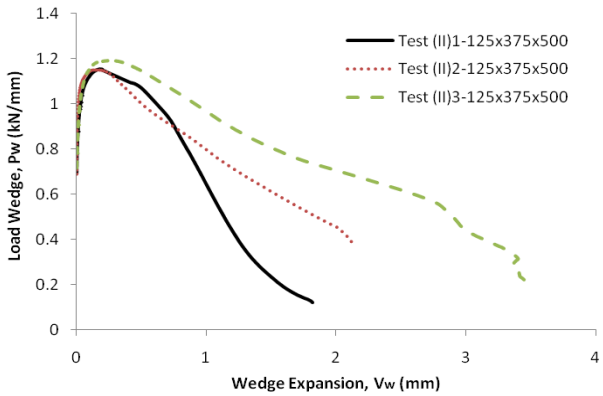

Figure 4.79: Load wedge – wedge expansion response of the prism Test(II)-125×375×500

The last analysis for prism Test(II)-125×375×500 is stress wedge σ_w and wedge expansion V_w response. The graph in Figure 4.80 indicates the wedge expansion increase slightly as the load increase up to peak load of 19MPa. After this point, the wedge expansion still increase considerably with a decrease of the stress. The pattern of the response is similar up to peak load however the scatter occurs on post-peak response.

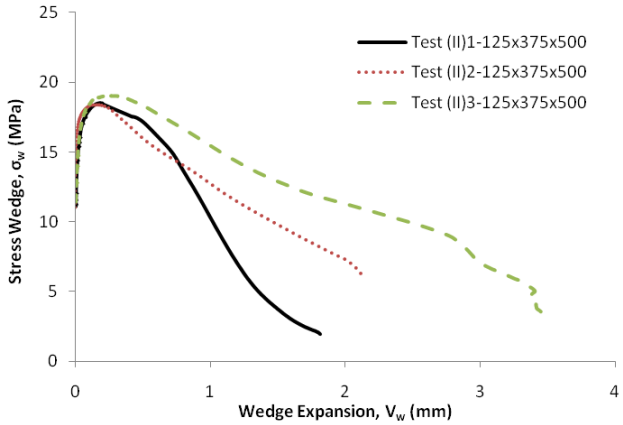

Figure 4.80: Stress wedge-wedge expansion response of the prism Test(II)-125×375×500

The parameters of prism Test(II)-125×375×500 such as L_p, P_p, P_{wp}, σ_{wp}, C_p, $C_p/2$, S_{wp}, E_p, $E_p/2$, and V_{wp} are clearly explained previously and shown graphically in Figure 4.71 to Figure 4.80. Those important parameters are listed in Table 4.5. It should be noting that these values are based on the individual results test.

Table 4.5: The important parameters of prism Test(II)-125×375×500 based on individual graph

Prism	L_p (kN)	P_p (kN)	P_{wp} (kN/mm)	σ_{wp} (MPa)	C_p (mm)	$C_p/2$ (mm)	S_{wp} (mm)	E_p (mm)	$E_p/2$ (mm)	V_{wp} (mm)
1	2	3	4	5	6	7	8	9	10	11
TEST(II)1-125×375×500	1156	578	1.16	19	1.04	0.52	0.24	0.53	0.26	0.18
TEST(II)2-125×375×500	1151	576	1.15	18	1.18	0.59	0.31	0.49	0.25	0.16
TEST(II)3-125x375 x500	1191	596	1.19	19	1.30	0.65	0.31	0.64	0.32	0.26
AVERAGE	1166	583	1.17	19	1.17	0.59	0.29	0.55	0.28	0.20

Table 4.5 gives the total deformations in axial direction C_p in column 6 and the total deformation in lateral direction E_p in column 9 at the peak of total axial load L_p at column 2. The average values of C_p, E_p and L_p are 1.17mm, 0.55mm, and 1,166kN respectively. At the peak load, the total axial deformation of prism is more than twice of its lateral deformation.

The same behaviour is also shown in one single wedge analysis. P_p, $C_p/2$ and $E_p/2$ represent the peak load on one single wedge, the axial deformation and lateral deformation on one single wedge respectively. The same behaviour occurs because P_p,

$C_p/2$ and $E_p/2$ are L_p, C_p and E_p divided by 2 respectively. The average values of P_p, $C_p/2$ and $E_p/2$ are 583kN, 0.59mm and 0.28mm respectively.

The load wedge P_w is determined by dividing the axial load P with prism length S while slip wedge S_w and wedge expansion V_w are quantified by removing the elastic deformation from the total defomation response. The peak of wedge load P_{wp}, the slip wedge S_{wp} and the wedge expansion V_{wp} at peak load of the three prisms in Test(II)-125×375×500 are listed in columns 4, 8 and 11 in Table 4.5 respectively. The average deformation due to micro-cracking in axial and lateral direction at peak load of 1.17kN/mm looks very similar, S_{wp} = 0.29mm and V_{wp} = 0.20mm.

The peak wedge stress σ_{wp} of all prisms in Test(II)-125×375×500 is listed in column 5 in Table 4.5. The parameter of σ_{wp} is also quite similar, that varies between 18MPa to 19MPa. The average value based on this individual peak values is 19MPa.

4.4.2.2 Tests at 125mm width and 250mm height (125×250×500)

There are three prism in Test(II)-125×250×500. The comparisons of those prisms in every step of analysis are described. First is the total axial contraction response for a given applied load. Figure 4.81 illustrates the *L*-*C* response of Test(II)-125×250×500. The behaviour of prisms is identical in pre-peak and post-peak branches but prism Test(II)4-125×250×500 more ductile compare to others prisms. The peaks of total axial load are in the range between 1,293kN to 1,329kN and the total axial contraction between 0.99mm to 1.15mm. The average values of L_p and C_p based on individual graph are 1,310kN and 1.07mm respectively. These parameters are listed in Table 4.6.

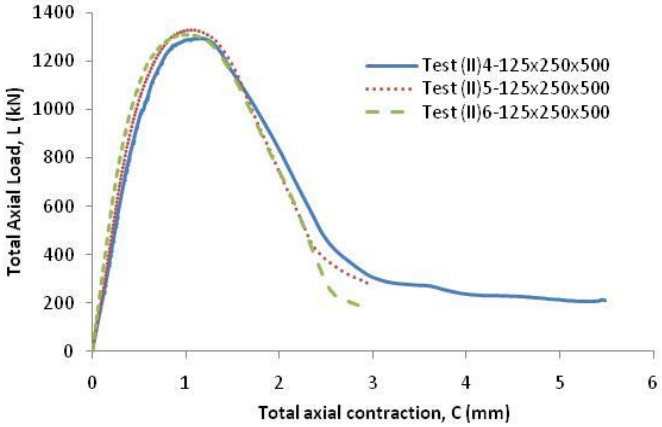

Figure 4.81: Total axial load-total axial contraction response of the prism Test(II)-125×250×500

The second part of the analysis that is the behaviour of one single wedge is described. The relationship of load and total axial contraction over one single wedge *P*-*C*/2 graphs of prism Test(II)-125×250×500 is illustrated in Figure 4.82. The pattern of the responses is similar. The average values of P_p and $C_p/2$ from individual graph are 655kN and 0.53mm respectively as listed in Table 4.6.

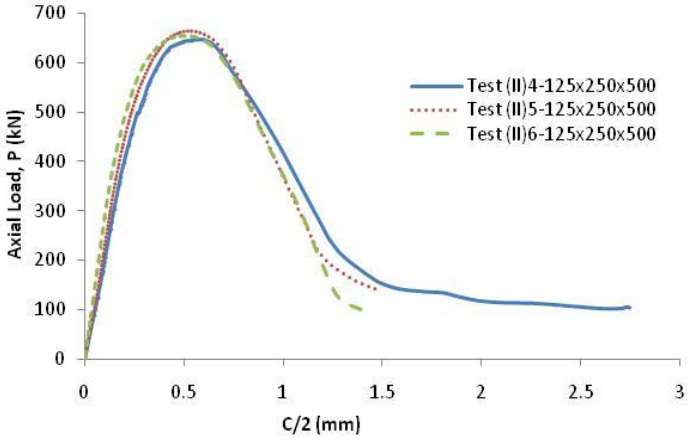

Figure 4.82: Axial load-C/2 response of the prism Test(II)-125×250×500

Next analysis is the relationship of axial load *P* and the slip wedge S_w of Test(II)-125×250×500 as depicted in Figure 4.83.The graphs indicate the similar response of the concrete prisms in Test(II)-125×250×500. The slip wedge starts at the axial load between 388kN to 399kN. The values of slip wedge at peak load S_{wp} of the prisms are quite the same that is between 0.24mm to 0.26mm.

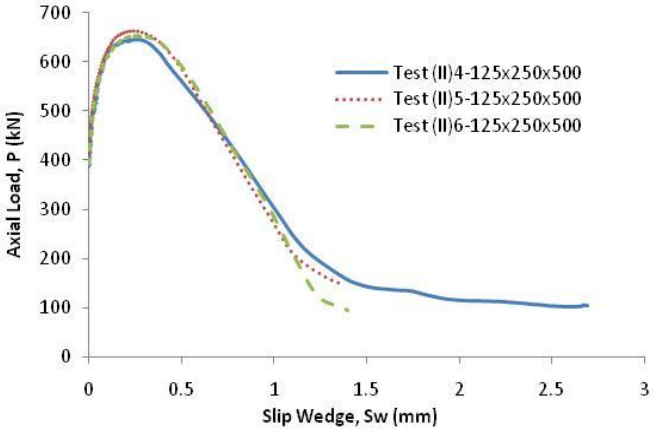

Figure 4.83: Axial load-slip wedge response of the prism Test(II)-125×250×500

The load wedge P_w is the load per 1 millimeter wedge thickness which is obtained from axial load P divided by the length of concrete prism S=500mm. Hence the P_w - S_w graphs of Test(II)-125×250×500 as depicted in Figure 4.84 have the same pattern with the P-S_w graphs as shown in Figure 4.83 previously. The average of the peak axial load P_{wp} is 1.31kN/mm and the average of slip wedge at peak load S_{wp} is 0.25mm.

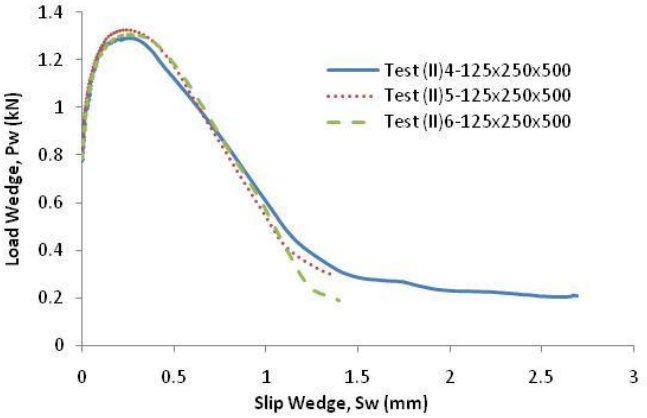

Figure 4.84: Load wedge-slip wedge response of the prism Test(II)-125×250×500

The last analysis in axial deformation is the stress wedge and the slip wedge response. Figure 4.85 illustrates the relationship between the stress wedge σ_w and slip wedge S_w of Test(II)-125×250×500. The responses look very similar. The peak wedge

stress σ_{wp} of three prisms are the same of 21MPa at slip wedge S_{wp} between 0.24mm to 0.26mm.

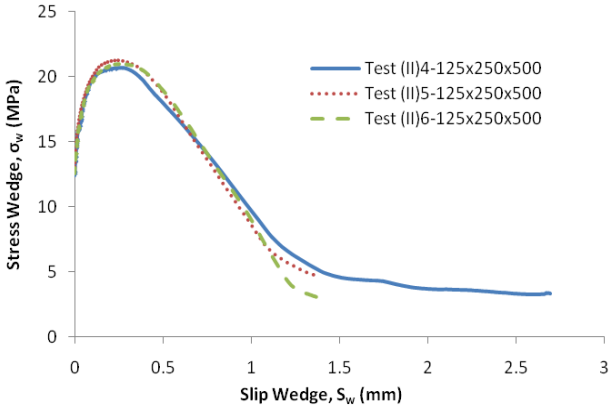

Figure 4.85: Stress wedge-slip wedge response of the prism Test(II)-125×250×500

After analysed the axial deformation, now lateral deformation is analysed. First is the total lateral expansion that is the expansion of the whole prism for a given applied load. Figure 4.86 shows the *L-E* responses of three prisms in Test(II)-125×250×500. The response is very similar up to peak load, however the small scatter occurred after that point on Test(II)5-125×250×500 as shown in dot line in Figure 4.86. Table 4.1 shows the total lateral expansion at peak load E_p is in the narrow range, between 0.74mm to 0.84mm.

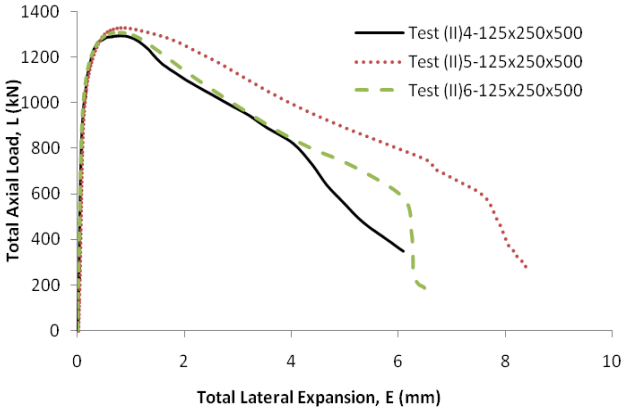

Figure 4.86: Total axial load-total lateral expansion for Test(II)-125×250×500

Figure 4.87 shows *P*-*E*/2 response of the prisms in Test(II)-125×250×500. The average of total lateral expansion over one single wedge at peak load $E_p/2$ is 0.40mm.

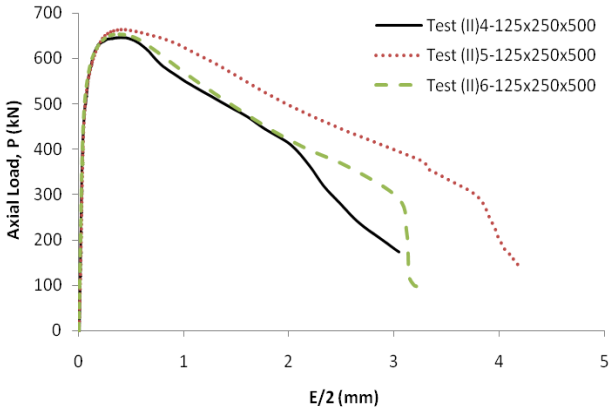

Figure 4.87: Axial load – E/2 response of the prism Test(II)-125×250×500

The relationship of *P*-V_w of Test(II)-125×250×500 is depicted in Figure 4.88. This graph is obtained by reducing the elastic expansion from the *P*-*E*/2 response in Figure 4.87. The graphs indicate the similar response until the peak load reached. The values of wedge expansion at peak load V_{wp} are quite the same; Test(II)4-125×250×500 is 0.34mm, Test(II)5-125×250×500 is 0.34mm and Test(II)6-125×250×500 is 0.31mm. The average of wedge expansion at peak load V_{wp} is 0.33mm. After the peak load, only the response of Test(II)4-125×250×500 and Test(II)5-125×250×500 are quite the same.

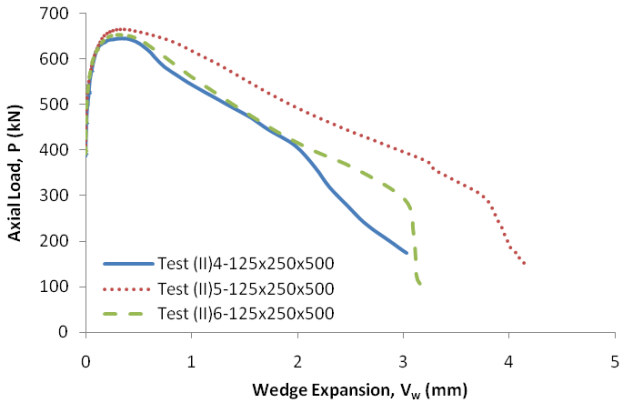

Figure 4.88: Axial load – wedge expansion response of the prism Test(II)-125×250×500

The response of load wedge and slip wedge per one millimeter wedge thickness P_w–V_w of three prism Test(II)-125×250×500 is shown in Figure 4.89. The values of P_w, when micro-cracking start, is the same as in axial direction. This indicated that micro-cracking occurs in axial and lateral direction at the same time.

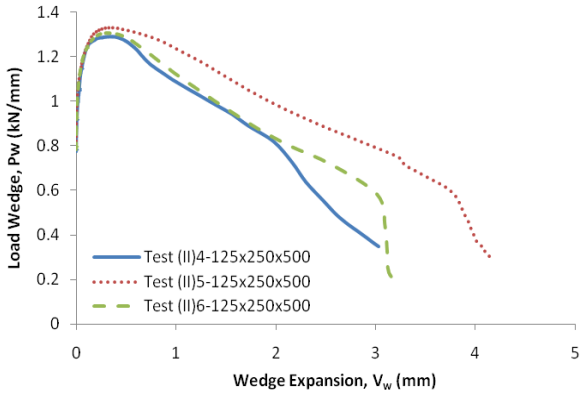

Figure 4.89: Load wedge – wedge expansion response of the prism Test(II)-125×250×500

The relationship of σ_w – V_w of Test(II)-125×250×500 is depicted in Figure 4.90. The graph illustrates all prisms in Test(II)-125×250×500 show the similar response but only in pre-peak region. In post peak region, the scatter occurs in Test(II)5-125×250×500 as shown in dot line in Figure 4.90.

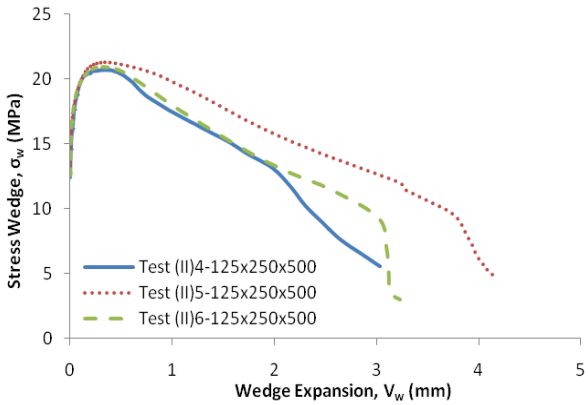

Figure 4.90: Stress wedge-wedge expansion response of the prism Test(II)-125×250×500

All parameter results of Test(II)-125×250×500 that was described in detail previously are listed in Table 4.6. The average values of all parameters are determined

based on the individual graph. These important parameter is of Test(II)-125×250×500 is discussed in detail below.

Table 4.6: The important parameters of prism Test(II)-125×250×500 based on individual graph

Prism	L_p (kN)	P_p (kN)	P_{wp} (kN/mm)	σ_{wp} (MPa)	C_p (mm)	$C_p/2$ (mm)	S_{wp} (mm)	E_p (mm)	$E_p/2$ (mm)	V_{wp} (mm)
1	2	3	4	5	6	7	8	9	10	11
TEST(II)4-125x250 x500	1293	646	1.29	21	1.15	0.58	0.26	0.79	0.40	0.34
TEST(II)5-125x250 x500	1329	665	1.33	21	1.06	0.53	0.24	0.84	0.42	0.34
TEST(II)6-125x250 x500	1309	654	1.31	21	0.99	0.50	0.26	0.74	0.37	0.31
AVERAGE	1310	655	1.31	21	1.07	0.53	0.25	0.79	0.40	0.33

Table 4.6 shows all parameters in axial and lateral directions of Test(II)-125×250×500 are quite same. The peak of total axial load L_p varies between 1,293kN to 1,329kN corresponds to total lateral at peak load C_p varies between 0.99mm to 1.15mm and to total lateral expansion varies between 0.74mm to 0.84mm. The average values of L_p, C_p and E_p based on the individual results are 1,310kN, 1.07mm and 0.79mm respectively. This means that axial deformation is larger than lateral deformation at the peak of applied load.

Next is analysis one single wedge. The average values of load corresponds to the total axial contraction and to total lateral expansion of one single wedge of Test(II)-125×250×500 are 655kN, 0.53mm and 0.40mm respectively.

The peak of wedge load P_{wp} corresponds to the slip wedge S_{wp} and wedge expansion V_{wp} of Test(II)-125×250×500 are quite similar as shown in columns 4 and 8 in Table 4.6. Based on the individual result, the average values of P_{wp}, S_{wp} and V_{wp} are 1.31kN/mm, 0.25mm and 0.33mm respectively. The lateral deformation due to micro-cracking is slightly larger than the axial deformation due to micro-cracking.

The peak of stress wedge σ_{wp} (column 5 in Table 4.6) of all prisms in Test(II)-125×250×500 is the same.

4.4.2.3 Tests at 125mm width and 125mm height (125×125×500)

The relationship between total axial load L and total axial contraction C of prism Test(II)-125×125×500 can be seen in Figure 4.91. The response on ascending branch is

quite similar, however, a small scatter occurred on descending branch. The peak load of Test(II)8-125×125×500 is a slightly higher than the others as shown in a dot line in Figure 4.91.

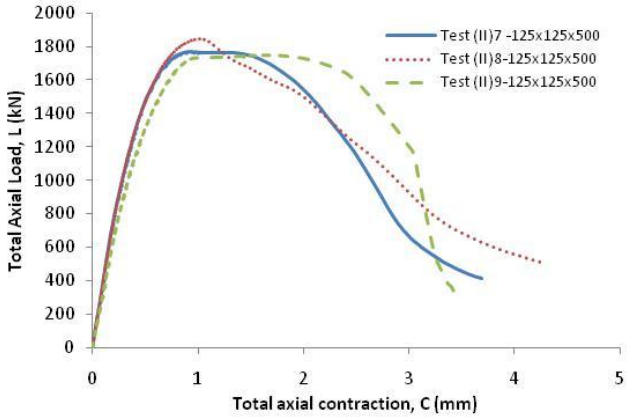

Figure 4.91: Total axial load-total axial contraction response of the prism Test(II)-125×125×500

After peak load reached, the total axial contraction of prisms Test(II)7-125×125×500 and Test(II)9-125×125×500 increases with a steady peak load while total axial contraction of prism Test(II)8-125×125×500 increase with a decrease of the load. The average values of L_p and C_p based on individual graph are 1,783kN and 0.97mm respectively.

The analysis in one single wedge of prism Test(II)-125×125×500 is shown in Figure 4.92. The pattern is the same with the response of L-C in Figure 4.91. The average values of P_p and $C_p/2$ are 891kN and 0.48mm respectively as summarised in

Table 4.7.

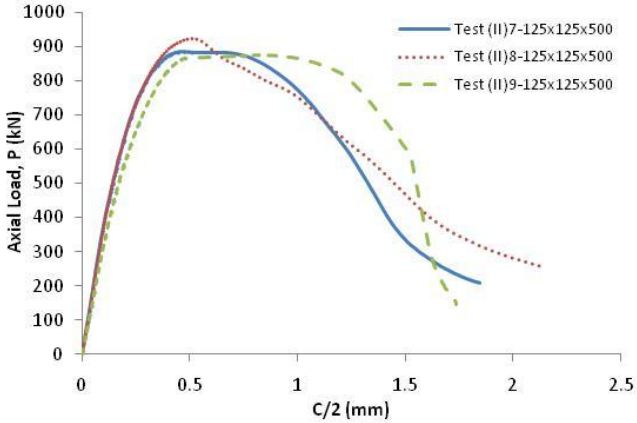

Figure 4.92: Axial load-C/2 response of the prism Test(II)-125×125×500

Once $C/2$ has been established, the axial load P versus the slip wedge S_w is determined by subtract the elastic contraction B from the total axial contraction of one single wedge $C/2$ (Figure 4.93). Up to αP_p there is no micro-cracking, there is only elastic deformation. After that the axial deformation due to micro-cracking or slip wedge increases slightly up to peak load and it is followed by a significant increasing of slip wedge at post peak region. The same response is also shown in Figure 4.94. The average of peak load wedge P_{wp} is 1.78kN/mm corresponds to slip wedge S_{wp} is 0.21mm.

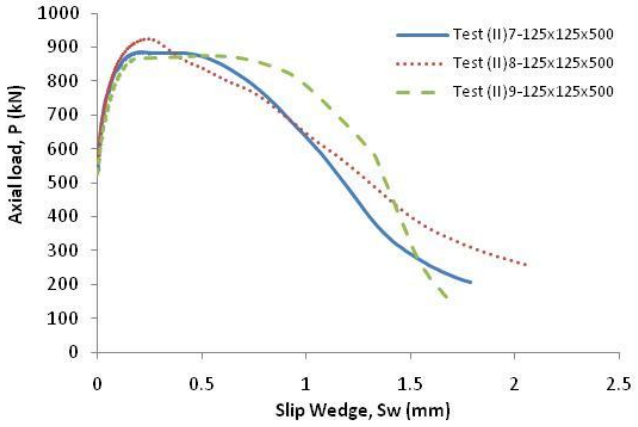

Figure 4.93: Axial load-slip wedge response of the prism Test(II)-125×125×500

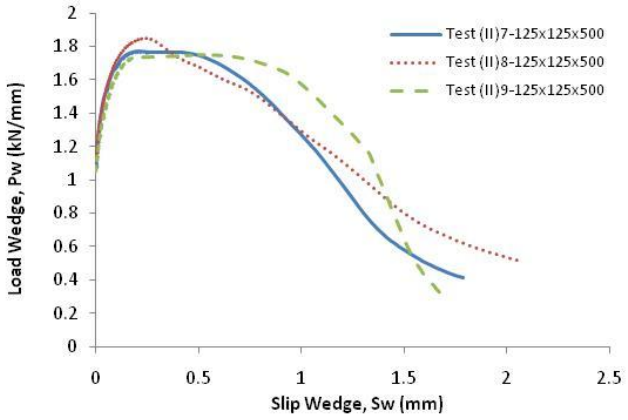

Figure 4.94: Load wedge-slip wedge response of the prism Test(II)-125×125×500

The last part of the analysis in axial deformation is the wedge stress against the axial deformation due to micro-cracking or slip wedge (σ_w-S_w) as depicted in Figure 4.95. The response is the same. Up to $\alpha\sigma_{wp}$ there is no deformation due to micro-cracking or slip wedge, after that point the slip wedge increases slightly up to peak load

and increases considerably with a decreasing of stress wedge until the prism failed. The response of three prisms in Test(II)-125×125×500 are similar in pre-peak stress but small scatter occurs in post peak stress.

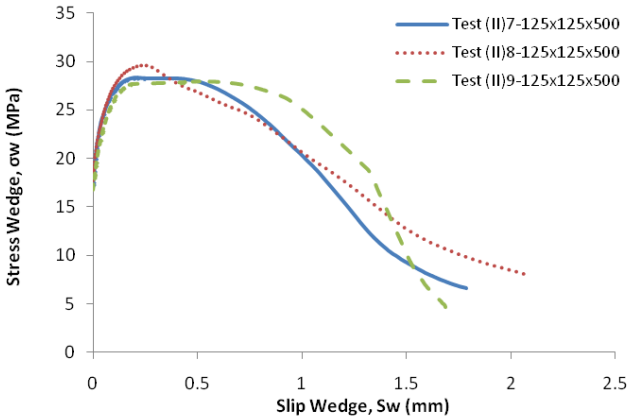

Figure 4.95: Stress wedge-slip wedge response of the prism Test(II)-125×125×500

The total axial load L and the total lateral expansion E response of Test(II)-125×125×500 is shown in Figure 4.96. The graph indicates that the curves of all specimens in Test(II)-125×125×500 have similar pattern, no scatter on ascending region of the curve. However, small scatter happens on descending region of the curve. The average of total lateral expansion at peak load E_p is 1.06mm.

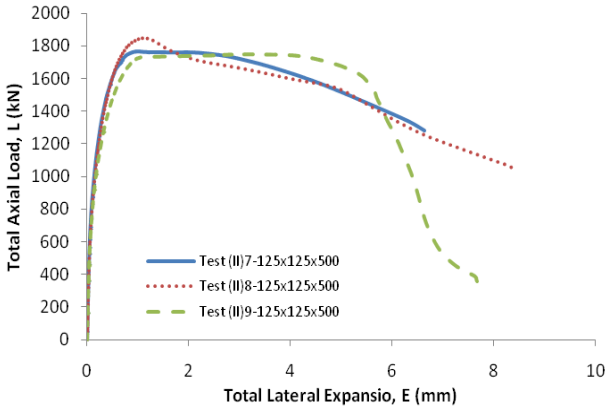

Figure 4.96: Total axial load-total lateral expansion for Test(II)-125×125×500

Analysis of one single wedge in lateral deformation that is relationship between load and total lateral expansion (P-E/2) is described. The P-E/2 graph has same pattern

with *L-E* graph because *P-E*/2 graph is *L-E* graph divided by 2. Figure 4.97 illustrates the relationship of *P-E*/2 of all experiment tests prism in Test(II)-125×125×500. The average of total lateral expansion over one single wedge at peak load $E_p/2$ is 0.53mm.

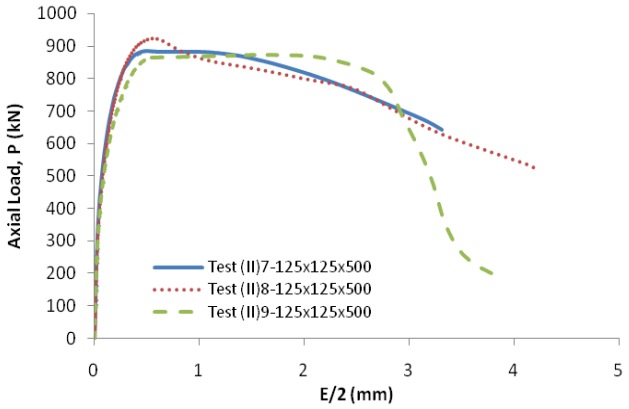

Figure 4.97: Axial load – E/2 response of the prism Test(II)-125×125×500

Figure 4.98 shows the P_p-V_w responses of Test(II)-125×125×500. The graph indicates a scatter occurred on descending region of Test(II)7-125×125×500 as shown in broken line while the descending region of P_p-V_w response on Test(II)7-125×125×500 (as shown in unbroken line) and Test(II)8-125×125×500 (as shown in dot line) are similar. The average of the wedge expansion at peak load V_{wp} is 0.37mm.

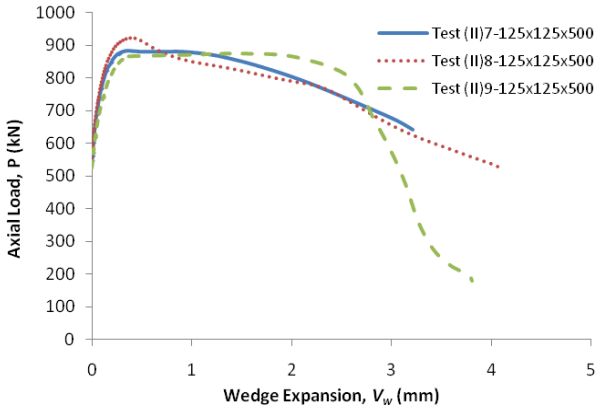

Figure 4.98: Axial load – wedge expansion response of the prism Test(II)-125×125×500

Figure 4.99 illustrates the relationship between load and wedge expansion per 1 mm wedge thickness P_w-V_w of prisms Test(II)-125×125×500. The graph indicates that

the similar response occurred in this graph like the P-V_w response before because P_w is P divided by prism length S (500mm).

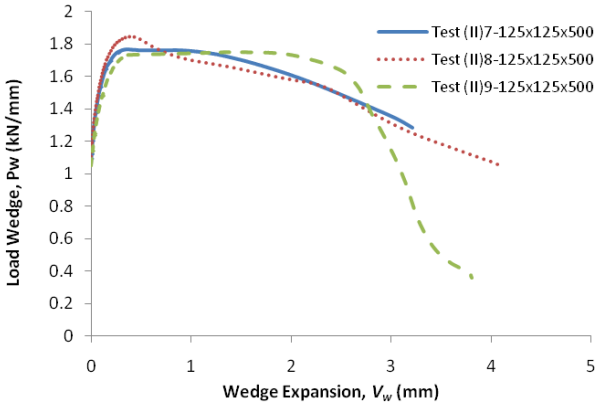

Figure 4.99: Load wedge – wedge expansion response of the prism Test(II)-125×125×500

The response of stress wedge and wedge expansion of Test(II)-125×125×500 is depicted in Figure 4.100. The peak stress of Test(II)8-125×125×500 is slightly higher than other prisms.

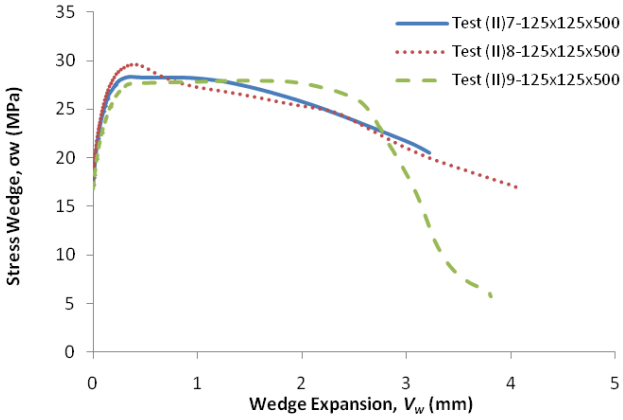

Figure 4.100: Stress wedge-wedge expansion response of the prism Test(II)-125×125×500

The individual results of Test(II)-125×125×500 were described and compared to other prisms in the other prisms in the same size previously. The important parameters such as L_p, P_p, P_{wp}, σ_{wp}, C_p, $C_p/2$, σ_{wp}, C_p, $C_p/2$, S_{wp}, E_p, $E_p/2$, and V_{wp} of all prisms of Test(II)-125×125×500 are listed in

Table 4.7. Based on this individual result, the average parameter is determined.

Table 4.7: The important parameters of prism Test(II)-125×125×500 based on individual graph

Prism	L_p (kN)	P_p (kN)	P_{wp} (kN/mm)	σ_{wp} (MPa)	C_p (mm)	$C_p/2$ (mm)	S_{wp} (mm)	E_p (mm)	$E_p/2$ (mm)	V_{wp} (mm)
1	2	3	4	5	6	7	8	9	10	11
TEST(II)7-125x125 x500	1769	884	1.77	28	0.92	0.46	0.20	0.99	0.49	0.36
TEST(II)8-125x125 x500	1848	924	1.85	30	1.02	0.51	0.24	1.12	0.56	0.39
TEST(II)9-125x125 x500	1732	866	1.73	28	0.96	0.48	0.19	1.08	0.54	0.37
AVERAGE	1783	891	1.78	29	0.97	0.48	0.21	1.06	0.53	0.37

Table 4.7 shows all parameters of Test(II)8-125×125×500 slightly higher than the other prisms. The total axial contraction at peak load C_p of all prisms in Test(II)-125×125×500 is higher than total lateral expansion at peak load E_p. The same pattern also occurs on C_p/2and E_p/2 because these values are half than C_p and E_p respectively. However, the deformation due to micro-cracking in lateral directions V_{wp} is higher than in axial direction S_{wp}. The wedge expansion V_{wp} varies in small range between 0.36mm-0.39mm while the slip wedge S_{wp} varies between 0.19-0.24mm.

4.4.2.4 Tests at 100mm width and 200mm height (100×200×400)

The relationship between total axial load and total axial contraction of prisms in Test(II)-100×200×400 can be seen in Figure 4.101. The graph indicates that the response of the prisms is quite similar. The total axial load at peak load C_p of Test(II)11-100×200×400 and Test(II)12-100×200×400 are the same 0.91mm, while Test(II)10-100×200×400 slightly lower 0.87mm. Hence the average values of L_p and C_p based on individual graph are 1,001kN and 0.89mm respectively.

The *P*-*C*/2 relationship of prisms in Test(II)-100×200×400 is depicted in Figure 4.102. The average values of axial load P_p and total axial contraction over one wedge at peak load C_p/2 are 501kN and 0.44mm respectively. The response of *P* against *C*/2 is half than the response of *L* against *C*. Hence the parameters P_p and C_p/2 are half than the parameters L_p and C_p. Hence the pattern of the response is same.

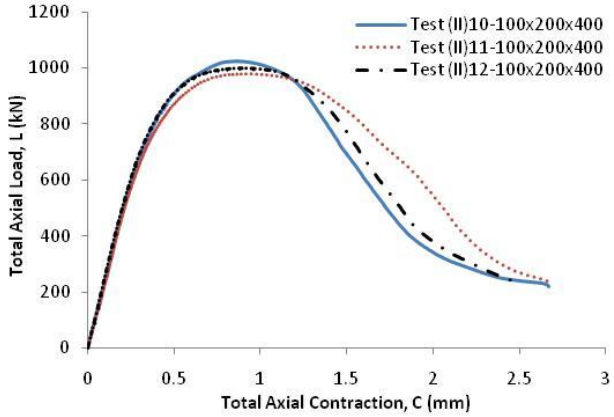

Figure 4.101: Total axial load-total axial contraction response of the prism Test(II)-100×200×400

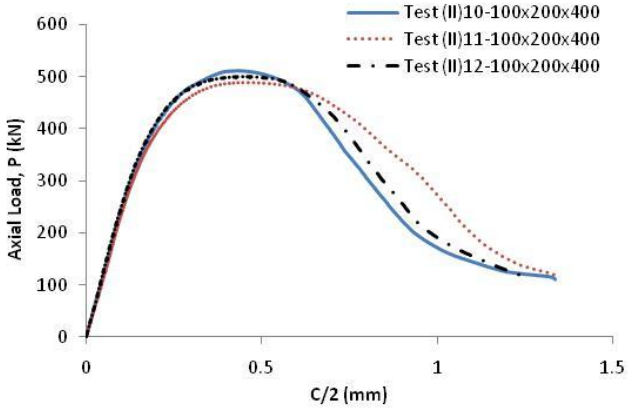

Figure 4.102: Axial load-C/2 response of the prism Test(II)-100×200×400

The response of P-S_w of Test(II)-100×200×400 is depicted in Figure 4.103. The graphs indicate similar response of all concrete prisms in Test(II)-100×200×400. The axial load when the slip wedges start to develop are varies in a narrow range between 294kN to 307kN. The values of slip wedge at peak load S_{wp} are quite same those are between 0.22mm to 0.25mm and the average of slip wedge at peak load S_{wp} is 0.23mm.

The axial loads P in Figure 4.103 are divided by the prism length S (400mm) equal to the load wedge P_w are shown in Figure 4.104. The graph indicates the similar response of the slip wedge for a given load wedge. The average of load wedge is 1.25kN/mm.

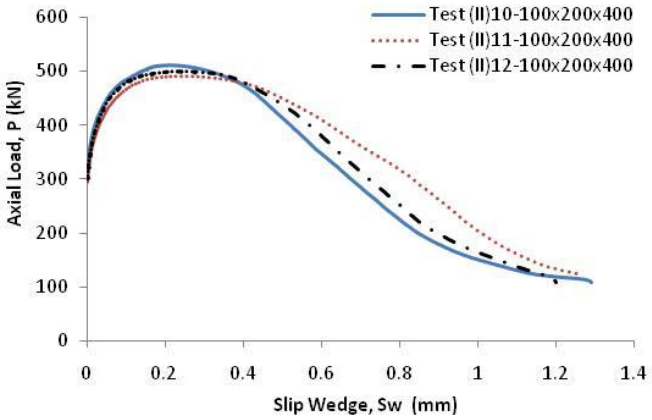

Figure 4.103: Axial load-slip wedge response of the prism Test(II)-100×200×400

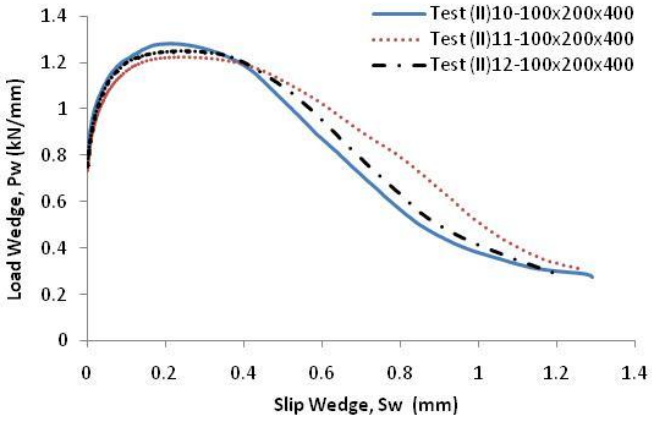

Figure 4.104: Load wedge-slip wedge response of the prism Test(II)-100×200×400

The relationship between stress wedge σ_w and slip wedge S_w of Test(II)-100×200×400 is illustrated in Figure 4.105. It can be seen that every concrete prism in Test(II)-100×200×400 has similar pattern. The slip wedge increases as stress wedge increases until the peak stress wedge reached. The slip wedge increases considerably with a decrease of stress wedge. The average of peak stress wedge σ_{wp} is 25MPa and the average of slip wedge at peak stress S_{wp} is 0.23mm.

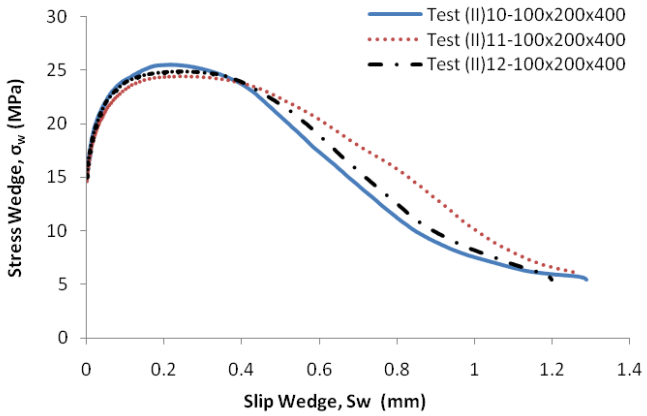

Figure 4.105: Stress wedge-slip wedge response of the prism Test(II)-100×200×400

In lateral deformation analysis, the response of total axial load and total lateral expansion, *L-E* is analysed first as depicted in Figure 4.106. The graph illustrates the pattern of the *L-E* response is quite the similar for all test prisms in Test(II)-100×200×400. The prism expands slowly up to peak load and after peak load the prism expands significantly until the prism failed. The average total lateral expansion at peak load E_p is 0.48mm.

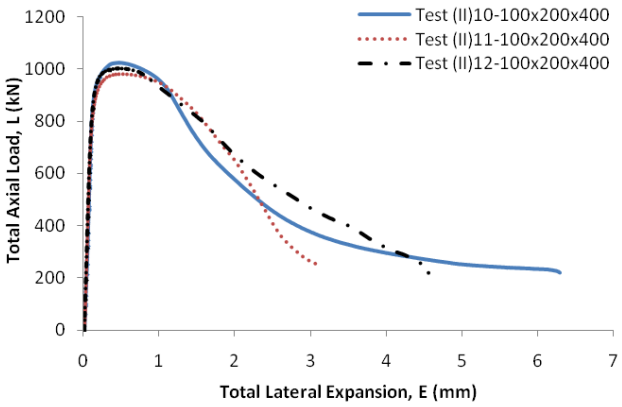

Figure 4.106: Total axial load-total lateral expansion for Test(II)-100×200×400

Figure 4.107 shows the response of load and total deformation of one single wedge, *P-E*/2 in Test(II)-100×200×400. The average of total lateral expansion over one single wedge at peak load $E_p/2$ is 0.24mm. The response is the same with the *L-E* response. The next figure illustrates the axial load and wedge expansion of one single

wedge (Figure 4.108). The micro-cracking deformation in lateral direction or wedge expansion V_w is obtained by removing the elastic expansion from $E_p/2$. The wedge expansion increases slightly up to peak load. At peak load, the wedge expansion V_{wp} is 0.18mm.

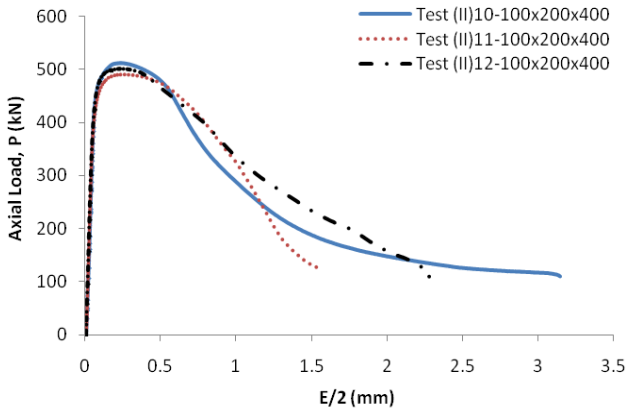

Figure 4.107: Axial load – E/2 response of the prism Test(II)-100×200×400

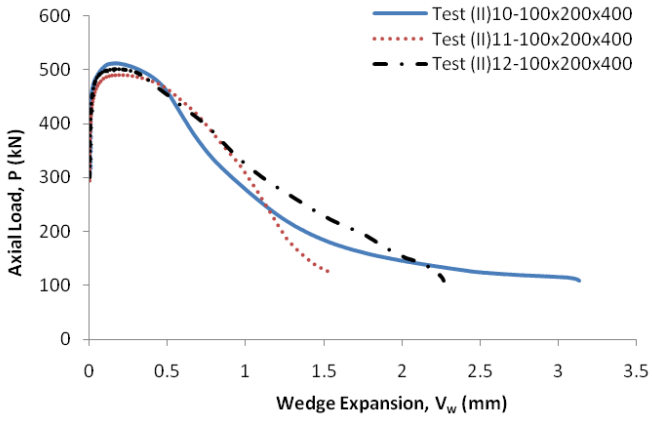

Figure 4.108: Axial load – wedge expansion response of the prism Test(II)-100×200×400

The load wedge P_w is the load per 1 millimeter wedge thickness which is obtained from axial load P in Figure 4.108 divided by the length of concrete prism S. Hence the P_w-V_w graphs of Test(II)-100×200×400 have the same pattern with P-V_w graphs as shown in Figure 4.109.

Figure 4.110 illustrates the stress wedge σ_w and the wedge expansion V_w response of prisms Test(II)-100×200×400. The concrete prisms in this size show the similar

pattern response. The wedges start to form in lateral direction when the stress reaches between 14MPa to 15MPa. The average of peak stress wedge σ_{wp} is 25MPa and the average wedge expansion at peak stress V_{wp} is 0.18mm.

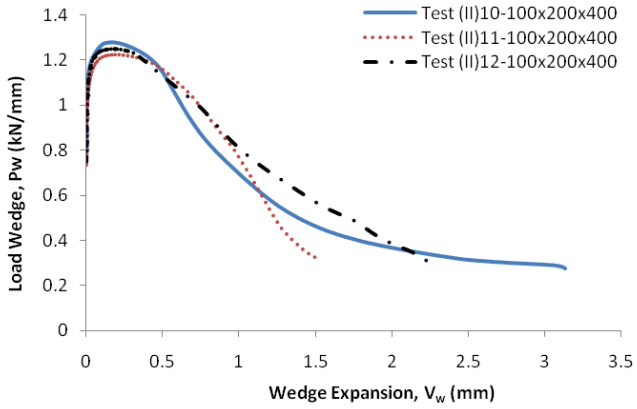

Figure 4.109: Load wedge – wedge expansion response of the prism Test(II)-100×200×400

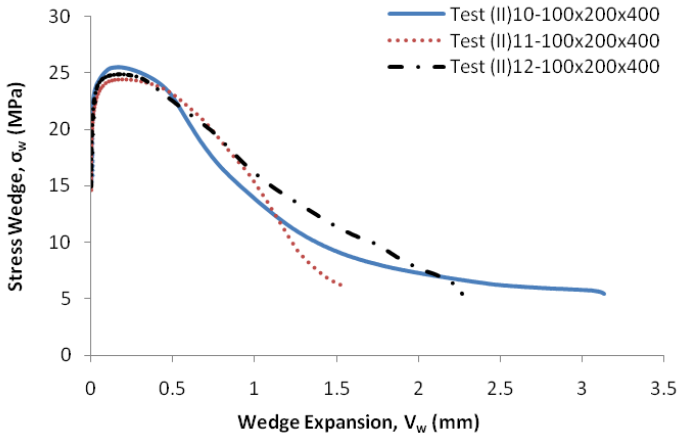

Figure 4.110: Stress wedge-wedge expansion response of the prism Test(II)-100×200×400

All the parameter results of the prisms Test(II)-100×200×400 are listed in Table 4.8. The average value of all parameters is determined based on individual results test. The important parameters are discussed in detail below.

Table 4.8: The important parameters of prism Test(II)-100×200×400 based on individual graph

Prism	L_p (kN)	P_p (kN)	P_p (kN/mm)	σ_{wp} (MPa)	C_p (mm)	$C_p/2$ (mm)	S_{wp} (mm)	E_p (mm)	$E_p/2$ (mm)	V_{wp} (mm)
1	2	3	4	5	6	7	8	9	10	11
TEST(II)10-100×200×400	1024	512	1.28	26	0.87	0.43	0.22	0.47	0.24	0.16
TEST(II)11-100×200×400	979	490	1.23	24	0.91	0.45	0.24	0.50	0.25	0.19
TEST(II)12-100×200×400	1001	500	1.25	25	0.91	0.45	0.25	0.48	0.24	0.18
AVERAGE	1001	501	1.25	25	0.89	0.44	0.23	0.48	0.24	0.18

The parameters in axial and lateral directions of prism Test(II)-100×200×400 looks identical. The parameters of three prisms vary in narrow range. The total axial contraction at peak load C_p higher very significant than total lateral expansion E_p that is almost two times than E_p for all prisms in Test(II)-100×200×400. The average values of C_p and E_p are 0.89mm and 0.48mm respectively. The same comparison occurs in one single wedge analysis. At peak load, $C_p/2$ is two times higher than $E_p/2$. The average value of $E_p/2$ is 0.24mm while $C_p/2$ is 0.44mm.

The micro-cracking starts to form in axial and lateral direction at $\alpha P_{p.}$ It means that the micro-cracking deformation start at the same time, however at peak load, axial deformation due to micro-cracking or slip wedge is 0,23mm while lateral deformation due to micro-cracking is only 0.18mm.

4.4.2.5 Tests at 75mm width and 150mm height (75×150×300)

Figure 4.111 illustrates the relationship *L*-*C* of prism Test(II)-75×150×300. It can be seen that the trend of the curves is very identical in pre-peak region while small scatter happen in post peak region. Total axial contraction at peak load C_p slightly larger than other prisms. The parameter C_p of Test(II)15-75×150×300 is 0.90mm while Test(II)13-75×150×300 is only 0.75mm and Test(II)14-75×150×300 is 0.79mm. The average values of L_p and C_p are 634kN and 0.82mm respectively.

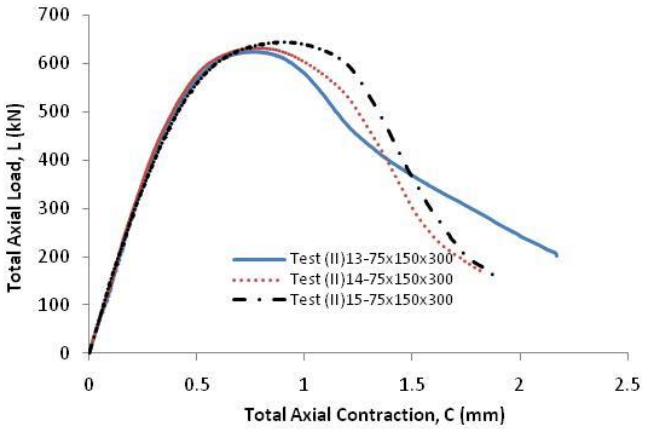

Figure 4.111: L-C response of the prism Test(II)-75×150×30

Figure 4.112 shows the relationship between axial load and total axial contraction over a single wedge only of prism Test(II)-75×150×300. The graph illustrates the same trend with Figure 4.111. The average values of peak P_p is 317kN and $C_p/2$ is 0.41mm.

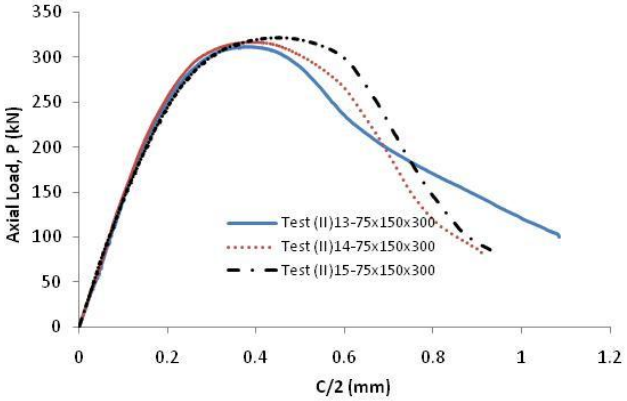

Figure 4.112: Axial load-C/2 response of the prism Test(II)-75×150×300

Figure 4.113 illustrates relationship between the axial load P and the slip wedge S_w of prisms Test(II)-75×150×300. The graphs indicate that the responses of all concrete prisms in Test(II)-75×150×300 are very similar but slight scatter at post peak region. The values of slip wedge at peak load S_{wp} of prism Test(II)15-75×150×300 slightly larger than others. The same trend occurs on P_w-S_w and σ_w-S_w in Figure 4.114 and Figure 4.115 respectively.

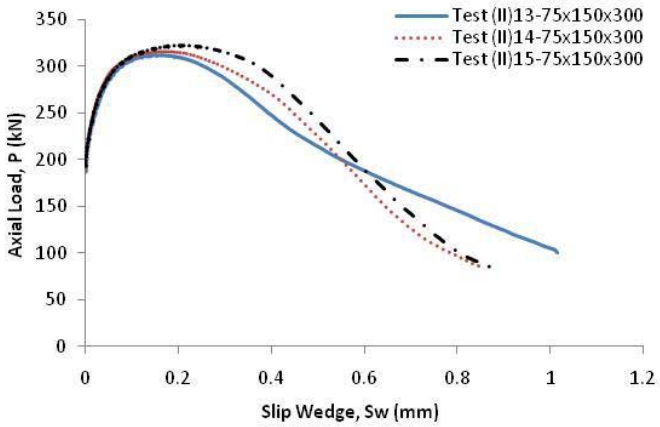

Figure 4.113: Axial load-slip wedge response of the prism Test(II)-75×150×300

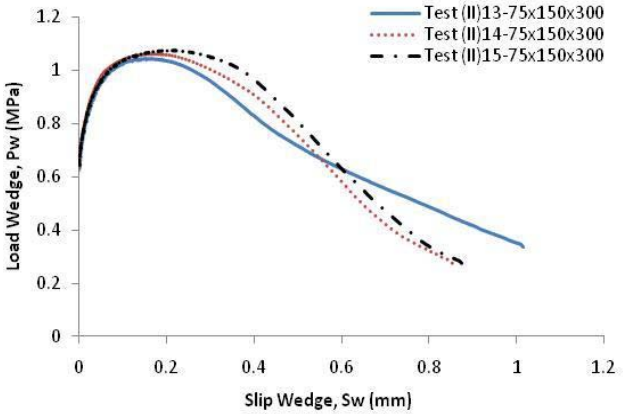

Figure 4.114: Load wedge-slip wedge response of the prism Test(II)-75×150×300

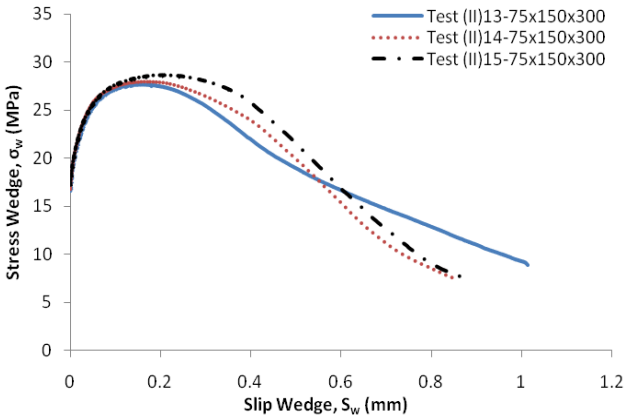

Figure 4.115: Stress wedge-slip wedge response of the prism Test(II)-75×150×300

The relationship of total axial load and total lateral expansion *L-E* of prism Test(II)-75×150×300 is depicted in Figure 4.116. It can be seen that the trend of the curves is identical in pre-peak and post peak regions. Total axial expansion at peak load E_p of Test(II)13-75×150×300 and Test(II)14-75×150×300 is the same 0.28mm while Test(II)15-75×150×300 is 0.32mm. The average value of E_p is 0.29mm. The same trend is shown in *P-E*/2 response (Figure 4.117)

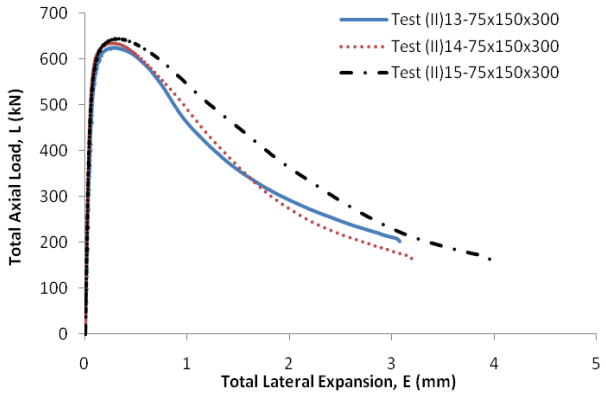

Figure 4.116: Total axial load-total lateral expansion for Test(II)-75×150×300

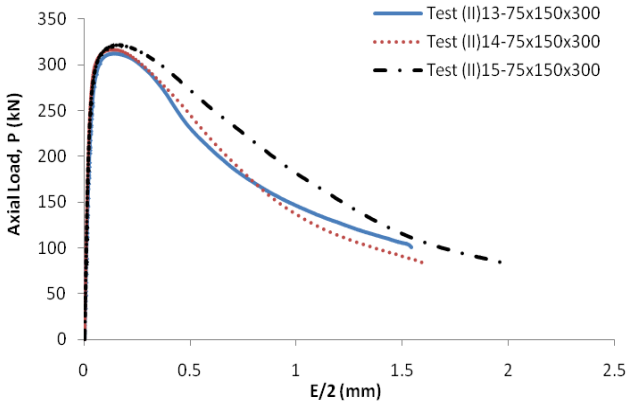

Figure 4.117: Axial load – E/2 response of the prism Test(II)-75×150×300

Figure 4.118 illustrates relationship between the axial load *P* and the wedge expansion V_w of prisms Test(II)-75×150×300. The graph indicates that the trend of the responses is similar. The values of wedge expansion at peak load V_{wp} is same between Test(II)13-75×150×300 and Test(II)14-75×150×300 while Test(II)15-75×150×300

slightly larger. The average of wedge expansion at peak load V_{wp} is 0.11mm. The same trend is shown in P_w-V_w and σ_{wp}-V_{wp} responses (Figure 4.119 and Figure 4.120)

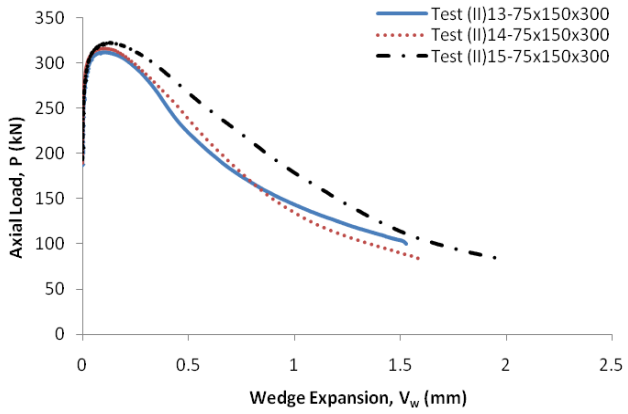

Figure 4.118: Axial load – wedge expansion response of the prism Test(II)-75×150×300

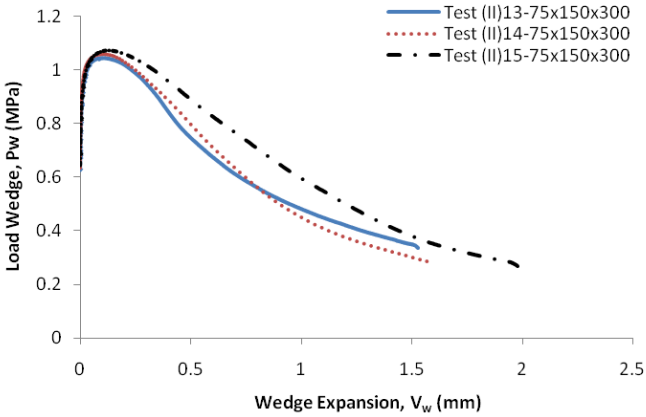

Figure 4.119: Load wedge – wedge expansion response of the prism Test(II)-75×150×300

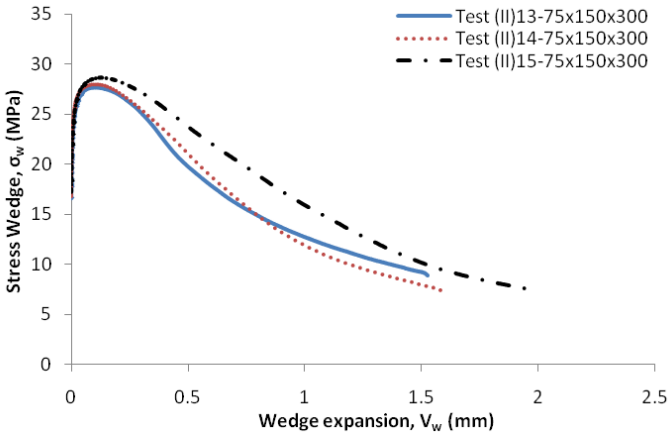

Figure 4.120: Stress wedge-wedge expansion response of the prism Test(II)-75×150×300

Table 4.9 shows the parameters of prisms Test(II)-75×150×300 such as L_p, P_p, P_{wp}, σ_{wp}, C_p, $C_p/2$, S_{wp}, E_p, $E_p/2$, and V_{wp}. The average values of those parameters are determined based on the individual results graph.

Table 4.9: The important parameters of prism Test(II)-75×150×300 based on individual graph

Prism	L_p (kN)	P_p (kN)	P_p (kN/mm)	σ_{wp} (MPa)	C_p (mm)	$C_p/2$ (mm)	S_{wp} (mm)	E_p (mm)	$E_p/2$ (mm)	V_{wp} (mm)
1	2	3	4	5	6	7	8	9	10	11
TEST(II)13-75×150×300	624	312	1.04	28	0.75	0.38	0.15	0.28	0.14	0.10
TEST(II)14-75×150×300	633	317	1.06	28	0.79	0.40	0.17	0.28	0.14	0.10
TEST(II)15-75×150×300	644	322	1.07	29	0.90	0.45	0.21	0.32	0.16	0.13
AVERAGE	634	317	1.06	28	0.82	0.41	0.18	0.29	0.15	0.11

The parameters of prisms Test(II)-75×150×300 are consider same. The parameter C_p is larger considerably than the parameter E_p. The average of C_p is large as 0.82mm while E_p is only 0.29mm. This means that at peak load, the prism deform in axial direction almost three times than deform in lateral direction. The same trend also occurs in one wedge analysis. The average of $C_p/2$ is 0.41mm while $E_p/2$ is only 0.15mm. However, in micro-cracking deformation, slip wedge at peak load S_{wp} is 0.18mm and wedge expansion V_{wp} is 0.11mm.

4.4.2.6 Tests at 50mm width and 100mm height (50×100×200)

The *L*-*C* relationship of prisms in Test(II)-50×100×200 is depicted in Figure 4.121. The curves trend is similar on ascending branch, however, a small difference of peak total axial load L_p occurred on Test(II)16-50×100×200 while the total axial contraction at peak load C_p of the prisms is similar (see again columns 2 and 4 in Table 4.10). The peak total axial load of Test(II)16-50×100×200 is 312kN that is lower than other prisms. Test(II)17-50×100×200 and Test(II)18-50×100×200 are 340kN and 345 respectively. The average values of L_p and C_p are 332kN and 0.51mm respectively. Prism Test(II)16-50×100×200 failed at *L* approximately 210kN corresponds to *C* is 1.2mm The same trend happens on *P*-*C*/2 as shown in Figure 4.122.

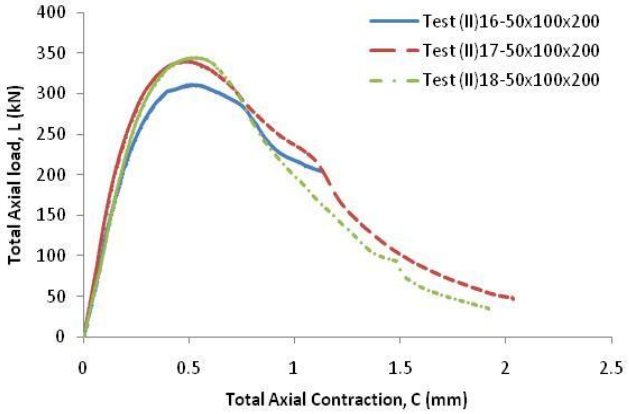

Figure 4.121: Total axial load-total axial contraction response of the prism Test(II)-50×100×200

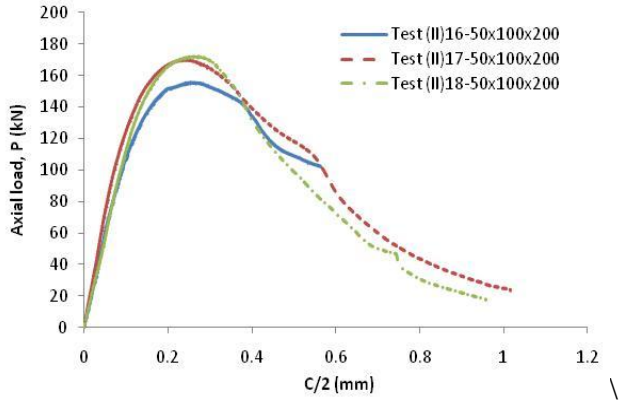

Figure 4.122: Axial load-C/2 response of the prism Test(II)-50×100×200

Figure 4.123 shows the P-S_w responses of three prisms in Test(II)-50×100×200. The three concrete prisms show the similar pattern on pre peak response. However the small scatter occurred in post peak branch of the P-S_w response. The peak of axial load of Test(II)16-50×100×200 lower than other prisms. However the slip wedge at peak load S_{wp} of all prisms is the same 0.12mm. The same pattern occurs on P-S_w and σ_w-S_w. The peak wedge stress σ_{wp} is 31MPa, 34MPa and 35MPa for Test(II)16-50×100×200, Test(II)17-50×100×200 and Test(II)18-50×100×200 respectively.

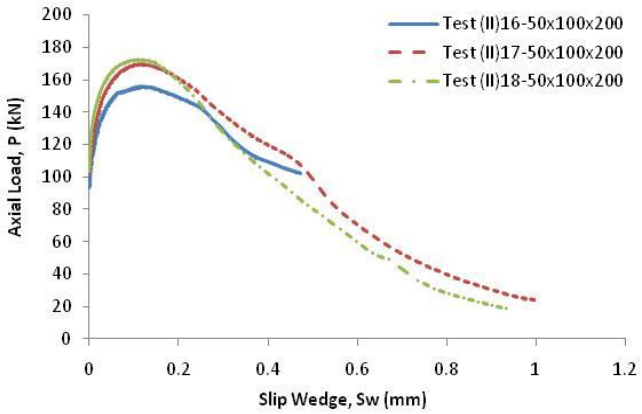

Figure 4.123: Axial load-slip wedge response of the prism Test(II)-50×100×200

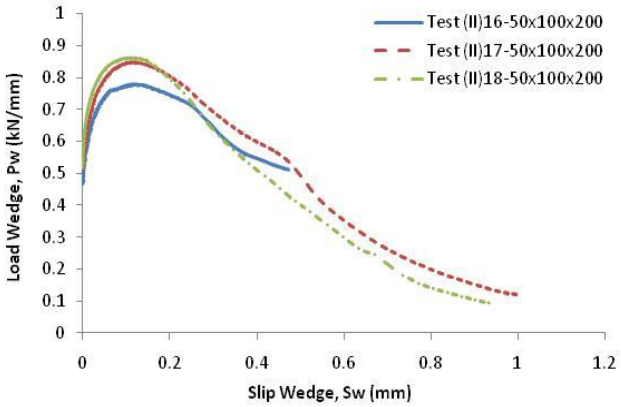

Figure 4.124: Load wedge-slip wedge response of the prism Test(II)-50×100×200

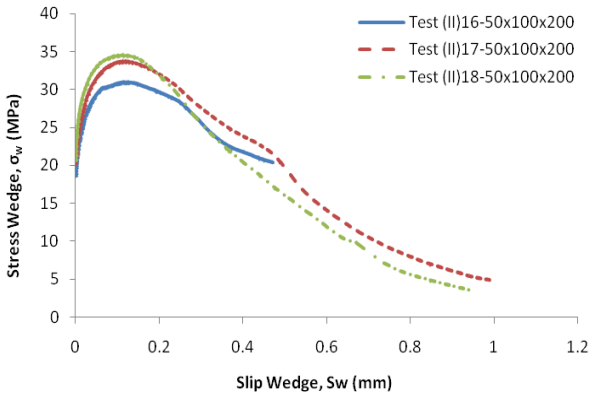

Figure 4.125: Stress wedge-slip wedge response of the prism Test(II)-50×100×200

Figure 4.126 shows the relationship of *L*-*E* of Test(II)-50×100×200. The graph illustrates the prisms start to expand when applied load approximately 300kN. After that the prisms expand slightly until the peak load reached. The total lateral expansion at peak load is between 0.17mm-0.20mm. The prisms expand significantly after the peak load reached. The big scatter occurs on post peak response. The same pattern is shown in *P*-*E*/2 response (Figure 4.127).

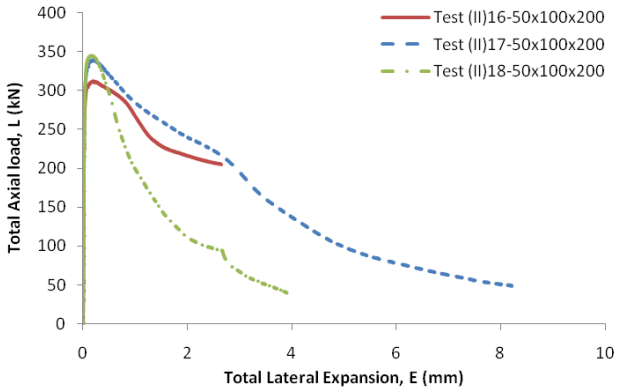

Figure 4.126: Total axial load-total lateral expansion for Test(II)-50×100×200

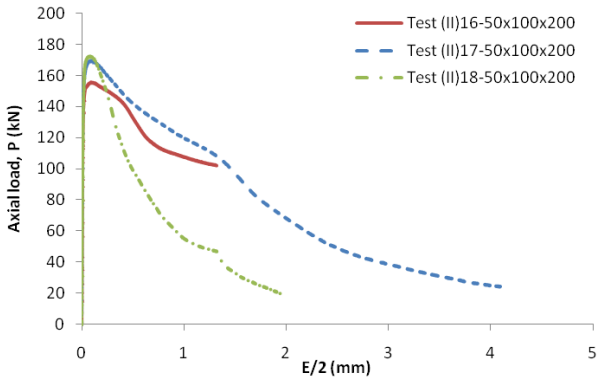

Figure 4.127: Axial load – E/2 response of the prism Test(II)-50×100×200

Figure 4.128 shows the P-V_w responses of Test(II)-50×100×200. The graph indicates the deformation due micro-cracking occurs near the peak load. After that the micro-cracking develop significantly until the prism failed. The wedge expansion at peak load V_{wp} is between 0.07mm to 0.09mm. The scatter looks on the response. The same trends occur on P_p-V_w and σ_w-V_w responses as shown in Figure 4.129 and Figure 4.130 respectively.

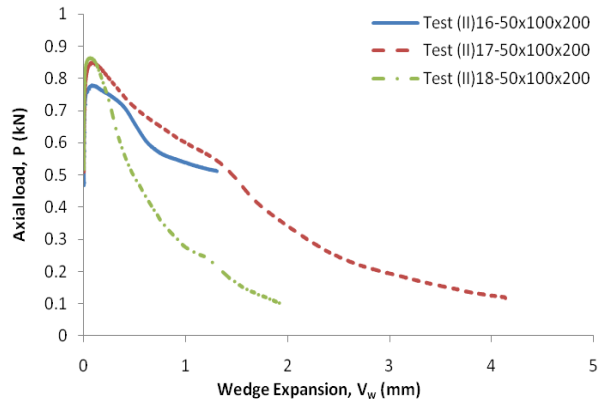

Figure 4.128: Axial load – wedge expansion response of the prism Test(II)-50×100×200

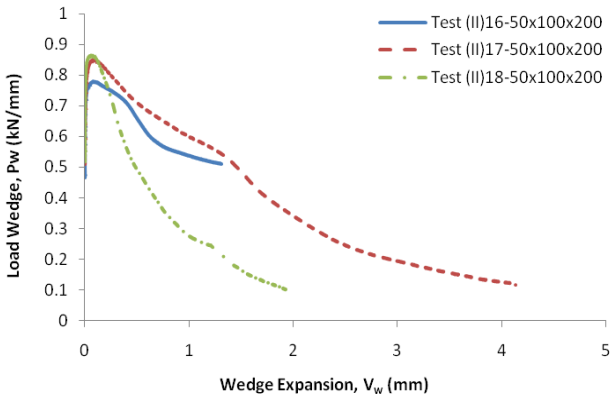

Figure 4.129: Load wedge – wedge expansion response of the prism Test(II)-50×100×200

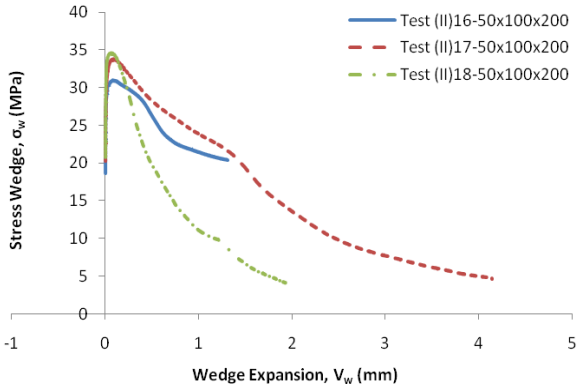

Figure 4.130: Stress wedge-wedge expansion response of the prism Test(II)-50×100×200

Table 4.10 shows the parameters of concrete prism Test(II)-50×100×200 such as L_p, P_p, P_{wp}, σ_{wp}, C_p, $C_p/2$, S_{wp}, E_p, $E_p/2$, V_{wp} and the average values of those parameters.

Table 4.10: The important parameters of prism Test(II)-50×100×200 based on individual graph

Prism	L_p (kN)	P_p (kN)	P_{wp} (kN/mm)	σ_{wp} (MPa)	C_p (mm)	$C_p/2$ (mm)	S_{wp} (mm)	E_p (mm)	$E_p/2$ (mm)	V_{wp} (mm)
1	2	3	4	5	6	7	8	9	10	11
TEST(II)16-50×100×200	312	156	0.78	31	0.51	0.25	0.12	0.19	0.09	0.08
TEST(II)17-50×100×200	340	170	0.85	34	0.49	0.25	0.12	0.20	0.10	0.09
TEST(II)18-50×100×200	345	173	0.86	35	0.53	0.27	0.12	0.17	0.09	0.07
AVERAGE	332	166	0.83	33	0.51	0.26	0.12	0.19	0.09	0.08

The table shows there is small scatter on the peak values of total axial load L_p, axial load per one single wedge P_p, the load wedge P_{wp}, the stress wedge σ_{wp} of Test(II)16-50×100×200. While the total axial contraction C_p, the total axial contraction of one single wedge $C_p/2$, total lateral expansion E_p, total lateral expansion of one single wedge $E_p/2$, and wedge expansion V_{wp} are similar for all prisms and the slip wedge at peak load S_{wp} is same 0.12mm.

The total axial contraction C_p is much larger than the total lateral expansion E_p. The average of C_p and E_p is 0.51mm and 0.19mm respectively. However the axial deformation due to micro-cracking S_{wp} 0.12mm is slightly larger than the lateral deformation due to micro-cracking V_{wp} 0.08mm.

4.4.3 Comparison of Axial Deformation

The same method is used as was used in the first set of experimental test. The individual results tests in one size are plotted together in one graph and then the average curve of every size is determined and compared to other size of prisms.

There are two types of analysis; first set of analysis is for the prisms with ratio width to height to length are 1:2:4 (type sizes of 2, 4, 5, and 6 in Table 4.4). This analysis is exactly same with the first set of experimental test analysis. This analysis refers to Test (II) A. The "*II*" indicate the second experimental test. The second set of analysis is for prisms with ratio height to width are 3, 2 and 1 (type sizes of 1, 2 and 3 in Table 4.4) and it refers to Test (II) B.

4.4.3.1 Total Axial Load – Total Axial Contraction Relationship

The average of *L*-*C* curves of prisms Test(II)-125×250×500, Test(II)-100×200×400, Test(II)15-75×150×300 and Test(II)15-50×100×200 in Section 4.4.2 are quantified in order to compare each other and to see the size effect of this research. To determine the average curve, first make the same interval of total axial contraction *C* then the average of total axial load *L* is calculated for a given *C*.

For example the average of *L*-*C* curves of prisms Test(II)-125×250×500 is determined. The same interval of total axial contraction *C* is determined first such as 0.001mm on every curve in prism Test(II)-125×250×500. Then the average of total axial

load L was calculated as $(L_1+L_2+ L_3)/3$ where L_1, L_2 and L_3 were the total axial load of Test(II)7-125×250×500, Test(II)8-125×250×500 and Test(II)9-125×250×500 respectively for a given total axial contraction. The same procedure is used to determine the average curve for other sizes prism. After that, the average curves are compared to other sizes prism.

Figure 4.131 shows the average of *L*-*C* curves for the prisms with ratio width to height to length are 1:2:4 [Test(II)A]. The value of C_p increases with an increase of the prism size. Bigger size of prism has steeper *L*-*C* curve. This means that the axial deformation is affected by specimen size.

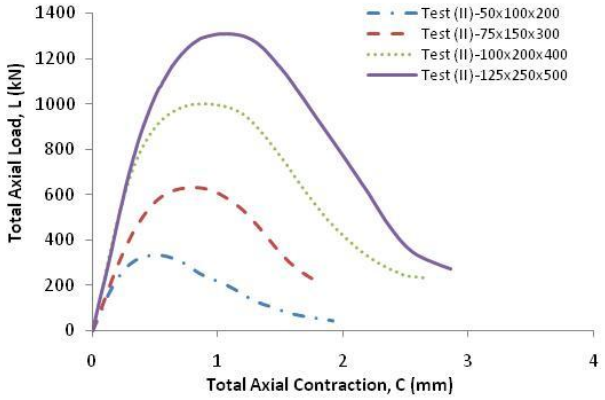

Figure 4.131: The average of total axial load-total axial contraction graph of Test (II) A

The comparison of the *L*-*C* response of Test (II) B is shown in Figure 4.132. The values of C_p are quite the same that is in a very narrow range between 1.02mm to 1.08mm. The peak of total axial load L_p of Test(II)-125×250×500 (as shown in unbroken line) slight higher than Test (II)-125×375×500 (as shown in dot line) while L_p of Test(II)-125×125×500 (as shown in broken line) considerable higher than Test(II)-125×375×500. Therefore slight variation differences in peak load between slenderness ratios (*H*/*W*) 2 and 3, however, significant variations on slenderness ratio 1 to others. A decreasing the slenderness ratio results increasing the total axial load L_p. It means that the peak load L_p is affected by the ratio of height to width however the total axial contraction C_p is not affected by the ratio of height to width.

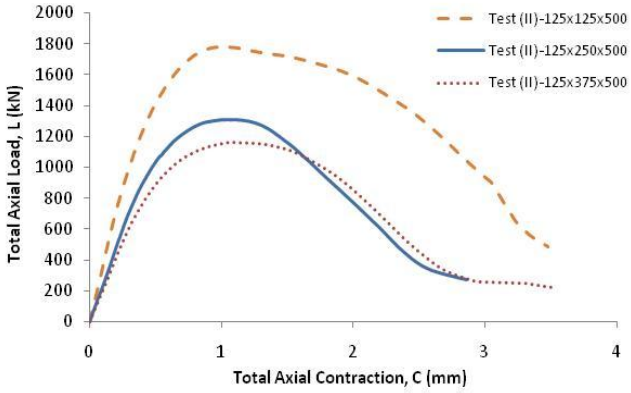

Figure 4.132: The average of total axial load-total axial contraction graph of Test (II) B

The peak of total axial load L_p correspond to total axial contraction C_p each sizes which are determined from the average graph are summarized in Table 4.11. It should be mention that this average values based on the average curve.

Table 4.11: Average of the peak value of concrete prism based on average curves (TEST II)

Size Type	Prism	L_p (kN)	P_p (kN)	P_{wp} (kN/mm)	σ_{wp} (MPa)	C_p (mm)	$C_p/2$ (mm)	S_{wp} (mm)	E_p (mm)	$E_p/2$ (mm)	V_{wp} (mm)
1	2	3	4	5	6	7	8	9	10	11	12
1	TEST(II)-125×375×500	1161	582	1.16	19	1.07	0.54	0.26	0.53	0.26	0.19
2	TEST(II)-125×250×500	1308	655	1.31	21	1.08	0.54	0.26	0.79	0.40	0.34
3	TEST(II)-125×125×500	1782	891	1.78	29	1.02	0.50	0.24	1.13	0.57	0.39
4	TEST(II)-100×200×400	1001	500	1.25	25	0.88	0.44	0.23	0.49	0.24	0.17
5	TEST(II)-75×150×300	632	316	1.05	28	0.80	0.40	0.18	0.29	0.15	0.11
6	TEST(II)-50×100×200	331	166	0.83	33	0.50	0.25	0.12	0.18	0.09	0.08

4.4.3.2 Axial Load – Total Axial Contraction of a Wedge

The same trend is shown in axial load and total axial contraction of a wedge, *P*-*C*/2 response as shown in Figure 4.133 and Figure 4.134 for Test(II)A and Test(II)B respectively. The average graph of *P*-*C*/2 is obtained by dividing the *L*-*C* graph in Figure 4.131 by 2. $C_p/2$ is total axial contraction of one wedge when the peak load P_p reached. The parameters can be seen in

.

Figure 4.133 illustrates the average curve of *P*-*C*/2 with ratio width to height to length are 1:2:4 [Test(II)A]. The graph indicates that the axial deformation is affected by the specimen size.

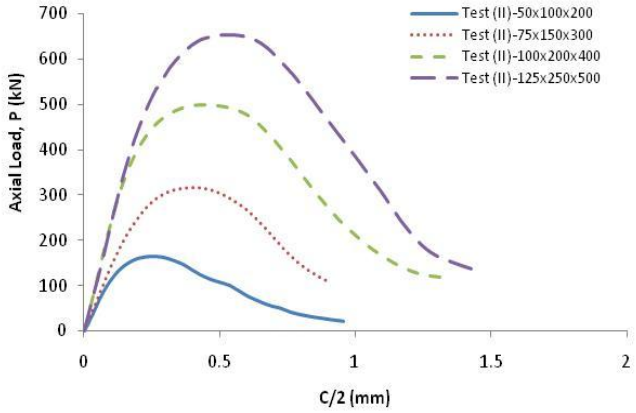

Figure 4.133: The average of axial load-C/2 graph of Test (II) A

The effect of the prism height is shown Figure 4.134. The graph illustrates the average graphs of prism with ratios of height to width are 3, 2 and 1 [Test (II) B]. The prism height decreases with increasing the total axial load L_p. The ratio of height to width give an effect to the load however the ratio H/W not affects to axial deformation.

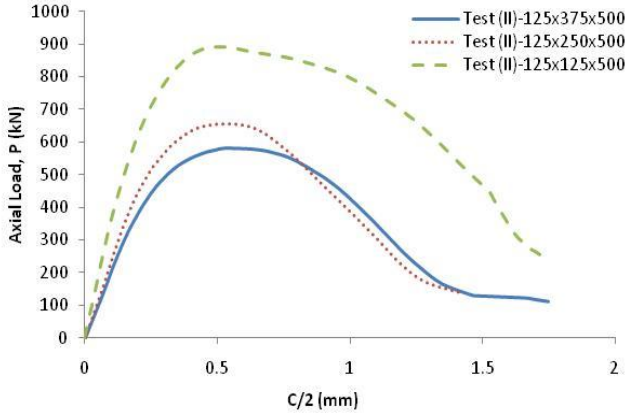

Figure 4.134: The average of axial load-C/2 graph of Test (II) B

The parameters of $C_p/2$ and P_p for every size of prism which are determined from the average graph can be seen in Table 4.11.

After analysed the load and axial deformation in one single wedge, next slip wedge for a given axial load is analysed.

4.4.3.3 Axial Load – Slip of Wedge Relationship

The relationship between axial load P and slip wedge S_w of every size of prism is described and depicted in Section 4.4.2 previously. The average graph of each size is quantified and shown in Figure 4.135 and in Figure 4.136 of Test (II) A and Test(II) B respectively. To determine the average curve the same method is used as was explained in detail in Sections 4.4.3.1 on page 267. Initially the same interval of slip wedge S_w is determined then the average of axial load P is calculated for a given S_w.

The average graph of Test (II) A is shown in Figure 4.135. All size shows the same pattern. The slip wedge S_w commences when the axial loads P are 102kN, 195kN, 307kN and 397kN of Test(II)-50×100×200, Test(II)-75×150×300, Test(II)-100×200×400 and Test(II)-125×250×500 respectively. Before these loads, there is no micro-cracking only the elastic contraction happens. The slip wedge at peak load S_{wp} increased as the size of prism increased. S_{wp} of Test (II) A is between 0.12mm – 0.26mm.

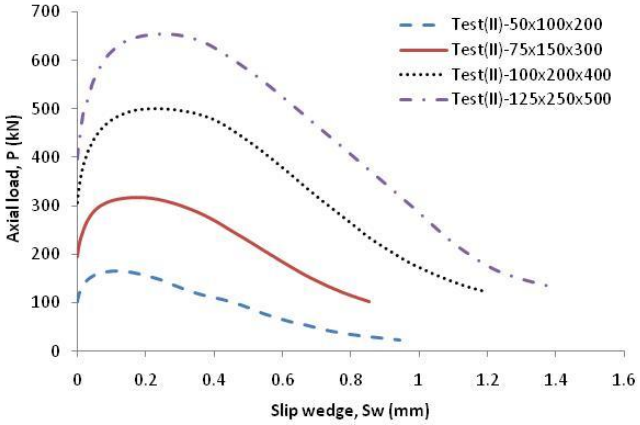

Figure 4.135: The average of axial load-slip wedge graph of Test (II) A

Consider analysis Test (II) B in Figure 4.136, the slip wedge at peak load S_{wp} of the prism with difference height were almost the same around 0.26mm except Test(II)-125×125×500 slightly lower than others around 0.24mm. This means that the slip due to micro-cracking or slip wedge S_{wp} is independent of the H/W ratio.

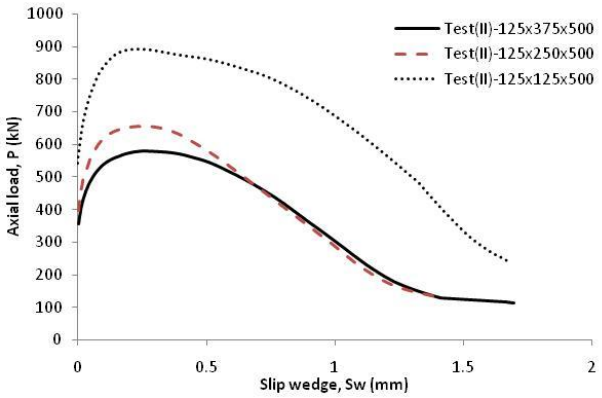

Figure 4.136: The average of axial load-slip wedge graph of Test (II) B

The parameters of S_{wp} for each size of prism can be seen in Table 4.11. After slip wedge for a given axial load is analysed, next step slip wedge for a given wedge load is analysed. This wedge load is the axial load divided by prism length *S*.

4.4.3.4 Load Wedge – Slip of Wedge Relationship

Now the axial load *P* as described previously divided by the length of the prism *S*. The individual result is plotted in same size as presented in Section 4.4.2. The average of those graphs is determined by using the same method as was described previously. First the same interval of slip wedge is determined then calculated the average of the load wedge for a given slip wedge. As a result the average curves of every size is shown in Figure 4.137 of Test (II) A and Figure 4.138 of Test (II)B.

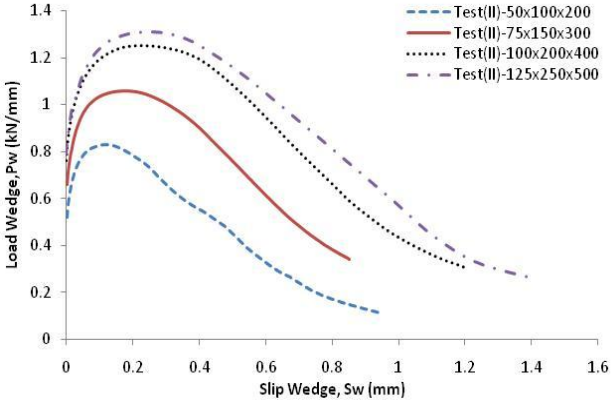

Figure 4.137: The average of load wedge-slip wedge graph of Test (II) A

Figure 4.137 shows decreasing the size of prism causes decreasing the load wedge maximum P_{wp}. P_{wp} increased significantly between Test(II)-50×100×200, Test(II)-75×150×300 and Test(II)-100×200×400 but increased slightly between Test(II)-100×200×400 and Test(II)-125×250×500.

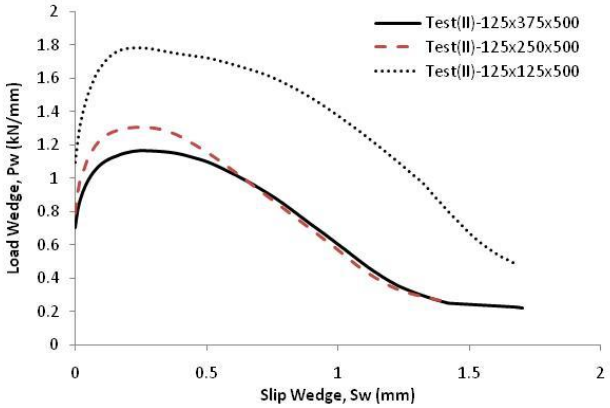

Figure 4.138: The average of load wedge-slip wedge graph of Test (II) B

Figure 4.138 illustrates the analysis Test (II) B. The graph indicates that the peak of load wedge P_{wp} increased as the height of prism decreased therefore the load wedge is affected by the *H*/*W* ratio however slip of the wedge is not affected by *H*/*W*.

4.4.3.5 Stress wedge – Slip wedge Relationship

The individual relationship between stress wedge and slip wedge of the prisms at the same size was discussed previously in Section 4.4.2. In this section the average of these responses is quantified and compared with others size. The average graph is determined using the same method as was used to determine the average graph of *L*-*C* in Section 4.4.3.1 in page 267. The average curve is plotted in Figure 4.139 and Figure 4.140 for Test (II) A and Test (II) B respectively.

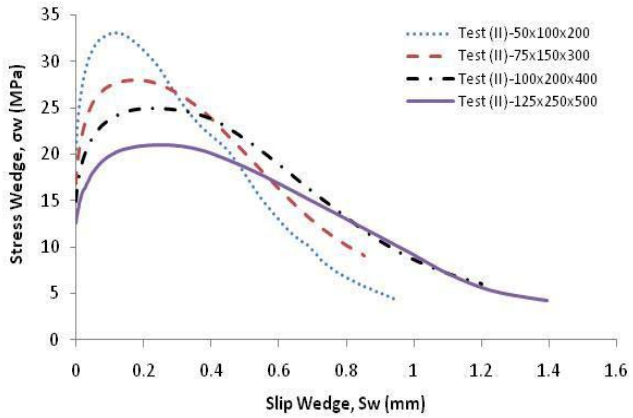

Figure 4.139: The average of stress wedge-slip wedge graph of Test (II) A

Figure 4.139 illustrates the peak of stress wedge σ_{wp} increased with decreasing the size of the prism. It indicates that the peak wedge stress of the prism is affected by the size of specimens. This phenomenon also occurred in the first set of experimental test. The slip wedge at peak stress S_{wp} varies depends on the prism size. The bigger size of prism causes the larger slip wedge.

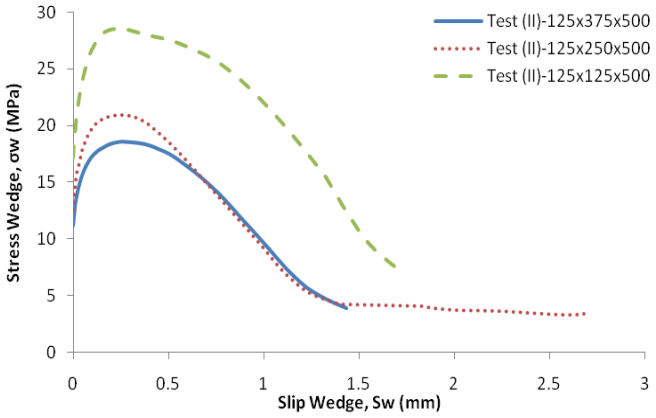

Figure 4.140: The average of stress-slip wedge graph of Test (II) B

Figure 4.140 illustrates the stress wedge-slip wedge response of three different ratios a height to width. It can be seen that decreasing the prism height causes increasing the peak of wedge stress. The slip wedge at peak load S_{wp} is not vary but same although the prism height decreases. This means that the slip wedge not affected by the slenderness ratio.

Friction restraint between prisms and loading platen cause a horizontal confinement at the ends of the prisms. This confined region is reduces with increasing distance from the specimen ends. In tall prism the unconfined region is larger than the short prism. In the short prism almost the whole prism is confined. The failure of concrete commence in the unconfined region at lower load. Hence the taller prism shows lower peak of wedge stress than shorter prism.

The peak of stress wedge increase approximately 54% due to the reducing of the prism ratio a height to width from 3 to 1. Meanwhile, the prism ratio a height to width was reduced from 2 to 1 the peak of stress wedge increase only 13% (Figure 4.141). The similar result was also occurred on other researcher (Sangha and Dhir 1972).

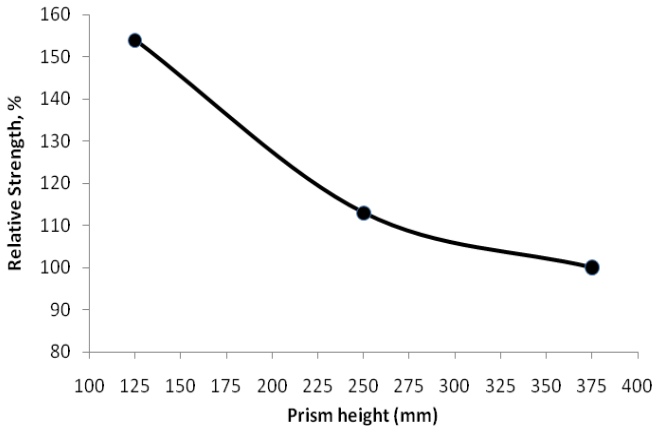

Figure 4.141: Relative strength-height of prism graph

The important parameters of analyses in axial deformation previously are listed in Table 4.11. After analysed the comparison in axial deformation, comparison the deformation in lateral direction is explained in details in the next section. The steps of the analysis are same with analysis the deformation in axial direction.

4.4.4 Comparison of Lateral Deformation

4.4.4.1 Total Axial Load – Total Lateral Expansion Relationship

The average curve of total axial load and total lateral expansion, *L-E* response of every size is determined then compared to other sizes. The average curve is obtained by using the same method as was used for other analyses previously. Figure 4.142

illustrates the comparison *L-E* curves of four different sizes [Test (II) A]. It can be seen that the slope of ascending branch of the curves is the same. It means that the ascending slope of *L-E* response is not affected by the size of prism. Contrary to the relationship between total axial load and total axial contraction, *L-C* where the slope of ascending branch depend on the prism size (see again Figure 4.131). The same behaviour occurred on the first set of experimental test (Chapter 3).

The graph indicates that the total lateral expansion E_p varies between 0.18mm to 0.79mm. A reduction the size of prism results a decrease of lateral expansion of prism, E_p. The values of E_p are smaller than total axial contraction C_p for all size (see Table 4.11). Total axial deformation is larger than total lateral deformation at peak load.

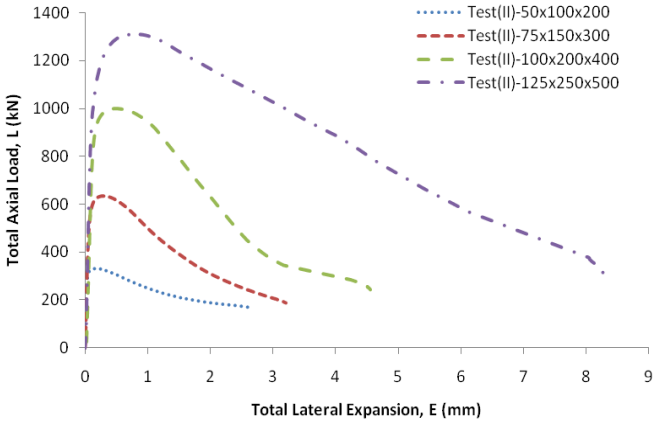

Figure 4.142: The average of L-E graph of Test(II) A

The analysis of Test (II)B is shown in Figure 4.143. The graph indicates that the slope of ascending branch of the curves is the same. The ascending slope of *L-E* of Test (II) B response is not influenced by the prism height. The pre peak response of load versus lateral deformation is not affected by the prism size. However the post peak response is affected by the prism size.

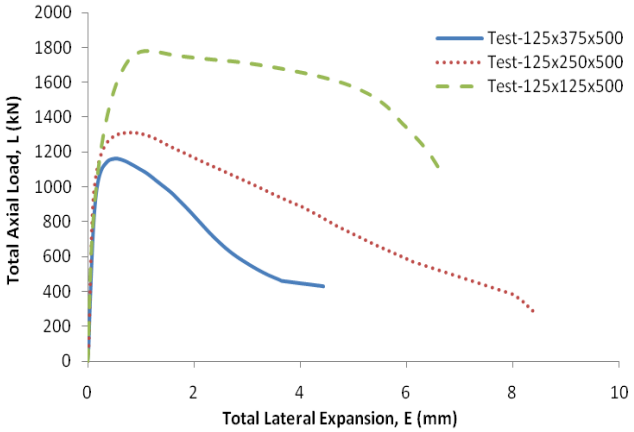

Figure 4.143: The average of L-E graph of Test (II) B

The value of E_p of Test (II) B varies between 0.53mm to 1.13mm. The total lateral expansion E_p increases with decreasing the prism height. It means that the total lateral expansion E_p is affected by H/W ratio however the total axial contraction C_p is not affected by H/W ratio.

4.4.4.2 Axial Load – Total Lateral Expansion of a Wedge

The *L-E* is the relationship between load and lateral deformation of the whole prism while *P-E*/2 is the relationship between load and lateral deformation of a wedge hence *P-E*/2 graph is obtained by dividing *L-E* graph with 2. Hence *P-E*/2 response is the same with the pattern of *L-E* response.

The average of *P-E*/2 graph is shown in Figure 4.144 and Figure 4.145 for Test(II)A and Test(II)B respectively. Figure 4.144 illustrates $E_p/2$ of Test (II) A varies between 0.09mm to 0.40mm. These values are listed in Table 4.11. The lateral deformation is affected by the size of the prism.

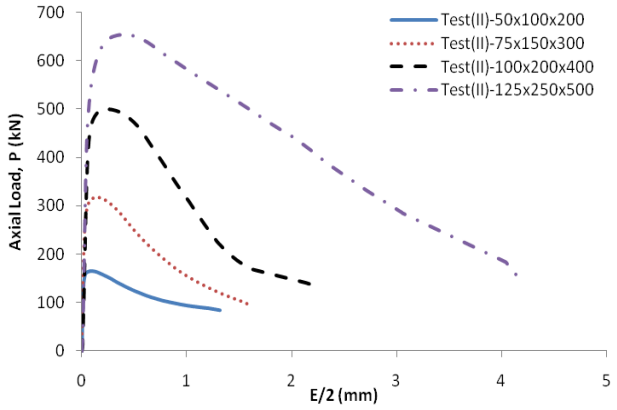

Figure 4.144: The average of axial load – E/2 graph of Test (II) A

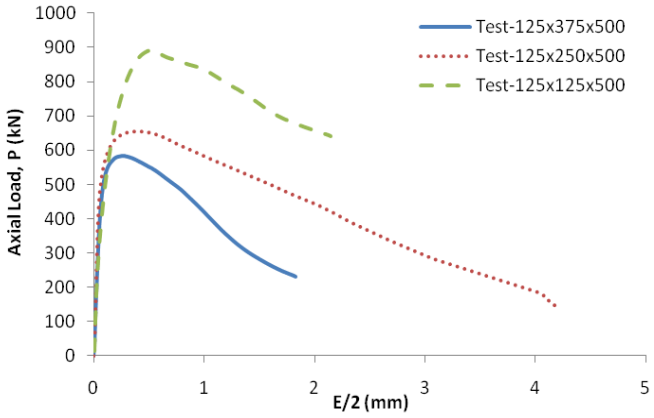

Figure 4.145: The average of axial load – E/2 graph of Test (II) B

The value of $E_p/2$ of Test (II) B varies between 0.53mm to 1.13mm. The total lateral expansion $E_p/2$ increases with decreasing the prism height. The parameter of E_p of each size is listed in Table 4.11

4.4.4.3 Axial Load – Wedge Expansion Relationship

The total lateral expansion of a wedge $E/2$ is consists of elastic expansion and expansion due to micro-cracking V_w. Thus the wedge expansion V_w is obtained by subtracting the elastic expansion from the total lateral expansion of a wedge $E/2$. The average graph uses the same method as was used by other analyses before.

Figure 4.146 shows the relationship between axial load and wedge expansion in Test (II) A. The graph indicates that the average wedge expansion on peak load V_{wp} is on

the range between 0.08mm-0.34mm. The wedge expansion at peak load V_{wp} increases as the size of prism increase therefore dependent of the prism size.

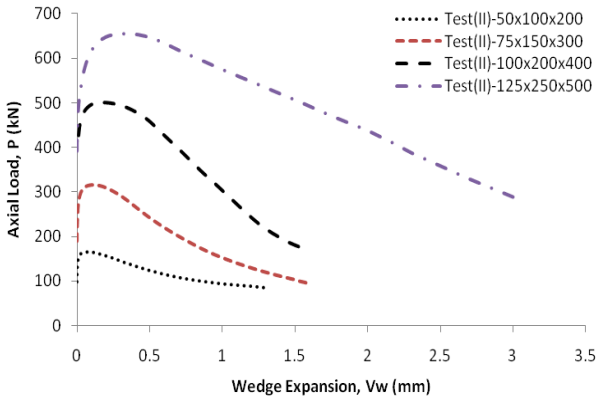

Figure 4.146: The average of axial load – wedge expansion graph of Test (II) A

Figure 4.147 illustrates the analysis Test (II) B. The graph indicates that the peak of load P_p increases as the H/W ratio decreases and the wedge expansion at peak load V_{wp} increases as the H/W ratio decreases. The parameter V_{wp} is between 0.26m to 0.57mm.

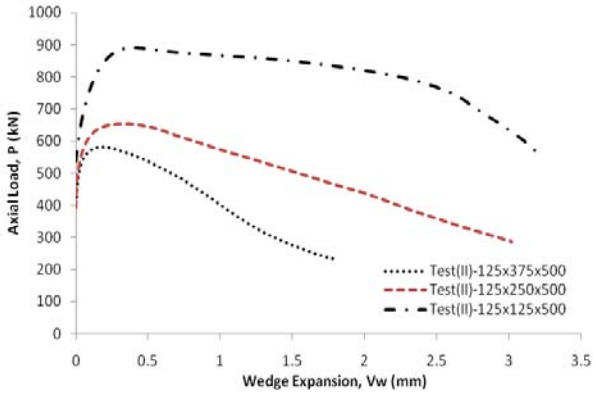

Figure 4.147: The average of axial load – wedge expansion graph of Test (II) B

After analysis the average of axial load and wedge expansion P-V_w response of Test (II) A and Test (II) B, next wedge expansion for a given load wedge is analysed.

4.4.4.4 Load Wedge – Wedge Expansion Relationship

The axial load P from the previous section is divided by the length of the prism S equal to wedge load P_w in kN/mm. The next two figures (Figure 4.148 and Figure 4.149)

present the load wedge P_w against wedge expansion V_w of Test (II) A and Test (II) B respectively.

The graphs show the wedge expansion commences prior to peak load wedge. For example Test(II)-50 as shown in a dot line in Figure 4.148, the wedge not expand laterally up to load wedge P_w approximately 0.8kN/mm then expands very slowly up to peak wedge load 0.83kN/mm however after that point the wedge expand significantly in lateral direction as the load decrease.

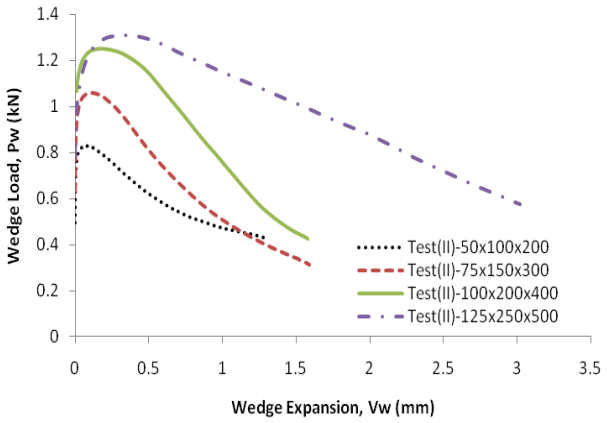

Figure 4.148: The average of load wedge – wedge expansion graph of Test (II) A

Figure 4.149 illustrates the lateral deformation due to micro-cracking in lateral direction or wedge expansion V_w occurs under increasing load wedge P_w. The micro-cracking is not occur until the load wedge approximately 1kN/mm (higher than αP_w) on Test(II)-125×375×500 as shown in broken line in Figure 4.149, as the load wedge increase the micro-cracking develop laterally up to peak load wedge 1.16kN/mm. After that the micro-cracking develop significantly until the prism failed. The same pattern occurs on Test(II)-125×250×500, the micro-cracking commences prior the peak load. While Test(II)-125×125×500 as shown in broken line, the micro-cracking start to develop at load wedge P_w approximately 1.05kN/mm (that is αP_w). It increases as increasing the load wedge up to peak load and increase significantly on post peak region until the prism failed.

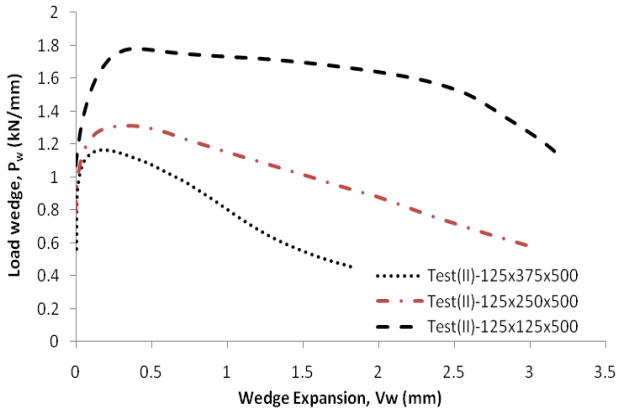

Figure 4.149: The average of load wedge – wedge expansion graph of Test (II) B

The parameter of P_w and V_w are listed in Table 4.11. The last analysis in lateral deformation is the wedge expansion for a given stress wedge.

4.4.4.5 Stress wedge – Wedge expansion Relationship

The average of the relationship between stress wedge and wedge expansion for each size is found out and depicted in Figure 4.150 for analysis Test (II) A and Figure 4.151 for analysis Test (II) B. It shown that wedge expansion at peak stress V_{wp} between 0.08mm to 0.34mm. The peak of wedge stress σ_{wp} increases when the prism size decreases while the wedge expansion V_{wp} increases as the prism size increases. This means that the stress wedge and wedge expansion are size dependent. The peak stress σ_{wp} corresponding to wedge expansion V_{wp} are listed in Table 4.11. The relationship of stress wedge σ_{wp} and wedge expansion V_{wp} of Test (II)B is depicted in Figure 4.151. The pattern is same with the relationship load wedge-wedge expansion P_w and V_w because the stress wedge σ_{wp} is the load wedge divided by the depth of the wedge d_w. The depth of the wedge for Test(II) B is same.

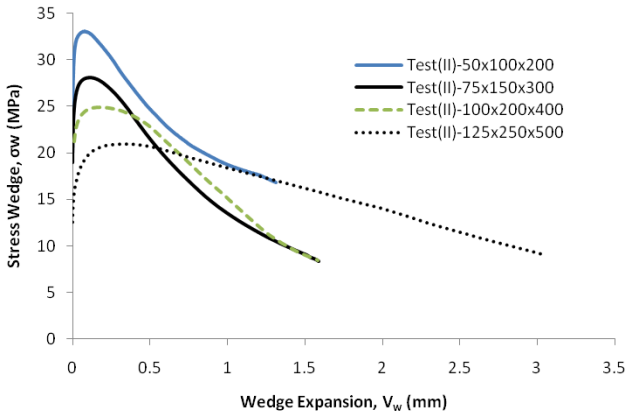

Figure 4.150: The average of stress wedge-wedge expansion graph of Test (II) A

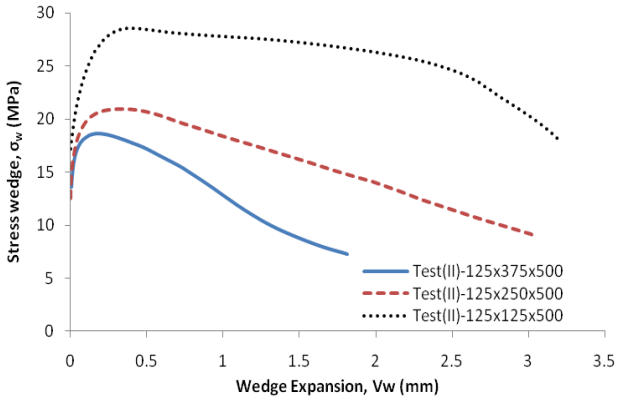

Figure 4.151: The average of stress wedge-wedge expansion graph of Test (II) B

The parameters of all concrete prisms such as L_p, P_p, P_{wp}, σ_{wp}, C_p, $C_p/2$, S_{wp}, E_p, $E_p/2$, and V_{wp} are listed in Table 4.11. It should be noted that this important parameter based on average graph. Column 1 in Table 4.11 indicates the size type. The size type 2,4,5 and 6 refers to Test(II) A where the ratio *W*/*H*/*S* is same 1:2:4 while size type 1, 2 and 3 refers to Test(II) B where *H*/*W* ratio are 3,2 and 1 respectively.

The stress wedge σ_{wp} that is represented in column 6, increases as the slenderness ratio (*H*/*W*) of prism decrease due to influence of the confining effect. The frictional restraints occur due to interaction between platens and specimen. As a result, the horizontal confinement occurs to at the top and bottom edges of the prisms. Hence for the short prism [Test(II)-125×125×500], the confined zone include the most of the specimen, while the

relatively large unconfined area develop when the specimens height increase. Therefore higher peak stress occurs at shorter prism. The similar behaviour have been observed by some researchers, e.g. Kotsovos (1983), Sangha and Dhir (1972), Van Vliet and Van Mier (1996), Van Mier and Shah et al (1997). The same pattern occurs in total axial load L_p, axial load P_p and load wedge P_{wp}. While a stress reduction occurs with increase in the prism size [Test(II)A].

The deformation in axial direction at peak such as the total contraction load C_p, $C_p/2$ and deformation due to micro-cracking S_w of prism different H/W ratio has almost the same value. While the deformation in lateral direction such as the total lateral expansion E_p, $E_p/2$ and wedge expansion V_{wp} increase as the H/W ratio decreases. With the same amount of axial deformation to all prisms cause the bigger lateral deformation to the shorter prism.

On the other hand, the axial and lateral deformations vary and depend on the prism size. The deformation in axial and lateral directions increases as the size of the prism increases.

At peak stress, total axial contraction C_p of all prism size considerable higher than total lateral expansion E_p. This means up to peak stress total deformation in axial direction is much higher than total deformation in lateral direction except TEST(II)-125×125×500 at which the slenderness (H/W) ratio 1, the deformations are almost similar. However, at peak stress there is slight difference between axial deformation and lateral deformation due to micro-cracking (S_{wp} and V_{wp}). This means that elastic contraction give more influence to the axial total deformation. The elastic contraction consists of material contraction, dental paste contraction and bedding down.

4.4.5 Wedges Analysis

The total deformation and micro-cracking deformation in both directions and the comparison results of all prisms have been analysed and discussed above. Next in this section behaviour of micro-cracking deformation or the wedges is analysed more detail. Begin with axial direction or slip wedge followed by deformation in lateral direction or the wedge expansion.

4.4.5.1 Stress wedge Wedge – Slip Wedge Relationship

One of the aims of this research develops the generic expression to simulate the stress wedge for a given slip wedge. Figure 4.152 illustrates the average graph of the stress and slip wedge of Test(II)A. The graph indicates that the peak of stress wedge σ_{wp} and slip wedge at peak stress S_{wp} are vary and depend on the prism size. The phenomenon may become clearer when non-dimensionalised of stress wedge-slip wedge is plotted.

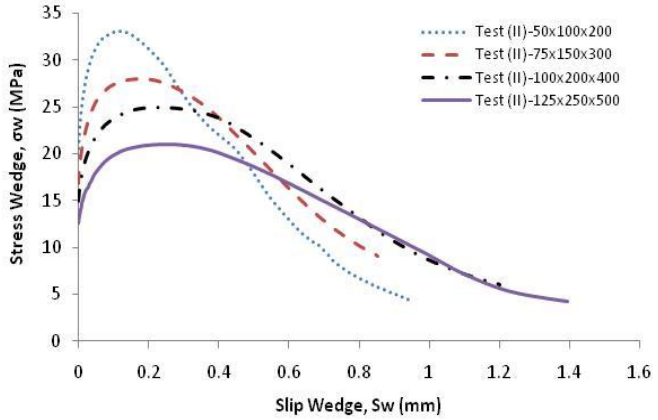

Figure 4.152: The stress-slip wedge of different size of prism-Test(II)A

The non-dimensionalised of σ_w-S_w is obtained by dividing the stress and slip wedge with the peak of stress and peak of slip wedge respectively. The non-dimensionalised of stress-slip wedge curves for all size is depicted in Figure 4.153. The graph illustrates the similar trend. The differences in the response for prisms almost disappear completely. The expression to represent the normalised stress of the wedge σ_w/f_p in terms of S_w/ S_{wp} is given in Eq. 4.3.

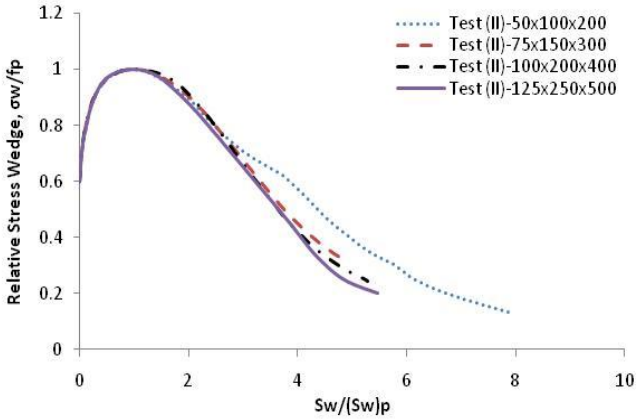

Figure 4.153: Non-dimensionalised stress wedge-slip wedge of Test (II) A

$$\frac{\sigma_w}{f_p} = \left[-0.01\left(\frac{S_w}{S_{wp}}\right)^2 + 5.14\left(\frac{S_w}{S_{wp}}\right) + 2.54 \right] \exp\left[0.02\left(\frac{S_w}{S_{wp}}\right)^2 - 0.72\left(\frac{S_w}{S_{wp}}\right) - 1.31 \right] \qquad \textit{Eq. 4.3}$$

where σ_w is the wedge stress, f_p is the average of the peak stress wedge σ_{wp} that is 27MPa, S_w and S_{wp} are slip wedge and slip wedge at peak stress respectively. S_{wp} is a function of depth of wedges d_w that is, it varies with prism width W as shown in Figure 4.154. It was assumed the wedge full develop hence the depth of the wedge d_w is half than prism width W. An expression for S_{wp} in terms of d_w is given in Eq. 4.4.

$$S_{wp} = 0.0044 d_w \qquad \textit{Eq. 4.4}$$

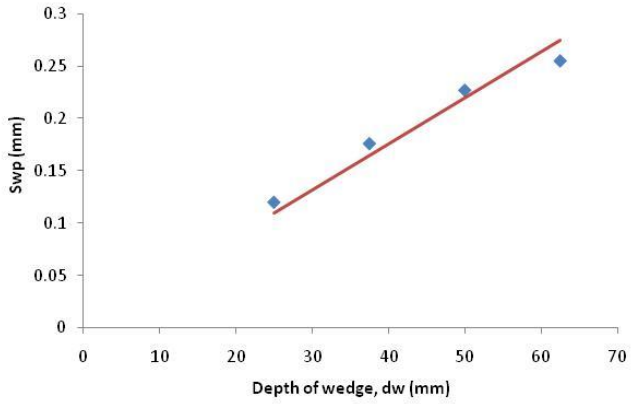

Figure 4.154: Slip wedge at peak stress wedge over depth of wedge graph of TEST (II) A

The mathematical expression of S_w / S_{wp} for a given σ_w/f_p as given in Eq. 4.3 shows the theoretical results fit well with the experimental tests, as shown in Figure 4.155, Figure 4.156, Figure 4.157 and Figure 4.158 for Test(II)-50×100×200, Test(II)-75×150×300, Test(II)-100×200×400 and Test(II)-125×250×500 respectively.

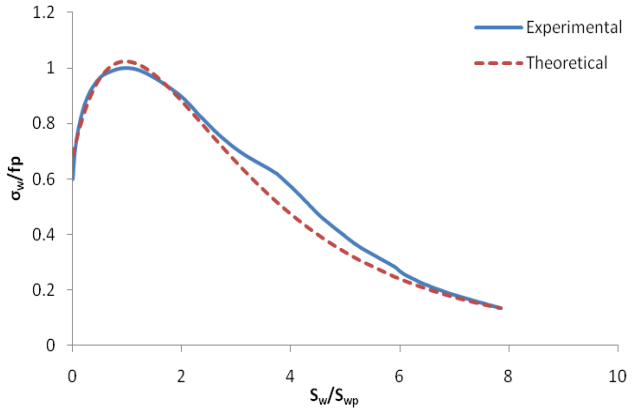

Figure 4.155: Stress-slip comparison response of Test(II)-50×100×200

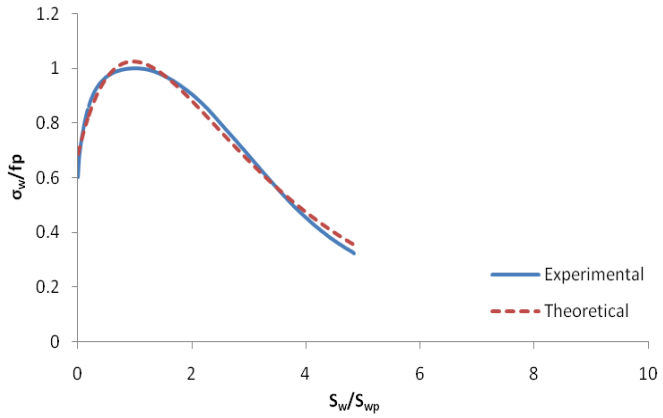

Figure 4.156: Stress-slip comparison response of Test(II)-75×150×300

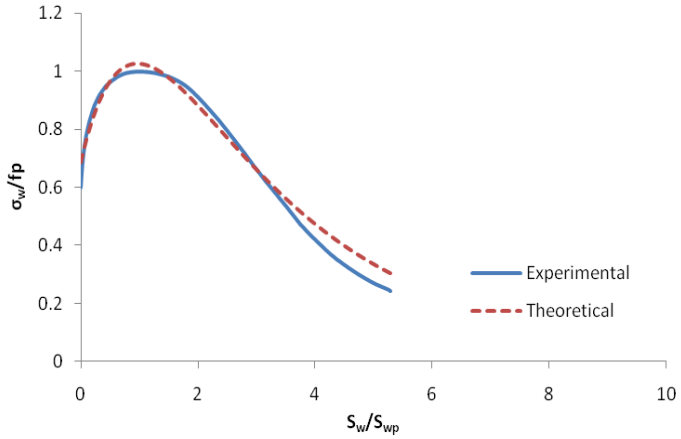

Figure 4.157: Stress-slip comparison response of Test(II)-100×200×400

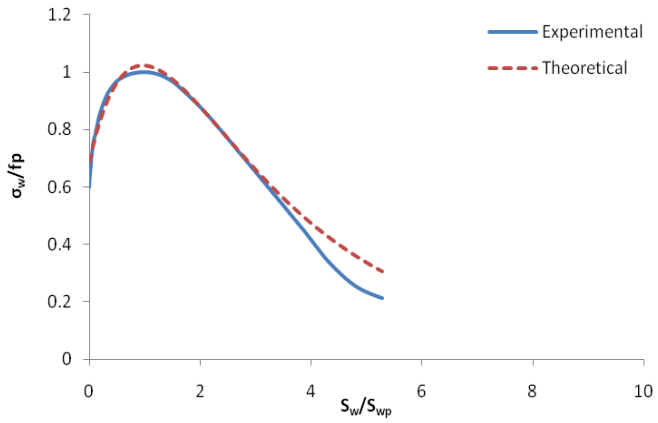

Figure 4.158: Stress-slip comparison response of Test(II)-125×250×500

Mathematical expression for different slenderness ratio [Test(II)B] is also developed to quantify the behaviour of the axial deformation due to micro-cracking for a given stress. The steps of analysis are the same as was used to determine the equation in different size above. First the relationship between stress and slip wedge is represented again in Figure 4.159. Then the non-dimensionalised curve of σ_w-S_w is determined as shown Figure 4.160 in order to get a good comparison between the curves. The normalised slip wedges are shown as a function of the normalised stresses. The normalised slip wedges and stresses are slip wedges and stresses divided by peak slip wedge and peak stress respectively. The scatter occurs on Test(II)-125×125×500 on post peak stress.

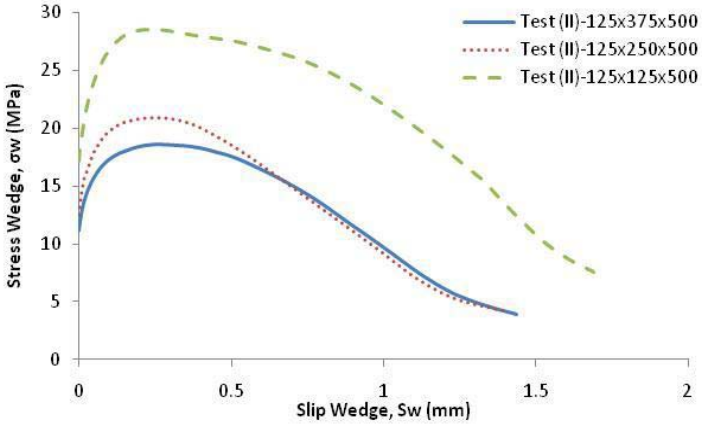

Figure 4.159: The stress-slip wedge of different slenderness ratio of prism-Test(II)B

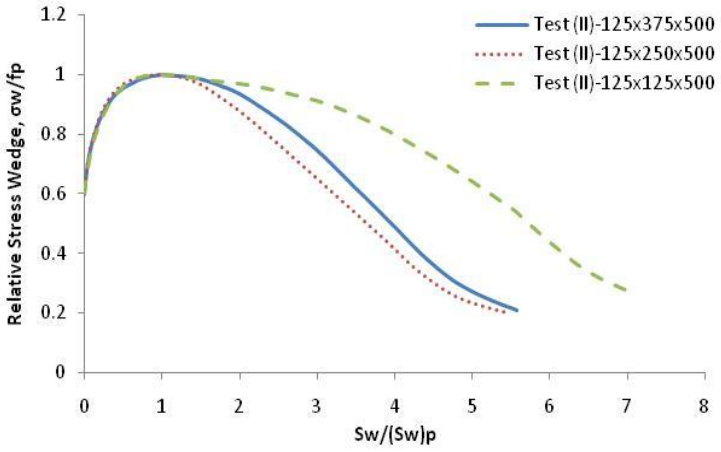

Figure 4.160: Non-dimensionalised stress-slip wedge of Test (II) B

The mathematical equation is quantified in order to represent the normalised stress-slip wedge in Figure 4.160. This expression of relative stress wedge σ_w/f_p in terms of S_w/S_{wp} is given as

$$\frac{\sigma_w}{f_p} = \left[0.07\left(\frac{S_w}{S_{wp}}\right)^2 + 4.50\left(\frac{S_w}{S_{wp}}\right) + 3.63\right]\exp\left[-0.01\left(\frac{S_w}{S_{wp}}\right)^2 - 0.50\left(\frac{S_w}{S_{wp}}\right) - 1.59\right] \qquad \textit{Eq. 4.5}$$

The slip wedge at peak load S_{wp} of prism in difference slenderness ratio is in a narrow range between 0.24mm to 0.26mm as listed in Table 4.11 in page 269. Thus the average of S_{wp} is determined equal to 0.25mm. Therefore Eq. 4-5 turns into

$$\frac{\sigma_w}{f_p} = \left[0.28S_w^{\,2} + 18S_w + 3.63\right]\exp\left[-0.04S_w^{\,2} - 2S_w - 1.59\right] \qquad \textit{Eq. 4.6}$$

The expression in Eq.4-6 shows that the relationship of stress and slip wedge in different slenderness ratio is not depend on the depth of the wedge d_w. This equation then compare with experimental result as shown in Figure 4.161, Figure 4.162 and Figure 4.163 for Test(II)-125×125×500, Test(II)-125×250×500 and Test(II)-125×375×500 respectively.

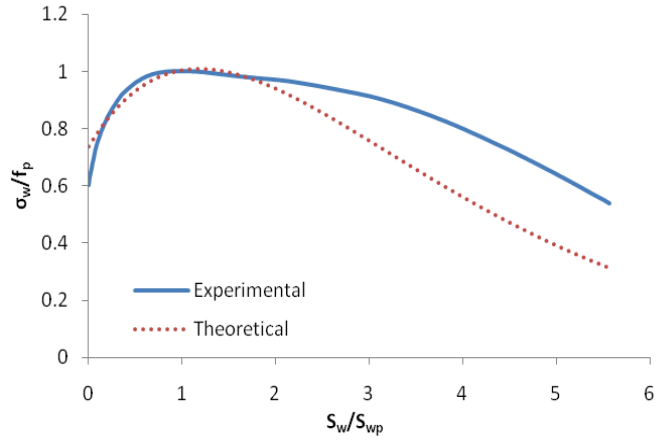

Figure 4.161: The stress-slip comparison response of Test(II)-125×125×500

The scatter occurs on comparison between experimental and theoretical in Test(II)-125×125×500 in Figure 4.161 but still acceptable. This happens because the response of Test(II)-125×125×500 is not the same line as shown in Figure 4.160 while the Eqs. 4.5 and 4.6 are determined by using that line. Hence the general mathematical expression at Eq. 4.6 can be used.

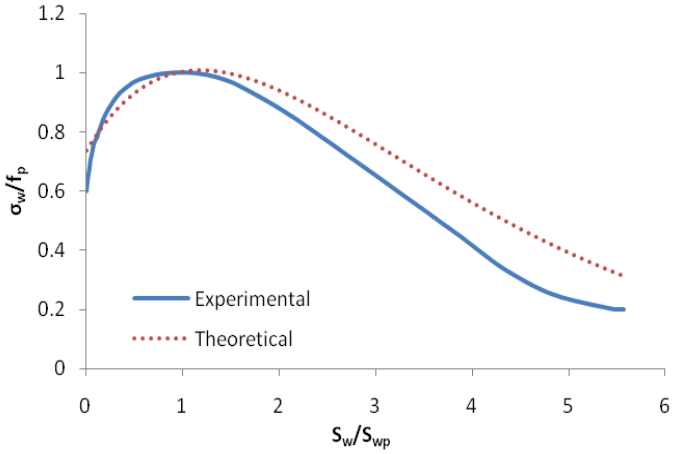

Figure 4.162: The stress-slip comparison response of Test(II)-125×250×500

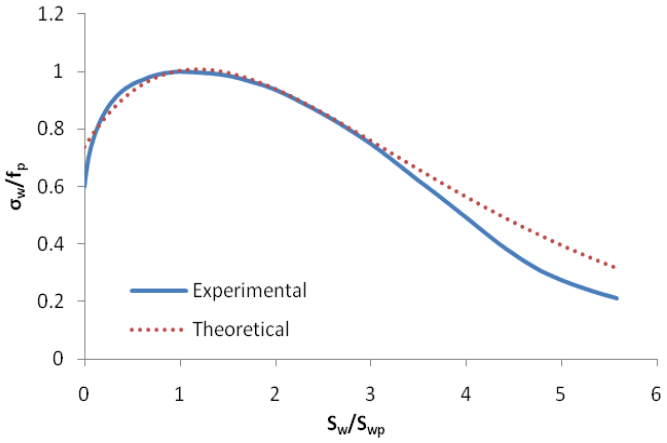

Figure 4.163: The stress-slip comparison response of Test(II)-125×375×500

The wedge analysis in axial direction and the general expression to represent the response of stress wedge in terms of slip wedge have been developed above. Next the same analysis is applied to lateral deformation of the wedge. The prism with different size [Test (II)A] is first analysed and followed by the prism with different slenderness ratio [Test (II)B].

4.4.5.2 Stress Wedge – Wedge Expansion Relationship

The relationship between the stress wedge and wedge expansion of Test (II)A is depicted again in Figure 4.164. From the data of parameters in Table 4.11 in page 269 reveal the wedge expansion V_{wp} varies between 0.08-0.34mm. The mathematical expression is developed to simulate the stress wedge for a given wedge expansion. The non-dimensionalised the stress wedge and wedge expansion response is determined first. The non-dimensionalised of the stress and wedge expansion is obtained by dividing the stress wedge and wedge expansion with the peak values of stress and wedge expansion respectively. Then a equation is developed to represent that relationship. More detail is described below.

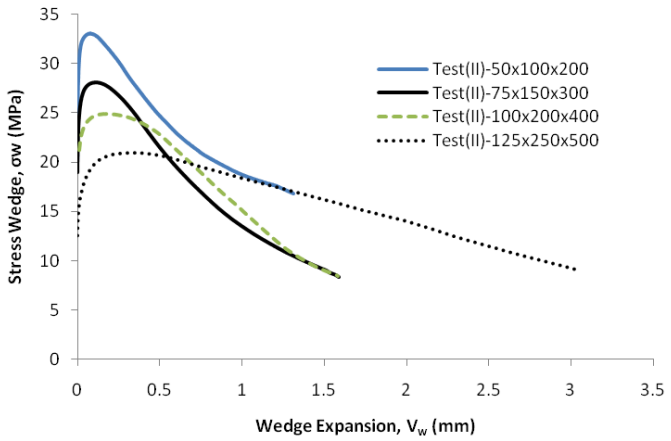

Figure 4.164: The average of stress-wedge expansion graph of Test (II) A

Figure 4.165 illustrates the normalized of the stress and the wedge expansion curves for all size. The responses of Test(II)-75×150×300, Test(II)-100×200×400 and Test(II)-125×250×500 are in one line and look very similar except Test(II)-50×100×200 where small scatter occurs on post peak response. The expression is determined to represent the relative normalised stress of the wedge σ_w/f_p in terms of V_w/V_{wp} as given in Eq. 4.7.

$$\frac{\sigma_w}{f_p} = \left[0.05\left(\frac{V_w}{V_{wp}}\right)^2 + 3.04\left(\frac{V_w}{V_{wp}}\right) + 5.58\right]\exp\left[0.01\left(\frac{V_w}{V_{wp}}\right)^2 - 0.36\left(\frac{V_w}{V_{wp}}\right) - 1.82\right] \qquad \textit{Eq. 4.7}$$

where σ_w is the wedge stress, f_p is the average of the peak stress wedge σ_{wp}, V_w is wedge expansion and V_{wp} is wedge expansion at peak stress.

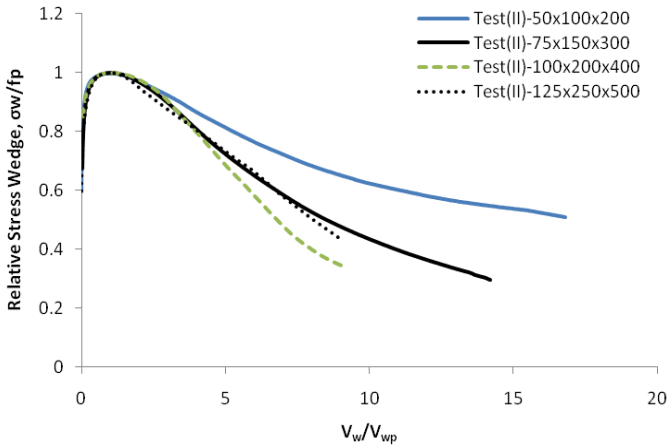

Figure 4.165: Non-dimensionalised stress-wedge expansion of Test (II) A

The wedge expansion at the peak stress V_{wp} varies and depends on the prism size as shown in Table 4.11 and Figure 4.164. V_{wp} for all prism in Test(II)A is similar except V_{wp} of Test(II)-125×250×500 almost two times than other sizes hence V_{wp} of Test(II)-125×250×500 is neglected to quantify the equation of V_{wp} as a function of d_w. Figure 4.166 illustrates the relationship between V_{wp} and d_w. The mathematical expression of the wedge expression V_{wp} for a given depth of wedge d_w as

$$V_{wp} = 0.0033 d_w \qquad \textit{Eq. 4.8}$$

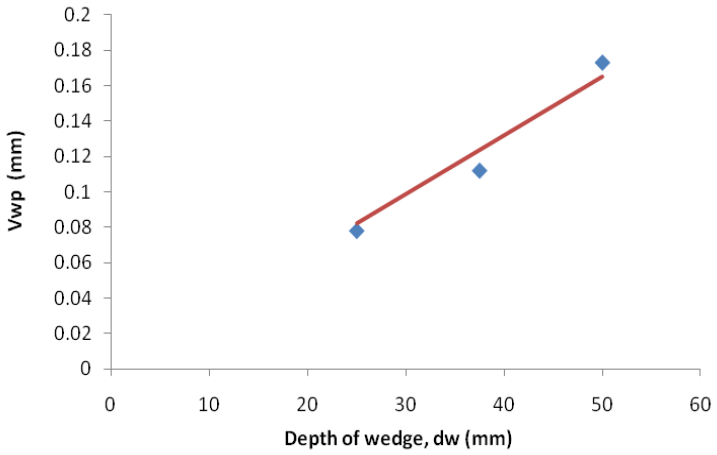

Figure 4.166: Wedge expansion at peak stress over depth of wedge graph [Test(II)A]

The general expression of σ_w/f_p in terms of V_w/V_{wp} in Eq. 4.8 provided an accurate fit to the experimental results, as shown in Figure 4.167, Figure 4.168, Figure 4.169, Figure 4.170 for Test(II)-50×100×200, Test(II)-75×150×300, Test(II)-100×200×400 and Test(II)-125×250×500 respectively.

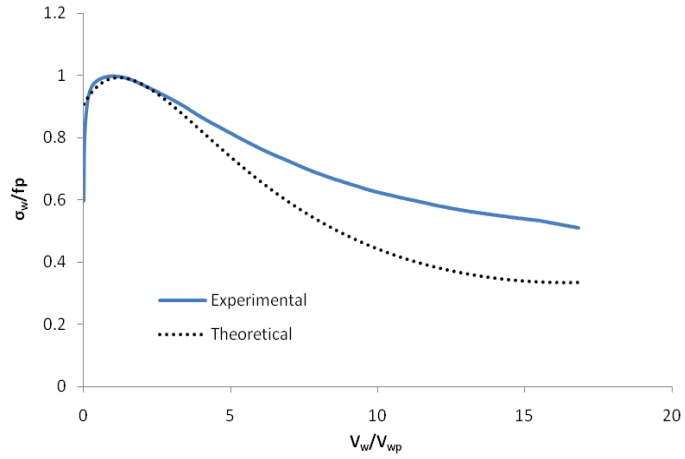

Figure 4.167: Stress-expansion comparison response of Test(II)-50×100×200

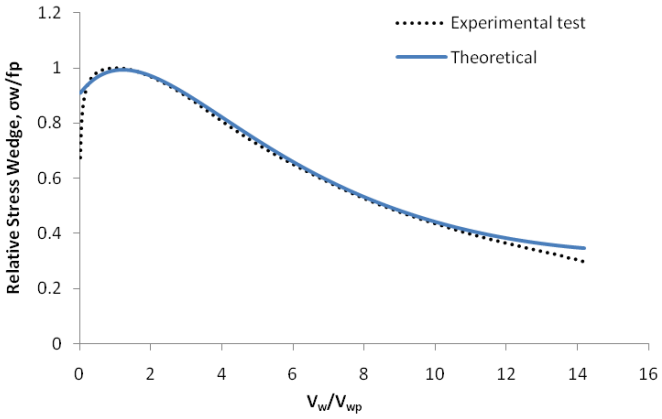

Figure 4.168: Stress-expansion comparison response of the prism Test(II)-75×150×300

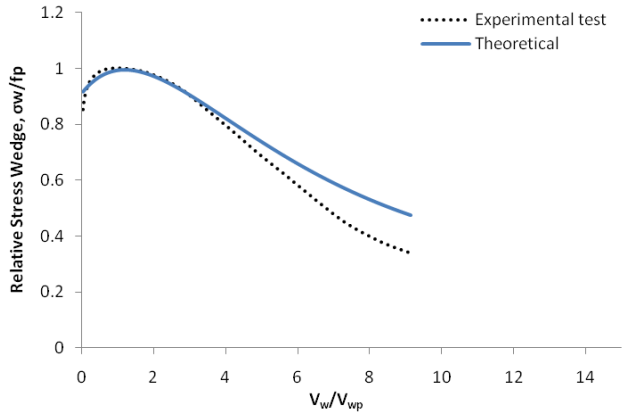

Figure 4.169: Stress-expansion comparison response of the prism Test(II)-100×200×400

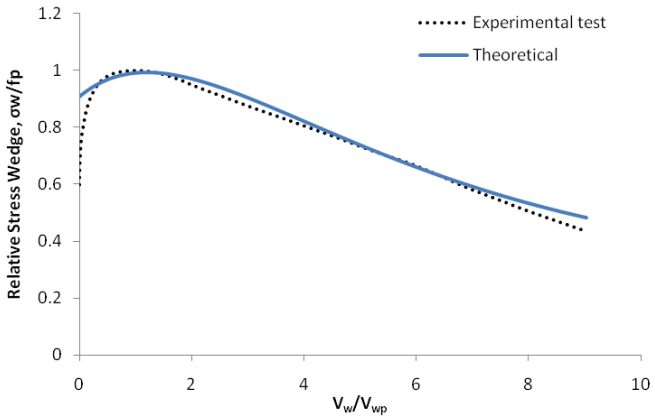

Figure 4.170: Stress-expansion comparison response of the prism Test (II)-125×250×500

Analysis the wedge expansion in different slenderness ration [Test(II)B] is described below. The stress-wedge expansion is depicted again in Figure 4.171 and the non-dimensionalised curve of σ_w-V_w is determined as shown in Figure 4.172. The mathematical equation is develop to represent the σ_w-V_w response given as.

$$\frac{\sigma_w}{f_p} = \left[0.01\left(\frac{V_w}{V_{wp}}\right)^2 + 2.87\left(\frac{V_w}{V_{wp}}\right) + 5.67\right] \exp\left[0.01\left(\frac{V_w}{V_{wp}}\right)^2 - 0.31\left(\frac{V_w}{V_{wp}}\right) - 1.87\right] \qquad \textit{Eq.4.9}$$

The wedge expansions at peak load V_{wp} of Test (II)-125×250×500 and Test (II)-125×125×500 are 0.34mm and 0.39mm respectively while V_{wp} of Test (II)-125×375×500 is much smaller than others approximately 0.19mm. The value of V_{wp} of Test (II)-

125×375×500 is neglected and the average of V_{wp} is 0.37mm. Hence expression in Eq. 4-9 change into

$$\frac{\sigma_w}{f_p} = \left[0.03V_w{}^2 + 7.76V_w + 5.67\right]\exp\left[0.03V_w{}^2 - 0.84V_w - 1.87\right] \qquad \textit{Eq. 4.10}$$

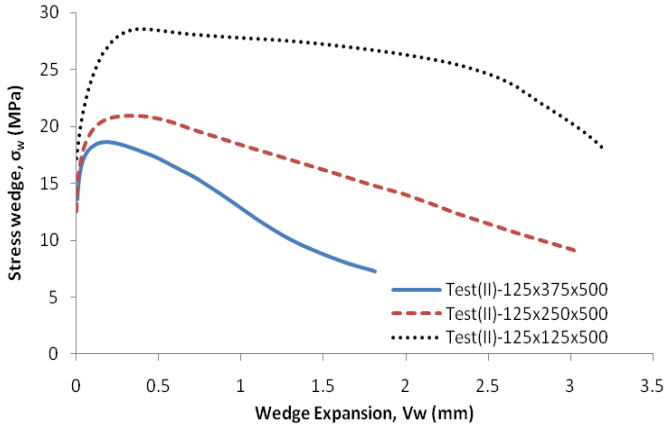

Figure 4.171: The average of stress-wedge expansion graph of Test (II) B

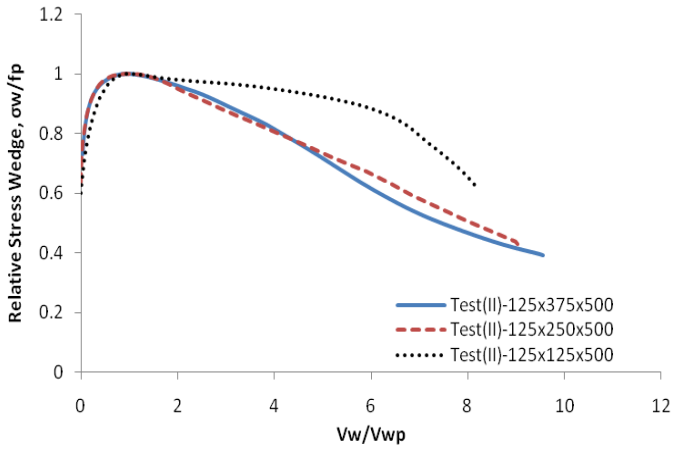

Figure 4.172: Non-dimensionalised stress-wedge expansion of Test (II) B

As expected the expression in Eq. 4.10 not too much accurate but still acceptable for Test(II)-125×125×500 as shown in Figure 4.173. This is because the response of Test(II)-125×125×500 in not the same line as shown in Figure 4.171 and the expression is developed by using that line. Hence the general mathematical expression at Eq. 4.10 can be used.

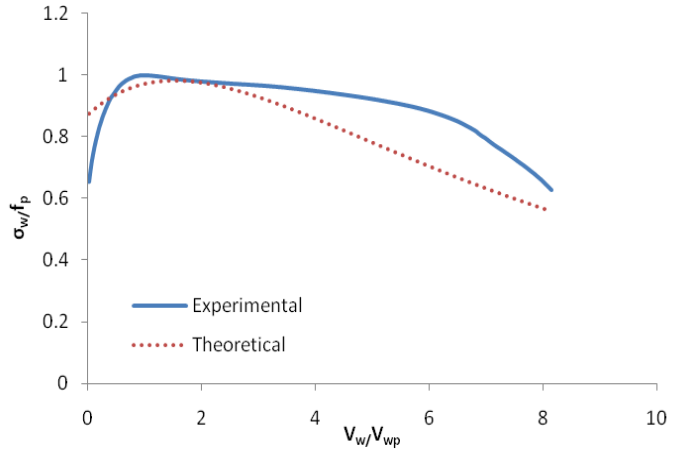

Figure 4.173: The stress-wedge expansion comparison response of Test(II)-125×125×500

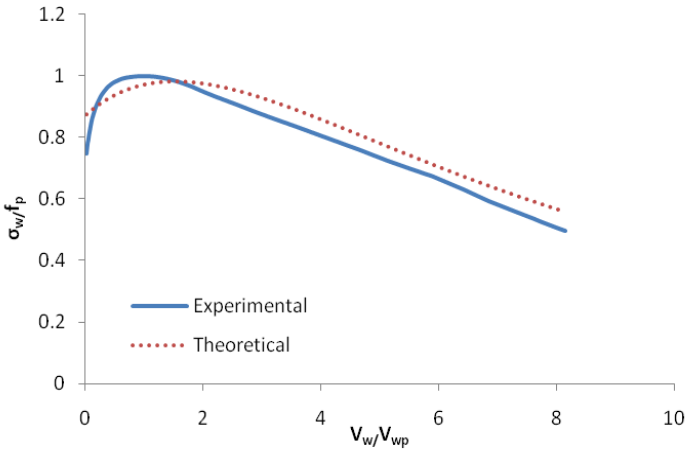

Figure 4.174: The stress-wedge expansion comparison response of Test(II)-125×250×500

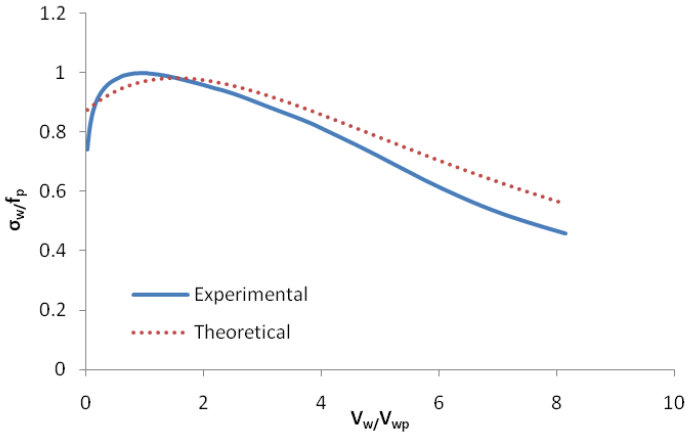

Figure 4.175: The stress-wedge expansion comparison response of Test(II)-125×375×500

The generic mathematical equations to simulate the deformation due to micro-cracking on both directions have been developed on different size and different slenderness ratio. The results show the equations were fit with the experimental results.

Chapter 5: MOMENT ROTATION ANALYSIS

5.1 Introduction

This chapter explains the application of the test results analysis in Chapter 3. The results from Chapter 3 are used to provide an example of the application of the softening properties of concrete, and mathematical equations of softening stress to simulate the behaviour of an eccentrically loaded prism. Although the results discussed in Chapter 4 can be used for the same purpose, Chapter 5 discusses an application and simulation that offer a new approach to moment rotation analysis.

In Chapter 3 and Chapter 4, prisms of varying dimensions were loaded uniaxially in order to illustrate how to quantify the behaviour of compression wedges in concrete where the deformation of the wedges was uniform. The current research proves that the results of the loadings can also be used to quantify the behaviour of compression wedges in flexural members, for example, beams, where the deformation is *not* uniform.

The experimental tests reported here were carried out on rectangular prisms of varying dimensions in order to quantify the softening properties of concrete in eccentrically loaded members. The chapter will explain how the softening properties can be quantified, and mathematical expressions for the softening stress σ_w in terms of the deformation S_w and mathematical expressions for the slip of the wedge S_w in terms of the depth of the wedge d_w were developed.

The softening was simulated during this research to illustrate softening in an eccentrically loaded prism. In tests on concentrically loaded prisms, the softening properties to deformation were constant over the depth of the wedge. In eccentrically loaded prisms, the deformation varied over the depth of the wedge, which simulates what happens in a beam. This is a simple way of simulating the softening of a concrete member when there is no reinforcement.

5.2 Concentrically Loaded Prisms

One millimeter thickness of a single wedge is shown in Figure 5.1. The height of the concrete $H/2$ is now referred to as L_{def}. The length of the wedge is referred to as L_w and it is assumed when the wedge is fully developed that the depth of the wedge d_w is

equal to half the width of the prism *W*. The thickness of the wedge into the page is considered to be one mm. The uniform displacement δ_w (referred to *C*/2 previously) occurs due to the stress σ_w which is applied to a one millimeter thickness of the wedge. Where σ_w is load wedge P_w divided by the depth of the wedge d_w (Eq. 3.4).

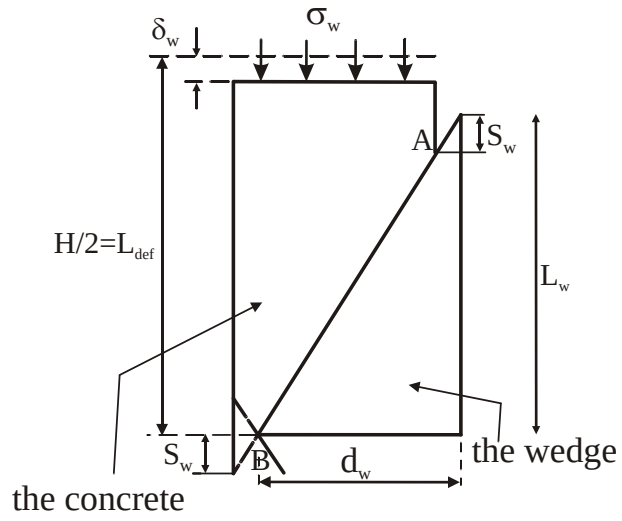

Figure 5.1: The wedge in millimeter thickness

By removing the elastic displacement, the relationship between wedge stress σ_w and slip wedge S_w is obtained. This is depicted in Figure 5.2 where S_{wp} is the wedge slip at the average of peak stress f_p which is 43MPa. The graph indicates that up to αf_p there is no micro-cracking or slip wedge, and the only deformation is elastic deformation. The micro-cracking starts at stress αf_p. In the analysis in Chapter 3, α was assumed to be 60%. The mathematical expression to represent the micro-cracking deformation S_w for a given stress of wedge σ_w (Eq. 3.8, repeated below) is shown in Figure 5.2 where S_{wp} is a function of the depth of the wedge d_w that is, it varies with the prism width *W*.

$$\frac{\sigma_w}{f_p} = \left[-0.65\left(\frac{S_w}{S_{wp}}\right)^2 + 5.71\left(\frac{S_w}{S_{wp}}\right) + 5.04 \right] \exp\left[0.03\left(\frac{S_w}{S_{wp}}\right)^2 - 0.50\left(\frac{S_w}{S_{wp}}\right) - 1.87 \right]$$

An expression for S_{wp} in terms of d_w was presented as Eq. 3.9 (repeated here),

$$S_{wp} = 0.0025\, d_w$$

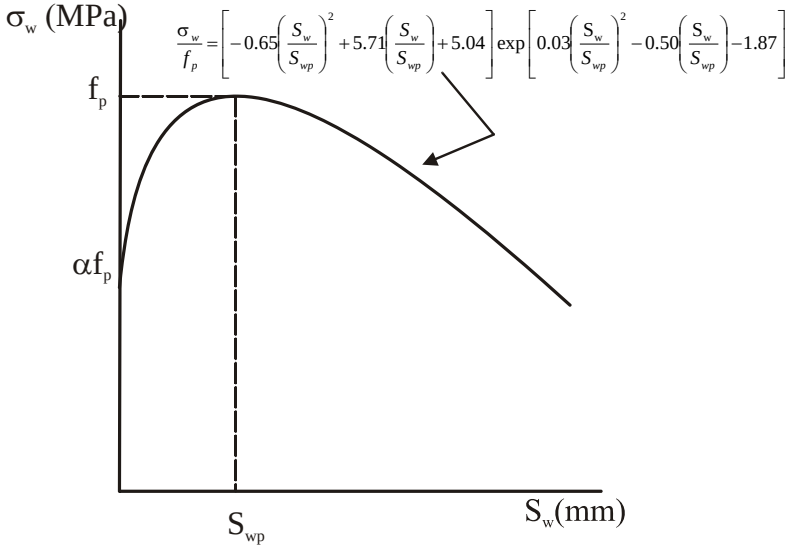

Figure 5.2: The stress - slip wedge response

5.3 Eccentrically Loaded Beams

Figure 5.3 illustrates a prism of height H or $2L_{def}$ and width W which is now referred to as d, subjected to a load P at eccentricity e. For this research there is a bearing plate on the top surface which is adhesively bonded to the concrete so that it can take tension. The prism can be visualised as in Figure 5.4 as a symmetrically loaded segment of height L_{def} with a maximum compression deformation δ_L and rotation θ that occurs within L_{def}.

The behaviour of this eccentrically loaded prism is similar to that of a flexurally loaded beam, where the deformation δ is not uniform, as it is for a concentrically loaded prism. Instead, it varies from δ_L on the left to δ_R on the right because of the eccentricity of the load, so that there is a linear variation in the effective strain δ/L_{def} and a rotation θ. Because of the eccentricity of the load, a wedge first forms on the loaded side of the prism, shown as shaded area in Figure 5.4. It can be seen from the figure that the depth of the wedge d_w is no longer equal to half the width of the eccentrically loaded prism d.

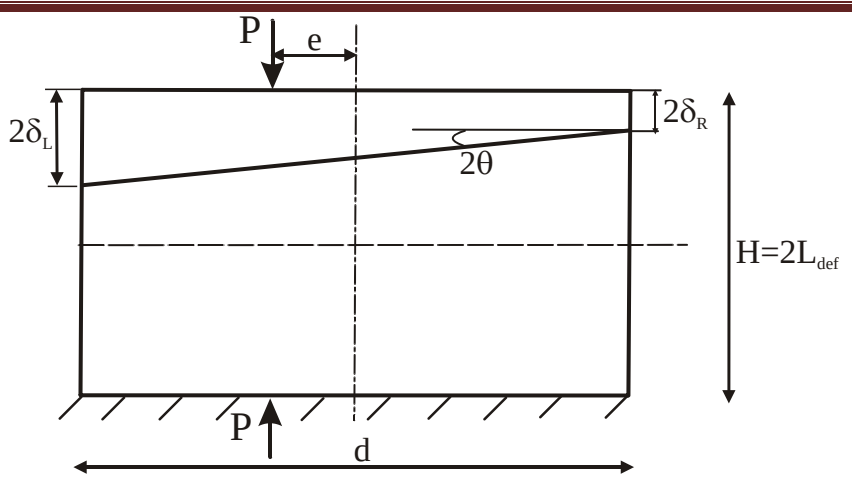

Figure 5.3; Eccentrically loaded prism

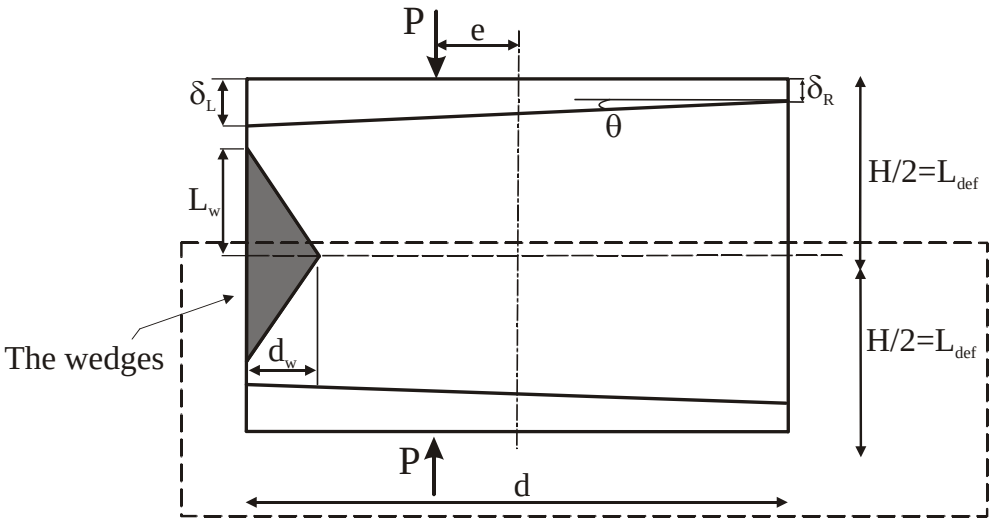

Figure 5.4: Graphic representation of an eccentrically loaded prism

The analysis is divided into two steps. Firstly, the elastic or linear condition where the wedge has not formed is considered, and, secondly, the non-linear condition, after the wedge has developed.

5.3.1 Elastic Condition

As load is gradually applied to the prism the deformation increases. At low load, that is, less than αP_p, no material softening occurs; therefore, the behaviour of the prism can be

simulated directly from material behaviour. That is, the material stress strain σ-ε relationships are appropriate to use.

The bottom half of the prism in Figure 5.4 is shown rotated by 90° clockwise in Figure 5.5(d). The wedge (shaded area in Figure 5.4) has not developed as this is the elastic case. The surface of the prism, A-A in Figure 5.5(d), is subjected to a compressive deformation at the top δ_T and a tensile deformation at the bottom δ_B so that there is a linear variation to the deformation.

Referring again to the information provided in Figure 5.2, it can be seen that up to αf_p only elastic deformation occurs. The wedge deformation S_w in Eq.3.8 which noted earlier equals zero. Using the equation to solve for σ_w when S_w=0, Eq.3.8 yields the stress level at which non-linear deformation commences. This analysis yields a value of α=77.7% which differs from the original assumption in chapter 3 with the value of α=60%. The response of the wedge stress σ_w and the average peak stress f_p is given as:

$$\sigma_w = 0.777\, f_p \qquad \textit{Eq.5.1}$$

Therefore, the deformation at which non-linear behaviour commences is given by:

$$\delta_w = \left(\frac{0.777\, f_p}{E_c} \right) L_{def} \qquad \textit{Eq. 5.2}$$

Where $(0.777f_p)/E_c$ is the concrete strain at which non-linearity commences.

Knowing the strain, and the length over which the strain acts [L_{def} in Figure 5.5(d)] the deformation at which non-linearity commences δ_w is $\varepsilon_{\text{non-lin}}\, L_{def}$. Where f_p is the average of the peak stress, E_c is the elastic Young's modulus which in this research is 32,368MPa, and L_{def} is half the prism height.

Equation 5.1 shows that the wedge starts at $0.777f_p$. The fact that α is not 60% as was assumed, but 77.7% is the result of the fact that the regression of the mathematical expression in Figure 5.2 resulted in 77.7%. Figure 5.6 illustrates the relationships between P-$C/2$ and σ_w-S_w where it was assumed that the non-linearity deformation or slip wedge would start (at $60\%P_p$). Up to $60\%f_p$ only elastic deformation occurs [Figure 5.6(b)]. There is some linearity behaviour in between 60% to 77.7%. Hence, for the next calculation and analysis, α is equals 77.68%. This α factor can be improved at a later

date if required for more accuracy. The deformation within the prism that is smaller than the deformation δ_w requires elastic deformation because δ_w is the deformation at which non-linear behaviour commences

The linear deformation C-E in Figure 5.5(d) produces the effective linear strain distribution F-H in Figure 5.5(c). Since the deformation δ is less than δ_w, this deformation is elastic and therefore the stress in Figure 5.5(b) can be determined directly by using Young's modulus. The procedures developed during the course of this research to quantify the moment rotation in elastic deformation are described below, and also illustrated in Figure 5.5.

1. The compressive deformation at the top δ_T is fixed in a small value, C, as a pivotal point. Corresponding to this fixed strain $\varepsilon_T=\delta_T/L_{def}$, fixed stress is $\sigma_T=(\delta_T/L_{def})E_c$ where E_c = 32,368MPa.
2. The depth of the compression region d_c is assumed.
3. Calculate the rotation θ, θ=Arc tan(δ_T/d_c).
4. Calculate the tensile deformation at the bottom δ_B, $\delta_B=(d-d_c)\tan\theta$.
5. Determine the corresponding fixed strain $\varepsilon_B=\delta_B/L_{def}$ and corresponding fixed stress $\sigma_B=(\delta_B/L_{def})E_c$
6. Divide the compressive and tensile deformation profiles into segments. The segment thickness is very small and it is assumed that the deformation in one segment is the average of the deformation in that segment, as shown in Figure 5.5(d). The segment thickness of the compressed portion is identified as *k* and tension portion as *j*.
7. Interpolate the deformations δ along the depth of the compression region d_c and the depth of the tensile region d_t [Figure 5.5(d)].
8. Determine the corresponding effective strain, $\varepsilon = \delta/L_{def}$ [Figure 5.5(c)].
9. Determine the corresponding stress, $\sigma = (\delta/L_{def})E_c$ [Figure 5.5(b)]. Where the concrete is cracking, it is in tension if the tensile strain ε_t is greater than the tensile strain capacity ε_{tc}, where $\varepsilon_{tc} = f_{tc}/E_c = 0.7\sqrt{f_p}/E_c$, f_{tc} is the tensile stress capacity (MPa), and f_p is the average peak stress (MPa).
10. Determine the corresponding compressive force of every segment, $F_{el.ci} = \sigma\ k\ b$, where *k* is the compressive segment thickness and *b* is the width of the prism [Figure 5.5(a)].

11. Determine the corresponding tensile force of every segment, $F_{el.ti} = \sigma\, j\, b$, where j is the tensile segment thickness [Figure 5.5(a)].
12. Determine the resultant elastic compressive force $F_{el.c}$ and elastic tensile force $F_{el.t}$ and their positions.
13. The resultant forces in Figure 5.5(a) need to be in line with P, obtained by pivoting the displacement C-E in Figure 5.5(d) about C until the resultant force is in line, or return to procedure point (2) and complete the steps again.
14. Determine moment M, $M=P\times e$. where e is eccentricity.
15. The solution n sequence recommences for increasing δ_T.

These procedures are for δ_T less than δ_w where δ_w is the deformation when the wedge starts to form (given by Eq. 5.2). If the deformation at the top is more than δ_w the procedures for elastic deformation cannot be used. The procedure for non-elastic deformation is described in the following section.

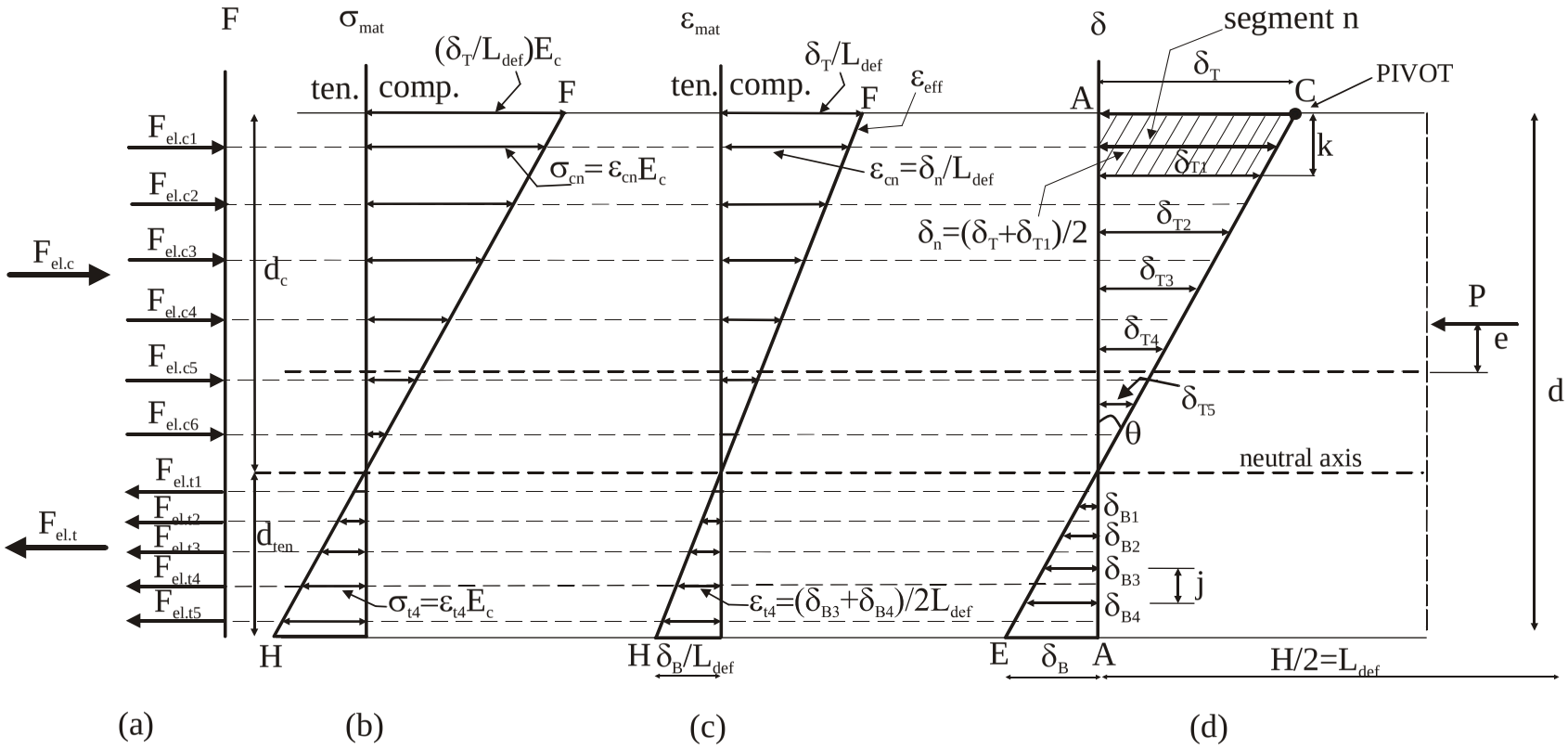

Figure 5.5: Moment rotation analysis in elastic deformation

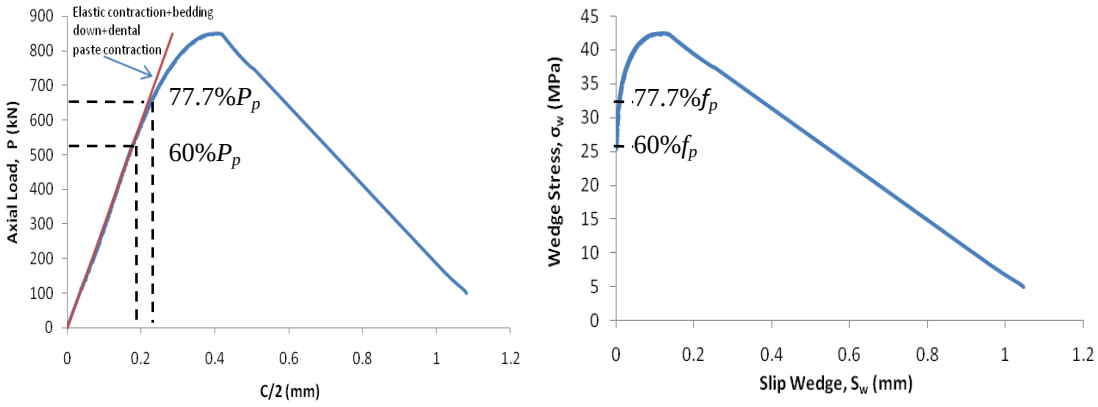

(a) *(b)*

Figure 5.6: The relationship between P-C/2 and σ_w-S_w of prism Test5-100

5.3.2 Non-elastic Condition

For deformations that are increasing, ultimately the maximum deformation will exceed δ_w, and hence non elastic deformation occurs. The stresses can no longer be obtained using Young's modulus (calculating from the stress-strain σ-ε relationship). Therefore, we must consider the formation of wedges and material softening.

Figure 5.7 offers an illustration of how we can calculate the details of a non-elastic condition. Figure 5.7(e) is the bottom half of the prism that was considered earlier in Figure 5.4. In this instance, it has been rotated 90° clockwise around the spot where the wedge, as shown shaded in Figure 5.4, formed. As in the inelastic condition, the surface of the prism, A-A in Figure 5.5(d), is subjected to a compressive deformation at the top δ_T and a tensile deformation at the bottom δ_B.

Micro-cracking starts to develop when the deformation exceeds δ_w (Eq. 5.1) as shown by line B-B in Figure 5.7(d). If the deformation on the top δ_T exceeds δ_w, this means that the analysis is not of an elastic condition but a non-elastic one. Any deformation above point C in Figure 5.7: Moment rotation analysis in the non-elastic deformation

(d) requires micro-cracking which, therefore, fixes the depth of the wedge d_w as shown.

The procedures to quantify the moment rotation after the wedge starts are described below, and also illustrated in the figure.

1. The deformation at the top δ_T is fixed and exceeds δ_w. D becomes the pivotal point in the analysis.
2. The depth of compression region d_c is assumed.
3. Calculate the rotation θ, θ=Arc tan(δ_T/d_c).
4. Calculate the deformation at the bottom δ_B, $\delta_B=(d-d_c)\tan\theta$.
5. Determine the depth of the wedge, d_w in Figure 5.7 (d). The depth of the wedge d_w is quantified as

$$d_w = \left(\frac{\delta_T - \delta_w}{\delta_T} \right) d_c \qquad \textit{Eq.5.3}$$

6. The deformation is divided into three regions: a non-elastic compressive region C-D; an elastic compressive region F-C; and a tensile region E-F.
7. Divide the deformation into segments. The segment thickness is very small and it is assumed that the deformation in one segment is the average of the deformation in that segment. The segment thickness of the elastic compression portion is identified as *k*, while the non-elastic compression portion is identified as *t*. The tension portion is identified as *j*.
8. Interpolate the deformations δ along the depth of the non-linear compressive region or depth of wedge d_w, the depth of the linear compressive region d_c and the depth of the tensile region d_t.
9. Determine the wedge force, F_w. (See Figure 5.7 (d) at segment *n*, and Figure 5.8 for detail).
    a. Segment *n* is where the total deformation that has to be accommodated is δ_n (H-I). This consists of the elastic deformation of prism H-J that is accommodated by concrete material straining ε_{mat} so that the deformation due to elastic contraction H-J is given by $(\sigma_n/E_c)L_{def}$. The additional deformation J-I due to micro-cracking or the slip wedge S_{wn} at the wedge interface is shown in Figure 5.7(e).
    b. Determine the total deformation at segment *n*, δ_n.
    c. The total deformation at segment *n*, δ_n consists of elastic deformation and deformation due to micro-cracking or slip wedge S_{wn} given as

$$\delta_n = \varepsilon_{mat} L_{def} + S_{wn} \qquad \textit{Eq.5.4}$$

    d. Guess the value of ε_{mat}

e. Determine the slip wedge at segment *n*, $S_{wn} = \delta_n - \varepsilon_{mat} L_{def}$.

f. Determine the slip wedge at peak stress S_{wp} by using Eq. 5.3 and Eq. 3.9

$$d_w = \left(\frac{\delta_T - \delta_w}{\delta_T} \right) d_c$$

and $S_{wp} = 0.0025 d_w$ respectively.

g. Determine the stress wedge at segment *n*, σ_{wn} by using Eq. 3-8 (repeated here)

$$\frac{\sigma_{wn}}{f_p} = \left[-0.65 \left(\frac{S_{wn}}{S_{wp}} \right)^2 + 5.71 \left(\frac{S_{wn}}{S_{wp}} \right) + 5.04 \right] \exp \left[0.03 \left(\frac{S_{wn}}{S_{wp}} \right)^2 - 0.50 \left(\frac{S_{wn}}{S_{wp}} \right) - 1.87 \right]$$

h. Determine the strain of the wedge at segment n, where $\varepsilon_{wn} = \sigma_{wn}/E_c$ at which σ_{wn} is taken from Eq.3.8.

i. The value of ε_{mat} should be same as ε_{wn}. If $\varepsilon_{mat} \neq \varepsilon_{wn}$, iterate until it does, beginning from step (d).

j. Determine the non-linear compression force or wedge force of segment *n*, F_{wn}, $F_{wn} = \sigma_{wn} t\, b$, where *t* is the segment thickness and *b* is the prism width.

k. Determine the resultant wedge force, $F_w = \sum F_{wn}$, and its position.

10. Where the deformation below point C [Figure 5.7(d)] is lower than δ_w consider this to be an elastic analysis. If the concrete crack is in tension at level K [Figure 5.7(c)], then K-M is an effective strain. The procedure to determine the resultant forces in the elastic compressive region $F_{el.c}$ and tensile region $F_{el.t}$ is the same as described in Section 5.3.1.

    a. Determine the corresponding effective strain, $\varepsilon_n = \delta_n / L_{def}$

    b. Determine the corresponding stress, $\sigma_n = (\delta_n / L_{def}) E_c$.

    c. Determine the corresponding compressive force of every segment, $F_{el.cn} = \sigma_n k\, b$

    d. Determine the corresponding tensile force of every segment, $F_{el.tn} = \sigma_n j\, b$

    e. Determine the resultant elastic compressive force $F_{el.c} = \sum F_{el.cn}$ and elastic tensile force $F_{el.t} = \sum F_{el.tn}$ and their positions.

11. The resultant forces [Figure 5.7(a)] need to be in line with the external load *P*. The values can be obtained by pivoting the displacement D-E [Figure 5.7(d)] about D until the resultant force is in line. In other words, if the resultant forces and *P* are not on the same line, go back to procedure point (2) and complete the steps again until the resultant force is in line.

If the resultant forces F and P are in line, the moment M is obtained by multiplying P and eccentricity e. The process is repeated for another top displacement δ_T in Figure 5.7(d).

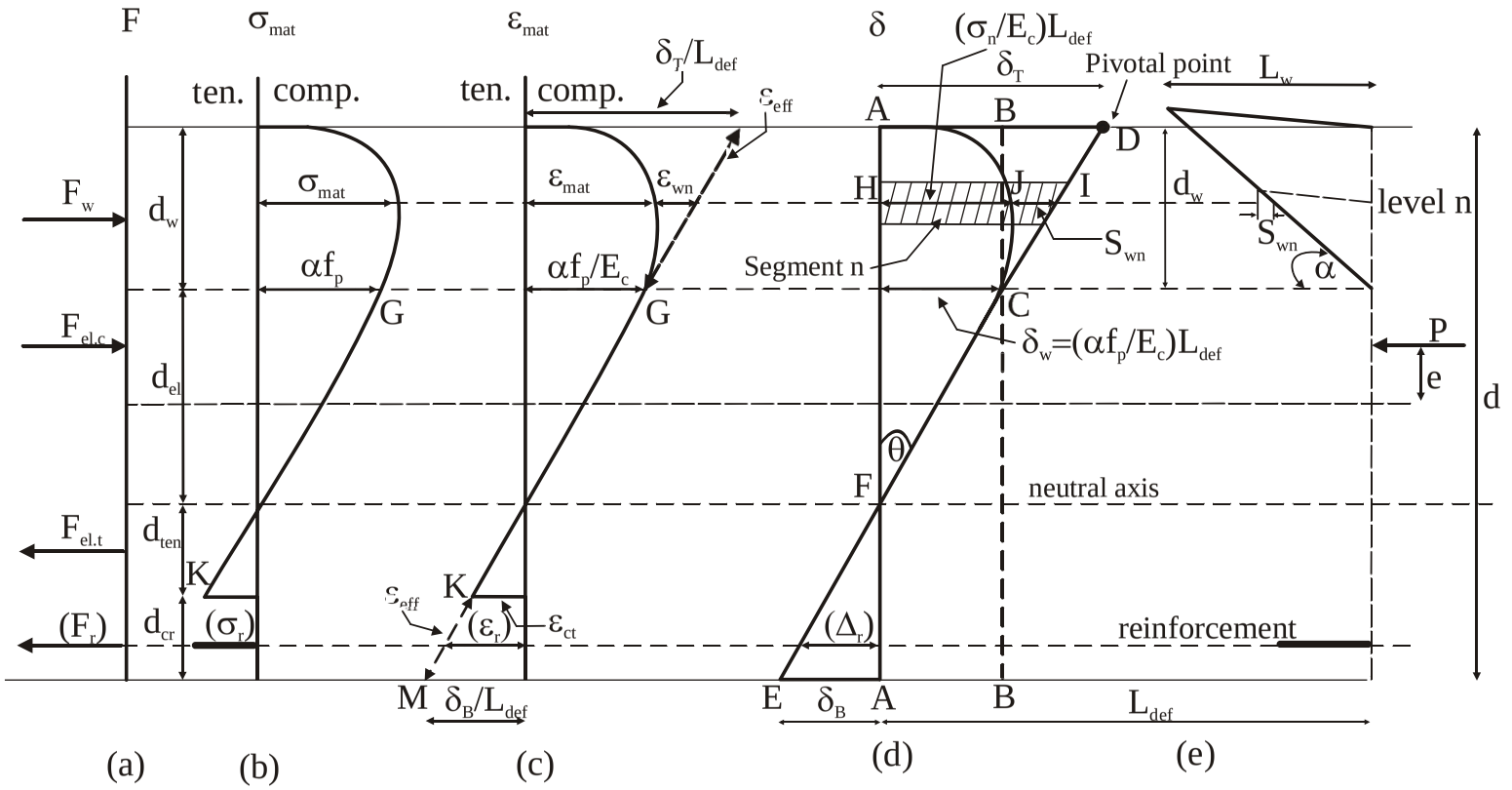

Figure 5.7: Moment rotation analysis in the non-elastic deformation

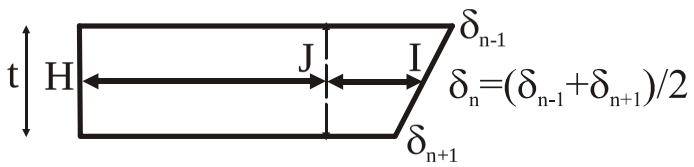

Figure 5.8: The segment n in the non-linear compressive region

5.3.3 The Results and Validation

The results of the moment rotation analysis of the eccentrically loaded prism (Figure 5.4), which are illustrated in Figure 5.5 and Figure 5.7, are described in this section. The peak stress f_p is 43MPa based on the results of the experimental tests described in Chapter 3. The results described in Chapter 4 are not used in this analysis because the goal of this chapter is to present a method for simulating softening and determining a theoretical M-θ response to compare to experimental results. It is not the purpose of this chapter thesis to present a generic and comprehensive softening relationship.

A theoretical M-θ response of an eccentrically loaded prism is shown in Figure 5.9. This response was obtained from the procedures illustrated by Figures 5.5 and 5.7 and followed the procedures described in Sections 5.3.1 and 5.3.2 respectively.

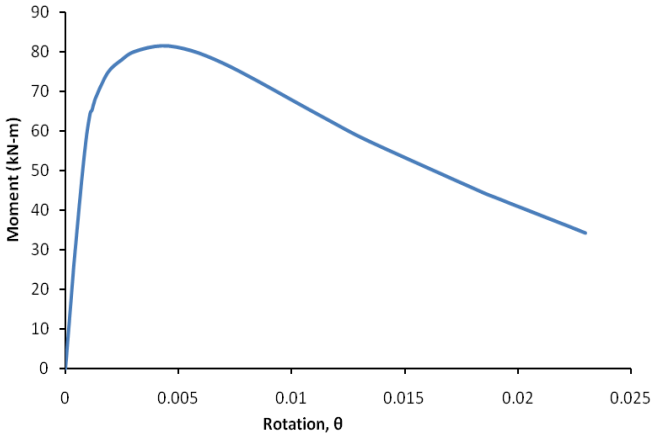

Figure 5.9: Moment Rotation for f_p = 43MPa, e = 70mm

The total rotation in Figure 5.9 consists of linear rotation and non-linear rotation. Let us consider Figure 5.10. Up to αM_p corresponding to θ_r, there is no rotation due to micro-cracking; only linear rotation occurs and this is due to curvature. After that point (αM_p,θ_r) non-linear rotation occurs due to the micro-cracking that begins to develop as shown in Figure 5.10. Non-linear rotation $\theta_{(non\text{-}lin)}$ is then obtained by removing the linear rotation from the total rotation θ as given.

$$\theta_{(non\text{–}lin)} = \theta - \frac{M\theta_r}{\alpha M_p} \qquad \textit{Eq.5-5}$$

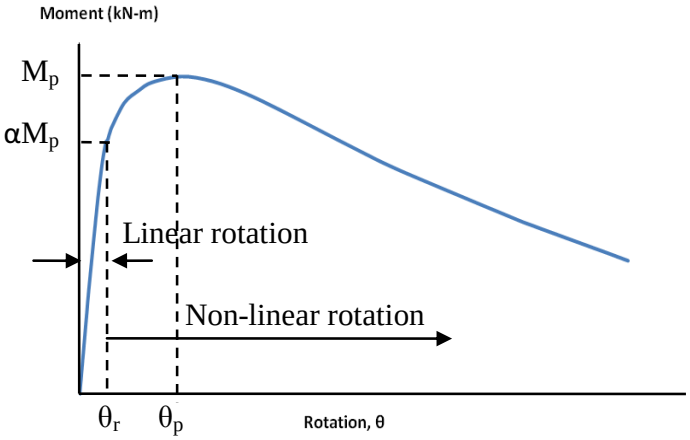

Figure 5.10: A typical the moment rotation response

The moment-non linear rotation $M\text{-}\theta_{(non\text{-}lin)}$ response is shown in Figure 5.11. The mathematical expression that has been developed can simulate the softening behaviour of an eccentrically loaded prism.

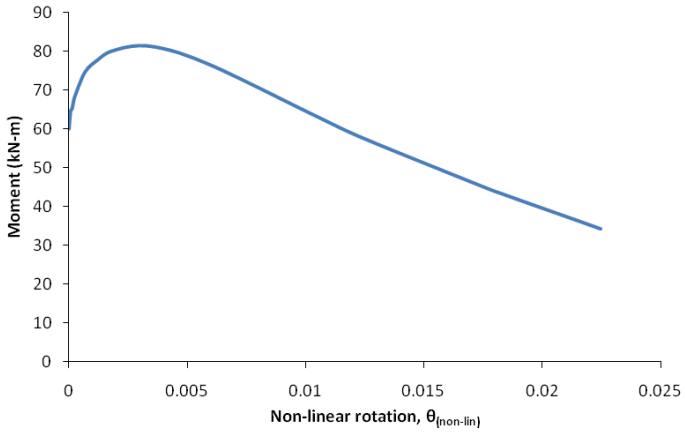

Figure 5.11: Moment - Non-linear rotation for fp = 43MPa, e = 70mm

The softening behaviour of concrete that is the objective of this research has clearly been captured. Therefore, the procedures that were described in Sections 5.3.1 for elastic and 5.3.2 for non-elastic analysis work; and mathematical expressions have been developed that can be used to simulate softening behaviour.

This eccentrically loaded prism analysis was applied to Daniell *et al.*'s test specimens [Daniell et. al, 2008]. The specimen is shown in Figure 5.12. The specimens

have a width d of 300mm, height H or now referred to $2L_{def}$ of 360mm, depth into the page of 180mm, an average concrete strength of 33MPa and were tested at eccentricities e of 60, 70, and 85mm. It should be noted that the average concrete strength of the prism that was used to derive Eqs. 3.8 and 3.9 in Chapter 3 was 43MPa. Therefore, the shape of the variations in material properties given by Eqs. 3.8 and 3.9 are really only applicable to this strength of concrete. However, to illustrate this analysis technique, the equations were applied to Daniell *et al.*'s specimens, which were a bit weaker at 33MPa.

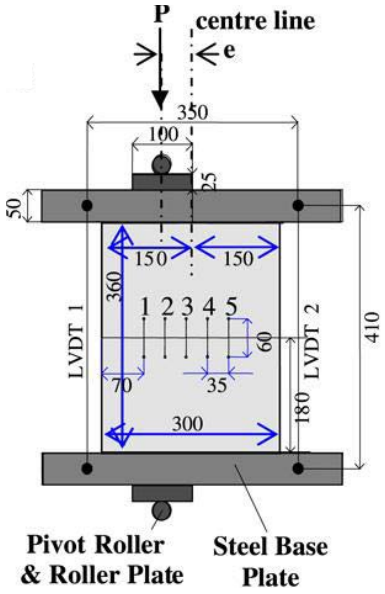

Figure 5.12: Specimen dimension of Daniell's specimen [Daniell et al., 2008]

A comparison of experimental test results and theoretical results for eccentricity e=70mm in the moment-rotation response is depicted in Figure 5.13.

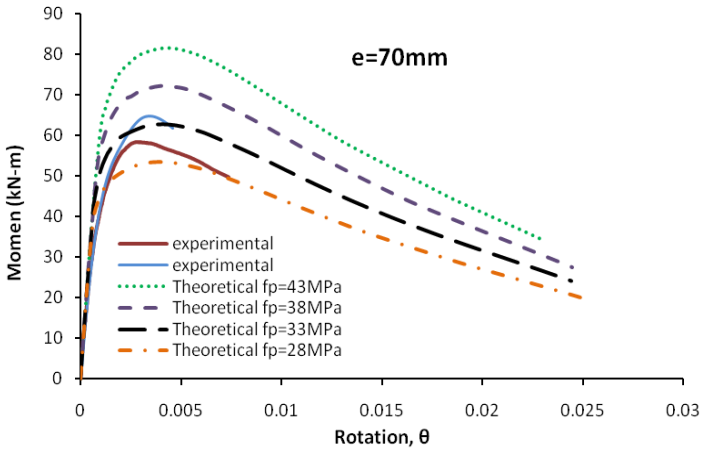

Figure 5.13: A typical moment-rotation comparison

A comparison of the moment-non-linear rotation has been plotted in Figure 5.14, Figure 5.15 and Figure 5.16 for each test specimen. The eccentricities were 60, 70 and 85mm respectivelly. Two experimental tests were performed at each eccentricity except the eccentricity of 85mm where only one experimental test occurred. These are shown as unbroken lines; the difference between these tests is a gauge of the scatter that can be expected even from supposedly identical specimens and tests.

The experimental test results were compared with the results of the theoretical analyses, with variations in concrete strength from 43MPa to 28MPa, which are shown as broken lines. Bearing in mind the scatter between the test results, it is suggested that the shape of the theoretical results compares well with those of the tests. It can be seen that this new approach can simulate the moment rotation softening without the need for empirical hinge lengths or the softening of stress-strain relationships.

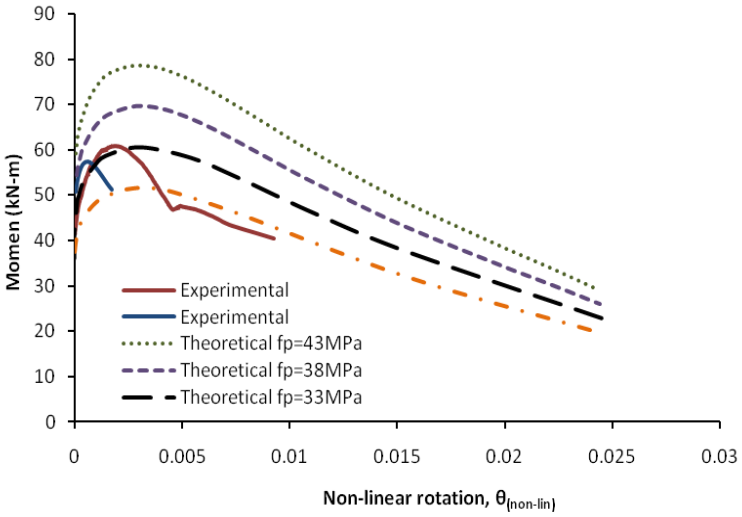

Figure 5.14: Moment-non-linear rotation for e = 60mm

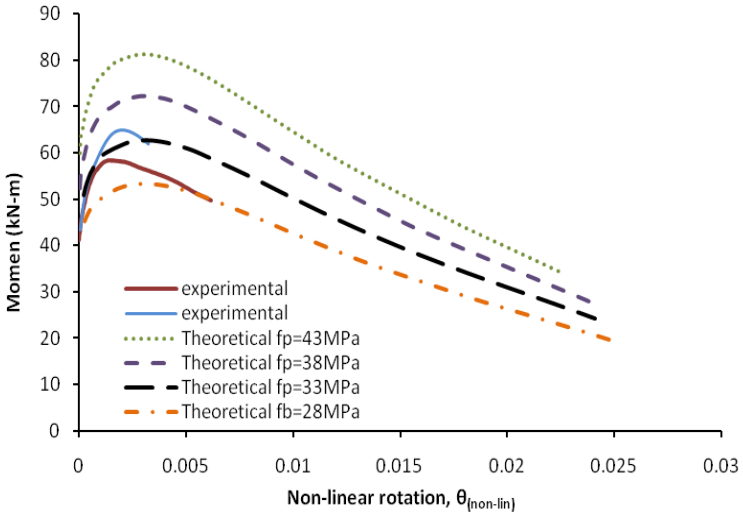

Figure 5.15: Moment-non-linear rotation for e = 70mm

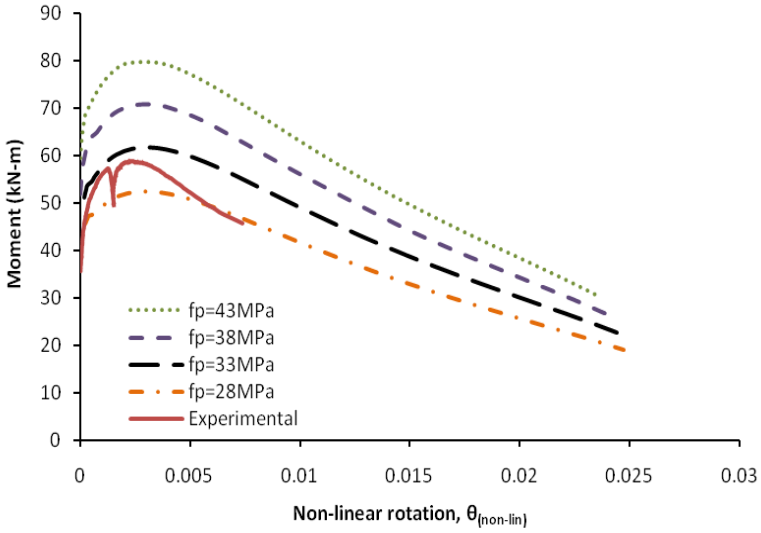

Figure 5.16: Moment-non-linear rotation for e = 85mm

The main interest of this research is the non-linearity due to micro-cracking, as already illustrated in Figure 5.2 for prism tests. Dividing the abscissa θ of Figure 5.13 by L_{def} gives the curvature χ as shown in Figure 5.17. The initial stiffness or tangent stiffness of the rising branch in Figure 5.13 would be elastic flexural rigidity *EI* and divergence from this would be due to flexural cracking and micro-cracking. This divergence due to cracking, which is the main interest of this research, has been plotted in Figure 5.14 to

Figure 5.16 for each test specimen. It is suggested that the results show that the model can closely represent softening.

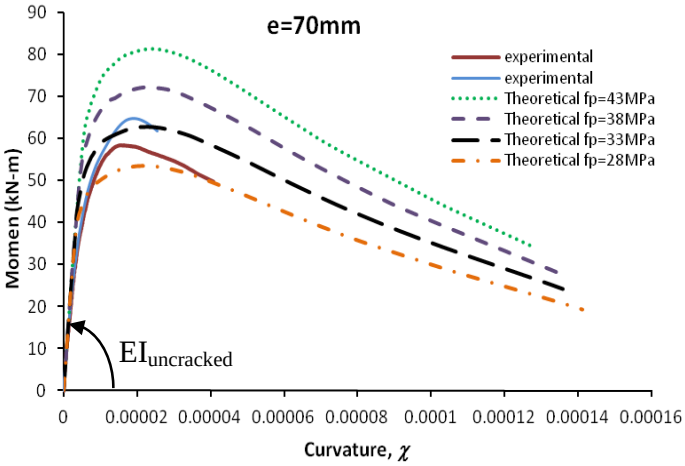

Figure 5.17: A typical of moment-curvature response

The above wedge analyses have been applied to eccentrically loaded flexural members without any reinforcement as illustrated in Figure 5.4. As already explained through the use of Figure 5.7, these analyses could also have been applied to reinforced flexural members where the force in the longitudinal reinforcement is a function of Δ_r , as shown in Figure 5.7(d) [Haskett *et al.* 2009; Muhammad *et al.* 2011 and Muhammad *et al.* 2011]. Therefore, it can be seen that once the wedge properties have been derived from prism tests, they can be used to derive the ductility of any reinforced concrete beam.

Chapter 6: CONCLUSION

In this thesis, empirical relationships are developed to simulate the gradual softening of concrete in compression. Uniaxial compression tests on long prisms are conducted to determine axial and lateral displacement in order to evaluate the softening response of concrete. Two of experimental sets are reported. The first set of experimental test contains 13 long prisms of varying dimensions in the same width to height to length ratio of 1:2:4 and the second experimental set contains 18 long prisms of varying dimension and slenderness ratio (height to width ratio).

A long prism, where the length of the prism is four times the prism width, is chosen as a specimen because to avoid the circumferential expansion that always occurs with cylinders and to simulate the deformation of cross-sections of prism as a two-dimensional behaviour. The total deformations in both axial and lateral directions consist of elastic deformation and non-elastic deformation due to micro-cracking. Up to αP_p, the deformation is considered elastic, and consists of material contraction in axial direction and lateral expansion in the lateral direction due to Poisson's ratio. In this research, α is considered to be 77.7%. For σ exceeding 77.7% non material deformation occurs due to micro-cracking, and where the total deformation consists of deformation due to sliding and material deformation. The material deformation can be separated from the total deformation to obtain non-linear deformation, which is the purpose of this research.

The results reveal that deformations due to micro-cracking in axial direction (the slip wedge S_{wp}) and in lateral direction (the wedge expansion V_{wp}) at the peak stress vary and depend on the prism size. The slip of the wedge S_{wp} and wedge expansion V_{wp} at peak load increase with increasing the size of prism. However, the slip wedge at peak load S_{wp} not influenced by the slenderness ratio.

The softening behaviours obtained from these experimental tests are used to develop mathematical expressions to simulate softening. The mathematical expression for the softening stress σ_w is the function of the average of peak stress f_p, the non linear deformation which is slip wedge S_w in axial direction and wedge expansion V_w in lateral direction, and non linear deformations at peak stress (S_{wp} and V_{wp}).

The mathematical expressions developed to quantify the stress of wedge σ_w for a given slip wedge S_w and wedge expansion V_w, and are shown below.

$$\frac{\sigma_w}{f_p} = \left[-0.65\left(\frac{S_w}{S_{wp}}\right)^2 + 5.71\left(\frac{S_w}{S_{wp}}\right) + 5.04 \right] \exp\left[0.03\left(\frac{S_w}{S_{wp}}\right)^2 - 0.50\left(\frac{S_w}{S_{wp}}\right) - 1.87 \right]$$

and

$$\frac{\sigma_w}{f_p} = \left[0.12\left(\frac{V_w}{V_{wp}}\right)^2 + 7.68\left(\frac{V_w}{V_{wp}}\right) + 18.18 \right] \exp\left[0.01\left(\frac{V_w}{V_{wp}}\right)^2 - 0.30\left(\frac{V_w}{V_{wp}}\right) - 3.01 \right]$$

Where S_{wp} equal to $0.0025d_w$ and V_{wp} is $0.0022d_w$. These expressions provided an accurate fit to the experimental results.

In the second set of experimental tests where slenderness varied, a similar expression was also developed. In this experimental set the slip of the wedge at peak stress, S_{wp} was independent of the prism dimension (due to slenderness ratio). S_{wp} was equal to 0.25mm, which was the average non-material slip S_{wp} across the experiments from the 3 prism slenderness ratios.

To demonstrate an application of these softening properties an eccentrically loaded prism is analyzed, where the deformation over the depth of the prism varies. A theoretical moment-rotation M-θ response is developed which consists of two separate conditions, the conditions as presented in Chapter 5. When the deformation within the prism that is smaller than the deformation δ_w at which softening commences, then there is only elastic deformation, and the behaviour of the prism can be simulated directly from material behaviour. When the deformation exceeds δ_w, non-elastic deformation occurs and therefore softening must be considered and is simulated by using the mathematical expressions presented above. This theoretical moment rotation M-θ response is then compared to the experimental test on eccentrically loaded prism. The shape of theoretical result compare well with the experiment tests prism.

The results reveal that the mathematical expression that has been developed can simulate the softening behaviour of eccentrically loaded prisms. Hence the method and analysis procedure presented and the subsequent mathematical expression developed, can be used to simulate that softening behaviour of concrete, which was the goal of this research.

REFERENCES

ACI Committee 363. (1993). "State of the art report on high-strength concrete." *ACI Publication 363R-92,* American Concrete Institute, Detroit.

B.S.1881, 1952. (1952). "Methods of Testing Concrete." *British Standard Institution* B.S.1881, BSI, London.

Barnard, P. R. (1964). "Research into the complete stress-strain curve for concrete." *Magazine of Concrete Research* (*Wexham Springs*), 16(49), 203-210.

Borges, J. U. A., Subramaniam, K. V., Weiss, W. J., Shah, S. P., and Bitterncourt, T. (2004). "Length effect on ductility on concrete in uniaxial and flexural compression." *ACI Structural Journal*, 101(6), 765-772.

Carreira, D. J., and Chu, K. H. (1985). "Stress-strain relationship for plain concrete in compression." *ACI Journal,* 82(6), 797-804.

Chin, M. S., Mansur, M. A., and Wee, T. H. (1997). "Effect of shape, size and casting direction of specimens of stress-strain curves of high-strength concrete." *ACI material Journal*, 94(3), 209-218.

Choi, S., Thienel, K. C., and Shah, S.P. (1996). "Strain softening of concrete in compression under different end constraints." *Magazine of Concrete Research,* 48(175), 103-115.

Daniell, J. E., Oehlers, D. J., Griffith, M. C., Mohamed Ali, M. S., and Ozbakkaloglu, T. (2008). "The softening rotation of reinforced concrete members." *Engineering Structures*, 30(11), 3159-3166.

Debernardi, P. G., and Taliano, M. (2001). "Softening behavior of concrete prisms under eccentric compressive forces." *Magazine of Concrete Research*, 53(4), 239-249.

Fantilli, A. P., Ferretti, D., Lori, I., and Vallini, P. (2002). "Mechanical model for failure of compressed concrete in reinforced concrete beams." *Journal of Structural Engineering-ASCE*, 128(5), 637-645.

Gobbi, M. E., and Ferrara, G. (1995). "Strain softening of concrete under compression." *ENEL-CRIS,* appr.250 pp.

Haskett, M., Oehlers, D. J., Mohamed Ali, M. S., and Sharma, S. K. (2011a). "Evaluation the shear-friction resistance across sliding planes in concrete." *Engineering Structures*, 33, 1357-1364.

Haskett, M., Oehlers, D. J., Mohamed Ali, M. S., and Sharma, S. K. (2011b). "The shear-friction aggregate-interlock resistance across sliding planes in concrete." *Magazine of Concrete Research*, 62(12), 907-924.

Haskett, M., Oehlers, D. J., Mohamed Ali, M. S., and Wu, C. (2009). "Rigid body moment-rotation mechanism for reinforced concrete beam hinges." *Engineering Structures*, 31, 1032-1041.

Hognestad, E. (1951). "A study of combined bending and axial load in reinforced concrete members." *University of Illinois Engineering Experimental Station, Bulletin Series*, 399, 128.

Jansen, D. C., and Shah, S. P. (1997). "Effect of length on compressive strain softening of concrete." *Journal of Engineering Mechanics*, 123(1), 25-35.

Kim, J. K., Yi, S. T., and Kim, J. H. J. (2001). "Effect of specimen sizes on flexural compressive." *ACI Structural Journal*, 98(3), 416-424.

Kim, J. K., Yi, S. T., and Yang, E. I. (2000). "Size effect on flexural compressive strength on concrete specimens." *ACI Structural Journal*, 97(2), 291-296.

Kim, J. K., Yi, S. T., Park, C. K., and Eo, S. H. (1999). "Size effect on compressive strength of plain and spirally reinforced concrete cylinders." *ACI Structural Journal*, 96(1), 88-94.

König, G., Simsch, G., and Ulmer, M. (1994). "Strain softening of concrete." *Technical University of Darmstadt*, 67 pp.

Kotsovos, M. D. (1983). "Effect of testing techniques on the post-ultimate behavior of concrete in compression." *Material and Structure*, 16, 3-12.

Kumar, P. (2004). "A compact analytical material model for unconfined concrete under uni-axial compression." *Materials and Structures*, 37, 585-590.

Lertsrisakulrat, T., Niwa, J., Yanagawa, A., and Matsuo, M. (2002). "Concepts of localized compressive failure of concrete in RC deep beams." *Journal of Materials Concrete Structures, Pavements, JSCE*, 54(697), 215-225.

Lertsrisakulrat, T., Watanabe, K., Matsuo, M., and Niwa, J. (2001). "Experimental study on parameters in localisation of concrete subjected to compression." *Journal of Materials Concrete Structures, Pavements, JSCE*, 50(669), 309-321.

Mansur, M. A., Vinayagam, T., and Tan, K. H. (2008). "Shear transfer across a crack in reinforced high-strength concrete." *Journal of Materials in Civil Engineering-ASCE*, 20(4), 294-302.

Mander, J. B., Priestley, M. J. N., and Park, R. (1988). "Theoretical stress-strain model for confined concrete." *Journal of Structural Engineering*, 114(8), 1804-1826.

Markeset, G. (1993). "Failure of concrete under compressive strain gradients." *Dr.Ing Thesis*, 110, Norwegian Institute of Technology, Trondheim.

Markeset, G. (2008). "Size effect of concrete in compression, state of the art." *Project report 13*, SINTEF Building and Infrastructure.

Markeset, G., and Hillerborg, A. (1995). "Softening of concrete in compression localization and size effects." *Cement and Concrete Research*, 25(4), 702-708.

Martinez, S., Nilson, A.H., and Slate, F.O. (1984). "Spirally reinforced high-strength concrete columns." *ACI Journal*, 81(5), 431-441.

Mattock, A. H., and Hawkins, N. M. (1972). "Shear transfer in reinforced concrete recent research." *Precast Concrete Institute Journal*, March-April, 55-75.

Mohamed Ali, M. S., Oehlers, D. J., and Griffith, M.C. (2010). "The residual strength of confined concrete." *Advances in Structural Engineering*, 13(4), 603-618.

Neville, A. M. (1956). "The influence of size of concrete test cubes on mean strength and standard deviation." *Magazine of Concrete Research*, Aug., 101-110.

Neville, A. M. (1966). "A general relation for strengths of concrete specimens of different shapes and sizes." *ACI Journal, Proceedings*, 63(10), 1095-1110.

Neville, A. M. (1988). "Properties of concrete." *Third edition, Longman*, England, pp.364-604.

Newman, K., and Lachance, L. (1964). "The testing of brittle materials under uniform uniaxial compression stress." *Proceeding ASTM*, 64, 1044-1067.

Oehlers, D. J., Mohamed Ali, M. S., and Griffith, M. C. (2008). "Concrete component of the rotational ductility of reinforced concrete flexural members." *Advances in Structural Engineering*, 11(3), 281-291.

Oehlers, D. J., Mohamed Ali, M. S., Griffith, M. C., and Ozbakkaloglu, T. (2007). "Fundamental issues that govern the rotation of FRP retrofitted RC columns and beams: the intractable plastic hinge ductility problem." *Asian Pacific Conference on FRP in Structures*, Hongkong, China, December.

Palmquist, S. M., and Jansen, D. C. (2001). "Postpeak strain-stress relationship for concrete in compression." *ACI Materials Journal*, 98(3), 213-219.

Park, R., and Paulay, T. (1975). "Reinforced concrete structure." *A Wiley-Interscience Publication*, p204.

Popovics, S. (1973). "Numerical approach to the complete stress-strain relation for concrete." *Cement and Concrete Research,* 3(5), 583-599.

Rahal, K. N. (2010). "Shear-transfer strength of reinforced concrete." *ACI Structural Journal*, 107(4), 419-426.

Read, H. E., Hegemier, G. A. (1984). "Strain softening of rock, soil and concrete – A review article." *Mechanics of Materials*, 3, 271-294.

RILEM TC 148-SSC. (2000). "Strain softening of concrete – Test methods for compressive softening. Test method for measurement of the strain-softening behaviour of concrete under uniaxial compression. Recommendations." *Materials and Structures*, 33, 347-351.

Saenz, L. P. (1964). "Discussion of 'Equation for the stress-strain curves of concrete' by Desai and Krishnan." *ACI Journal*, 61(9), 1229-1235.

Sangha, C. M., and Dhir, R. K. (1972). "Strength and complete stress-strain relationships for concrete tested in uniaxial compression under different test conditions." *Materials and Structures*, 5(30), 361-370.

Sargin, M. (1971). "Stress-Strain Relationship for Concrete and Analysis of Structural Concrete Sections." Study No.4, *Solid Mechanics Division*, University of Waterloo, Ontario, Canada, 167.

Schickert, G. (1980). "Schwellenwerte beim betondruckversuch (Threshold value in compressive tests on concrete)." *Deutscher Ausschuss für stahlbeton*, 312, Berlin (in German).

Shah, S. P., and Sankar, R. (1987). "Internal cracking and strain softening response of concrete under uniaxial compression." *ACI Materials Journal*, 84(3), 200-212.

Sigvaldason, O. (1966). “The influence of testing machine characteristic upon the cube and cylinder strength of concrete.” *Magazine of Concrete Research*, 18(57), 197-206.

Torrenti, J. M., Benaija, E. H., and Boulay, C. (1993). “Influence of boundary conditions on strain softening in concrete compression test.” *Journal of Engineering Mechanics-ASCE*, 119(12), 2369-2384.

Van Geel, E. (1998). “Concrete behaviour in multiaxial compression.” *Experimental Research*, Technische Universiteit Eindhoven, Faculteit Bouwkunde.

Van Mier, J. G. M. (1984). “Strain-softening of concrete under multiaxial loading condition.” *PhD Thesis*, Eindhoven University of Technology, The Netherlands.

Van Mier, J. G. M. (1986). “Multiaxial strain-softening of concrete, part I: Fracture, partII: Load histories.” *Material structure-RILEM*, 19, 179-191.

Van Mier, J. G. M., and Man, H. K. (2009). "Some notes on microcracking, softening, localization, and size effects." *International Journal of Damage Mechanics*, 18(3), 283-311.

Van Mier, J. G. M., Shah, S. P., Arnaud, M., Balayssac, J. P., Bascoul, A., Choi, S., Dasenbrock, D., Ferrara, G., French, C., Gobbi, M. E., Karihaloo, B. L., König, G., Kotsovos, M. D., Labuz, J., Lange-Kornbak, D., Markeset, G., Pavlovic, M. N., Simsch, G., Thienel, K.C., Turatsinze, A., Ulmer, M., Van Geel, H. J. G. M., Van Vliet, M. R. A. and Zissopoulos, D. (1997). “Strain softening of concrete in uniaxial compression.” *Material and Structures-RILEM*, 30, 195–209.

Van Vliet, M. R. A., and Van Mier, J. G. M. (1996). “Experimental investigation of concrete fracture under uniaxial compression.” *Mechanics of Cohesive-Frictional Materials*, 1, 115-127.

Visintin, P., Oehlers, D. J., Wu, C., and Haskett, M. “A mechanics solution for hinges in RC beams with multiple cracks.” Submitted Engineering Structures 17/6/11.

Vonk, R.A. (1992). “Softening of concrete loaded in compression.” *PhD Thesis*, Eindhoven University of Technology, The Netherlands.

Del Viso, J.R., Carmona, J.R., and Ruiz, G. (2008). “Shape and size effects on the compressive strength of high-strength concrete.” *Cement and Concrete Research*, 38, 386-395.

Walraven, J. C., and Reinhardt, H. W. (1981). “Theory and experiments on mechanical behaviour of cracks in plain and reinforced concrete subjected to shear loading.” *Heron*, 26(1A), 1-68.

Walraven, J., Frenay, J., and Pruijssers, A. (1987). “Influence of concrete strength and load history on the shear friction capacity of concrete members.” *PCI journal*, 32(1), 66-84.

Wang, P. T., Shah, S.P., and Naaman, A. E. (1978). “Stress-strain curves of normal and lightweight concrete in compression.” *ACI Journal*, 75(11), 603-611.

Watanabe, K., Niwa, J., Yokota, H., and Iwanami, M. (2004). “Experimental study on stress-strain curve of concrete considering localized failure in compression.” *Journal of Advanced Concrete Technology*, 2(3), 395-407.

Weiss, W. J., Guler K., and Shah, S. P. (2001). “Localization and size-dependent response od reinforced concrete beams.” *ACI Structural Journal*, 98(5), 686-695.

Xie, J., Elwi, A. E., and MacGregor, J. G. (1995). “Mechanical properties of three high-strength concretes containing silica fume.” *ACI Materials Journal*, 92(2), 135-145.

Yi, S. T., Kim, J. H. J., and Kim, J. K. (2002). “Effect of specimen sizes on ACI rectangular stress block for concrete flexural members.” *ACI Structural Journal*, 99(5), 701-708.

Yi, S. T., Yang, E. I., and Choi, J. C. (2006). “Effect of specimen sizes, specimen shapes, and placement directions on compressive strength of concrete.” *Nuclear Engineering and Design*, 236,115-127.

Yip, W. K. (1998). “Generic form of stress-strain equations for concrete.” *Cement and Concrete Research*, 28(4), 499-508.

Muhamad, R., Mohamed Ali, M. S., Oehlers, D.J., and Sheikh, A.H. (2011). “Load-slip relationship of tension reinforcement in reinforced concrete members.” *Engineering Structures*, 33, 1098-1106.

Muhamad, R., Mohamed Ali, M.S., Oehlers, D.J., and Griffith, M.C. “The tension stiffening mechanism in reinforced concrete prisms.” Submitted International Journal of Advances in Structural Engineering.

NOTATION

χ	=	curvature
B	=	elastic contraction
C	=	total axial contraction
C_k	=	contraction corresponding to αP_p
C_p	=	total axial contraction at peak stress
d_c	=	depth of compression region
d_{el}	=	depth of elastic compression region
d_{ten}	=	depth of tension region
d_w	=	depth of the wedge
E	=	total lateral expansion
e	=	eccentricity
E_c	=	elastic Young's modulus
EI	=	flexural rigidity
E_p	=	total lateral expansion at peak stress
f_c	=	compressive strength of concrete
f_{ct}	=	tensile strength of concrete
$F_{el.c}$	=	compression elastic force
$F_{el.t}$	=	tensile elastic force
f_p	=	the average peak stress
F_w	=	wedge force
G	=	elastic expansion
H	=	the prism height
H_b	=	length of bulk zone
h_{cr}	=	separation of the crack
H_d	=	length of damage zone
j	=	the segment thickness of tensile region
k	=	compressive segment thickness

L	=	total axial load
L_{def}	=	the effective length (H/2)
L_p	=	the peak total axial load
L_w	=	the length of the wedge
m	=	the length of total axial contraction caused by settle down the position
M	=	moment
M_p	=	peak moment
P	=	axial load
P_p	=	the peak axial load
P_{ult}	=	ultimate load
P_w	=	load wedge
P_{wp}	=	the peak load wedge
R_x	=	expansion corresponding to αP_p
S	=	the prism length
S_w	=	slip wedge
S_{wp}	=	slip wedge at peak stress
V_w	=	wedge expansion
V_{wp}	=	wedge expansion at peak stress
W	=	the prism width
α	=	the constant when the non-linearity commence
δ	=	deformation
Δ	=	sliding of the crack
δ_w	=	deformation at which non-linear behavior commence
ε_c	=	compression strain
ε_{ct}	=	maximum tensile strain
ε_{eff}	=	effective strain
$\varepsilon_{non\text{-}lin}$	=	non-linear strain
ε_p	=	strain at peak stress
θ	=	rotation
θ_p	=	rotation at peak moment

θ_r	=	rotation at αM_p
σ	=	stress
σ_N	=	normal stress
σ_{ult}	=	ultimate stress
σ_w	=	stress wedge
σ_{wp}	=	peak stress wedge
τ_N	=	shear stress